2018

# Study of New Materials for Sodium-ion Batteries

Boyang Ruan

# Study of New Materials for Sodium-ion Batteries

This thesis is presented as part of the requirements for the conferral of the degree

**DOCTOR of PHILOSOPHY**

**Candidate: Boyang Ruan, B.Sc.**

**Supervisor: Prof. Jiazhao Wang**

Institute for Superconducting and Electronic Materials

Australian Institute of Innovative Materials

University of Wollongong, NSW, Australia

February, 2018

This research has been conducted with the support of an Australian Government Research Training Program Scholarship.

# Abstract

Sustainable energy sources, such as solar panels and wind turbines, have attracted ever-growing attention due to concerns about the issue of climate change. The utilization of these energy sources relies on the availability of large-scale energy storage systems. Currently, lithium-ion batteries (LIBs) have been widely used as power sources for portable electronic devices due to their high voltage, long cycle life, and ability to operate at ambient temperature, but the low abundance of lithium resources will make it hard to meet the demands of large-scale applications. Sodium-ion batteries (SIBs) are believed to be a promising alternative to LIBs due to the abundant natural resources of sodium. As is well-known, the key to success in the development of advanced SIBs to meet the renewable energy market demands is the electrode materials. It is thus necessary to develop and employ cost-effective electrode materials with the capacity for high energy density, high cycling stability, and excellent rate capability. Thus, more and more investigations on sodium ion batteries (SIBs) have been emerging in recent years.

The conducting polymer polypyrrole (PPy) and N-doped carbon especially with three-dimensional (3-D) structure have been proved to be excellent supporting and conducting agents due to their high electrical conductivity and structural stability. For enhancing the sodium diffusion coefficient and the conductivity, loading active materials onto PPy or N-doped carbon substrates to form carbonaceous composites are the most popular and most highly effective methods to achieve improved electrochemical performance. In this doctoral work, red phosphorus, tin dioxide, and tin were chosen as the most promising objects of study for anode materials in SIBs, although some of them still have unsatisfactory cycling performances. Through reducing the particle size and forming composites with nitrogen-containing conducting polymers, red phosphorus/N-doped carbon nanofibers, $SnO_2$–polypyrrole nanotubes, and carbon encapsulated Sn@N-doped carbon nanotubes composites were synthesized. Moreover, the influences of the morphology and the sodium storage mechanism of these electrode materials were investigated through various characterization techniques, including field emission scanning electron microscopy, transmission electron

microscopy, Fourier transform infrared spectroscopy, X-ray powder diffraction, Raman spectroscopy, thermogravimetric analysis, and X-ray photoelectron spectroscopy.

To study the reversibility of red P for sodium storage, a red phosphorus/N-doped carbon nanofiber composite (P/NCF) was prepared via a simple evaporation/deposition strategy. Because the poor electronic conductivity and huge volume expansion of red P are the main barriers which impede its reversibility and cycling stability, I chose porous N-doped carbon fiber with 3-D structure as the substrate to support the phosphorus particles in order to reduce the volume expansion of P, while also increasing the conductivity of the composite and shortening the paths for sodium ion transport. In the as-prepared P/NCF, most of the phosphorus was homogeneously distributed in the N-doped carbon fiber. Accordingly, the resultant composite as anode material demonstrated good sodium storage ability.

For the second subproject, $SnO_2$-coated polypyrrole (PPy) with a 3-D structured nanotube network was fabricated via a facile hydrothermal approach, which was achieved by hydrolyzing tin dichloride into tin dioxide on PPy tubes. The obtained $SnO_2$-coated polypyrrole nanotube has a 3-D structure with a uniform distribution of crystalline $SnO_2$ nanoparticles on the surfaces of the PPy tubes. Its structural properties result in good performance as an anode for application in SIBs.

A good reversible capacity of nearly 288 mA h $g^{-1}$ was delivered when discharging at 100 mA $g^{-1}$, with more than 69.1% capacity retention and stable coulombic efficiency of 99.6% over 150 cycles. The good electrochemical performance compared to the 151 mAh $g^{-1}$ achieved by bare $SnO_2$, which was fabricated by the same method in the absence of PPy, could be mainly attributed to the good dispersion of $SnO_2$ on the 3-D matrix of PPy tubes, which facilitates the diffusion of $Na^+$ ions and buffers the large volumetric changes during charge/discharge.

Carbon encapsulated Sn@N-doped carbon nanotubes were obtained via the simple reduction of C@$SnO_2$@N-doped carbon composite, which was fabricated by hydrothermal and carbon coating approaches. The Sn nanoparticles encapsulated in carbon layers were distributed uniformly on the surfaces of N-doped carbon nanotubes. The electrochemical performance of the composite was systematically investigated as anode material in sodium-ion batteries. The composite electrode could attain a good

reversible capacity of 398.4 mAh $g^{-1}$ when discharging at 100 mA $g^{-1}$, with capacity retention of 67.3 % and stable coulombic efficiency of 99.7 % after 150 cycles. This good electrochemical performance compared to only 17.5 mAh $g^{-1}$ delivered by bare Sn particles prepared by the same method without the N-doped carbon could be mainly ascribed to the good dispersion of the precursor $SnO_2$ on the substrate of N-doped carbon nanotubes with three-dimensional tructure, which provides more reaction sites to reduce the diffusion distance of $Na^+$, further facilitating the diffusion of $Na^+$ ions, and buffer the large volume expansion during charging/discharging.

In summary, PPy and N-doped carbon as carbon sources were employed to fabricate 3-D structured P/NCF, $SnO_2$–polypyrrole nanotubes, and carbon encapsulated Sn@N-doped carbon nanotube anode materials. The 3-D structured P/NCF, $SnO_2$–polypyrrole, and C@Sn@N-doped carbon anode materials performed well, with improved cycling stability and rate behavior in different energy storage systems. Therefore, I believe that these strategies using N-doped carbon materials as substrates to accommodate active materials such as P, $SnO_2$, Sn, etc. to prepare carbon composites will be very promising ways of obtaining anode materials with good electrochemical performance in SIBs.

# Acknowledgements

I would like to extend my sincere gratitude to my principal supervisor, Prof. Jiazhao Wang, who offered me an open PhD position in the Institute for Superconducting and Electronic Materials (ISEM) back in 2014. Prof. Wang provided me constant encouragement and guidance on my work and my life. Without her help, I couldn't have this precious opportunity to do my research work especially as my old age in ISEM and finish my PhD study. During the past four years, Prof. Wang created a free and warm work atmosphere which encouraged me to extend the knowledge vision and develop the potential research passions.

High tribute shall be paid to my co-supervisor, distinguished Prof. Huakun Liu and A/Prof.Shulei Chou for their advices and suggestions during my PhD career.

I would like to express my deeply gratitude to highly respected distinguished Prof. Dhixue Dou who provided me a lot of great supports in ISEM.

My sincere thanks to Prof. Xiaolin Wang, Jun Chen, Zaiping Guo, Zhenxiang Cheng; A/Prof. Konstantin Konstantinov, Dr. Zhenguo Huang, Dongqi Shi, Xun Xu, Yi Du for their kindly helps.

I also would like to thank Dr. Tania Silver, who always carefully read every manuscript and polish English during my PHD study.

Many thanks to Prof. William E. Price, A/Prof. Germanas Peleckis, Ms Joanne George, Narelle Badger, Crystal Mahfouz, Candace Gabelish, Paul Scully, Chris Peacock, Mr Tony Romeo, Gilberto Casillas Garcia, Mitchell Nancarrow for their supports during my study in AIIM.

I am grateful to Mr. Robert Morgan and other staffs for providing vital timely mechanical workshop support on the experimental devices.

I would like to thank Dr. Wenbin Luo, Xuanwen Gao, Jiantie Xu, Yunxiao Wang, Weijie Li, Chao Han, Wenping Sun, Zhijia Zhang, Jun Wang, Lanling Zhao, Lili Liu, Rejaul Kaiser, Yuhai Dou, Lei zhang, Zheyin Yu, Zhixin Tai, who gave me a lot of help in my primary research studies.

I would like to express my sincere thanks to Prof. Jianmin Ma, Dongliang Tian and Zhian Zhang, who provided me a lot of supports in my research works.

A big thanks to my colleagues, including Mr. Haipeng Guo, Ms. Qiannan Liu, Mr. Yuyang Hou, Ms. Fang Li, Lijuan Zhang, Mr. Weihong Lai, Zhe Hu, Mingzhe Chen, Ms. Qiuran Yang, Li Wang, Mr. Chunsheng Fang, Binwei Zhang, Ms. Yajie Liu, Hong Gao for their support to my research works in ISEM.

Finally, I would like to express my deepest gratitude to lovely wife sunny and son yuxi for their support and encouragement, as well as the pleasant time spent with them. I believe that my four-year PhD study in ISEM is a special and meaningful time for all of my family members.

# Table of Contents

# List of Figures

# List of Tables

# List of Schemes

# Lists of Nomenclature

## Abbreviations

| | |
|---|---|
| **3-D** | Three-dimensional |
| **APS** | Ammonium persulfate |
| **BET** | Brunner-Emmet-Teller |
| **BJH** | Barrett-Joyner-Halenda |
| **CV** | Cyclic voltammetry |
| **cm** | Centimeter |
| **CE** | Coulombic efficiency |
| **CMC** | Sodium carboxymethyl cellulose |
| **CVD** | Chemical vapour deposition |
| **CPE** | Constant phase element |

| | |
|---|---|
| **CTAB** | Cetyl-trimethylammonium bromide |
| **DEC** | Diethyl carbonate |
| **DI** | De-Ionized |
| **EC** | Ethylene carbonate |
| **EDS** | Energy dispersive X-ray spectroscopy |
| **EIS** | Electrochemical impedance spectroscopy |
| **EVs** | Electric vehicles |
| **ESS** | Energy storage system |
| **EC** | Ethylene Carbonate |
| **FEC** | Fluoroethylene carbonate |
| **FTIR** | Fourier transform inferior red Spectroscopy |

| | |
|---|---|
| **FSEM** | Field emission scanning electron microscopy |
| **GHG** | Greenhouse gas |
| **HMTA** | Hexamethylenetetramine |
| **LIBs** | Lithium-ion batteries |
| **MO** | Methyl orange |
| **mm** | Millimeter |
| **nm** | Nanometer |
| **PPy** | Polypyrrole |
| **RF** | Resorcinol-Formaldehyde |
| **SAED** | Selected area electron diffraction |
| **SEI** | Solid electrolyte interphase |

| | |
|---|---|
| **SEM** | Scanning electron microscopy |
| **SIBs or NIBs** | Sodium-ion batteries |
| **STEM** | Scanning transmission electron microscope |
| **TEM** | Transmission electron microscopy |
| **TMO** | Transition metal oxide |
| **TGA** | Thermogravimetric analysis |
| **TMS** | Transition metal sulphide |
| **XRD** | X-ray diffraction |
| **XPS** | X-ray photoelectron spectroscopy |

# List of Symbols

| Symbol | Name | Unit |
|---|---|---|
| **θ** | Angle of incidence with the lattice plane | degree |
| **λ** | X-ray wavelength of the incident beam | nm |
| **η** | Coulombic efficiency | % |
| **d** | Distance between lattice planes | nm |
| **f** | Frequency in the EIS test | Hz |
| **I** | Current density | A $cm^{-2}$ |
| **L** | Crystal size | nm |
| **m** | Active material weight | g |
| **P** | Relative pressure | $P_a$ |

| | | |
|---|---|---|
| **$P_0$** | Saturation pressure | $P_a$ |
| ***$R_{ct}$*** | Charge transfer resistance | Ω |
| ***$R_i$*** | Electrolyte resistance | Ω |
| **T** | Celsius temperature | °C |
| **T** | Kelvin temperature | K |
| **t** | Time | hour |
| ***W*** | Warburg impedance | Ω |
| **Zim** | Imaginary part of the impedance | Ω |
| **Zre** | Real part of the impedance | Ω |
| **Tm** | Melting point | °C |
| **Tb** | Boiling point | °C |

| | | |
|---|---|---|
| **Tf** | Flash point | ˚C |
| ***η*** | the viscosity (cP) 25 °C | |
| **ε** | the dielectric constant 25° C | |
| **$M_w$** | Molar mass | g $mol^{-1}$ |
| **σ** | Electrical conductivity | mS $cm^{-1}$ |
| **AN (DN)** | the acceptor and donor numbers | |

# List of Organisations

| | |
|---|---|
| **ISEM** | Institute for Superconducting and Electronic Materials |
| **EMC** | Electron Microscopy Centre |
| **AIIM** | Australian Institute of Innovative Materials |
| **UOW** | University of Wollongong |
| **ARC** | Australian Research Council |
| **IUPAC** | International Union of Pure and Applied Chemistry |

# Chapter 1

# 1. Introduction

## 1.1. General Background

With world concerns about climate change, which is commonly known as global warming and caused by greenhouse gas emissions (GHG, such as carbon dioxide, methane, nitrous oxide, and fluorinated gases),[1-4] the development of clean and renewable energy systems to meet increasing energy consumption is becoming more and more urgent. The Paris climate agreement has set out a global action plan to put the world on track to avoid dangerous climate change by keeping global temperature rise this century well below 2 degrees Celsius above pre-industrial levels and to pursue efforts to limit the temperature increase even further to 1.5 Celsius. Nowadays, there is a race on to find solutions for fulfilling this aim around the world. Although the technology for obtaining sustainable energy, such as with better solar panels, wind turbines, photovoltaic cells, etc., has made obvious progress in recent years,[5-7] the development of an energy storage system (ESS), which can integrate the renewable energy into the grid smoothly and effectively has lagged behind in relative terms.[8-11] So, it is important to rapidly develop such an ESS to satisfy the requirements for the widespread use of renewable energy. Among the various energy storage technologies, storage batteries are one of the most promising means for storing electricity on a large scale, due to their flexibility and high energy conversion efficiency. [12-17]

Lithium ion batteries (LIBs), due to their high energy density, long cycle life, and environmental friendliness, have been become the most common type of power source in the portable electronics market, for instance, in electric vehicles (EVs), portable devices, mobile phones, etc. [18-31] Nevertheless, the large-scale demand for Li would force us to consider the growing price of Li resources because of the low abundance of Li in the Earth's crust. Most of the easily accessible global lithium reserves are in remote or politically sensitive areas.[32-34] Based on calculations, total global Li

consumption in 2008 was approximately 21,280 tons; hence, mineable Li resources could be sustained for approximately 65 years from the present at most, considering an average growth of 5% per year.[32] For this reason, there is an urgent need to search for low-cost, highly safe, and long-cycle-life rechargeable batteries based on abundant resources.

Sodium is the fourth most abundant element in the Earth's crust and has seemingly unlimited distribution.[35-37] Na possesses similar chemical and physical properties to Li in many aspects, while sodium has a higher redox potential of -2.71 V versus standard hydrogen electrode and lower gravimetric capacity of 1165 mAh $g^{-1}$ compared with lithium (redox potential of -3.01 V and gravimetric capacity of 3829 mAh $g^{-1}$, respectively).[38-40] This makes the energy density of sodium ion batteries lower than for lithium ion batteries. In consideration of the requirements of large-scale energy storage systems, based on the abundant supply and widespread terrestrial reserves of Na mineral salts, this provides a compelling rationale for the development of sodium-ion batteries (SIBs) to be used as alternatives to LIBs.

## 1.2. A brief history and leading challenges for sodium-ion batteries

In the 1980s, SIBs were first investigated for electrochemical energy storage. SIBs have since turned into one of the hottest research topics for intensive investigations. Many electrode materials for lithium ion batteries have been examined for sodium ion storage, but their cycling performance, specific capacity, and rate capability are not desirable.[41-45] This is because the ionic radius of Na (1.06 Å) is larger than that of Li (0.76 Å), so the kinetic diffusion and storage mechanisms of Na are different from those of lithium ion batteries (LIBs). In exploring cathode materials for SIBs, the main problem is that the insertion of $Na^+$ is very difficult compared with $Li^+$, so the specific energy and power density of SIBs are smaller compared to LIBs. With regard to anode materials for SIBs, there are two main difficulties arising from the bigger ionic radius of Na. One is that the transformation reactions take place at relatively high potentials, consequently leading to a decrease in the overall cell voltage, especially in the cases of oxides, fluorides, chlorides, bromides, etc. Another relates to its volume changes, which

are larger than for its lithium-based equivalents on account of the bigger ionic radius of Na than that of Li. Generally, these factors are responsible for mechanical degradation in anode materials, leading to poor cycle life. Hence, to overcome these hurdles, our most important task is to find suitable electrode materials with high energy density and have electrochemical performances that can be improved through various approaches, such as controlling the morphology, structure, and size of the particles, and forming composites and compounds. This is not easy to do, however, because successful reversible intercalation hosts must possess channels and interstitial sites large enough to accept the larger $Na^+$ cation. For example, some electrode materials with excellent electrochemical properties in LIBs are electrochemically inactive in SIBs; for example, graphite and silicon cannot store sodium.

## 1.3. The objectives of this work

For the ultimate purpose of developing promising anode materials for SIBs with the properties of low cost, long cycle life, and environmental friendliness, the detailed objectives of this thesis are:

- Synthesis and evaluation of a number of anode materials (containing red phosphorus, tin dioxide, metal tin) for sodium-ion batteries;
- Characterization of the synthesized electrode materials using various techniques to understand their structural, morphological, physical, and electrochemical properties;
- Understanding the fundamental electrochemistry of sodiation /de-sodiation processes;
- Contributing to the next technological breakthrough in the field by opening up a pathway for the next generation sodium-ion batteries.

## 1.4. Thesis Structure

In order to achieve the goal of exploring new electrode materials with good electrochemical performances, different carbon containing composites including phosphorus/N-doped carbon nanofibers, $SnO_2$–polypyrrole nanotubes, and carbon

encapsulated Sn@N-doped carbon nanotubes synthesized different preparation methods have been employed in this work.

Moreover, in order to investigate the electrochemical performances of these electrode materials, detailed structural characterizations and electrochemical measurements have also been carried out. The scope of this thesis work is briefly outlined as follows:

Chapter 1 simply introduces the general background, main challenges, some approaches for improving the electrochemical performance of SIBs, and the outline of this study.

Chapter 2 presents a literature review on SIBs, consisting of basic concepts and working principles, electrode materials, and electrolytes.

Chapter 3 presents the chemicals and methods used for preparing electrode materials. This chapter also briefly introduces the characterization methods used to characterize the electrode materials: X-ray diffraction (XRD), photoelectron spectroscopy (XPS), Raman spectroscopy, thermogravimetric analysis (TGA), scanning electron microscopy (SEM), field emission scanning electron microscopy (FESEM), transmission electron microscopy (TEM), selected area electron diffraction (SAED), energy dispersive X-ray spectroscopy (EDS), and electrochemical measurements, which include cyclic voltammetry (CV), galvanostatic charge-discharge cycling, and electrochemical impedance spectroscopy (EIS).

Chapter 4 discusses the electrochemical reversibility of composites consisting of phosphorus and N-doped carbon nanofibers. A nanostructured phosphorus composite material (P/NCF) was fabricated from N-doped carbon and red phosphorus via an evaporation/deposition strategy. The P/NCF composite delivered an initial discharge capacity of 2752 mAh $g^{-1}$, and 26.5 % of the initial reversible capacity still remained after 55 cycles. In the composite, N-doped carbon nanofiber played an important role in the reversibility of the P/NCF composites. The N-doped carbon with porous 3-D structure acts as a buffer to alleviate the enormous stresses from the volume changes of the P particles and impedes the pulverization of particles. Meanwhile, the network of N-doped carbon provides the pathways for the electron transport, which can maintain good connections among the red phosphorus particles themselves and with the current

collector. (Results presented in Chapter 4 have been published, see Appendix: Publications.)

Chapter 5 presents a facile hydrothermal approach to obtain 3-D structured $SnO_2$–polypyrrole (PPy) nanotubes, which delivered a good reversible capacity of nearly 288 mA h $g^{-1}$ when discharged at 100 mA $g^{-1}$, with more than 69.1% capacity retention and stable coulombic efficiency of 99.6% after 150 cycles. These outcomes are attributed to the uniform coating of nanoscale tin dioxide particles on the PPy matrix with its unique 3-D structure, which can significantly improve the electronic conductivity of composites and accommodate the strain resulting from the volume changes in the electrode during cycling. At the same time, the diffusion speed of sodium ions is accelerated. On the other hand, a positive synergetic effect between the PPy interfaces and the $SnO_2$ particles is responsible for maximization of the $SnO_2$ conductivity. (Results presented in Chapter 5 have been published, see Appendix: Publications.)

Chapter 6 presents a user-friendly hydrothermal method to obtain carbon encapsulated Sn@N-doped carbon nanotubes. The electrochemical performance of the composite was systematically investigated as anode material in sodium-ion batteries (SIBs). The composite electrode could attain a good reversible capacity of 398.4 mAh $g^{-1}$ when discharged at 100 mA $g^{-1}$, with capacity retention of 67.3 % and very high coulombic efficiency of 99.7 % over 150 cycles. This good cycling performance, when compared to only 17.5 mAh $g^{-1}$ delivered by bare Sn particles prepared via the same method without the presence of N-doped carbon could be mainly ascribed to the uniform distribution of the precursor $SnO_2$ on the substrate of N-doped carbon tubes with three-dimensional structure, which provides more reaction sites to reduce the diffusion distance of $Na^+$, further facilitating $Na^+$ ion diffusion, and relieves the huge volume expansion during charging/discharging. These outcomes imply that such a Sn/C composite would provide more options as an anode candidate for SIBs. (Results presented in Chapter 6 have been published, see Appendix: Publications.)

Chapter 7 summarizes the work in this thesis and provides some prospects for the synthesis of other materials and for applications in other areas.

## 1.5. References

1. Meinshausen, M.; Meinshausen, N.; Hare, W.; Raper, S. C.; Frieler, K.; Knutti, R.; Frame, D. J.; Allen, M. R., Greenhouse-gas emission targets for limiting global warming to 2 C. *Nature* **2009,** *458* (7242), 1158-1162.

2. Allen, M. R.; Frame, D. J.; Huntingford, C.; Jones, C. D.; Lowe, J. A.; Meinshausen, M.; Meinshausen, N., Warming caused by cumulative carbon emissions towards the trillionth tonne. *Nature* **2009,** *458* (7242), 1163-1166.

3. Van Vliet, O.; Brouwer, A. S.; Kuramochi, T.; van Den Broek, M.; Faaij, A., Energy use, cost and $CO_2$ emissions of electric cars. *J. Power Sources* **2011,** *196* (4), 2298-2310.

4. Liu, C.; Li, F.; Ma, L. P.; Cheng, H. M., Advanced materials for energy storage. *Adv. Mater.* **2010,** *22* (8).

5. Tyagi, V.; Rahim, N. A.; Rahim, N.; Jeyraj, A.; Selvaraj, L., Progress in solar PV technology: Research and achievement. *Renewable and sustainable energy reviews* **2013,** *20*, 443-461.

6. Singh, G. K., Solar power generation by PV (photovoltaic) technology: A review. *Energy* **2013,** *53*, 1-13.

7. Bhutta, M. M. A.; Hayat, N.; Farooq, A. U.; Ali, Z.; Jamil, S. R.; Hussain, Z., Vertical axis wind turbine–A review of various configurations and design techniques. *Renewable and Sustainable Energy Reviews* **2012,** *16* (4), 1926-1939.

8. Li, L.; Wu, Z.; Yuan, S.; Zhang, X.-B., Advances and challenges for flexible energy storage and conversion devices and systems. *Energy Environ. Sci.* **2014,** *7* (7), 2101-2122.

9. Dunn, B.; Kamath, H.; Tarascon, J.-M., Electrical energy storage for the grid: a battery of choices. *Science* **2011,** *334* (6058), 928-935.

10. Pan, H.; Hu, Y.-S.; Chen, L., Room-temperature stationary sodium-ion batteries for large-scale electric energy storage. *Energy Environ. Sci.* **2013,** *6* (8), 2338-2360.

11. Yang, Z.; Zhang, J.; Kintner-Meyer, M. C.; Lu, X.; Choi, D.; Lemmon, J. P.; Liu, J., Electrochemical energy storage for green grid. *Chem. Rev.* **2011,** *111* (5), 3577-3613.

12. Yoshimoto, K.; Nanahara, T.; Koshimizu, G.; Uchida, Y. In *New control method for regulating state-of-charge of a battery in hybrid wind power/battery energy storage*

*system*, Power Systems Conference and Exposition, 2006. PSCE'06. 2006 IEEE PES, IEEE: 2006; pp 1244-1251.

13. Poullikkas, A., A comparative overview of large-scale battery systems for electricity storage. *Renewable and Sustainable Energy Reviews* **2013,** *27*, 778-788.

14. Koohi-Kamali, S.; Tyagi, V.; Rahim, N.; Panwar, N.; Mokhlis, H., Emergence of energy storage technologies as the solution for reliable operation of smart power systems: A review. *Renewable and Sustainable Energy Reviews* **2013,** *25*, 135-165.

15. Díaz-González, F.; Sumper, A.; Gomis-Bellmunt, O.; Villafáfila-Robles, R., A review of energy storage technologies for wind power applications. *Renewable and sustainable energy reviews* **2012,** *16* (4), 2154-2171.

16. Lawder, M. T.; Suthar, B.; Northrop, P. W.; De, S.; Hoff, C. M.; Leitermann, O.; Crow, M. L.; Santhanagopalan, S.; Subramanian, V. R., Battery energy storage system (BESS) and battery management system (BMS) for grid-scale applications. *Proceedings of the IEEE* **2014,** *102* (6), 1014-1030.

17. Ribeiro, P. F.; Johnson, B. K.; Crow, M. L.; Arsoy, A.; Liu, Y., Energy storage systems for advanced power applications. *Proceedings of the IEEE* **2001,** *89* (12), 1744-1756.

18. Song, J.; Wang, Y.; Wan, C. C., Review of gel-type polymer electrolytes for lithium-ion batteries. *J. Power Sources* **1999,** *77* (2), 183-197.

19. Lu, L.; Han, X.; Li, J.; Hua, J.; Ouyang, M., A review on the key issues for lithium-ion battery management in electric vehicles. *J. Power Sources* **2013,** *226*, 272-288.

20. Zhang, S. S., A review on electrolyte additives for lithium-ion batteries. *J. Power Sources* **2006,** *162* (2), 1379-1394.

21. De las Casas, C.; Li, W., A review of application of carbon nanotubes for lithium ion battery anode material. *J. Power Sources* **2012,** *208*, 74-85.

22. Zhang, W.-J., A review of the electrochemical performance of alloy anodes for lithium-ion batteries. *J. Power Sources* **2011,** *196* (1), 13-24.

23. Etacheri, V.; Marom, R.; Elazari, R.; Salitra, G.; Aurbach, D., Challenges in the development of advanced Li-ion batteries: a review. *Energy Environ. Sci.* **2011,** *4* (9), 3243-3262.

24. Aurbach, D., Review of selected electrode–solution interactions which determine the performance of Li and Li ion batteries. *J. Power Sources* **2000,** *89* (2), 206-218.

25. Scrosati, B., Recent advances in lithium ion battery materials. *Electrochim. Acta* **2000,** *45* (15), 2461-2466.

26. Tarascon, J.-M.; Armand, M., Issues and challenges facing rechargeable lithium batteries. *Nature* **2001,** *414* (6861), 359-367.

27. Malini, R.; Uma, U.; Sheela, T.; Ganesan, M.; Renganathan, N., Conversion reactions: a new pathway to realise energy in lithium-ion battery. *Ionics* **2009,** *15* (3), 301-307.

28. Wang, Y.; Cao, G., Developments in nanostructured cathode materials for high‐performance lithium‐ion batteries. *Adv. Mater.* **2008,** *20* (12), 2251-2269.

29. Doerffel, D.; Sharkh, S. A., A critical review of using the Peukert equation for determining the remaining capacity of lead-acid and lithium-ion batteries. *J. Power Sources* **2006,** *155* (2), 395-400.

30. Robertson, A.; West, A.; Ritchie, A., Review of crystalline lithium-ion conductors suitable for high temperature battery applications. *Solid State Ionics* **1997,** *104* (1), 1-11.

31. DO KYUNG, K.; Muralidharan, P.; LEE, H.-W.; RUFFO, R.; YANG, Y.; CHAN, C. K.; PENG, H.; HUGGINS, R. A.; CUI, Y., Spinel $LiMn_2O_4$ Nanorods as Lithium Ion Battery Cathodes. *Nano Lett.* **2008,** *8* (11), 3948-3952.

32. Zu, C.-X.; Li, H., Thermodynamic analysis on energy densities of batteries. *Energy Environ. Sci.* **2011,** *4* (8), 2614-2624.

33. Kucinskis, G.; Bajars, G.; Kleperis, J., Graphene in lithium ion battery cathode materials: A review. *J. Power Sources* **2013,** *240*, 66-79.

34. Tarascon, J.-M., Is lithium the new gold? *Nature chemistry* **2010,** *2* (6), 510-510.

35. de la Llave, E.; Borgel, V.; Park, K.-J.; Hwang, J.-Y.; Sun, Y.-K.; Hartmann, P.; Chesneau, F.-F.; Aurbach, D., Comparison between Na-Ion and Li-Ion cells: understanding the critical role of the cathodes stability and the anodes pretreatment on the cells behavior. *ACS Appl. Mater. Interfaces* **2016,** *8* (3), 1867-1875.

36. Slater, M. D.; Kim, D.; Lee, E.; Johnson, C. S., Sodium‐ion batteries. *Adv. Funct. Mater.* **2013,** *23* (8), 947-958.

37. Linden, D.; Reddy, T., Handbook of Batteries. 4th. McGraw-Hill. New York: 2010.
38. Adelhelm, P.; Hartmann, P.; Bender, C. L.; Busche, M.; Eufinger, C.; Janek, J., From lithium to sodium: cell chemistry of room temperature sodium–air and sodium–sulfur batteries. In *Beilstein journal of nanotechnology*, 2015; Vol. 6, p 1016.
39. Kim, S. W.; Seo, D. H.; Ma, X.; Ceder, G.; Kang, K., Electrode materials for rechargeable sodium ‐ ion batteries: potential alternatives to current lithium ‐ ion batteries. *Adv. Energy Mater.* **2012,** *2* (7), 710-721.
40. Hwang, J.-Y.; Myung, S.-T.; Sun, Y.-K., Sodium-ion batteries: present and future. *Chem. Soc. Rev.* **2017**.
41. Ellis, B. L.; Nazar, L. F., Sodium and sodium-ion energy storage batteries. *Current Opinion in Solid State and Materials Science* **2012,** *16* (4), 168-177.
42. Kim, H.; Kim, H.; Ding, Z.; Lee, M. H.; Lim, K.; Yoon, G.; Kang, K., Recent Progress in Electrode Materials for Sodium ‐ Ion Batteries. *Adv. Energy Mater.* **2016**.
43. Kim, Y.; Ha, K. H.; Oh, S. M.; Lee, K. T., High ‐ Capacity Anode Materials for Sodium ‐ Ion Batteries. *Chemistry-A European Journal* **2014,** *20* (38), 11980-11992.
44. Ong, S. P.; Chevrier, V. L.; Hautier, G.; Jain, A.; Moore, C.; Kim, S.; Ma, X.; Ceder, G., Voltage, stability and diffusion barrier differences between sodium-ion and lithium-ion intercalation materials. *Energy Environ. Sci.* **2011,** *4* (9), 3680-3688.
45. Yabuuchi, N.; Kubota, K.; Dahbi, M.; Komaba, S., Research development on sodium-ion batteries. *Chem. Rev.* **2014,** *114* (23), 11636-11682.

# Chapter 2

# Literature Review

## 2.1. General background

The development of lithium and sodium ions as charge carriers for electrochemical energy storage dates back to the 1970s.[1-6] When $TiS_2$ was first reported for lithium electrochemical intercalation and application in energy storage devices at ambient temperature in 1980,[7-9] almost the same time, it also demonstrated the feature of intercalating sodium ions in a highly reversible manner and the possibility of being applied for electrochemical energy storage at room temperature.[10] The development of $LiCoO_2$, a lithium-containing layered oxide synthesized by Goodenough as a positive electrode material for lithium storage,[11] marked the beginning of lithium ion batteries suitable for application. Even though $Na_xCoO_2$, the sodium containing layered oxide, was also reported during the same period as positive electrode for sodium ion storage,[12] studies on room-temperature sodium ion batteries almost stagnated in the following several decades. Meanwhile, the higher energy density of lithium, owing to its higher potential and lower mass, resulted in the significant research efforts being put into LIBs. The advancement of LIBs was further facilitated by the appearance of disordered carbon [13,14] and graphite anodes. [15-17] In particular, the commercialization of LIBs achieved by Sony in 1991[18] led to the exponential growth in the portable electronics market since the 1990s.[19-24]

When Stevens and Dahn demonstrated that hard carbon can deliver a high reversible capacity of 300 mAh $g^{-1}$ for sodium ion storage in 2000,[25] even though its cycle life was insufficient for battery applications at that time, investigations on sodium ion batteries attracted researchers' interest once again. To date, hard carbon has been extensively explored as a promising anode candidate for SIBs.[26-31] In cathode materials for SIBs, the most important discovery for SIBs was the first report of the cathode

properties of α-$NaFeO_2$ in 2006.[32] Since then, many cathode materials have been investigated for SIBs. [33]

Studies on sodium ion batteries have increased dramatically in recent years since 2010, owing to the ever-increasing worldwide demand for large-scale batteries for renewable energy storage systems. In term of large-scale applications, LIBs have been developed as the main power sources and are playing more and more important roles in the emerging market for electric vehicles and energy storage.[34-37] Nevertheless, the high geographic concentration and limited reserves of lithium in nature will severely restrict the prospects for LIBs in grid energy storage applications. Based on the calculations, overall global Li consumption in 2008 was about 21, 280 tons; hence, present mineable resources could be sustained for approximately 65 years at most at an average growth rate of 5% per year,[38,39] making it very difficult to meet the increasing demand for lithium.

Sodium, the fourth most abundant element in the Earth's crust, has a seemingly unlimited distribution.[40] It is located below lithium in the periodic table of elements and has similar chemical and physical properties to Li in many aspects, as shown in Table 2.1.[41] Sodium is heavier than lithium (23 g $mol^{-1}$ versus 6.9 g $mol^{-1}$) and possesses a higher standard electrode potential (-2.71 V vs. standard hydrogen electrode (SHE) as compared to -3.02 V vs. SHE for lithium), so, there is a lower gravimetric capacity of 1165 mAh $g^{-1}$ for sodium than the gravimetric capacity of 3829 mAh $g^{-1}$ for Li. In addition, $Na^+$ ions (1.02 Å) are larger compared to $Li^+$ ions (0.76 Å), which could affect the phase stability, transport properties, and interphase formation.[42] The manufacturing costs of Li-ion batteries and Na-ion batteries are presented in Table 2.2.[43] It can be found that the cost of cathode material in SIBs is l3.6% lower than in LIBs. Beyond that, compared with the expensive copper used for Li-ion batteries, cheap Al can also be used as a substitute for the current collector in Na-ion batteries, since Al does not react with Na, which can bring about an 8 % cost reduction. Therefore, LIBs are estimated to be probably about 10% less expensive in total cost than LIBs. In regard to low cost and sustainability, the question of whether the batteries have high energy density becomes unimportant. This is why the sodium ion battery is considered as a promising candidate for application in large-scale energy storage systems.[44-54]

**Table 2.1** Comparison of Lithium and Sodium characteristics. Reproduced with permission [41].

| Category | Sodium | Lithium |
|---|---|---|
| Atomic mass (g $mol^{-1}$) | 23 | 6.9 |
| Ionic radius (Å) | 1.02 | 0.76 |
| $E^{\theta}$ (vs. SHE)/V | -2.71 | -3.04 |
| Melting point (°C) | 97.7 | 180.5 |
| Capacity of metal electrode (mAh $g^{-1}$) | 1165 | 3829 |
| Coordination preference | Octahedral and tetrahedral | Octahedral and prismatic |

**Table 2.2** Comparison of the manufacturing costs for Li-ion batteries and Na-ion batteries. Reproduced with permission [43].

| Components | percentage cost in SIBs | percentage cost in LIBs |
|---|---|---|
| Cathode | 32.4% | 36% |
| Anode | 13% | 13% |
| Electrolyte | 8% | 9% |
| Separator | 14% | 14% |
| Current collector | 8% with Al foil | 16% with Al & Cu foil |
| Others | 12% | 12% |

## 2.2 Basic concepts

The configuration and fundamental working principles of sodium ion batteries are shown in Scheme. 2.1. An SIB consists of two sodium insertion materials, the positive (cathode) and negative (anode) electrodes, which are divided by the separator. Sodium ions are shuttled between the cathode and anode through the electrolyte as a pure ionic conductor (in general, a sodium salt dissolved in aprotic polar solvents) between the electrodes on discharge and charge. During the discharge process, the electrons are released from the anode, causing an oxidation reaction, and transferred via the external

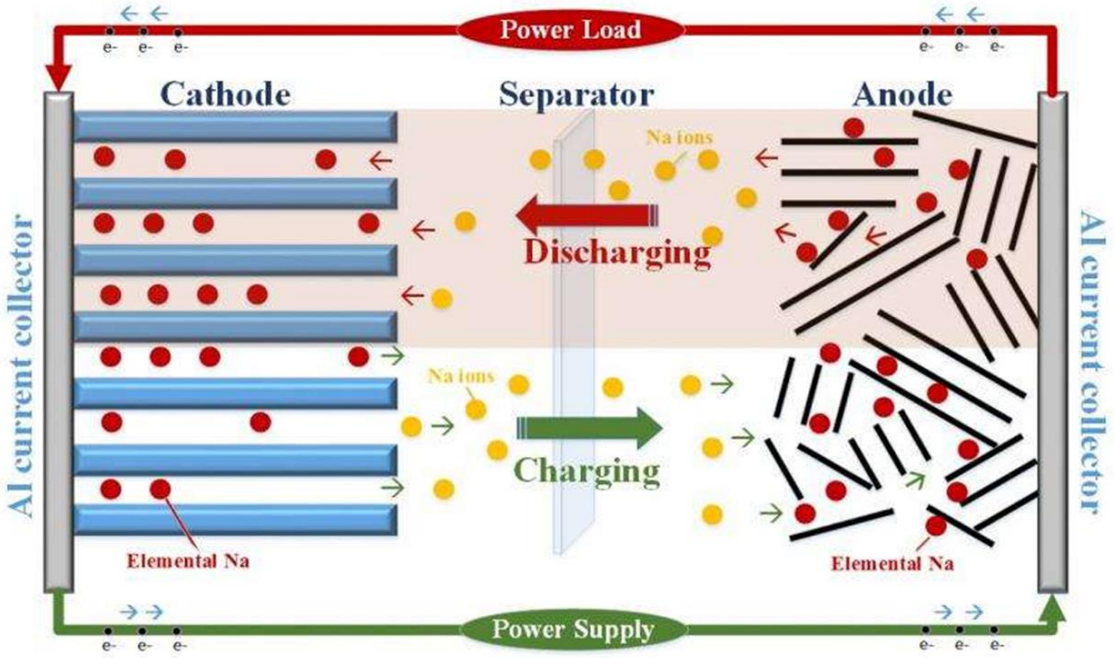


**Scheme 2.1** Schematic illustrations of battery components and electric storage mechanisms for SIBs.

circuit to the cathode, where the reductive chemical reactions take place. The reverse transfer of electrons occurs during the charge process.

## 2.3. Current cathode materials for sodium ion batteries

In a full battery cell, the cathode undertakes the most crucial role in terms of both the electrochemical performance and the total manufacturing cost for advanced commercial SIBs, which are needed to satisfy the requirements of a large-scale energy storage system. Therefore, it is very important to develop promising cathode materials for SIB technology. To date, major efforts have been devoted to the search for high performance cathode materials in layered systems of the $O_3$ and $P_2$ types, as well as polyanionic compounds, Prussian blue analogues, organic compounds, etc., as shown in Fig. 2.1.[55]

### 2.3.1. Layered sodium transition metal oxides (TMO)

The most common layered structures of transition metal oxides are built up from sheets of edge-sharing $MeO_6$ octahedra, where Me is a metal. Polymorphisms appear when the sheets of edge-sharing $MeO_6$ octahedra are stacked with different stacking sequences along the *c*-axis direction. [56] In general, these crystal structures consist of sheets of edge-sharing $MeO_6$ octahedral layers sandwiched between Na ion layers, into

which ionic species are in inserted in an octahedral (O) or a prismatic (P) environment. Accordingly, sodium-based layered compounds can be categorized into two major groups: $O_3$ type and $P_2$ type, in which the sodium ions are accommodated at octahedral and prismatic sites, respectively, as shown in Fig. 2.2.[57]

$O_3$-type $NaMeO_2$ comprises a cubic close-packed (ccp) oxygen array where sodium and 3d transition-metal ions are located on the clear octahedral sites because the ionic radius of sodium ions (1.02 Å) is much larger than those of 3d transition-metal ions with a trivalent state (< 0.7 Å).[58] $O_3$-type layered phases are categorized as one of the cation-ordered rock-salt superstructure oxides.[59] Edge-sharing $NaO_6$ and $MeO_6$ octahedra order themselves into alternate layers perpendicular to [111], forming the $NaO_2$ and $MeO_2$ slabs, respectively.There are three different $MeO_2$ layers (AB, CA, and BC layers) existing along the $NaMeO_2$ crystallographic axis. As for the $P_2$-type, $Na_xMeO_2$ is composed of two $MeO_2$ layers (AB and BA layers). The sodium surroundings are different from in the $O_3$ type. All the $Na^+$ ions are located in the

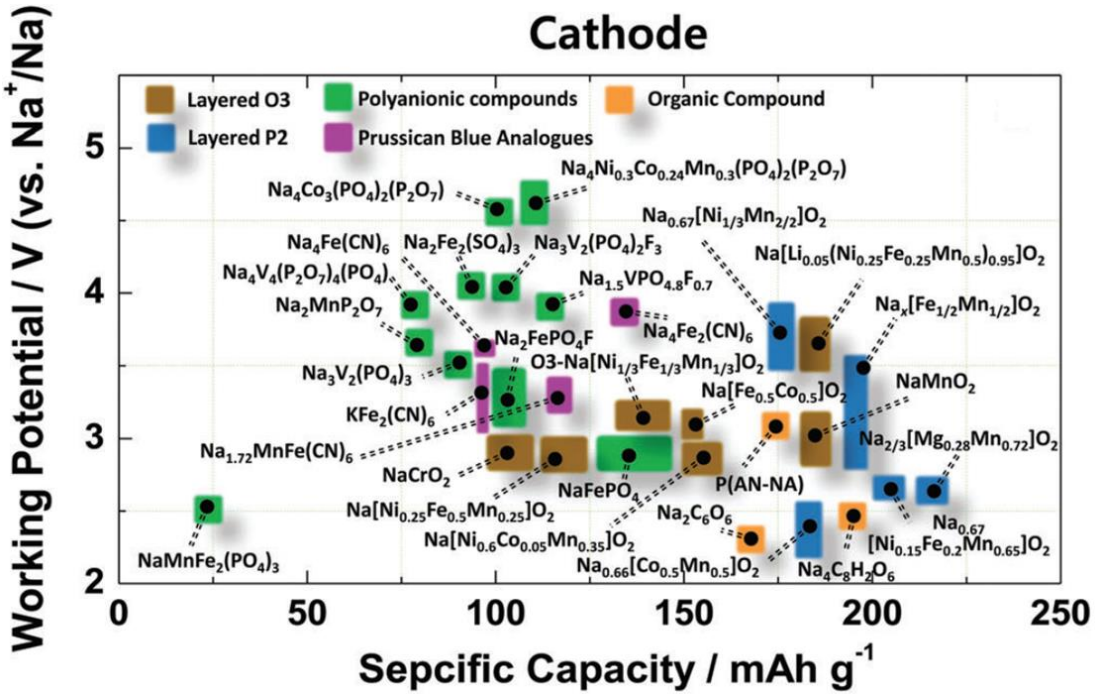


**Figure 2.1** Recent research progress on cathode materials for SIBs. Reproduced with permission [55].

trigonal prismatic sites of the Na layers. The $P_2$-type layered structure is also often classified as a 2H phase with space group $P6_3/mmc$.[60]

A phase transition generally occurs when the sodium is extracted from $O_3$- and $P_2$-type phases. In the $O_3$-type phase, sodium ions are originally stabilized at edge-sharing octahedral sites with $MeO_6$ octahedra. When sodium ions are partly extracted from the $O_3$-type phase, Na ions at prismatic sites become energetically stable, which is related to the formation of vacancies, similar to what happens in the $P_2$-type phase. The formation of prismatic sites is obtained by the sliding of $MeO_2$ slabs without breaking Me−O bonds.[61] Consequently, the oxygen packing changes from "AB CA BC" to "AB BC CA", and this phase is classified as a $P_3$-type phase, as presented in Fig. 2.2. In some cases, this $P_3$-type phase can be directlt crystallized without electrochemical sodium extraction in SIBs. For example, $P_3$- and $P_2$-type $Na_{2/3}[Ni_{1/3}Mn_{2/3}]$ $O_2$ are believed to be low- and high-temperature phases, respectively.[62] The phase transition from $P_2$-/$O_3$- to $P_2$-type in SIBs is impossible because its phase transition can only be attained by breaking/reforming Me−O bonds and therefore requires a higher temperature environment. On the contrary, $P_2$ phase can be transformed into an $O_2$-type phase in Na cells. This is because large prismatic sites in the $P_2$-type phase are energetically stabilized by large sodium ions. The gliding of $MeO_2$ slabs to form octahedral sites can only proceed after the extraction of sodium ions [63,64] or the exchange of $Na^+$ ions. [65] This movement of $MeO_2$ leads to the formation of a new phase with a unique oxygen packing, "AB AC AB", as seen in Fig.2.2. This phase contains two crystallographically different $MeO_2$ layers with AB and AC oxygen arrays. Vacancies left in between the AB and AC layers are octahedral sites, i.e., the $O_2$-type phase. Both of $O_3$-and $O_2$-type phases have close-packed oxygen arrays. An ABC-type oxygen arrangement (namely the ccp array) is the characteristic feature of $O_3$-type phase, and $NaO_2$ layers share only edges with $MeO_2$ layers on both sides. $O_2$-type phase consists of two oxygen arrangements, i.e. ABA-type and ACA-type, which are classified as a hexagonal close-packed (hcp) oxygen array. According to the oxygen packing, the $O_2$-type structure is classified as an intergrowth structure between ccp and hcp arrays. This intergrowth structure usually results in the formation of stacking faults after sodium extraction from

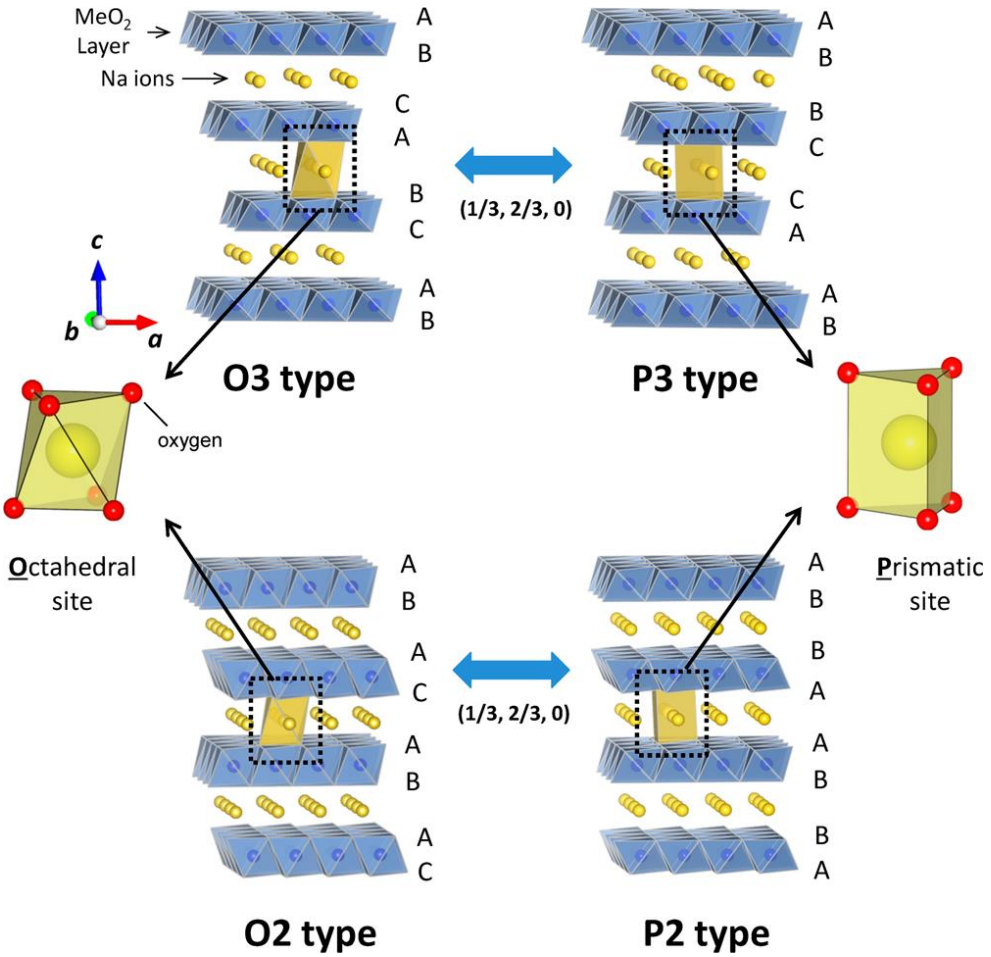


**Figure 2.2.** Categories of Na−Me−O layered materials with sheets of edge-sharing $MeO_6$ octahedra and phase transition processes induced by sodium extraction. Reproduced with permission [57].

the $P_2$ phase.[63] There are some reports on $P_2$−$O_2$ phase transitions in SIBs by $Na^+$ ion exchange, including the formation of a variety of stacking faults.[66-72]

Usually, the series of materials with the $O_3$-type and $P_2$-type layered structures are prepared by conventional solid-state reaction. The clear difference between them in their X-ray diffraction (XRD) patterns between them is displayed in Figure 2.3.[73] These Bragg diffractions that are indexed to the hexagonal layered structure with space group *C2/m* (indicative of a typical $O_3$-type layered structure) [74] and space group Cmcm (indicative of a typical $O_3$-type layered structure) [75] confirm their structural characteristics.

Many researchers have focused on the investigation of phase transitions during the

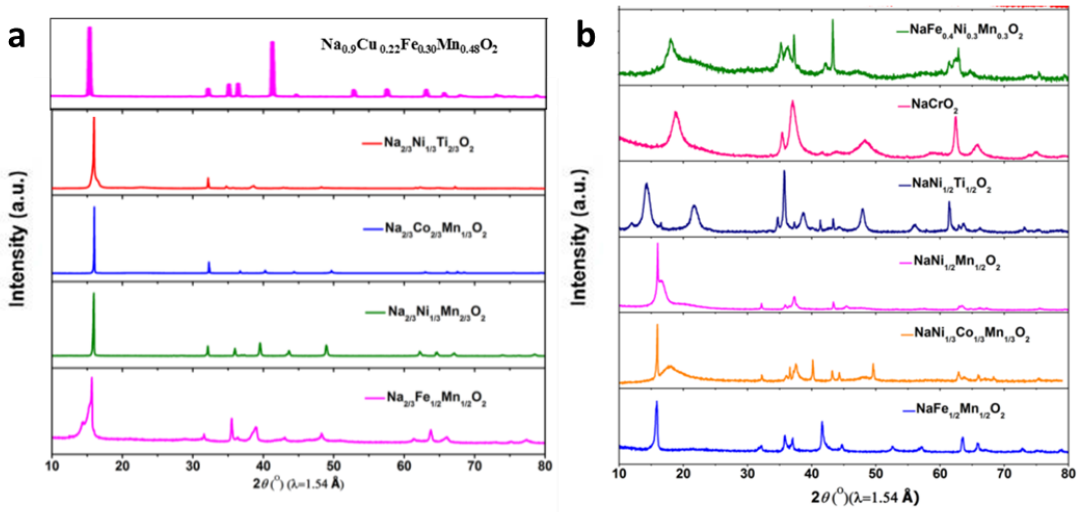


**Figure 2.3** XRD profiles of (a) $O_3$-type and (b) $P_2$-type $Na_xMe_yO_2$. Reproduced with permission [73].

charge-discharge process, which lead to serious degradation in both the capacity and cycle life.[76-83] From the in situ XRD patterns shown on Fig. 2.4, characteristic peaks which represent different phase types can be clearly found during charge/discharge processes. For example, the $O_3$ material $Na_{0.9}[Cu_{0.22}Fe_{0.30}Mn_{0.48}]O_2$ performed a reversible phase transition process of $O_3 \rightarrow P_3 \rightarrow O_3' \rightarrow P_3 \rightarrow O_3$.[73] Accordingly, $Ni_{0.45}Cu_{0.05}Mn_{0.4}Ti_{0.1}O_2$ also displayed a similar phase transition of $O_3 \rightarrow P_3 \rightarrow O_3$ during the process of electrochemical Na deintercalation and intercalation[83] On the other hand, some materials such as $NaNi_{0.25}Co_{0.25}Fe_{0.25}Mn_{0.125}Ti_{0.125}O_2$ and $Na[Li_{0.05}(Ni_{0.25}Fe_{0.25}Mn_{0.5})_{0.95}]O_2$ are not capable of reversible structure change.[80] Most materials with $O_3$-type and $P_2$ layered structures are usually composed of large particles with the distribution of particle size ranging from micrometer to submicron and have very similar morphologies, as shown on Fig.2.5.[73,80,83-85]

$Na[Li_{0.05}(Ni_{0.25}Fe_{0.25}Mn_{0.5})_{0.95}]O_2$ was prepared via a coprecipitation method and crystallized to form an $O_3$-type α-$NaFeO_2$ layered structure with $R\bar{3}m$ space group.[79] This electrode exhibited very high capacity (180.1 mA h $g^{-1}$ at the 0.1 C-rate), as well as excellent capacity retention (0.2 C-rate: 89.6%, 0.5 C-rate: 92.1%) and good rate capabilities at various C-rates (0.1 C-rate: 180.1 mA h $g^{-1}$; 1 C-rate: 130.9 mA h $g^{-1}$; 5 C-rate: 96.2 mA h $g^{-1}$) that were achieved due to the Li supporting structural stabilization on its introduction into the transition metal layer. Another cathode, lithium-

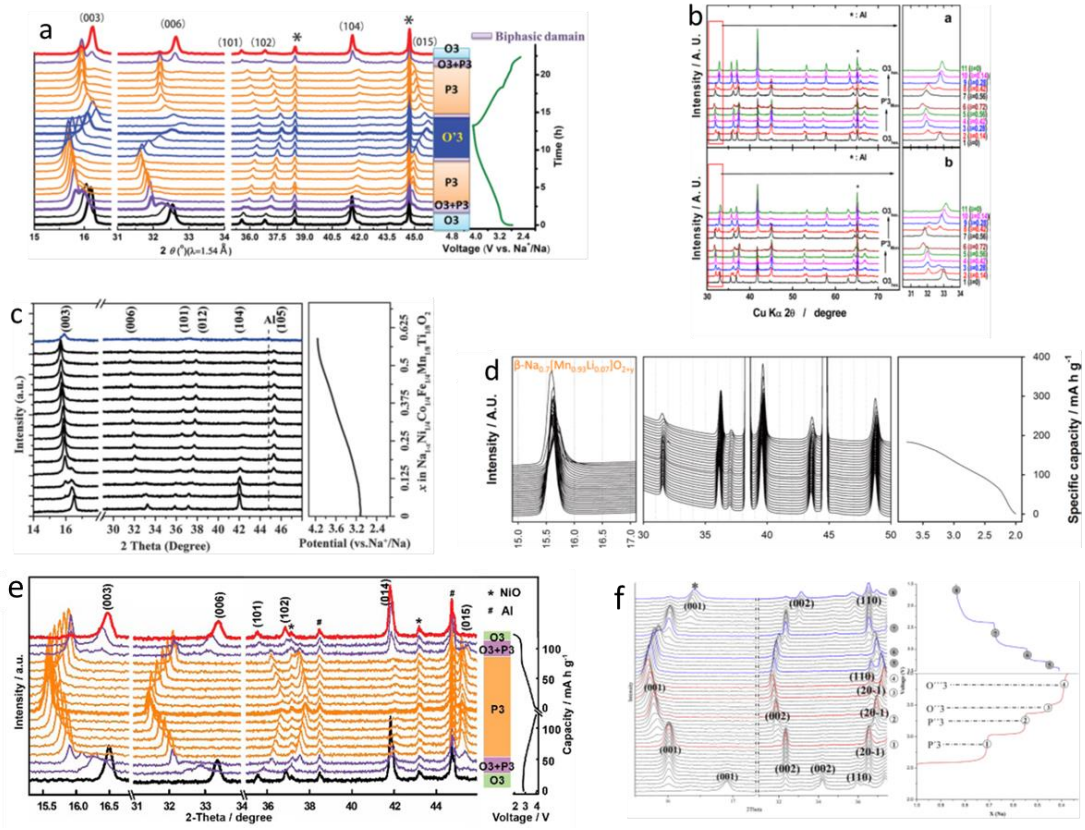


**Figure 2.4** In-situ XRD patterns from electrochemical charge/discharge process of $Na_{0.9}[Cu_{0.22}Fe_{0.30}Mn_{0.48}]O_2$ (a), $Na[Li_{0.05}(Ni_{0.25}Fe_{0.25}Mn_{0.5})_{0.95}]O_2$ (b), $NaNi_{0.25}Co_{0.25}Fe_{0.25}Mn_{0.125}Ti_{0.125}O_2$ (c), $\beta$-$Na_{0.7}[Mn_{0.93}Li_{0.07}]O_{2+y}$ (d), $NaNi_{0.5}Mn_{0.4}Ti_{0.1}O_2$ (e) and $NaNiO_2$ (f). Reproduced with permission [73][78][79][80][82][83].

free $Na[Ni_{0.25}Fe_{0.25}Mn_{0.5}]O_2$ was also produced for comparison, as displayed in Fig.2.6.

Combined structural modulation was employed to improve the air stability of the $O_3$-type metal oxide $NaNi_{0.45}Cu_{0.05}Mn_{0.4}Ti_{0.1}O_2$ (NaNCMT) by reducing the interlayer distance of Na layers in $NaNi_{0.5}Mn_{0.5}O_2$ (NaNM) via Cu/Ti co-substitution, and simultaneously increasing the valence state of the transition metals.[83] As displayed in Fig. 2.7, the stable NaNCMT cathode shows a smooth charge/discharge profile, delivering an initial discharge capacity of 124 mAh $g^{-1}$ and good cycling performance. After 500 cycles at 1 C, the NaNCMT can still show 70.2% capacity retention. Furthermore, the NaNCMT cathode exhibits superior rate performance. At a rate of 10 C, NaNCMT even delivered a capacity as high as 81 mAh $g^{-1}$.

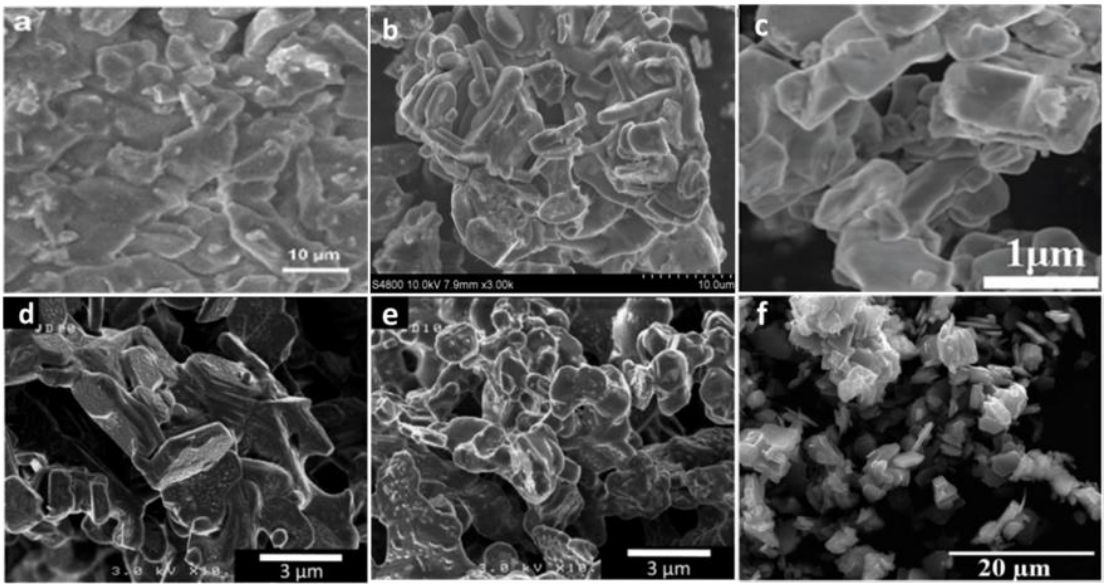


**Figure 2.5** Typical SEM images of $O_3$-type $NaNi_{0.45}Cu_{0.05}Mn_{0.4}Ti_{0.1}O_2$ (a), $Na_{0.9}[Cu_{0.22}Fe_{0.30}Mn_{0.48}]O_2$ (b), $NaNi_{0.25}Co_{0.25}Fe_{0.25}Mn_{0.125}Ti_{0.125}O_2$ (c), $Na_{0.82}Mn_{1/3}Fe_{2/3}O_2$ (d), $P_2$-type $Na_{0.71}Mn_{0.5}Fe_{0.5}O_2$ (e), and $Na_{2/3}[Fe_{0.5}Mn_{0.5}]O_2$ (f). Reproduced with permission [73][80][83][84][85].

Some $P_2$–type cathodes, such as $Al_2O_3$ coated $Na_{2/3}[Ni_{1/3}Mn_{2/3}]O_2$ cathode, was prepared through a solid state reaction and wet chemistry method.[86] This strategy takes advantage of an $Al_2O_3$ coating to suppress the unfavourable side reaction at high voltage and the exfoliation of the metal oxide layers. The as-prepared composite can present a 164 $mAh/g^{-1}$ initial specific discharge capacity within the voltage window from 2.5 V to 4.3 V and an enhanced 73.2% retention after 300 cycles, as shown in Fig. 2.8.

Another series of $P_2$-type cathode materials $Na_xNi_{0.167}Co_{0.167}Mn_{0.67}O_2$ with different sodium contents ($x$ = 0.45,0.55, 0.67, 0.8, 0.9, 1) were synthesized, and the effects of sodium content on their structure and electrochemical performance were investigated.[87] The results reveal that $Na_xNi_{0.167}Co_{0.167}Mn_{0.67}O_2$ ($x$ = 0.45, 0.55) consists of $P_2$-phase and $P_3$-phase, while $Na_xNi_{0.167}Co_{0.167}Mn_{0.67}O_2$ ($x$ = 0.67, 0.8, 0.9, 1) exhibits pure $P_2$-phase. Among them, $Na_{0.67}Ni_{0.167}Co_{0.167}Mn_{0.67}O_2$ shows excellent cycling stability and rate performance, as shown in Fig. 2.9(g) and (h). After 200 cycles, the $P_2$ structure of $Na_xNi_{0.167}Co_{0.167}Mn_{0.67}O_2$ ($x$ = 0.67, 0.8, 0.9, 1) was well maintained.

### 2.3.2. Polyanionic compounds

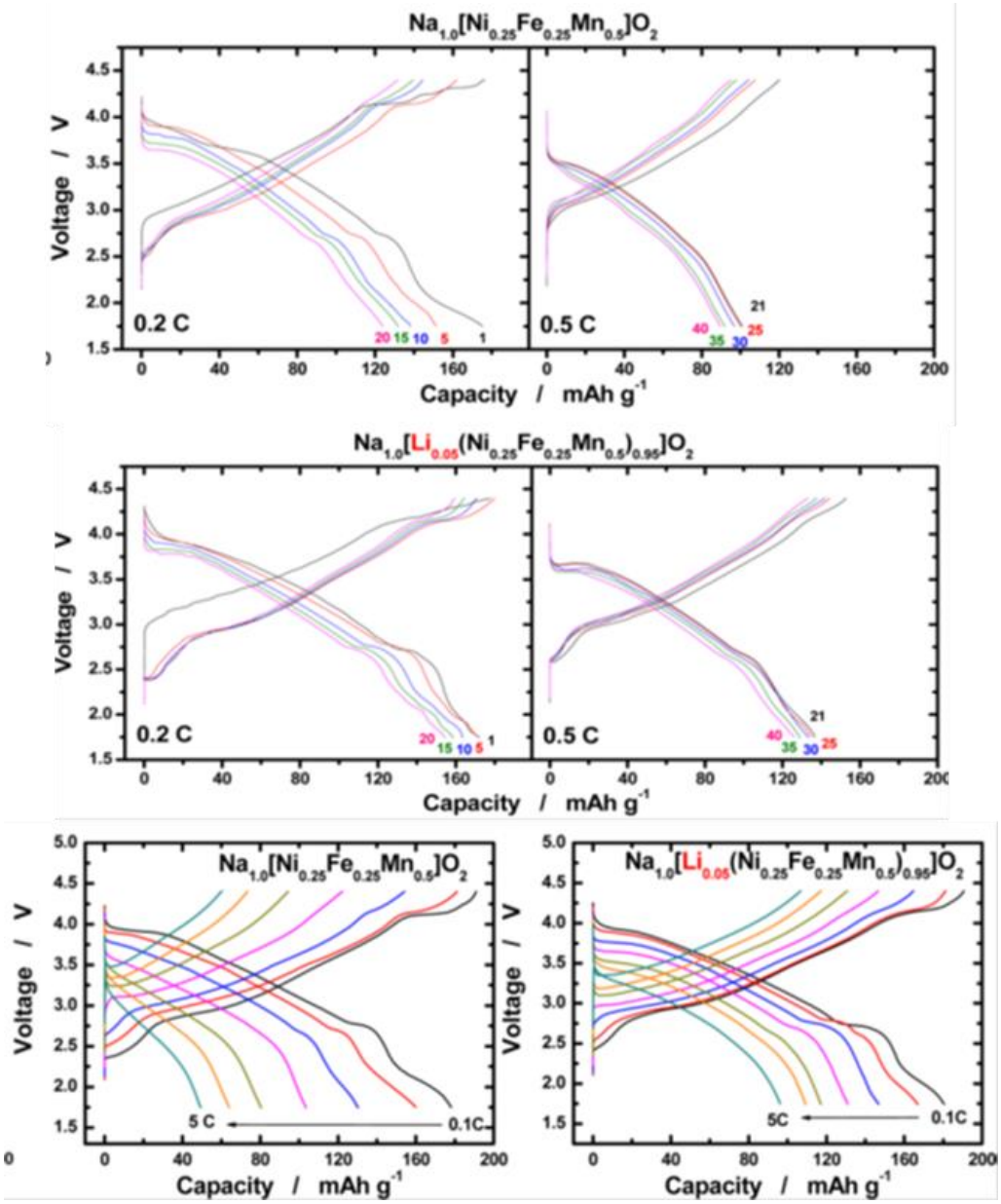


**Figure 2.6** Charge and discharge curves of $Na[Li_{0.05}(Ni_{0.25}Fe_{0.25}Mn_{0.5})_{0.95}]O_2$ and Na $[Ni_{0.25}Fe_{0.25}Mn_{0.5}]$ $O_2$ at different C-rates. Reproduced with permission [79].

Polyanionic compounds have been receiving intensive interest as Na intercalation cathodes for SIBs owing to their structural diversity and stability, as well as the strong inductive effect of the anions.[88-95] They can be mainly classified into these groups: Phosphates, including $NaMPO_4$, M = transition metal, sodium superionic conductor

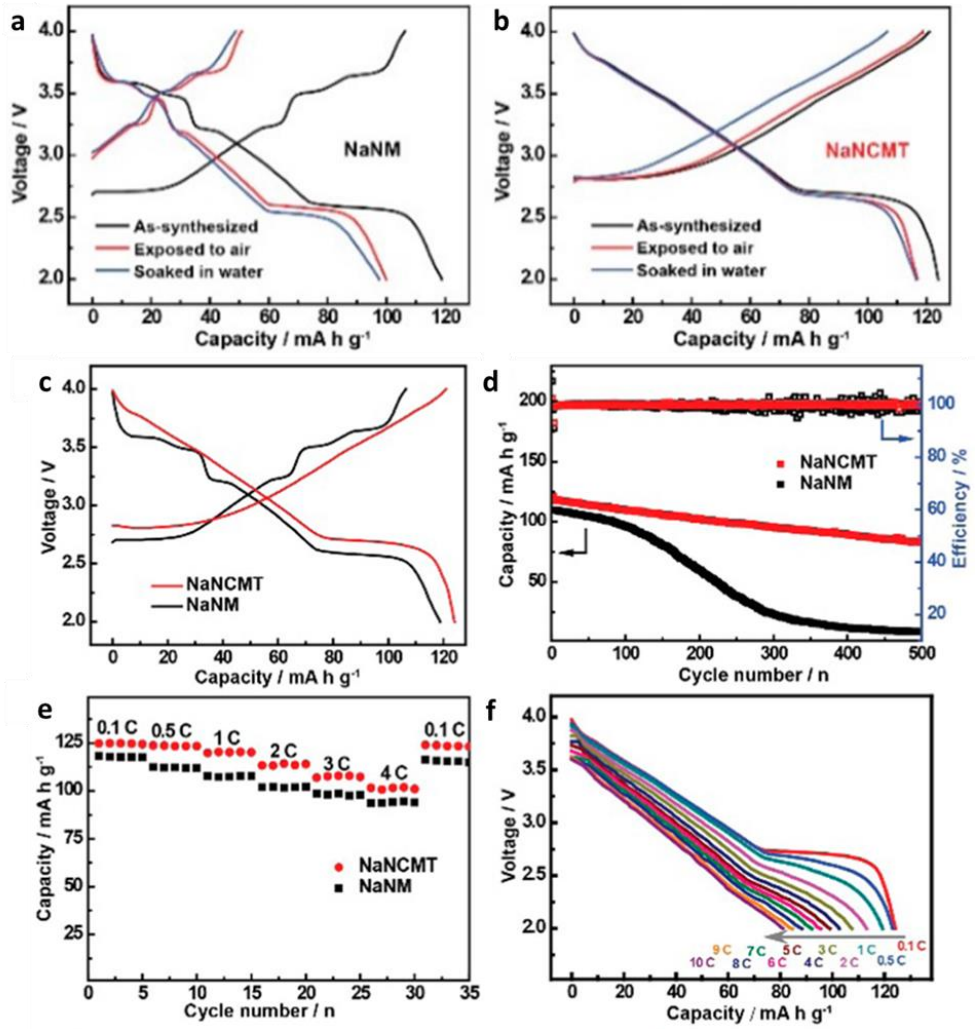


**Figure 2.7** Initial charge/discharge curves of as-synthesized and aged (a) NaNM and (b) NaNCMT. Comparison of the first charge/discharge curves tested at 0.1 C (c) and the cycling stability and Coulombic efficiency tested at 1 C (d) for both samples. Rate capability of both samples (e). Discharge curves of NaNCMT cycled at constant charge at 0.5 C/discharge rates from 0.1C to 10 C (f). Reproduced with permission [83].

(NASICON)-type $Na_xM_2(PO4)_3$, and vanadyl phosphate. Pyrophosphates ($Na_2MP_2O_7$ (M = Fe, Mn, Co) and $Na_4M_3(PO_4)_2P_2O_7$). Fluorophosphates ($Na_2MPO_4F$, $Na_3(VO_x)_2(PO_4)_2F_{3-2x}$, M = Fe, Co, Mn). Sulphates ($Na_2Fe_2(SO_4)_3$, $Na_2Fe(SO_4)_2{\cdot}2H_2O$). The structures of these phosphates are shown in Fig. 2.10.[33]

### 2.3.2.1. Phosphates

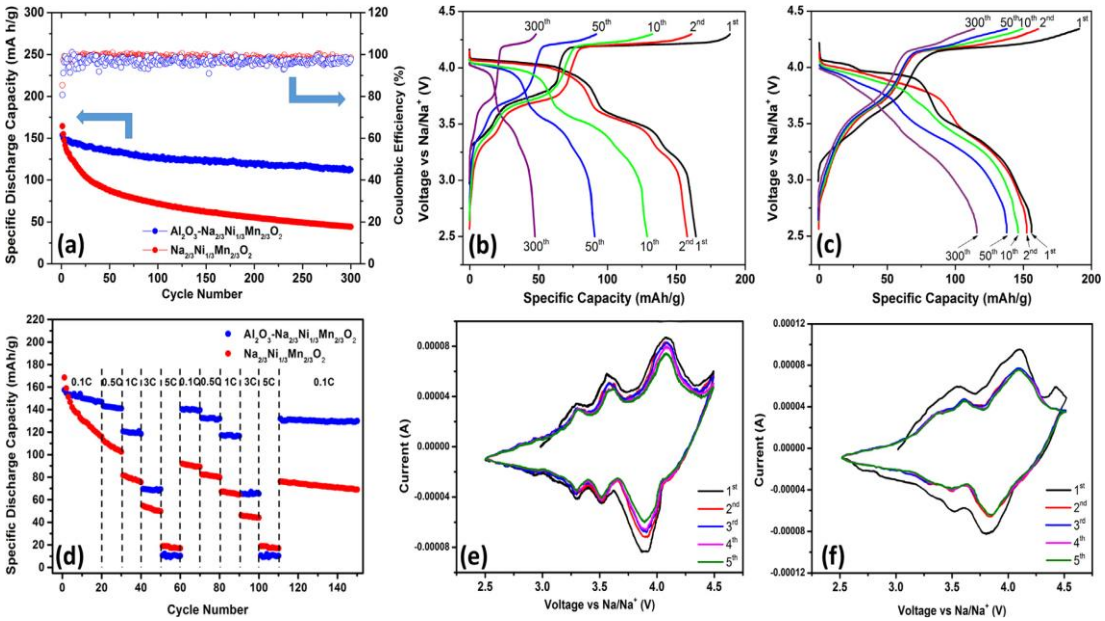


**Figure 2.8** Cycling performance of the as-prepared $Na_{2/3}[Ni_{1/3}Mn_{2/3}]O_2$ and $Al_2O_3$-$Na_{2/3}[Ni_{1/3}Mn_{2/3}]O_2$ (a) . The charge and discharge profiles of $Na_{2/3}[Ni_{1/3}Mn_{2/3}]O_2$ electrode (b) and $Al_2O_3$-$Na_{2/3}[Ni_{1/3}Mn_{2/3}]O_2$ electrode (c). Rate performance of the as-prepared $Na_{2/3}[Ni_{1/3}Mn_{2/3}]O_2$ and Al2O3-$Na_{2/3}[Ni_{1/3}Mn_{2/3}]O_2$ (d) . Cyclic voltammetry profiles of as-prepared $Na_{2/3}[Ni1/3Mn_{2/3}]O_2$ cathode (e) and $Al_2O_3$-$Na_{2/3}[Ni_{1/3}Mn_{2/3}]O_2$ cathode (f). Reproduced with permission [86].

The lattice framework in the olivine-$NaFePO_4$ structure is preferable for sodium-ion insertion and transmission, ensuring superior reversibility and a long cycle life. Due to the poor electrical conductivity and low $Na^+$-diffusion coefficient, however, the practical capacity of olivine $NaFePO_4$ is always much lower than the theoretical capacity. Therefore, many approaches have been employed to alleviate this issue via modifying the structure. Hollow amorphous $NaFePO_4$ nanospheres fabricated by an in-situ hard template method exhibited high storage capacity and rate capability.[96]From the images displayed in Fig. 2.11, it can be seen that large-scale uniform hollow spherical particles with an average diameter of about 20 nm have been obtained, where the average shell thickness is about 2 nm. The hollow nanospheres are assembled from tiny nanoparticles and exhibit a rough surface with interconnected porous structures. These hollow $NaFePO_4$ nanospheres exhibited long-term cycling stability. When cycled at a current density of 0.1 C, 144.3 mA h $g^{-1}$ capacity still remained after 300 cycles. The

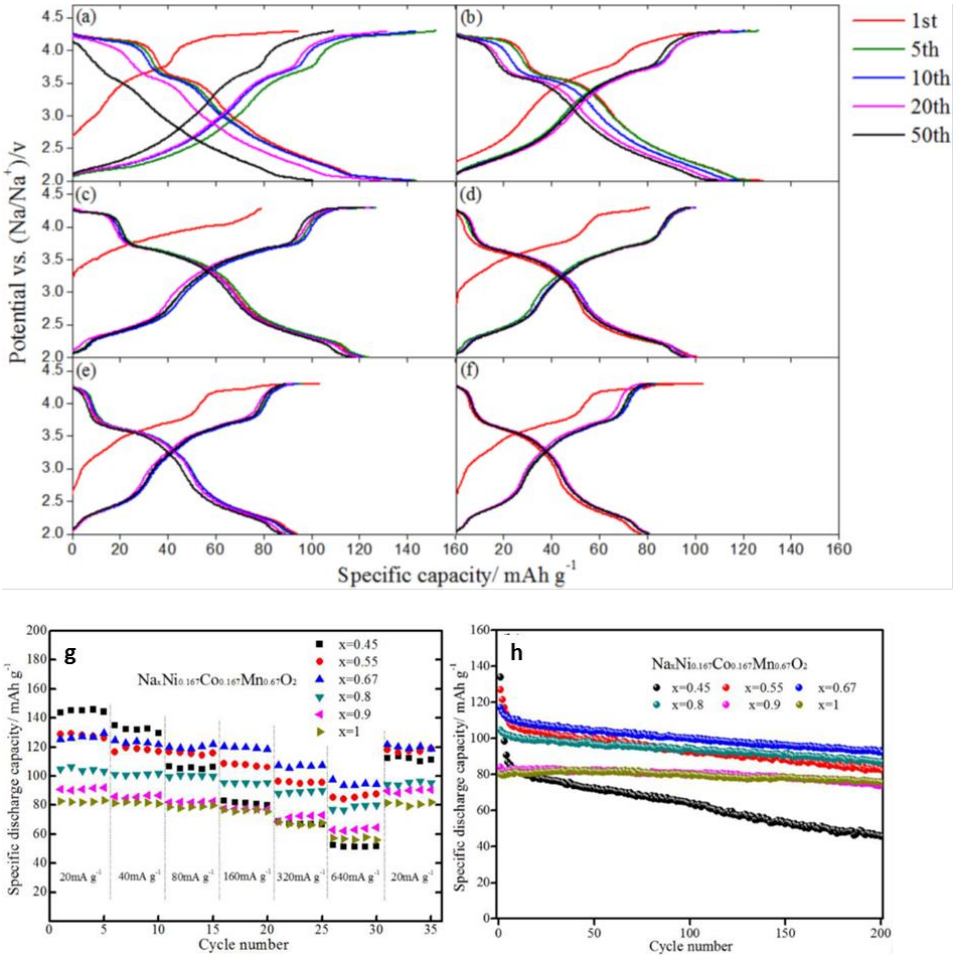


**Figure 2.9** Charge/discharge curves of $Na_xNi_{0.167}Co_{0.167}Mn_{0.67}O_2$ [(a). x = 0.45, (b). x= 0.55, (c). x = 0.67, (d). x = 0.8, (e). x= 0.9, (f). x = 1)] from 2 to 4.3 V at a current rate of 20 mA $g^{-1}$ in the first 50 cycles. Rate capability (g) and cycling performance (h) of $Na_xNi_{0.167}Co_{0.167}Mn_{0.67}O_2$ at a current rate of 160 mA $g^{-1}$. Reproduced with permission [87]

excellent rate capability was also tested at charge–discharge current rates ranging from 0.2–10 C. The average specific capacities were 147.8, 138.3, 124.6, 107.2, 88.1, and 67.4 mA h $g^{-1}$ at current rates of 0.2, 0.5, 1, 2, 5, and 10 C, respectively.

NASICON-type $Na_3V_2(PO_4)_3$ has been has been considered as a potential cathode material for SIBs with its highly covalent three-dimensional (3D) framework, crystalline structure, high theoretical energy density (~400 Wh/kg), and good thermal stability.[97] Carbon-coated nanosized $Na_3V_2(PO_4)_3$ embedded in a porous carbon matrix

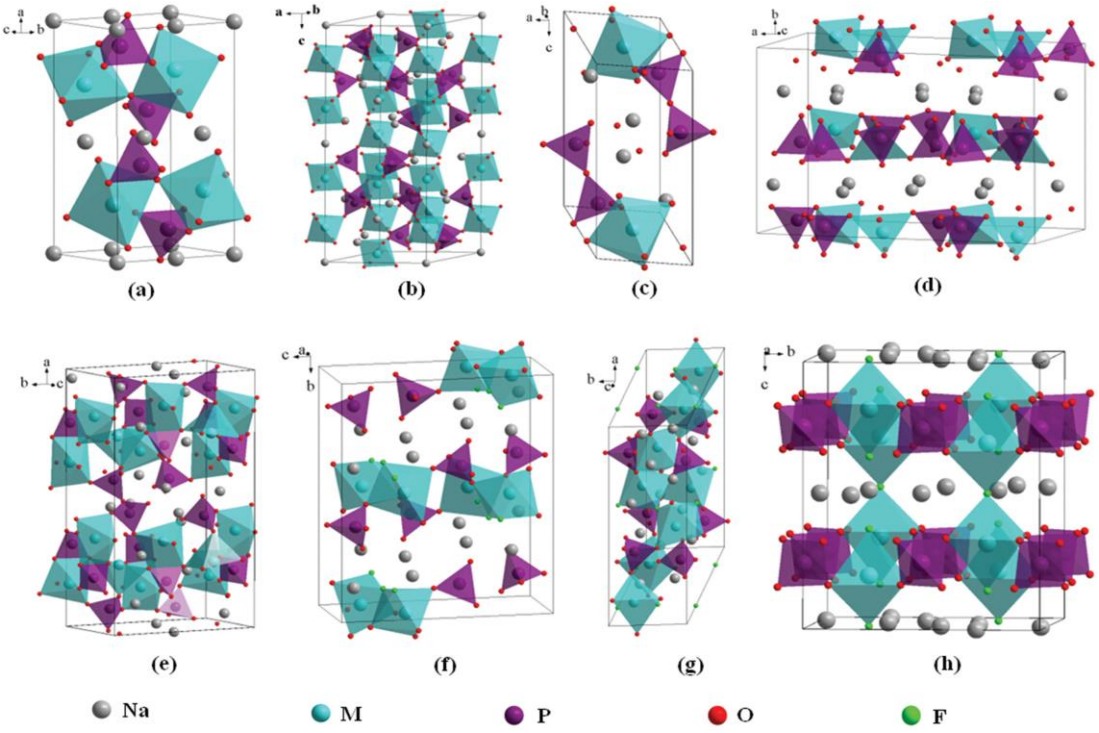


**Figure 2.10** Crystal structures of: olivine $NaMPO_4$ (a), NASICON$Na_3V_2(PO_4)_3$ (b), triclinic $Na_2MP_2O_7$ (c), orthorhombic $Na_2MP_2O_7$ (d), orthorhombic $Na_4M_3(PO_4)_2P_2O_7$ (e), orthorhombic $Na_2MPO_4F$ (f), monoclinic $Na_2MPO_4F$ (g), and tetragonal $Na_3M_2(PO_4)_2F_3$ (M = transition metal) (h). Reproduced with permission [33].

was prepared via a facile soft-chemistry-based double carbon-embedding approach.[98] Transmission electron microscope (TEM) images show microsized clusters with agglomerated nanosized grains. The grain sizes are around 20−40 nm for (C@NVP)@PC, where NVP is N-vinylpyrrolidone, and well dispersed in the porous carbon matrix. They exhibit 2−5-nm-thick carbon layers as a surface coating, as shown in Fig. 2.12. The composite exhibits an impressive capacity of 74 mA h $g^{-1}$ at 100 C and retains 70% of its capacity after 1000 cycles.

### 2.3.2.2. Pyrophosphates

Pyrophosphate $Na_2MP_2O_7$ (M = Fe, Mn, Co) is a family of attractive cathode materials for SIBs owing to its structural diversity and stability, as well as its good $Na^+$ mobility. $Na_2MP_2O_7$ can crystallize into different polymorphic forms, including triclinic, orthorhombic, and tetragonal structures.[99] A $Na_2FeP_2O_7$ – multiwalled carbon

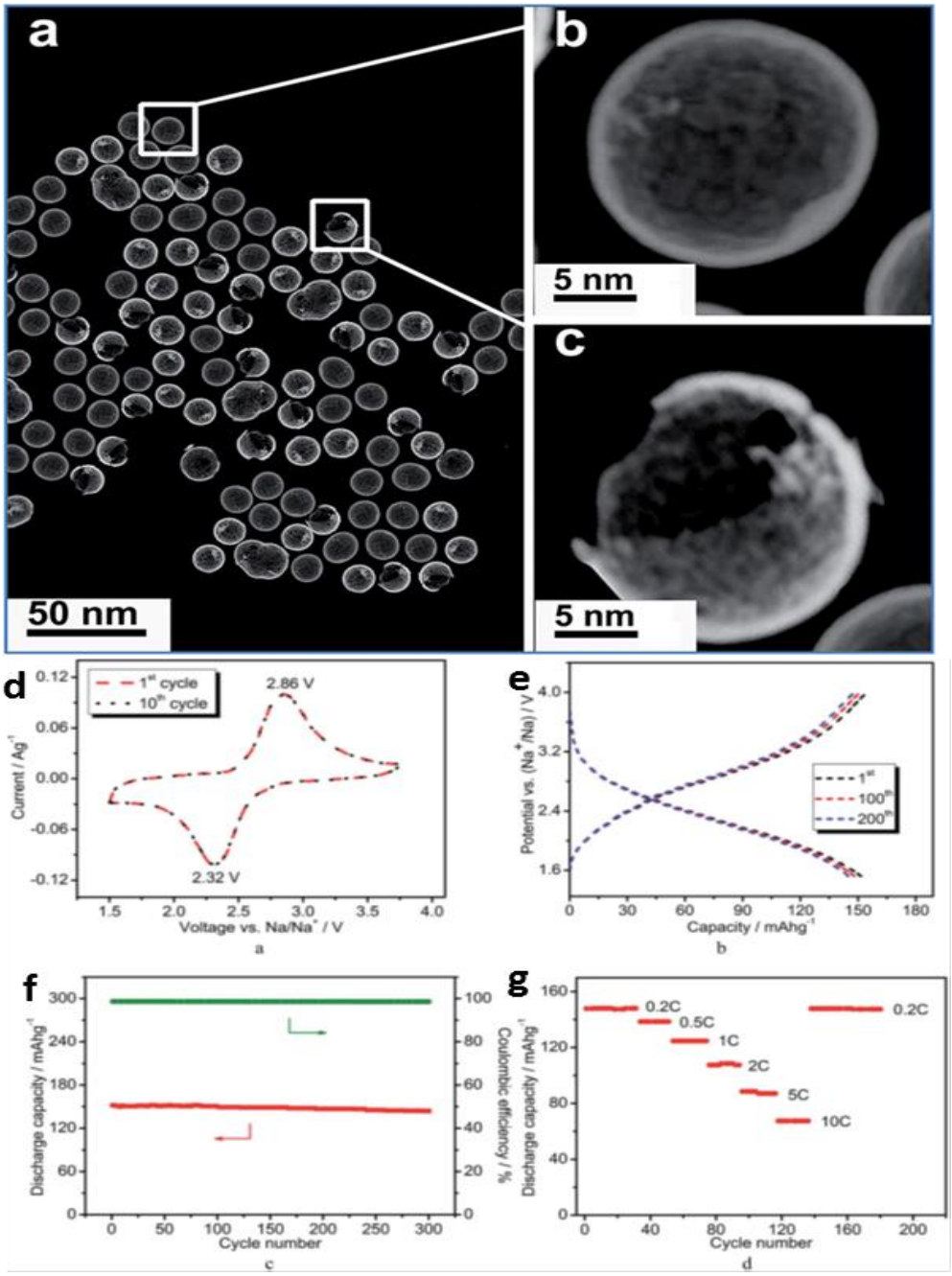


**Figure 2.11** (a) Low magnification scanning electron microscope (STEM) image; (b) and (c) enlarged STEM images of single nanospheres framed in (a) for $NaFePO_4$ nanospheres; (d) cyclic voltammetry (CV) curves for the 1st and 10th cycles; (e) galvanostatic discharging–charging profiles performed at a current density of 0.1 C, (f) the corresponding cycling performance, and (g) the rate capability. Electrolyte: $NaPF_6$ (1M) dissolved in a solution of ethylene carbonate (EC) and dimethyl carbonate (1:1 v/v). Cut-off voltage: 1.5–4.0 V (1 C = 155 mA $g^{-1}$). Reproduced with permission [96].

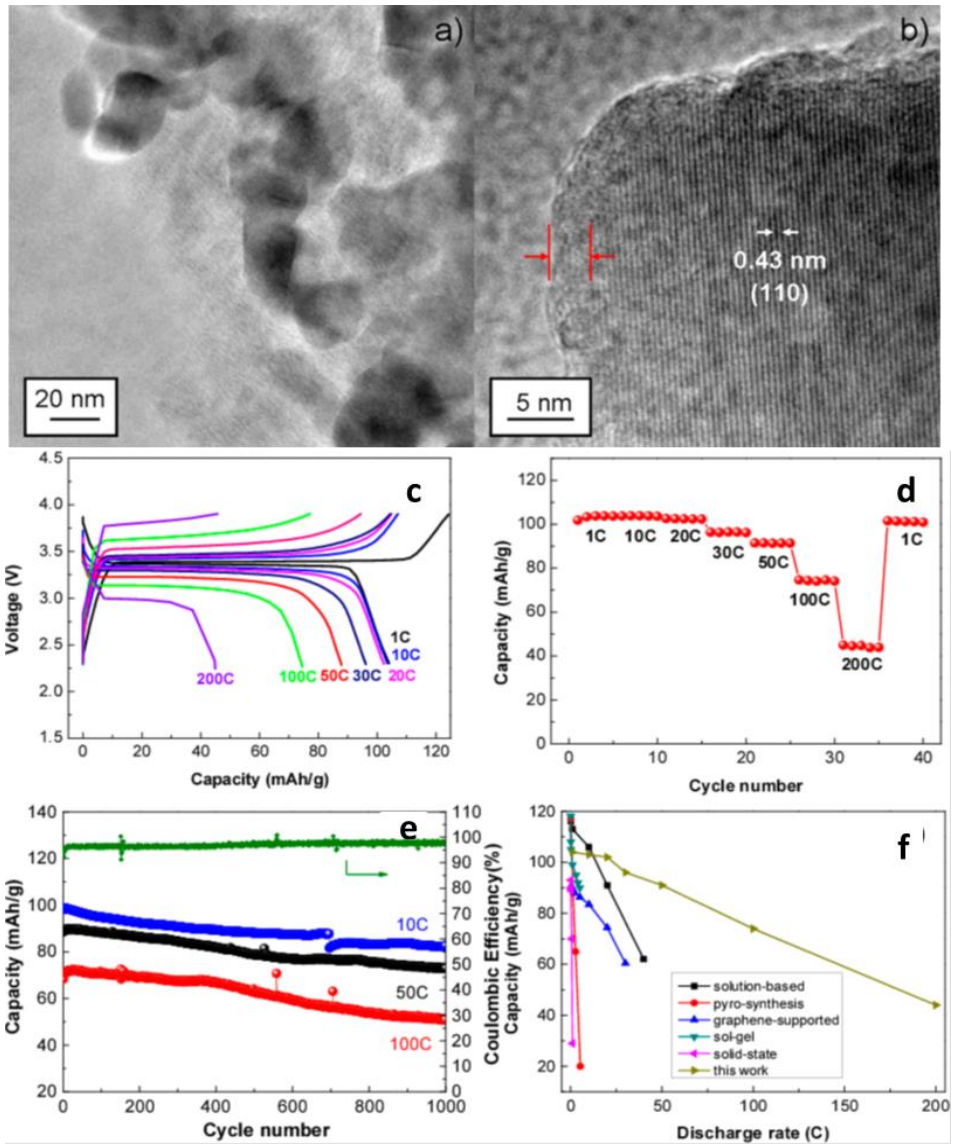


**Figure 2.12** TEM (a) and high resolution TEM (HRTEM) (b) images of (C@NVP)@pC. Galvanostatic charging−discharging profiles of (C@NVP)@pC at different current rates (c). Rate performance and capacity retention ability of (C@NVP)@pC(d). Cycling stability of (C@NVP)@pC at various current rates and Coulombic efficiency for 1000 cycles at 100 C (e). Comparison of rate performance of (C@NVP)@pC to the recently reported results in the literature for NVP (f). Reproduced with permission [98].

nanotube composite ($Na_2FeP_2O_7$/MWCNT) with triclinic structure was obtained by facile coprecipitation and post-heat-treatment approach. [100] The scanning electron microscope (SEM) and TEM images reveal micrometer-sized particles of composite with large globular agglomerates larger than 5 mm on its relatively rough surface, as

seen in Fig. 2.13. On the other hand, carbon nanotubes partially embedded in smaller and rougher particles can be easily spotted. This material displayed toutstanding high-rate performances with a reversible specific capacity of 86 mAh $g^{-1}$ for 140 cycles at 1 C and 68 mAh $g^{-1}$ at 10 C.

### 2.3.2.3. Fluorophosphates

Fluorophosphates have been proven to possess higher operating potential than phosphates, due to the strong inductive effect of the fluorine, which can greatly tune the electrochemical activity of the transition metal redox $M^{3+}/M^{4+}$couples (M = Ti, Fe, V).

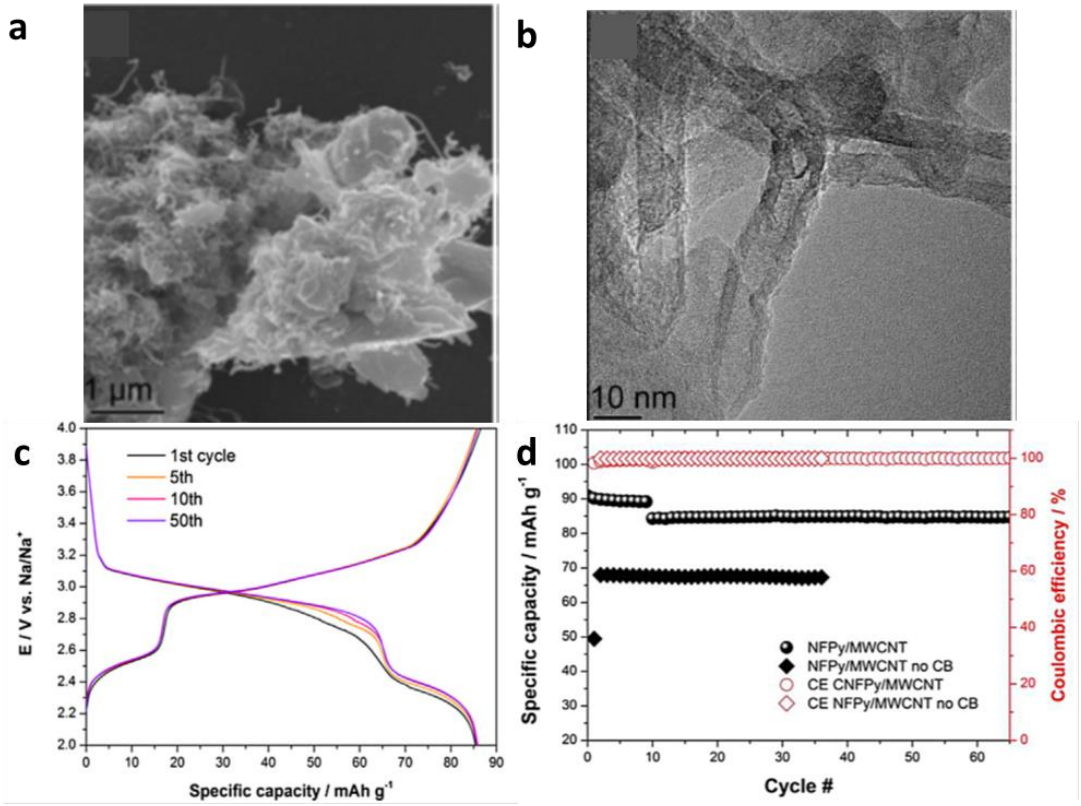


**Figure 2.13** SEM (a) and TEM (b) micrographs of $Na_2FeP_2O_7$/MWCNT; Charge-discharge profiles (c) of composite recorded after cycling the electrode at 2C (97 mA $g^{-1}$); Capacity retention tests (d) for $Na_2FeP_2O_7$/MWCNT at 1 C (with the first 10 cycles recorded at C/10). Reproduced with permission [100].

[101,102] The enhanced inductive effect and high working potential can be the key to moderating the energy-density issue of the cathode materials for SIBs.[103] Among them,

vanadium-based fluorophosphates have received the most attention, owing to the highly redox active $V^{3+}/V^{4+}$ couple, with an operating voltage expected to be 3.9 V.[104]

$Na_4V_2(PO_4)_2F_3$ was obtained via an easily scalable ball-milling approach, which relies on the use of metallic sodium, to prepare a variety of sodium-based alloys.[105] As shown in Fig. 2.14, the TEM image and energy dispersive spectroscopy (EDS) mapping clearly show that the crystallites of the main phase are surrounded by Na nanoparticles with sizes of 20–50 nm. When it was assembled in a full cell having carbon as the negative electrode, the composite exhibited an overall charging capacity of 167 mAh $g^{-1}$ and a discharge capacity of 110 mAh $g^{-1}$, which is a 24% enhancement compared with $Na_3V_2(PO_4)_2F_3$/C.

### 2.3.2.4. Sulphates

A few sulfates are also being considered as cathode candidates for SIBs, such as alluaudite-type $Na_2Fe_2(SO_4)_3$ and kröhnkite-type $Na_2Fe(SO_4)_2{\cdot}2H_2O$.[106-108] $Na_2Fe_2(SO_4)_3$ with a very high $Fe^{3+}/Fe^{2+}$ redox potential of 3.8 V (the highest known value among all Fe-based insertion compounds) has excellent rate kinetics and cycling stability, as seen in Fig. 2.15.

## 2.3.3. Prussican blue analogues

In recognition that lattice volume expansion/contraction during redox reactions is more problematic for the larger $Na^+$ ion than $Li^+$, the so-called Prussian-blue analogues (PBAs) have been investigated as intriguing alternative cathode materials to the layered oxide polyanion structures.[109-116] The prototype ideal Prussian blue, ($K[Fe^{III}Fe^{II}(CN)6]y{\cdot}H_2O$, y ≈ 1–5) has a cubic structure consisting of $Fe^{II}$ and $Fe^{III}$ ions sitting on alternate corners of corner-sharing iron octahedra bridged by cyano $(C{\equiv}N)^-$ ligands. The structure of a typical PBA is shown in Fig. 2.16.[109,110]

A variable sodium composition $Na_{0.61}Fe[Fe(CN)_6]_{0.94}$ was prepared by a facile synthetic procedure using $Na_4[Fe(CN)_6]$ as the only iron-source.[111] The high quality PB nanocrystals $Na_{0.61}Fe[Fe(CN)_6]_{0.94}$ (HQ-NaFe) display a cubic structure with sizes of 300 –600 nm, while the low-quality PB nanoparticles (LQ-NaFe) used as reference and

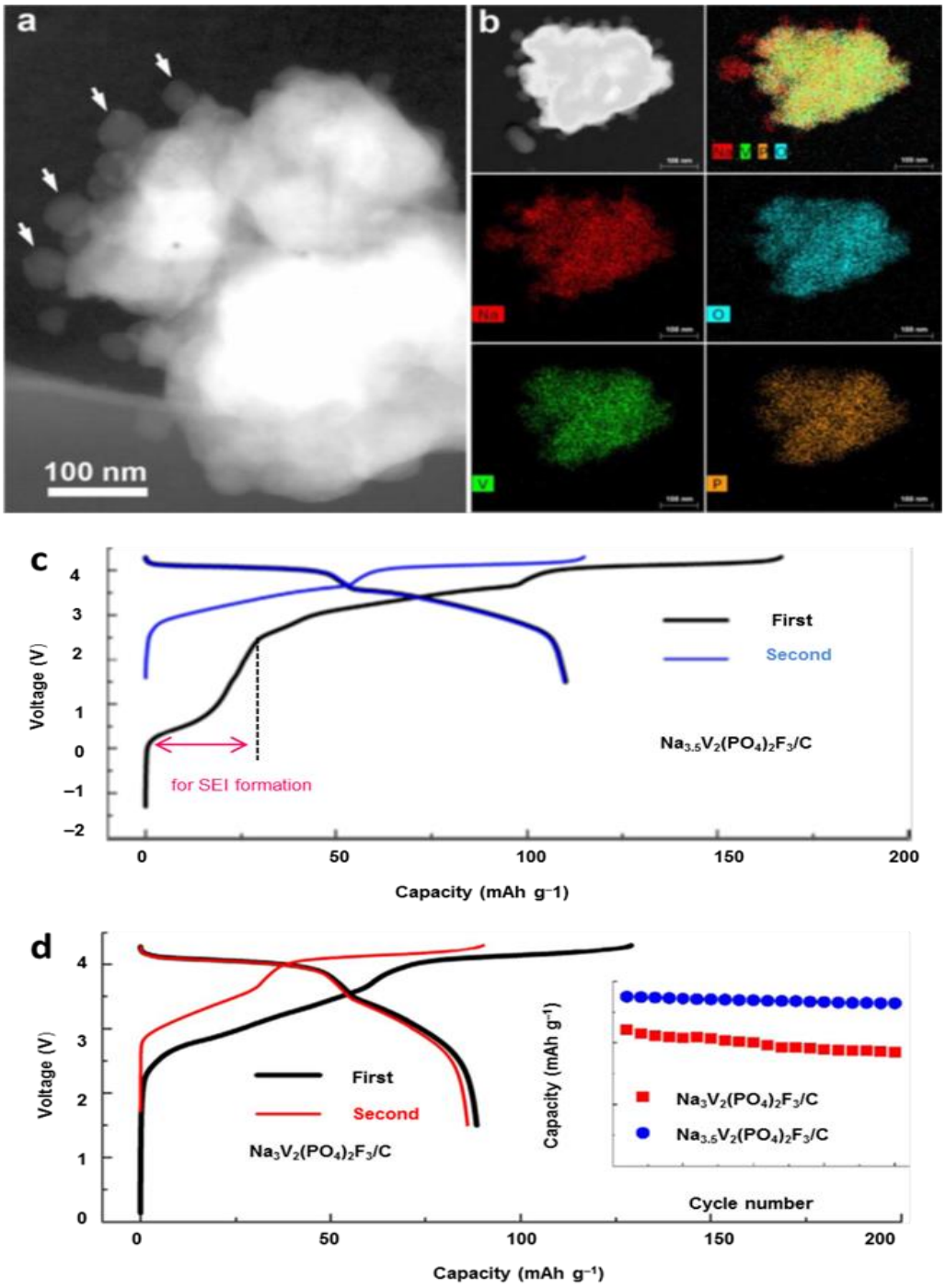


**Figure 2.14** STEM image of the $Na_4V_2(PO_4)_2F_3$ crystallites surrounded by Na nanoparticles (marked with arrows) (a); Energy dispersive spectroscopy (EDX) compositional maps (b); Voltage-composition profiles of $Na_{3.5}V_2(PO_4)_2F_3/C$ (c); Capacity retention of $C/Na_{3+x}V_2(PO_4)_2F_3/C$ full cells (cycled at a 0.2C rate) in the first 20 cycles (d). Reproduced with permission [105].

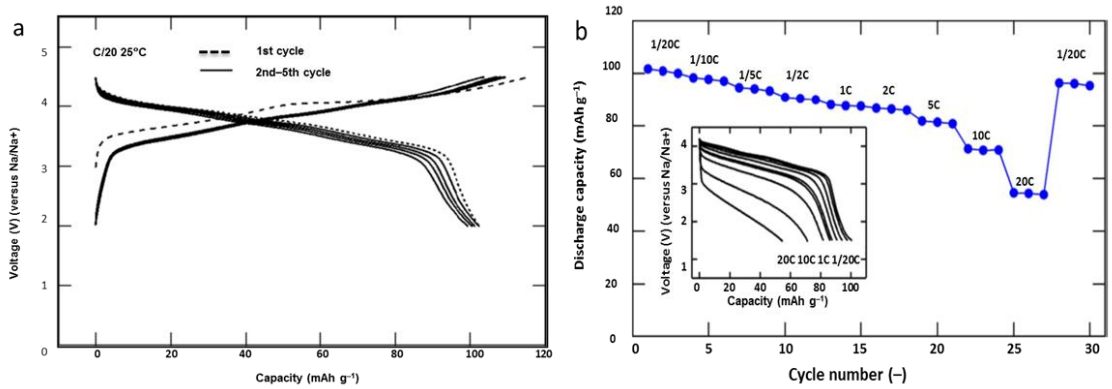


**Figure 2.15** Electrode properties of $Na_{2-x}Fe_2(SO_4)_3$ in Na cell. (a) Galvanostatic charging and discharging profiles of $Na_{2-x}Fe_2(SO_4)_3$ cathode cycled between 2.0 and 4.5V at a rate of C/20. (b) Capacity retention upon cycling up to 30 cycles under various rates from C/20 to 20C. Inset: discharge curves of $Na_{2-x}Fe_2(SO_4)_3$ as a function of rate (from C/20 to 20 C). Reproduced with permission [106].

produced via different fabrication methods presents a granular morphology with a size of 20 nm, as seen in Fig. 2.17. HQ-NaFe shows good electrochemical performance with a capacity of 170 mAh $g^{-1}$ and no apparent capacity loss for 150 cycles. Single-crystal $[Fe^{III}Fe^{III}(CN)_6]$ nanoparticles were prepared by controlling the purity and crystallinity of the composite.[115] As shown in Fig. 2.18, the as-obtained $FeFe(CN)_6$ nanoparticles are well crystallized and appear to be well-dispersed nanocrystals with cubic geometry. The electron diffraction pattern also demonstrates the single crystal structure of the nanocrystals. They have been proved to undergo sodium insertion with a reversible

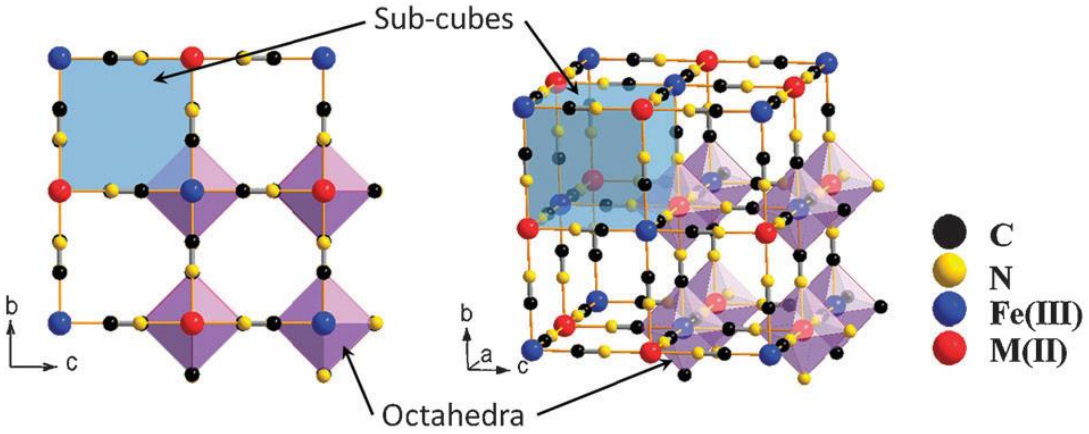


**Figure 2.16** Framework of Prussian blue analogues. Reproduced with permission [110].

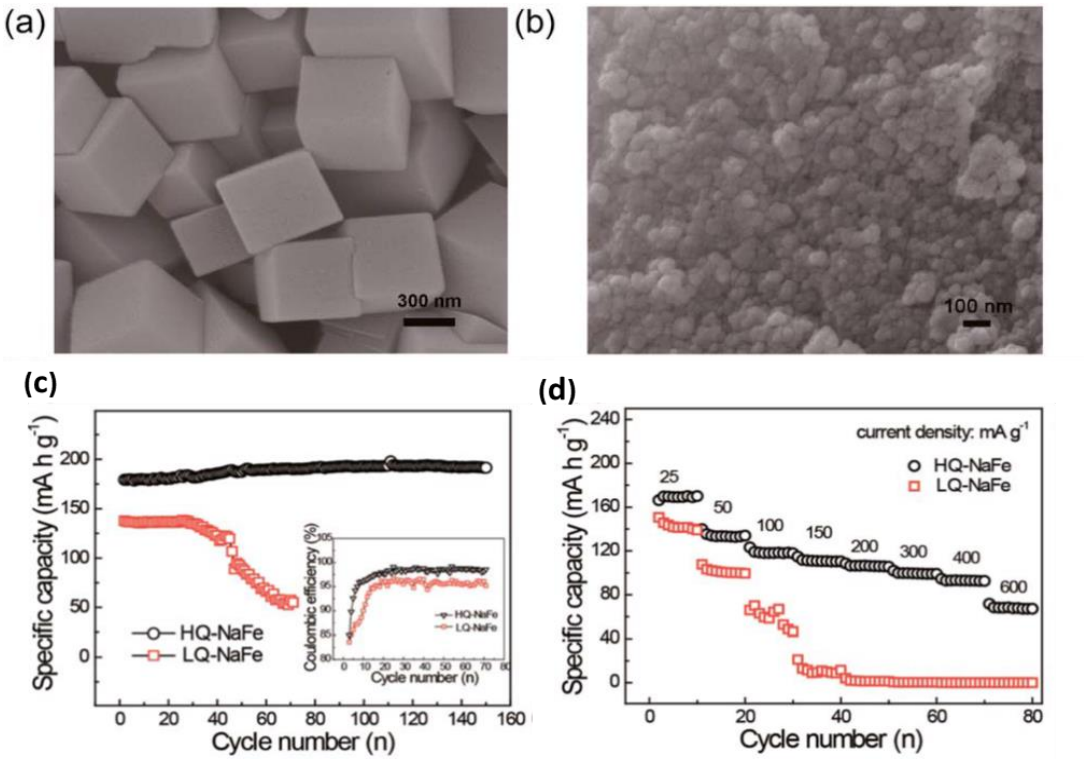


**Figure 2.17** Typical SEM images of (a) HQ-NaFe and (b) LQ-NaFe; Cycling performances of HQ-NaFe and LQ-NaFe (c), Rate capability of HQ-NaFe and LQ-NaFe (d). Reproduced with permission [111].

capacity of 120 mAh $g^{-1}$ at a moderate rate of 0.5 C, with 87% capacity retention over 500 cycles. They also exhibited an exceptional rate capability with 70% of their capacity retained at the 20 C rate.

## 2.3.4. Organic compounds

Organic molecules can undergo a reversible electrochemical redox reaction. The advantages of such a reaction are structural diversity, flexibility, molecular level controllability, and resource renewability. Various organosulfur compounds, radical compounds, carbonyl compounds, and functional polymers have been investigated as electrode materials for rechargeable batteries.[116–124] Among them, a carbonyl-based organic salt, $Na_2C_6O_6$, sodium rhodizonate (SR) dibasic, was systematically investigated for high-performance sodium-ion batteries.[123] Wang et al. synthesized different $Na_2C_6O_6$ structures by a facile antisolvent method, which exhibited strong size-dependent sodium-ion-storage properties; it was demonstrated that the $Na_2C_6O_6$

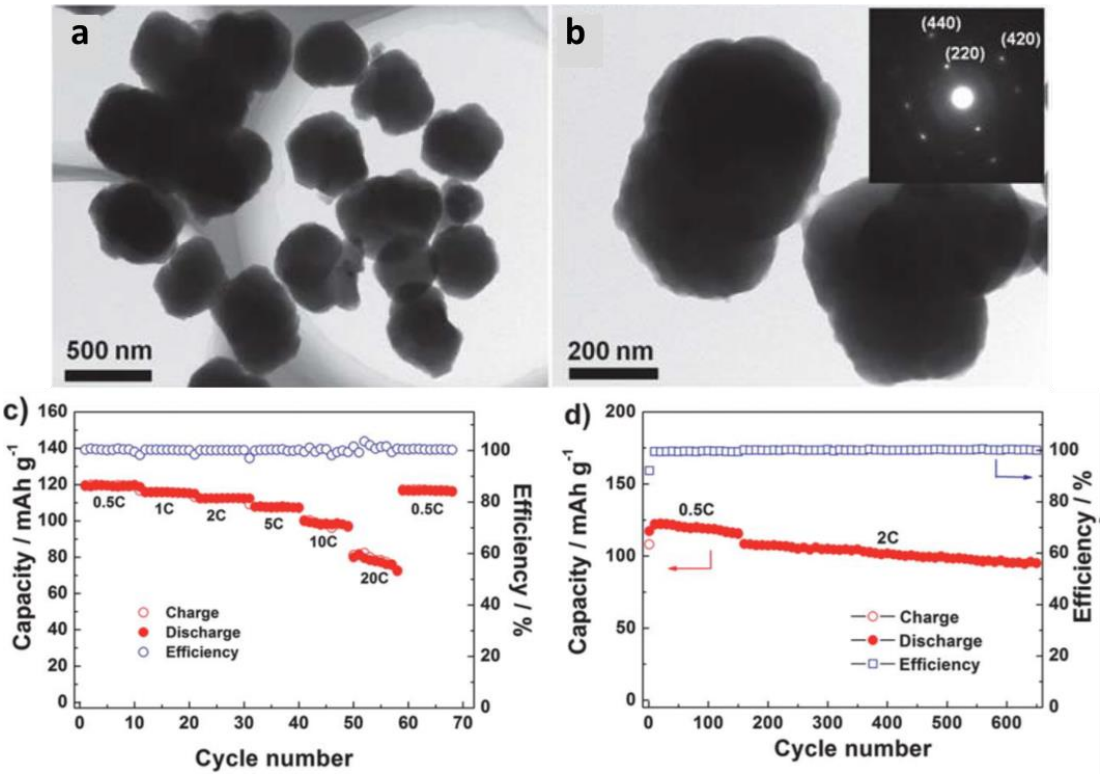


**Figure 2.18** TEM images (a and b) of $FeFe(CN)_6$, inset is the electron diffraction pattern of a single particle; (c) rate performances when cycled at changing rates (1 C = 120 mA $g^{-1}$); (d) cycling stability at constant currents of 0.5 C and 2 C. Reproduced with permission [115].

nanorods, as SIB cathode, could deliver a reversible capacity of ~190 mA h $g^{-1}$ at 0.1 C for an operating voltage of 1.6–2.8 V vs. Na/Na+, capacity retention of 50% at 10 C, and good thermal stability, as shown in Fig. 2.19.

## 2.4. Current anode materials for sodium ion batteries

As the cathode counterpart, identification of a suitable negative electrode is a critical issue for the successful development of SIBs. Currently, research on negative electrode materials for SIBs has been conducted on the three main categories, in term of the reaction mechanism during sodiation/ desodiation processes: (1) The insertion reaction, including carbonaceous materials and titanium-based oxides;[125,126] (2) the conversion reaction, including transition metal oxides (TMOs) or transition metal sulphides (TMSs);[127] and (3) the alloying reaction including p-block elements.[128,129] Some

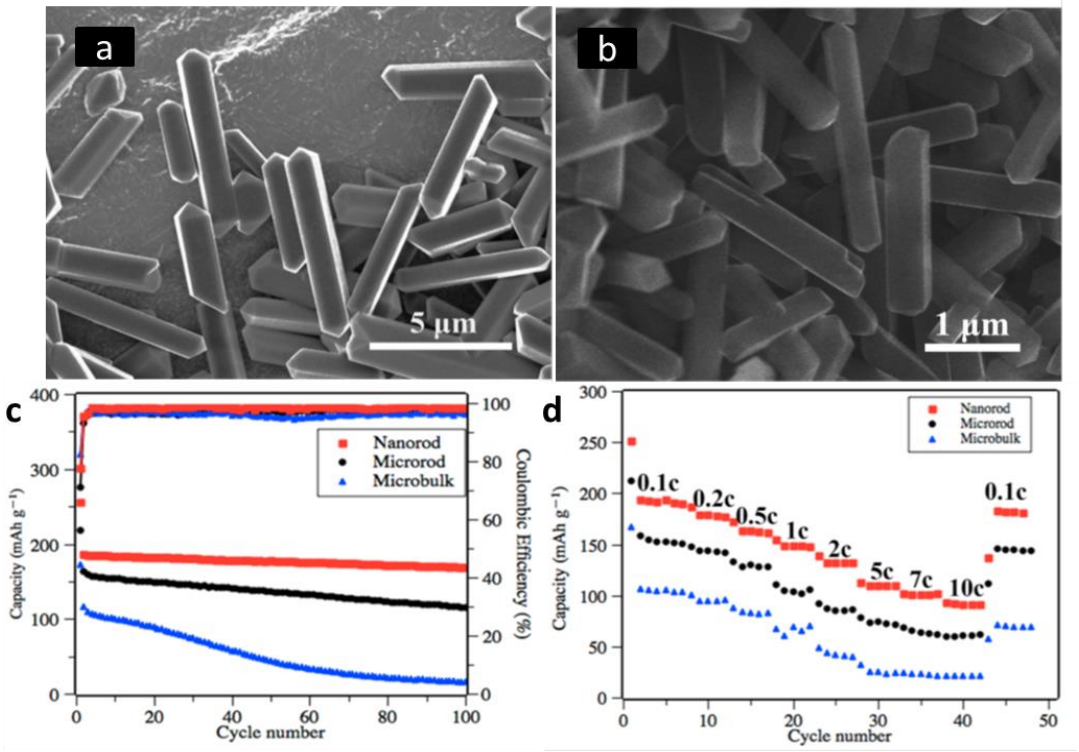


**Figure 2.19** SEM images of SR microrod (a) and nanorod (b) structured samples; Cycling test (c) and rate capability (d) of SR microbulk, microrod, and nanorod samples. Reproduced with permission [124].

representative candidate materials are illustrated in Figure 2.20.

## 2.4.1. Carbon-based materials

Over the past decades, various carbonaceous materials have been investigated experimentally and theoretically as electrode materials for SIBs.[130-135] Among them, carbon-based materials have distinguished themselves as a promising solution, as they are cheap, easily attainable, and non-toxic. Currently, hard carbon is broadly deemed to be one of potentially practical negative electrodes for SIBs. Since the first report of using hard carbon as anode material in SIBs,[136] hard carbon materials have been attracting tremendous attention due to their large interlayer distance and disordered structure, which facilitates Na-ion insertion−extraction. Usually, various factors, including the carbon precursor, manufacturing process, particle size, pore volume, and surface area, will affect the structure of hard carbon, further determining its electrochemical properties. Therefore, many studies have been reported that have

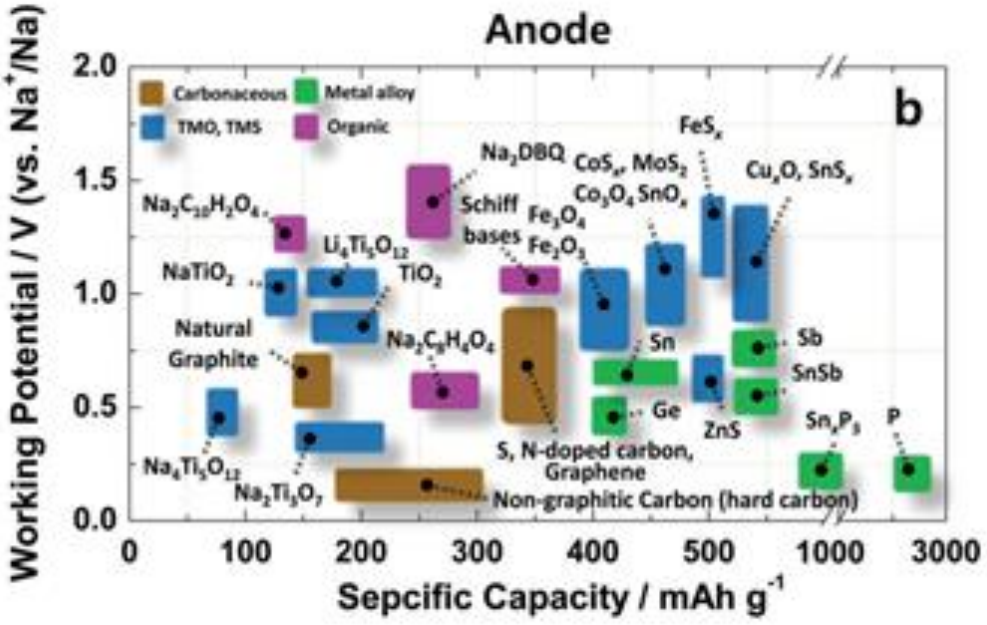


**Figure 2.20** Anode materials and corresponding electrochemical performances in current SIBs. Reproduced with permission [55].

focused on controlling the morphology of hard carbon materials by using typical synthesis methods, such as hydrothermal treatment, templating methods, self-assembly, etc. [137-142]

Hard carbon spherules (HCS) was prepared by Hu *et al.* from an abundant biomass of sucrose by a pyrolysis method.[138] HCS display a spherical shape with a uniform particle size of about 1 μm and a smooth surface, as shown in Fig. 2.21(a). The electrochemical performance testing results showed that HCS1600 (carbonized at 1600˚C) exhibited excellent cycling performance with a capacity of 290 mA h $g^{-1}$ at a current density of 30 mA $g^{-1}$ (0.1 C) and capacity retention of 93% after 100 cycles. It also achieved very good rate capability when discharged and charged at various rates from 0.1 C to 20 C, as shown in Fig. 2.22(c) and(d). Komaba and co-authors synthesized a new hard carbon (Argan-1200W) via carbonization of argan shell biomass with pretreatment by HCl aqueous solution, as presented in Fig. 2.21(b).[141] This work revealed the relationship between the specific capacity and the graphene interlayer distance, which is affected by carbonization temperature. Argan-1200W delivered a very high reversible capacity of 333 mAh $g^{-1}$ and excellent capacity retention of 96.0% after 100 cycles, as shown in

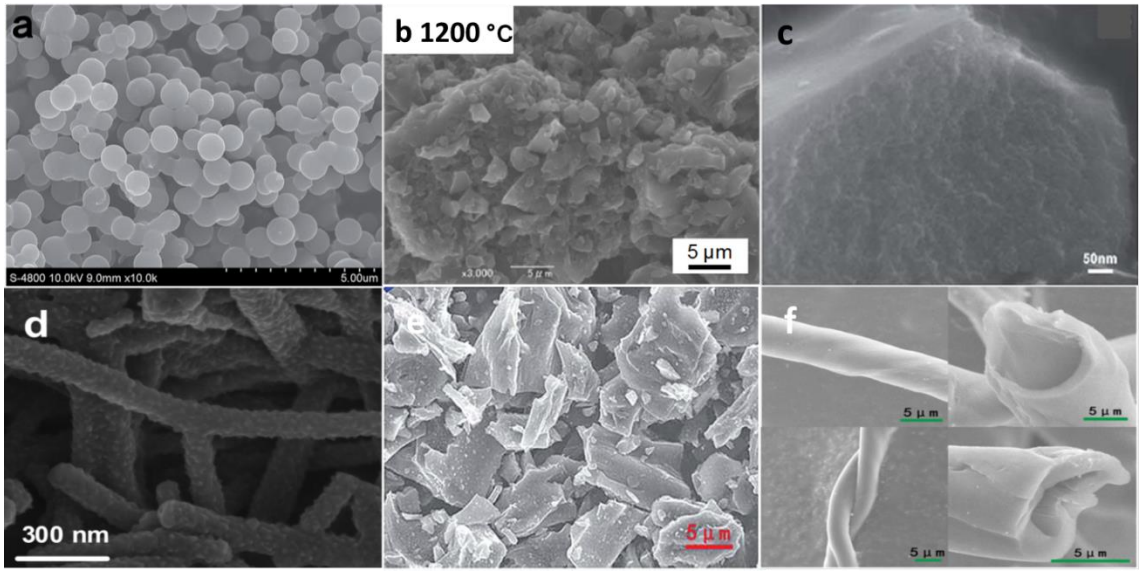


**Figure 2.21** Typical morphologies of hard carbon spherules (HCS1600) (a), Argan hard carbon-1200W (b), mesoporous carbon M700 (c), hollow carbon nanowires (HCNWs) (d), hard carbon from corn cob (HCC) (e), and hard carbon microtubes (HCTs) (f). Reproduced with permission [137][138][139][140][141][142].

Fig.2.22(i), (j). Gelatin-pyrolyzed mesoporous carbon (M700) was reported by Wang's group.[139] They pyrolyzed the commercial gelatin at relatively low temperature from 600 to 900 °C. The morphology of the as-prepared M700 presented well-developed interconnected mesopores and some macropores, as shown in Fig. 2.21(c). On investigating the electrochemical properties of pyrolytic carbons, M700 displayed the best cycling stability and rate performance, as shown in Fig. 2.22(e), (f). Another hollow carbon nanowire (HCNW) sample was obtained by Cao. *et al.* through pyrolyzation of a hollow polyaniline nanowire precursor combined with a self-assembly approach.[137] HCNW exhibits a uniform tube-like structure with the tubes about 120 nm in diameter and has a slightly rough surface, as indicated in Fig. 2.21(d). This novel carbon nanostructure displayed a moderate capacity of approximately 251 mA h $g^{-1}$ at a current density of 50 mAh $g^{-1}$ and excellent cycling stability, retaining a reversible capacity of 206.3 mAh $g^{-1}$ after 400 cycles. It also showed good rate performance, even at 500 mA $g^{-1}$ (2 C), a high reversible capacity of 149 mAh $g^{-1}$ could still be obtained, as shown in Fig. 2.22(a), (b). In 2016, Hu's group synthesized another kind of hard carbon (HCC) derived from the abundant biomass of corn cobs using a simple

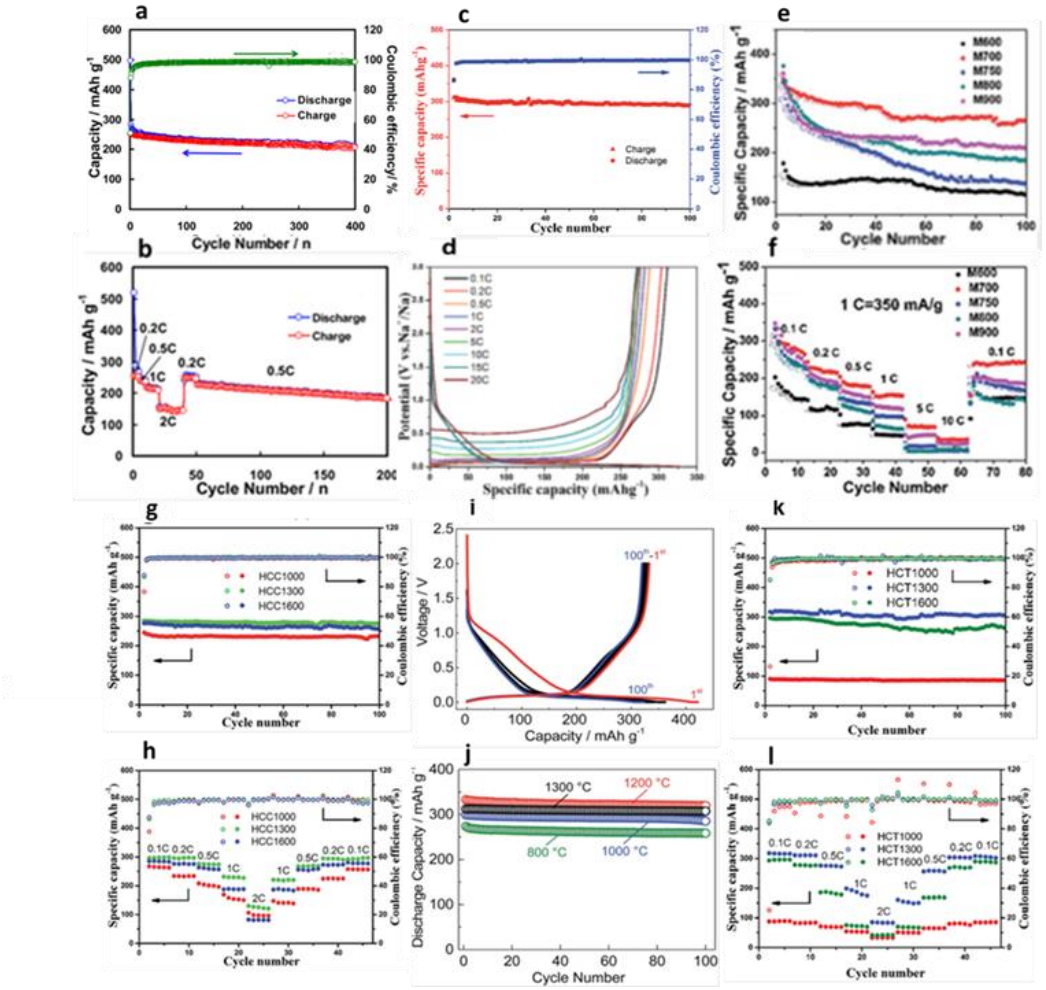


**Figure 2.22** Cycling performances of HCNW at a current rate of 50 mA $g^{-1}$ (0.2 C) (a), HCS1600 at 0.1C (c), M700 and other samples at a current density of 50 mA $g^{-1}$ (e), corn cob (HCC) at a current rate of 0.2C (g), Argan-1200W with a current rate of 25 mA $g^{-1}$ (j), and HCT at a current rate of 0.1 C (k); and charge/discharge curves on extended cycles of the Argan-1200W at a rate of 25 mA $g^{-1}$ (i) ; Rate capability of HCNW at 50 (0.2 C), 125 (0.5 C), 250 (1 C), and 500 (2 C) mAh $g^{-1}$(b) , HCS1600 from 0.1C to 20 C (d), M700 from 0.1C to 10 C(f), corn cob (HCC) from 0.1C to 2C (h),and HCT from 0.1 C to 2 C (l). Reproduced with permission [137][138][139] [140][141][142].

carbonization method.[140] From Fig. 2.21(e), it can be found that HCC has an irregular granular morphology with a particle size distribution range of 5–10 μm. The HCC1300 sample shows the best sodium storage performance, delivering a reversible capacity of

298 mA h $g^{-1}$ with the high initial coulombic efficiency of 86% at the current rate of 0.2 C (60 mA $g^{-1)}$. It also exhibits good cycling stability, retaining a capacity of 275 mAh $g^{-1}$ after 100 cycles, corresponding to capacity retention of 97%. Excellent rate performance was observed for HCC1300: even at the current rate of 2 C, it still delivered a capacity of 211 mAh $g^{-1}$, as displayed in Fig. 2.22(g), (h). Hard carbon microtube (HCT) was made from natural cotton through one simple carbonization process.[142] The morphology of HCT is clear in Fig. 2.21(f). The image shows that HTC has a typical linear and braided fibrous morphology with hollow structures. The HCT1300 (carbonized at 1300 °C) exhibits the best sodium storage performance, with a high reversible capacity of 315 mAh $g^{-1}$, a high initial Coulombic efficiency of 83% at a current rate of 0.1 C, and excellent cycling stability, retaining a capacity of 305 mAh $g^{-1}$ after 100 cycles, corresponding to capacity retention of 97%. Meanwhile, HCT1300 shows better rate performance than the other samples, delivering a specific capacity of 275 and 180 mAh $g^{-1}$ at current rates from 0.5 C to 1 C, as shown in Fig. 2.22(k), (l).

Other carbonaceous materials are also being intensively investigated, such as graphene and N-doped carbon materials.[143-147] Wang *et al.* from our Institute prepared reduced grapheme oxide (RGO) by the simple modified Hummer's method.[142] The images of RGO presented in Fig. 2.23(a), (b) show that the RGO features a layered structure with interlayer spacing of the (002) planes of 0.371 and 0.365 nm in different areas. As shown in Fig. 2.23(c), (d), the RGO can tolerate significant sodium ion insertion, leading to a reversible capacity as high as 174.3 mAh $g^{-1}$ at 0.2 C (40 mA $g^{-1}$), and even 93.3 mAh $g^{-1}$ at 1 C (200 mA $g^{-1}$) after 250 cycles. Furthermore, it also achieved the good capacity retention of 141 mAh $g^{-1}$ at 0.2 C (40 mA $g^{-1}$) over 1000 cycles. Amorphous carbon nitride (ACN) derived from zeolitic imidazolate framework-8 (ZIF-8) by pyrolysis was reported as anode for SIBs by Dong's group.[147] From the Fig. 2.24(a-d), it can be found that ACN composite particles show a uniform rhombic dodecahedral shape about 300 nm in size with microporous structure. In the cycling measurementd, the composite shows a capacity of 175 mAh $g^{-1}$ after 2000 cycles at a current density of 1.67 A $g^{-1}$, with only 0.016% capacity degradation per cycle and almost 100% Coulombic efficiency. The excellent rate performance was also demonstrated by changing the current rate from 83 mA $g^{-1}$ to 8.33 A $g^{-1}$ to obtain a

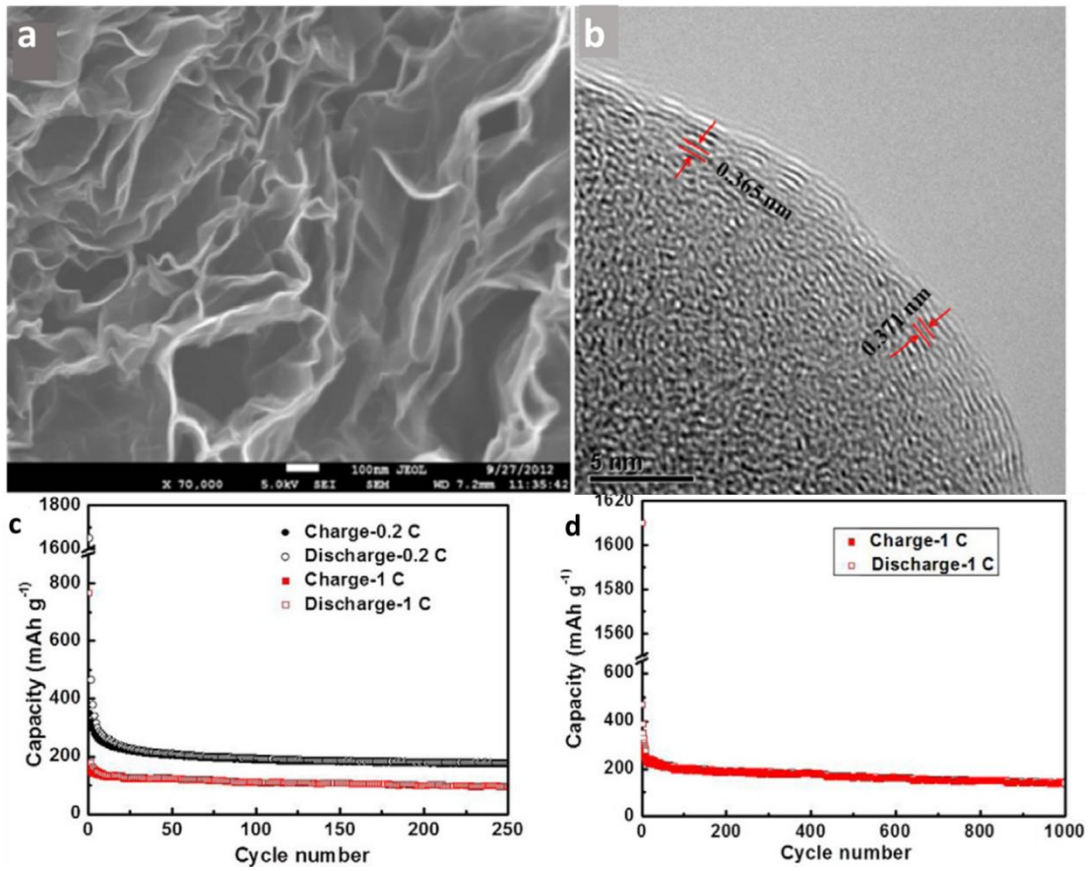


**Figure 2. 23** Field emission SEM (FESEM) (a) and TEM (b) images of RGO; Cycling performance of RGO at 0.2 and 1 C for 250 cycles (c), and cycling performance of RGO at 1 C for 1000 cycles (d). Reproduced with permission [143].

reversible capacity of 430 mAh $g^{-1}$ and 146 mAh $g^{-1}$, respectively.

## 2.4.2. Transition metal oxide (TMO) based anode materials

Transition metal oxides are appealing candidates as anode materials for SIBs, owing to their intrinsically low cost, high capacity, and enhanced safety. Since Alcantara *et al.* first introduced the conversion material concept by using $NiCo_2O_4$ spinel oxide as an anode material for SIBs,[147] Many research groups have explored various transition metal oxides (TMOs), including iron oxides ($Fe_3O_4$, $Fe_2O_3$),[149-154] cobalt oxide ($Co_3O_4$),[155-161] tin (di)oxides (SnO, $SnO_2$),[162-170] copper oxide (CuO),[171-176] nickel oxides (NiO, NiO/Ni),[177-179] and manganese oxides ($MnO_2$, $Mn_3O_4$),[177,180,181] etc.

### 2.4.2.1. Iron oxides ($Fe_3O_4$, $Fe_2O_3$) anode materials

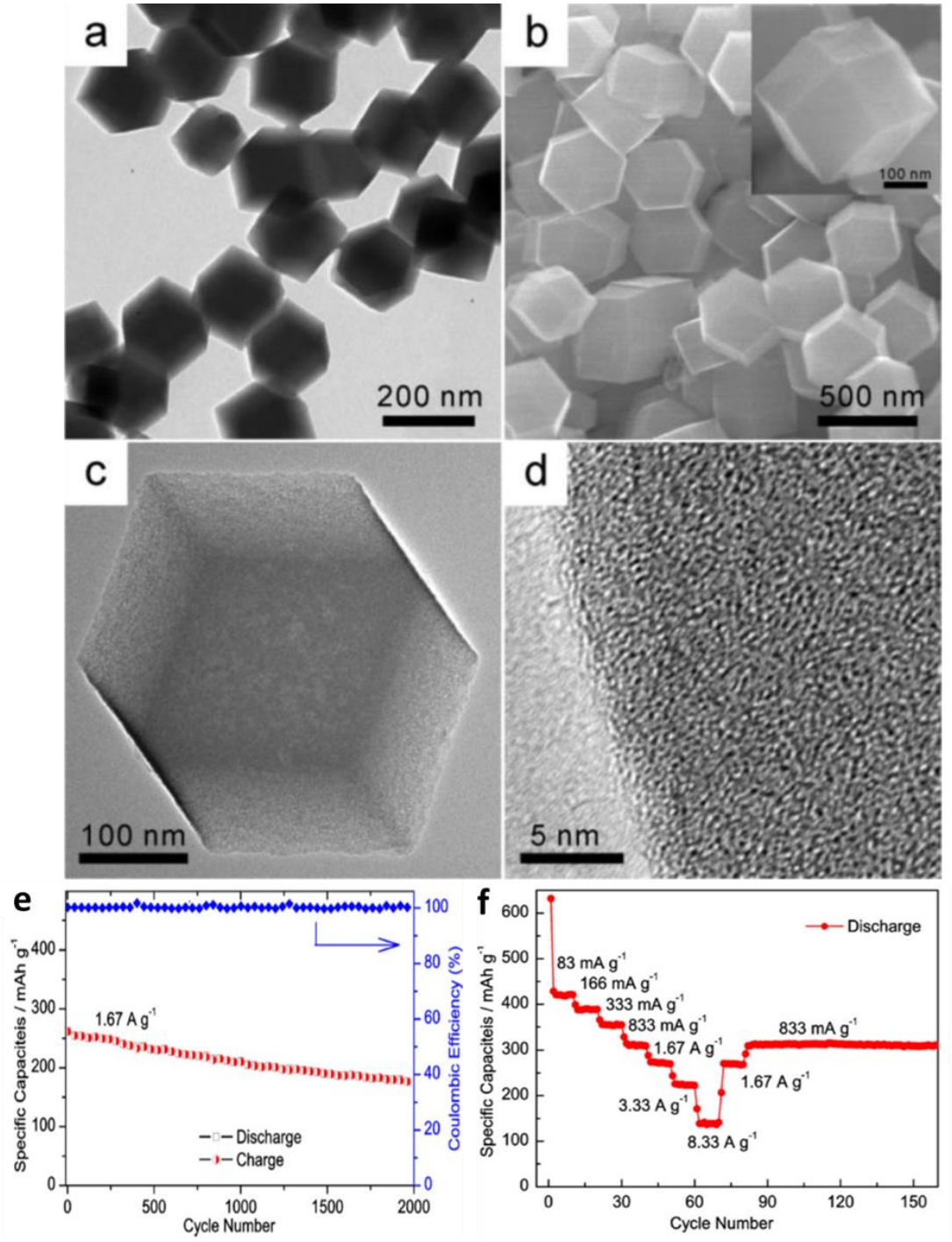


**Figure 2.24** TEM image of as-prepared ZIF-8 (a).SEM image of ACN composite (b). TEM (c) and HRTEM (d) images of ACN composite. Reproduced with permission [147].

In the conversion reaction mechanism, the sodiation/desodiation process of a TMO can be described by the following equation (2.1):

$$MOx + 2xNa+ + 2xe- \longleftrightarrow xNa2O + M \quad (2.1)$$

It was reported that the following reaction (2.2) could occur when $Fe_3O_4$ material hosts the $Na^+$.[150]

$$Fe_3O_4 + 8e^- + 8Na^+ \longleftrightarrow 3Fe + 4Na_2O \quad (2.2)$$

Theoretically, up to 8 mol of Na (926 mAh $g^{-1}$) could be stored in $Fe_3O_4$, although the discharge capacity value of $Fe_3O_4$ is lower than the theoretical limit in practice, due to the sluggish kinetics of sodiation/desodiation.

Liu *et al.* introduced a composite of $Fe_3O_4$-quantum dots (QDs) on hybrid carbon nanosheets ($Fe_3O_4$-QDs/CNs) by strongly bonding ultrafine $Fe_3O_4$ quantum dots on hybrid carbon nanosheets.[152] This work took graphene oxide (GO) as a matrix via in-situ dehydration and crosslinking reactions of glucose under hydrothermal conditions to obtain the precursor, hydrothermal carbon, on the surface of HTC-coated reduced GO (rGO) from the ferric salt due to its hydrophilicity. This is the key point that mitigates the mobility and agglomeration of $Fe_3O_4$ clusters at high temperature, eventually ensuring homogenously dispersed $Fe_3O_4$-QDs on HTC-coated rGO. $Fe^{3+}$ can be spontaneously adsorbed on dispersed $Fe_3O_4$-QDs on hybrid CNs. The micromorphology of $Fe_3O_4$-QDs/CNs was confirmed by TEM images, with the QDs having an average size of 3.8 nm on hybrid CNs, as shown in Fig. 2.25(a), (b). $Fe_3O_4$-QDs/CNs displayed stable capacity retention, maintaining a high capacity of 360 mAh $g^{-1}$ after cycling at varied current densities from 0.1 to 2 and then 0.1 A $g^{-1}$. There was also excellent durability for long-term cycling of $Fe_3O_4$-QDs/CNs. A capacity of 252 mAh $g^{-1}$ and capacity retention of over 70% were obtained after 1000 cycles at the high current density of 1.0 $Ag^{-1}$, as presented in Fig. 2.25(d), (e).

### 2.4.2.2. Cobalt oxides ($Co_3O_4$) anode materials

The reversible conversion reaction mechanism of $Co_3O_4$ with sodium ions was proposed by Rahman *et al.* as follows:[153]

$$Co_3O_4 + 8Na^+ + 8e^- \longleftrightarrow 4Na_2O + 3Co \quad (2.3)$$

Theoretically, cobalt oxide can deliver discharge capacity of 890 mAh $g^{-1}$. Due to this point, it has aroused much attention.

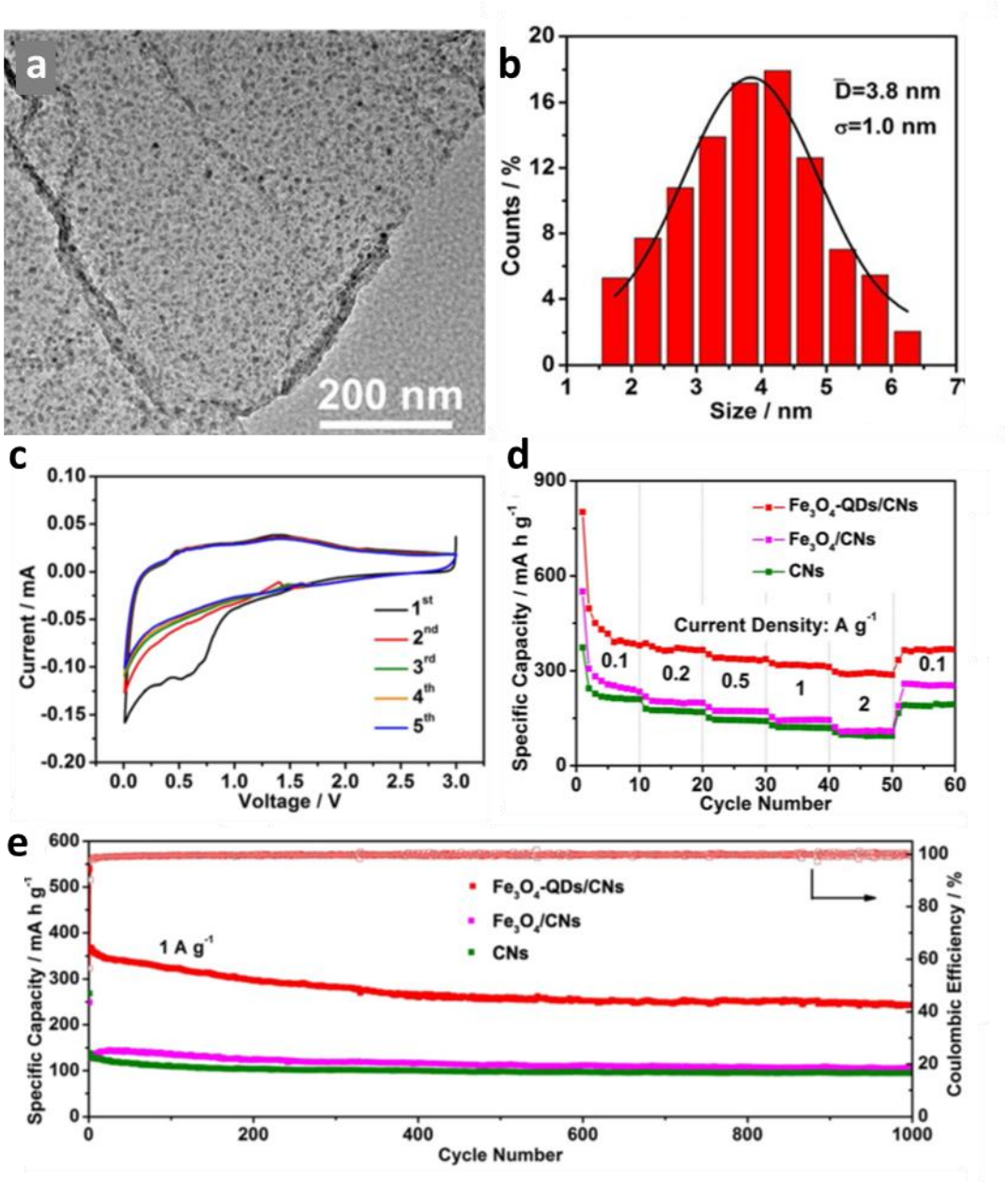


**Figure 2.25** TEM image of $Fe_3O_4$-QDs/CNs (a), size distribution of $Fe_3O_4$-QDs (b). CV curves for $Fe_3O_4$-QDs/CNs at a scan rate of 0.2 $mVs^{-1}$ (c); Rate capability of $Fe_3O_4$-QDs/CNs, $Fe_3O_4$/CNs and CNs electrodes at varied current densities (d); Cycling stability of $Fe_3O_4$-QDs/CNs, $Fe_3O_4$/CNs and CNs electrodes at 1.0 $Ag^{-1}$(e). Reproduced with permission [152].

Nitrogen-doped carbon-coated $Co_3O_4$ nanoparticles ($Co_3O_4$@NC) with excellent electrochemical properties in SIBs were reported by Wang *et al.* from our institute in 2016.[161] The $Co_3O_4$@NC was fabricated by utilizing a metal–organic framework, ZIF-

67, as precursor through a controlled two-step annealing process to convert Co ions and organic linkers to $Co_3O_4$ nanoparticle cores and nitrogen-doped carbon shells, respectively. As shown in Fig. 2.26(a), (b), it can be observed from the SEM and TEM images that the $Co_3O_4$@NC polyhedron consists of closely packed nanoparticles (NPs) with a size of ~100 nm that form a rough surface. $Co_3O_4$@NC demonstrated very high electrochemicalperformance in SIBs, delivering a high reversible capacity of 175 mA h $g^{-1}$ after 1100 cycles at a high current density of 1000 mA $g^{-1}$, and rate capability of 506, 317, and 263 mAh $g^{-1}$ at 100, 400, and 1000 mA $g^{-1}$, respectively, as presented in Fig. 2.26(c-e).

### 2.4.2.3. Tin-based oxide anode materials

Recently, many nanostructured tin-based oxide (SnO, $SnO_2$) composites have been proposed.[165,169,170] It was confirmed that SnO and $SnO_2$ were able to store sodium in their structure through combined conversion and alloying reactions:[164]

SnO $\quad SnO + 2Na^+ + 2e^- \longleftrightarrow 2\,Sn + Na_2O$ conversion reaction (2.4)

$\quad Sn + Na_2O + xNa^+ + xe^- \longleftrightarrow Na_xSn + Na_2O$ alloying reaction (2.5)

$SnO_2$ $\quad SnO_2 + 4Na^+ + 4e^- \longleftrightarrow Sn + 2Na_2O$ conversion reaction (2.6)

$\quad Sn + 2Na_2O + xNa^+ + xe^- \longleftrightarrow Na_xSn + 2Na_2O$ alloying reaction (2.7)

The theoretical capacity of SnO and $SnO_2$ in the conversion reaction are 398 and 711 mAh $g^{-1}$, respectively. Therefore, for different materials, the capacity depends on the degree of alloying reactions.

Su *et al.* synthesized mesoporous SnO microspheres via a hydrothermal method utilizing $NaSO_4$ as the morphology directing agent.[165] As displayed in Fig. 2.27, SnO microspheres present a spherical shape with a homogenous size distribution of ~3 μm. A typical free-standing individual SnO microsphere consists of many nanosheets with a thickness of about 20 nm. Each nanosheet has a mesoporous structure with a pore size of approximately 5 nm. Its discharge and charge curves verified the combined conversion and alloying reaction. The microspheres delivered the discharge capacities of 403 mAh $g^{-1}$ at 20 mA $g^{-1}$, 371 mAh $g^{-1}$ at 40 mA $g^{-1}$, 310 mAh $g^{-1}$ at 80 mA $g^{-1}$, and 287 mAh $g^{-1}$ at 160 mA $g^{-1}$, respectively, after 50 cycles.

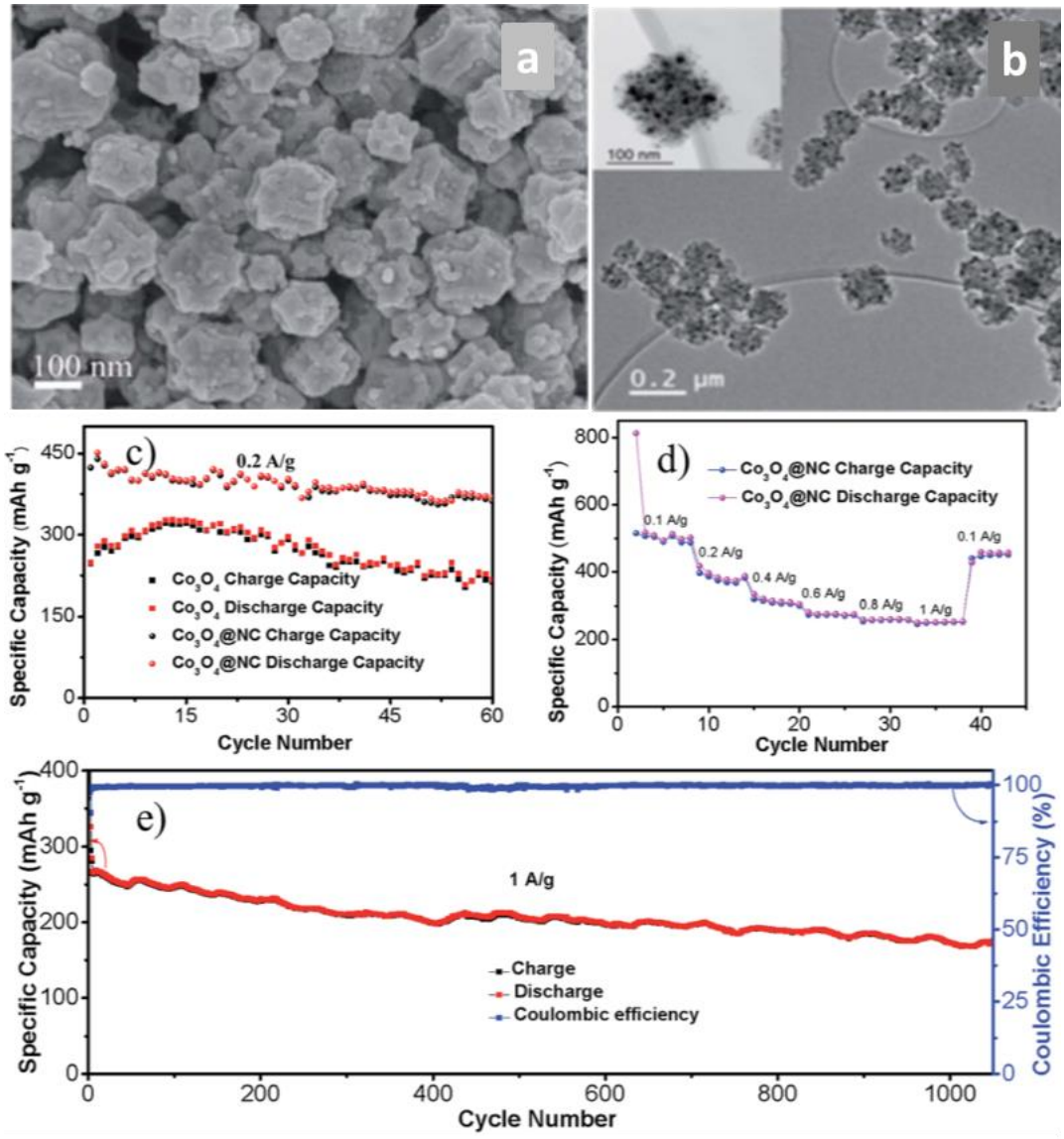


**Figure 2.26** SEM (a) and TEM (b) images of $Co_3O_4$@NC; (c) Cycling performance of pure $Co_3O_4$ and $Co_3O_4$@NC electrodes for the first 60 cycles at 200 mA $g^{-1}$; (d) Rate capability and (e) cycling stability of $Co_3O_4$@NC electrode. Reproduced with permission [161].

Su *et al.* also reported the fabrication of single crystalline $SnO_2$ nanocrystals with a uniform octahedral shape by a similar hydrothermal approach.[169] As displayed in Fig. 2.28, the $SnO_2$ nanocrystals have a uniform octahedral shape and a homogeneous size distribution, with an average size of less than 60 nm, an edge-to-edge width iof about 40 nm, and an apex-to-apex length of around 60 nm. This anode material with its unique structure exhibited excellent cycling performance and good rate performance, delivering

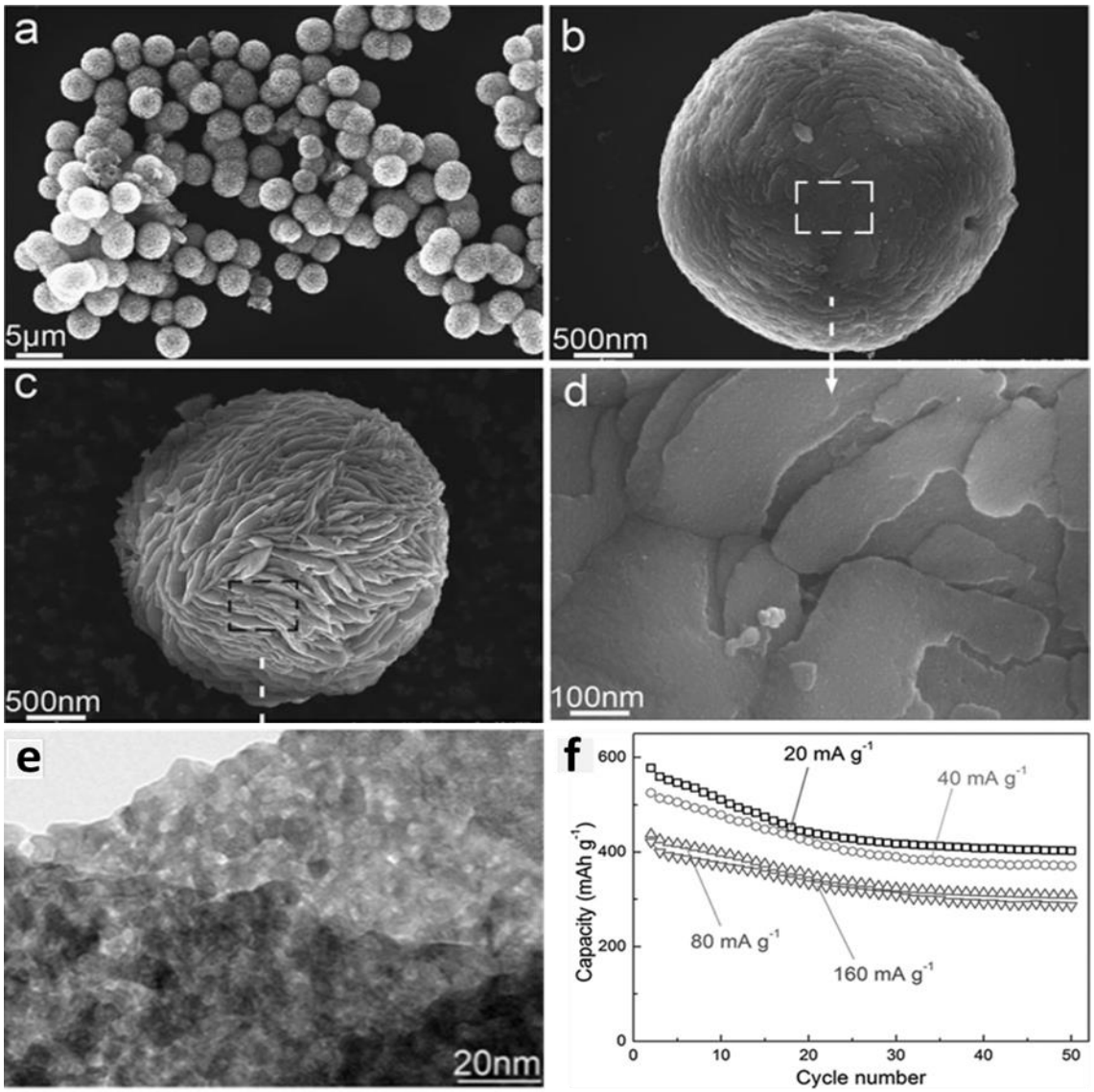


**Figure 2.27** SEM images of SnO microspheres (a), and free-standing individual SnO microspheres- (b), (c). Medium-resolution TEM image of SnO microspheres (d) taken from the region marked with a rectangle in (b). High-resolution TEM image of SnO microspheres (e). Cycling performance of SnO microspheres at the current densities of 20, 40, 80, and 160 $mAg^{-1}$(f). Reproduced with permission [165].

a capacity of 432 mA h $g^{-1}$ at the current density of 20 mA $g^{-1}$ and 175 mA h $g^{-1}$ at the current rate of 160 mA $g^{-1}$ after 100 cycles.

Another tin-based oxide composite $SnO_2$@3DG was proposed by Chen's group.[170] They utilized ice-templating to obtain ultrasmall $SnO_2$ nanoparticles embedded in three-

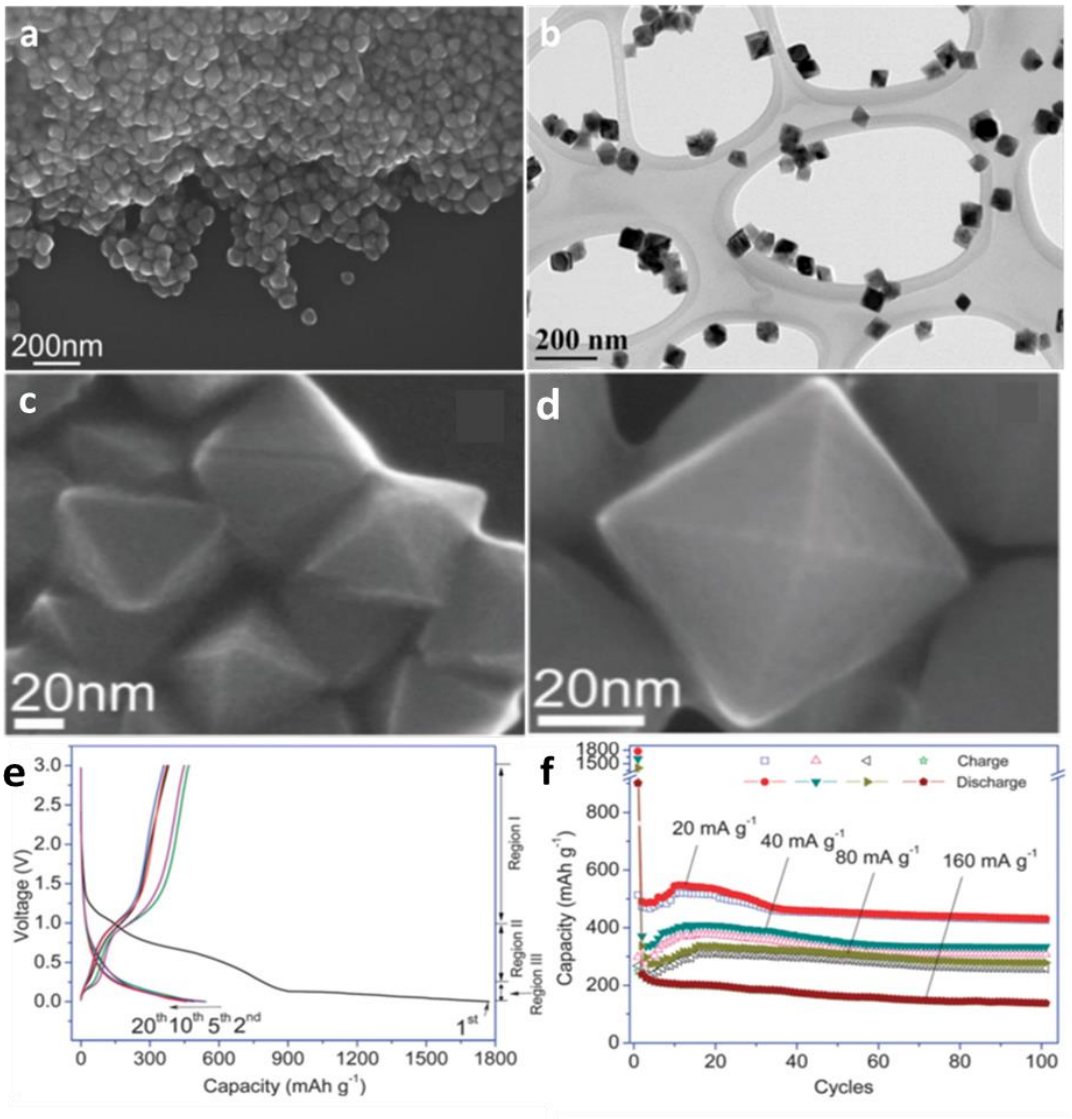


**Figure 2.28** SEM image (a) and TEM image (b) of octahedral $SnO_2$ nanocrystals**.** SEM images of typical free standing octahedral $SnO_2$ nanocrystals (c) and (d). Discharge-charge curves of octahedral $SnO_2$ nanocrystals in the 1st, 2nd, 5th, 10th, and 20th cycle at a current rate of 20 $mAg^{-1}$(e). Cycling performance of octahedral $SnO_2$ nanocrystals at current densities of 20, 40, 80 and 160 mA $g^{-1}$(f). Reproduced with permission [169].

dimensional (3D) graphene ($SnO_2$@3DG). The 3D structure of $SnO_2$@3DG is clearly shown in Fig. 2.29, where the uniform nanocrystals of $SnO_2$ with an average particle size of 3.4 nm are homogeneously distributed on the graphene sheets. The high distribution of $SnO_2$ nanoparticles in the 3DG network is the main feature of $SnO_2$@3DG, which improves electron/ion transport in the electrode. The composite displayed high cycling stability and high rate performance, delivering a reversible

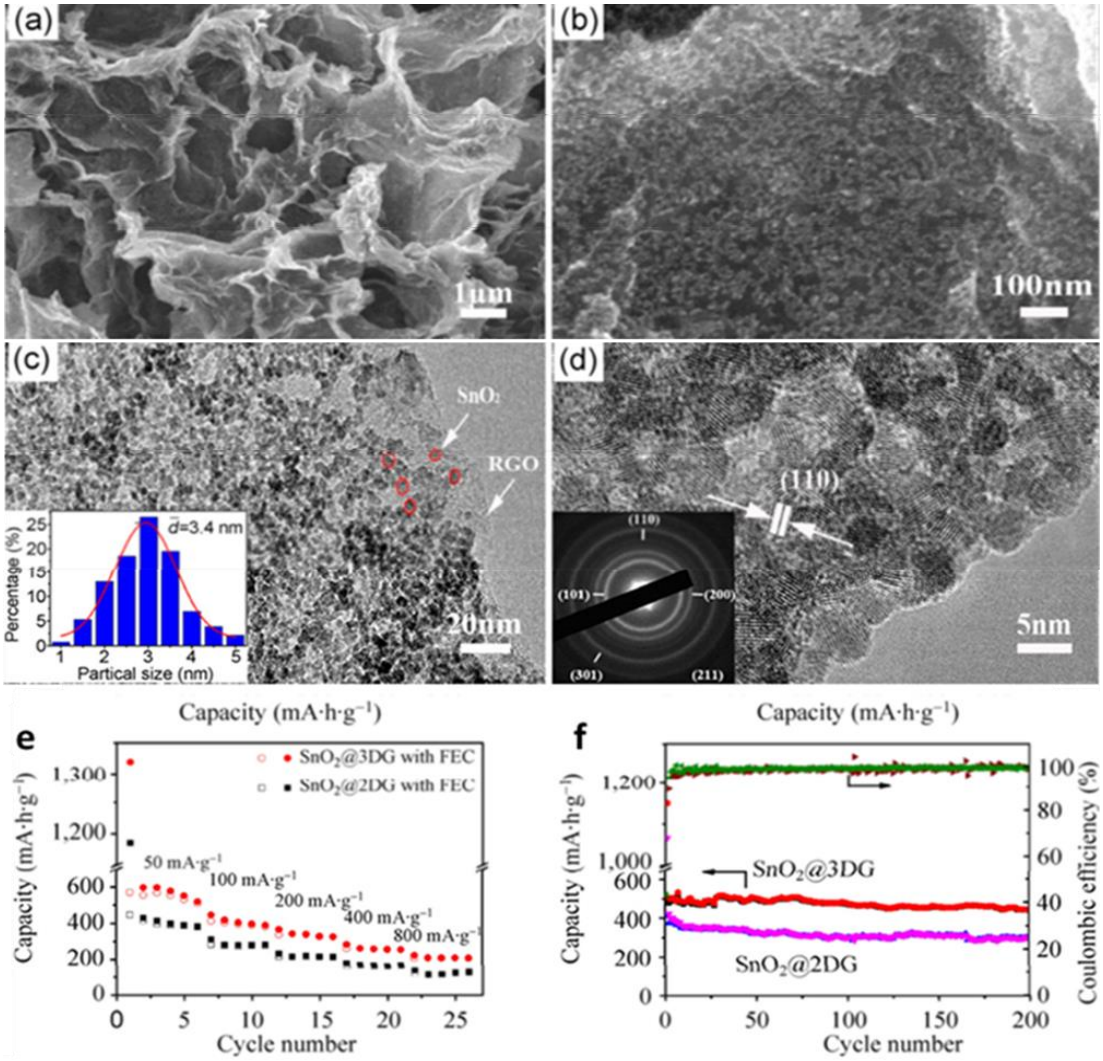


**Figure 2.29** SEM images of $SnO_2$@3DG (a), (b). TEM images of $SnO_2$@3DG (c), (d), with the inset of (c) showing the particle size distribution and the inset of (d) showing the corresponding selected area electron diffraction pattern. Rate performance of $SnO_2$@3DG and $SnO_2$@2DG cycled at varied current densities from 50 to 800 $mA \cdot g^{-1}$ (e). Cycling performance comparison of $SnO_2$@3DG and $SnO_2$@2DG at the current rate of 100 $mA \cdot g^{-1}$ (f). Reproduced with permission [170].

capacity of 432 mAh $g^{-1}$ after 200 cycles at 100 mA $g^{-1}$ with a capacity retention of 85.7%. Even at a high current density of 800 mA $g^{-1}$, a reversible capacity of 210 mAh $g^{-1}$ was still observed.

### 2.4.3. Transition metal sulphide (TMS) based anode materials

Transition metal sulphide (TMS) materials have also been believed to be promising sodium storage materials due to their high theoretical capacities through electrochemical conversion reactions as along with the transition metal oxides. In the sodiation/desodiation process, compared to the related transition metal oxides, transition metal sulphides have great advantagesbecause the M–S bonds in metal sulphide are weaker than the corresponding M–O bonds in metal oxides, which can be kinetically favorable for conversion reactions with $Na^+$ ions.[181] Therefore, many metal sulfides have been extensively explored as high anode candidates for SIBs including iron sulphides (FeS, $FeS_2$),[183,184] cobalt sulphides (CoS, $CoS_2$),[185,186] molybdenum sulfides ($Mo_2S$, $MoS_2$),[187,188] zinc sulfide (ZnS),[189] tin sulfides (SnS, $SnS_2$),[190-192] etc.

In the case of $MoS_2$, the intercalation and conversion reactions are described as the following two-step reactions: [193]

$$MoS_2 + xNa^+ + xe^- \longrightarrow Na_xMoS_2 \quad (2.8)$$

$$Na_xMoS_2 + (4- x)\ Na^+ + (4 - x)\ e^- \longrightarrow 2Na_2S + Mo \quad (2.9)$$

Xiong *et al.* prepared a flexible membrane consisting of $MoS_2$/carbon nanofibers ($MoS_2$-CNFs) via a simple electrospinning approach.[188] As displayed in Fig. 2.30(a) and (b), $MoS_2$-CNFs consist of some interconnected one-dimensional nanofibers with an average diameter of about 150 nm and a smooth surface. The TEM images clearly show that $MoS_2$ nanosheets with layered structure are uniformly distributed on the surface and/or embedded in the CNF framework, as seen in Fig.2.30 (c). Due to their great self-standing and flexible properties, $MoS_2$-CNFs were made into a binder-free electrode, which presented the excellent cycling performance, achieving a charge capacity of 283.9 mAh $g^{-1}$ at 100 mA $g^{-1}$ after 600 cycles and superior rate capability, delivering the capacities of 283.3, 246.5, and 186.3 mAh $g^{-1}$ at 0.5, 1, and 2 A $g^{-1}$, respectively, as displayed in Fig. 2.30(e), (f). Equations (2.8) and (2.9) are well confirmed by the typical peaks on the cyclic voltammetry (CV) curves.

In the case of SnS, the following combined conversion （1） and alloying （2） reactions as following were proposed by Wu *et al.*[192]

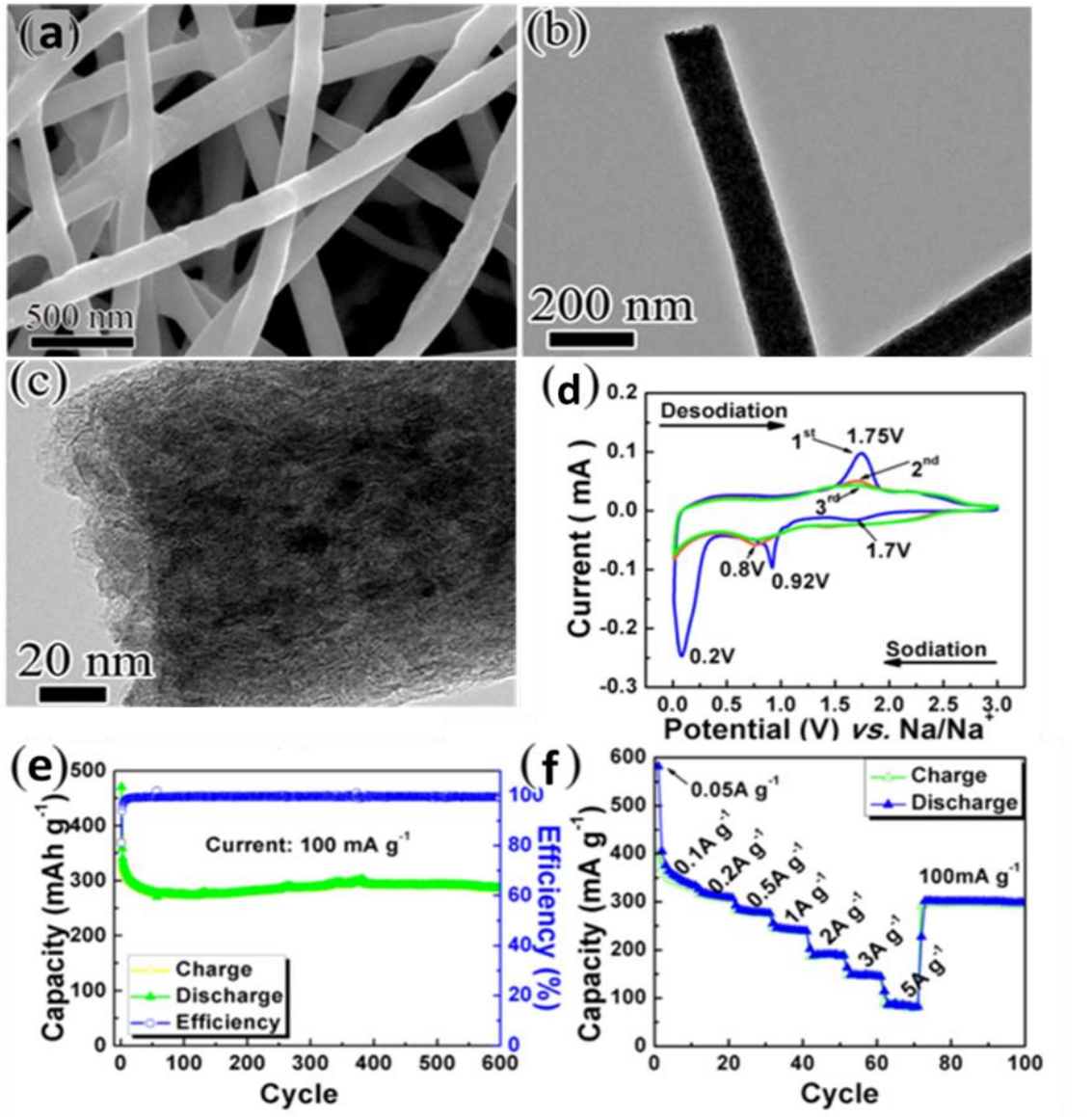


**Figure 2.30** Morphologies of $MoS_2$-CNFs nanofibers in SEM (a) and TEM (b), (c) images. Initial three cycles of CV curves for $MoS_2$-CNFs (d). Cycling performance of the $MoS_2$-CNFs electrode at a current rate of 100 mA $g^{-1}$ (e). Rate capability of $MoS_2$-CNFs at different current densities (f). Reproduced with permission [188].

$SnS + 2Na^+ + 2e^- \longleftrightarrow Na_2S + Sn$ (theoretical capacity 355 mA h $g^{-1}$) (2.10)

$Sn + 3.75Na^+ + 3.75e^- \longleftrightarrow Na_{3.75}Sn$ (theoretical capacity 667 mA h $g^{-1}$) (2.11)

Therefore, the overall theoretical capacity of SnS in SIBs is 1022 mAh $g^{-1}$. In this work, they fabricated a tin (II) sulfide–carbon (SnS–C) nanocomposite via a facile high energy mechanical milling (HEMM) approach under an argon atmosphere. In the SnS–C nanocomposite, well-crystallized SnS nanoparticles with a size of about 15 nm were

embedded uniformly in the conductive carbon matrix, as shown in Fig. 2.31. This is the crucial factor for providing good electrical conductivity and buffering the volume change during cycling. The reductive and oxidative peaks appearing on the CV curves are all consistent with the conversion (2.10) and alloying (2.11) reactions. The composite also exhibited good cycling stability, delivering a capacity of 548 mAh $g^{-1}$ over 80 cycles, and excellent rate capability, offering a reversible capacity of 452 mAh $g^{-1}$ even at the current density of 800 mA $g^{-1}$.

## 2.4.4. Alloy materials

Alloying materials that have the ability to form binary alloy compounds with Na can be suggested as attractive anodes for SIBs because they can store a large number of sodium ions in the host structure with a relatively low operating potential (below 1.0 V).[128,129] A single atom may combine with multiple Na atoms leading to a high specific capacity during the electrochemical insertion/extraction reactions.[3] Depending on the host materials and electrochemical sodiation levels, however, the large $Na^+$ ion can give rise to huge volume expansion during the alloying–dealloying reaction. These repetitive volume changes under the restraints compelled by the battery packaging are responsible for complex mechanical stresses in the active particles, ultimately leading to their fracture or pulverization.[43] Many strategies have been employed to fix this problem, by focusing on investigating the electrochemical and mechanical responses to Na interactions of alloy materials such as Si, Ge, Sn, P, Sb, Bi, etc.[194-205]

### 2.4.4.1. Tin and Si-based alloying compounds

Sn has been regarded as one of the most promising anode materials owing to its high theoretical specific capacity of 847 mAh $g^{-1}$, based on the full sodiation state of $Na_{15}Sn_4$.[206,207] The sodiation process of Sn has been proposed to proceed through the following a series of steps: [206,209,212]

Step one: $Na + Sn \rightarrow NaSn_3$, step two: $Na + NaSn_3 \rightarrow$ α-NaSn, step three: $5Na + 4(\alpha\text{-}NaSn) \rightarrow Na_9Sn_4$, step four: $6Na + Na_9Sn_4 \rightarrow Na_{15}Sn_4$.

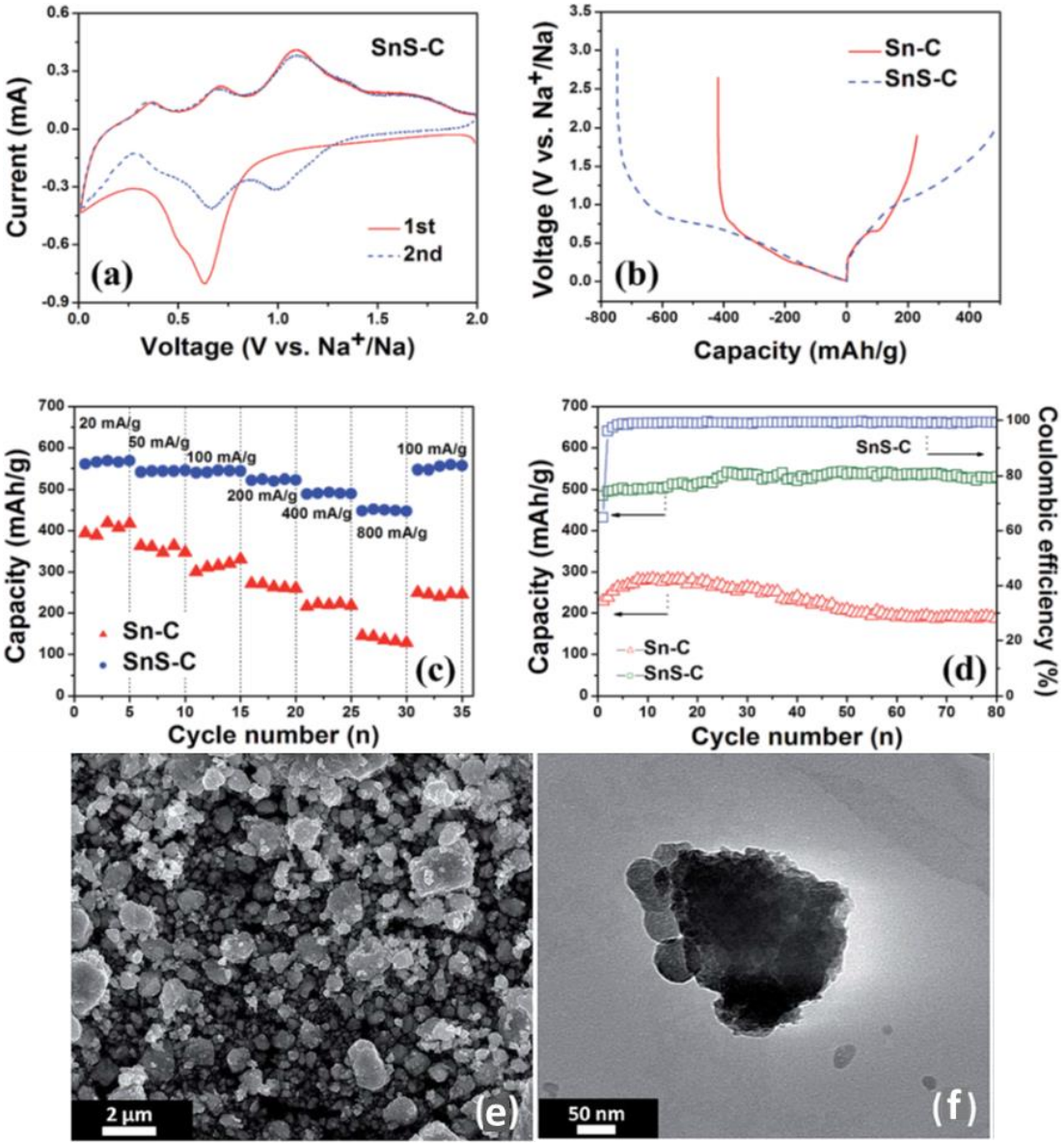


**Figure 2.31** CV curves of the SnS–C nanocomposite (a). Initial discharge–charge profiles of the SnS–C and Sn–C electrodes (b). Rate capability of the SnS–C and Sn–C electrodes at different current rates (c). Cycling performances of the SnS–C and Sn–C electrodes at a current rate of 100 mA $g^{-1}$ (d). Morphologies of the SnS–C nanocomposites SEM image (e), TEM image (f). Reproduced with permission [192].

It can be noted that the big volumetric expansion occurring in the sodiation process is the main problem that needs to be overcome for the tin-based materials, as shown in

Scheme 2.2. To date, various approaches have been devoted to addressing this issue.[198, 199, 208, 210, 211]

Liu and co-workers prepared Sn nanodots that were finely encapsulated in porous N-doped carbon nanofibers (NDs@PNC) by an electrospinning technique and subsequent thermal treatment.[199] From the SEM and TEM images shown in Fig. 2.32, it can be found that the fibers are smooth and continuous, with an uniform diameter of about 120 nm, which interlink into a 3D network, with many Sn nanodots homogeneously encapsulated in the porous carbon matrix. When the as-prepared NDs@PNC with a flexible free-standing membrane was directly used as binder- and current-collector-free anode, it demonstrated exceptional electrochemical performance, delivering a reversible capacity of 633 mAh $g^{-1}$ at the current rate of 200 mA $g^{-1}$ and impressive rate capability, achieving the capacity of 450 mA h $g^{-1}$ even at 10 000 mA $g^{-1}$ and 483 mAh $g^{-1}$ over 1300 cycles at 2000 mA $g^{-1}$.

Another Sn/N-doped carbon microcage composite (Sn/NMCs) was fabricated via a simple spray drying approach by Ying *et al*. [211] The microspheres of Sn/NMCs are about 3 mm in size with Sn nanodots uniformly embedded inside, as presented in Fig. 2.33. This typical structure of Sn/NMCs significantly improved the Na-storage capacity and cycle life of Sn as well as its rate capability. It could exhibit very promising cycling and rate performance, delivering a capacity of 332 mAh $g^{-1}$ over 300 cycles at 50 mA $g^{-1}$ and obtaining 149 mAh $g^{-1}$ after changing the current density to 5A $g^{-1}$.

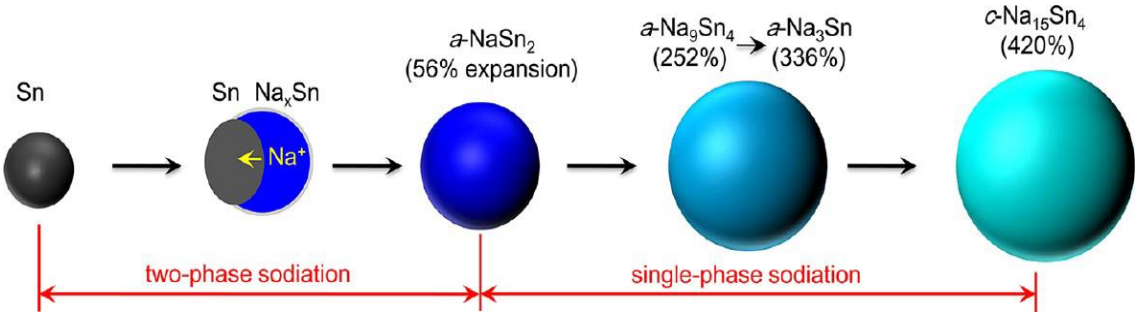


**Scheme 2.2** Schematic illustration of the structural evolution of Sn electrode during the sodiation. Reproduced with permission [209].

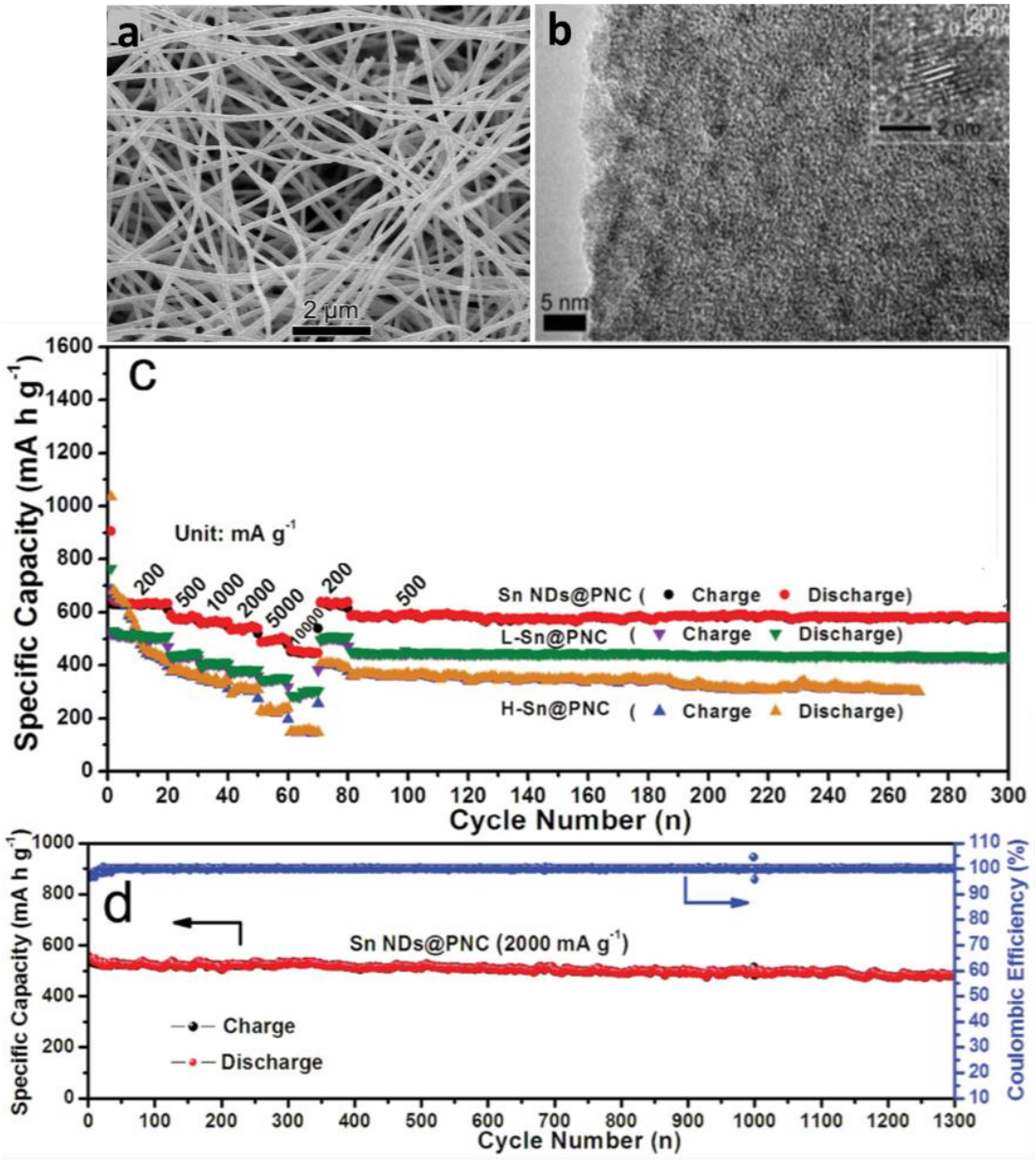


**Figure 2.32** SEM (a) and, TEM (b) images of Sn NDs@PNC nanofibers. Rate capability and cycling performance of Sn NDs@PNC with different Sn contents (c). Long-term cycling stability of Sn NDs@PNC at a current density of 2A $g^{-1}$ (d). Reproduced with permission [199].

Among the alloying materials, Si-based anode materials have been attracting more and more attention because they have demonstrated reversible Na-ion uptake through electrochemical alloying reactions with Na.[194,195] During the sodiation process, a two-phase equilibrium reaction will occur as follows: $x$Na + Si ↔ $x$NaSi + (1− $x$) Si, which

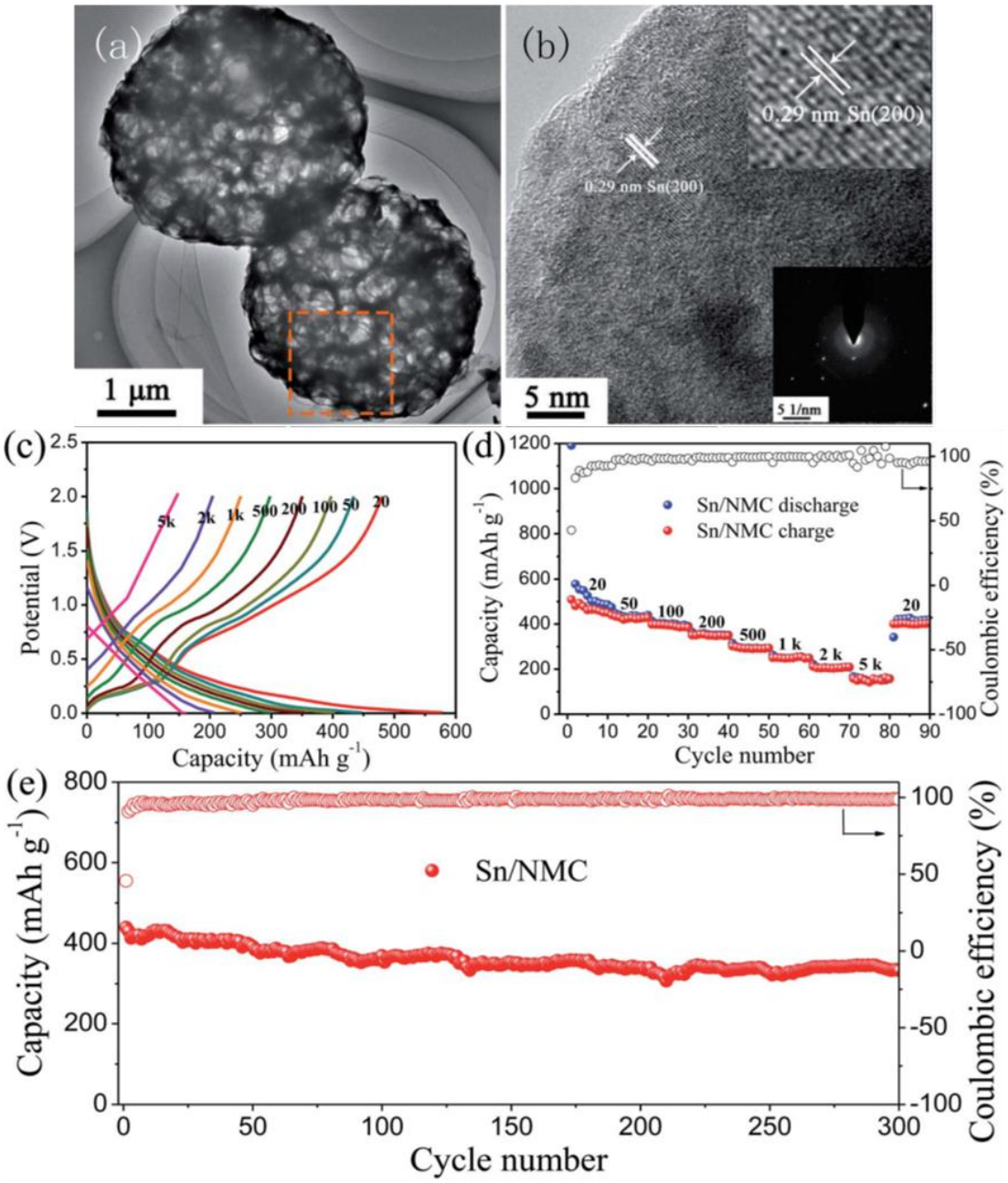


**Figure 2.33** TEM (a) and HRTEM (b) images of Sn/NMCs. (c) Galvanostatic discharge/charge profiles of Sn/NMCs tested at different rates (from 20 to 5000 mA $g^{-1}$) (c). Rate performance of Sn/NMCs (d). Cycling performance of Sn/NMCs at 50 mA $g^{-1}$ (e). Reproduced with permission [211].

would enable a sizeable capacity of 954 mAh $g^{-1}$, although the low conductivity and large volume changes during cycling are the main challenges facing the development of

Si-based anode materials. Thus far, some research works have obtained positive results towards addressing these issues.[213-215]

Zhang *et al.* from our institute reported the fabrication of a binder-free bamboo-rattle type Si/C film via electrospinning technology. [215] It can be seen from the SEM and TEM images in Fig. 2.34 that the flexible Si/C film is composed of Si/C nanofibers. In a single Si/C nanofiber, yolk–shell structured carbon/void/Si (CVS) particles are embedded inside the bamboo-like Si/C nanofiber. When the composite was tested as a free standing electrode, it exhibited high reversible capacity, ultrafast sodium storage, and outstanding cyclability, achieving a capacity of 454.5 mAh $g^{-1}$ at 50 mA $g^{-1}$ after 200 cycles, and 312 mAh $g^{-1}$ over 2000 cycles, even at a current density as high as 5A $g^{-1}$.

### 2.4.4.2. Phosphorus-based alloying compounds

Phosphorus (P) is the most promising anode materials for SIBs due to its electrochemical reaction with sodium to form $Na_3P$ at an attractive potential and its light atomic weight, obtaining the highest theoretical capacity of 2596 mA h $g^{-1}$. Phosphorous exists in three main allotropes: white phosphorus, red phosphorus, and black phosphorus. Among these allotropes, white phosphorus is not chemically stable, while the synthesis of black phosphorus is not facile. Red phosphorus is usually amorphous in nature and is widely commercially available.[216] Similarly, P-based electrode materials also face the same challenges as the others, the low conductivity and large volume changes during cycling. Therefore, many researchers have explored various strategies to address this issue.[217-226]

Yang's group, the pioneers in developing phosphorus-based materials for SIBs, reported an amorphous phosphorus/carbon (a-P/C) nanocomposite synthesized by high-energy ball-milling of commercial red phosphorus powder and amorphous carbon black.[217] a-P/C shows a disordered structure, and the phosphorus clusters are highly dispersed in a carbon matrix. a-P/C exhibited greatly enhanced electrochemical performance with initial charge/discharge capacities of 2015 mAh $g^{-1}$ and 1764 mAh $g^{-1}$, respectively, remaining steady for up 930 mAh $g^{-1}$ over 140 cycles at a current rate of 250 mA $g^{-1}$. It also presented excellent rate capability, achieving capacity of 1764 to

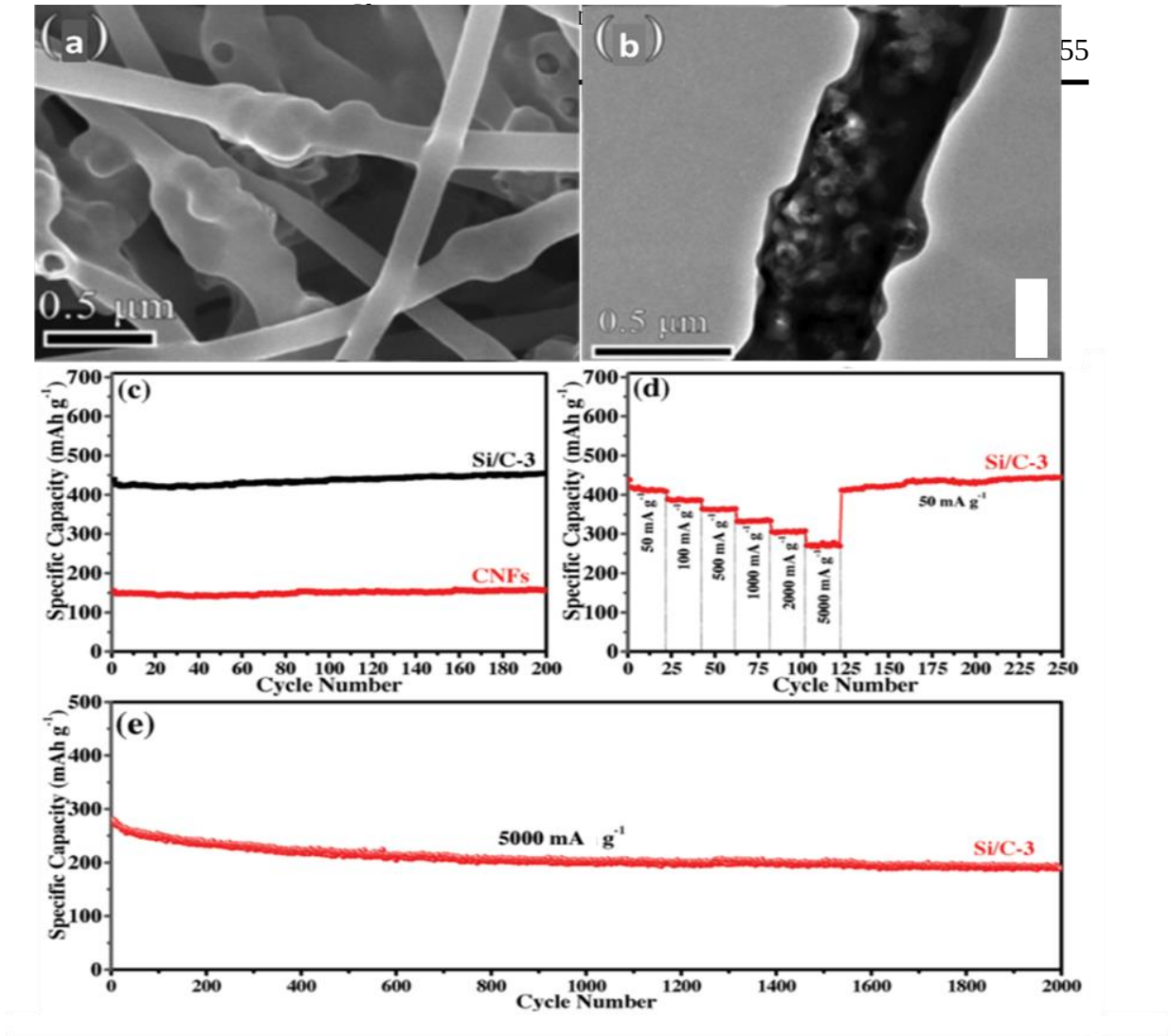


**Figure 2.34** SEM (a) and TEM (b) images of bamboo-rattle-like architecture of Si/C-3 composite. Cycling performances of Si/C-3 and pure CNFs at a current rate of 50 mA $g^{-1}$ (c). Rate capability of Si/C-3 at different current densities (d). Cycling stability test at a current rate of 5 A $g^{-1}$ (e). Reproduced with permission [215].

640 mAh $g^{-1}$ at various charge/discharge current densities, ranging from 250 to 4000 mA $g^{-1}$, as displayed in Fig. 2.35(a), (c), (e).

In 2014, Song *et al.* prepared a phosphorus/graphene nanosheet composite (P/G hybrid) via ball milling of red phosphorus and graphene stacks.[219] This approach made use of the large surface area and flexibility of graphene nanosheets to conform to the phosphorus particles during milling, thus enhancing the overall conductivity and

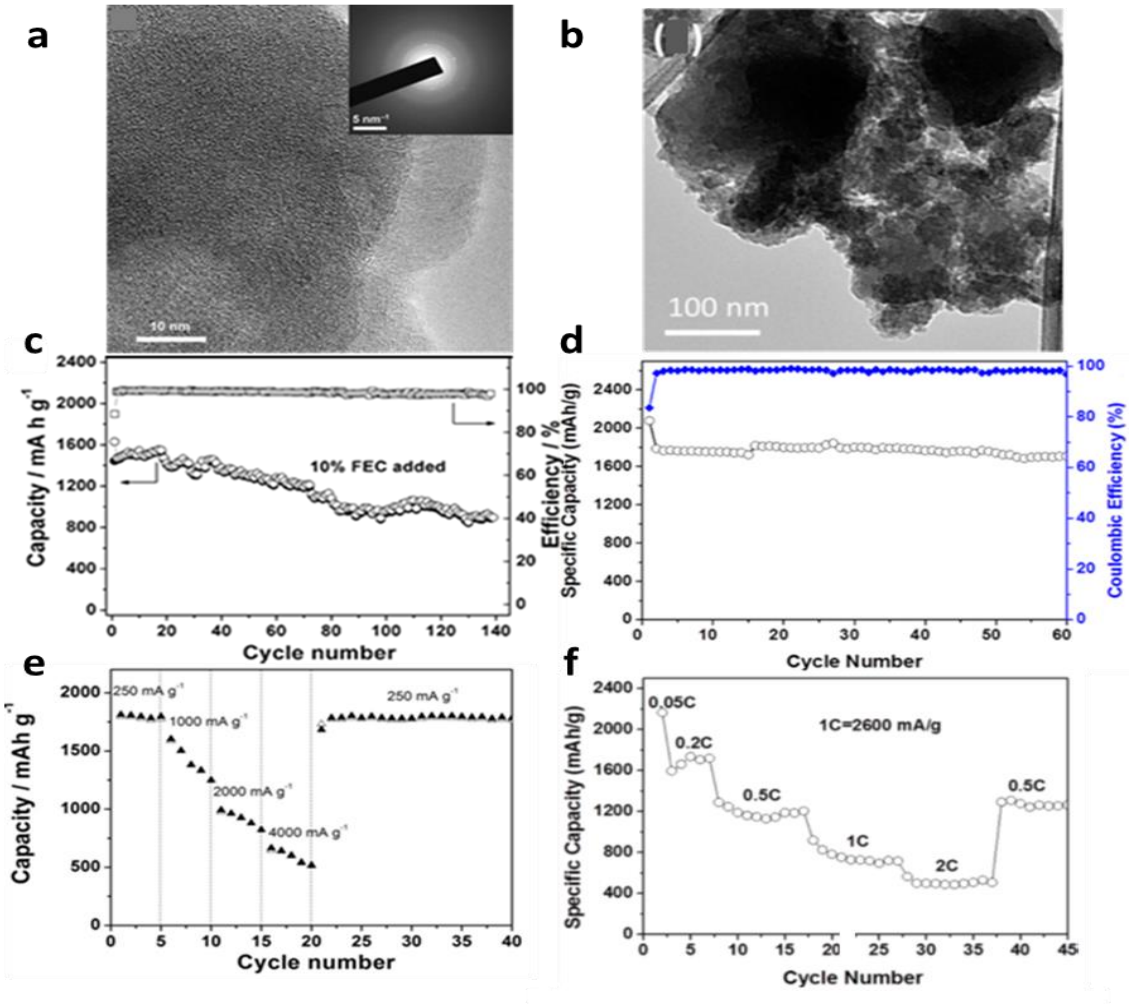


**Figure 2.35** TEM images of the a-P/C composite (a) and the P/G hybrid (b). Long-term cycling performance of a-P/C (c) and P/G hybrid (d). Rate performance of a-P/C (e) and P/G hybrid (f). Reproduced with permission [217][219].

improving the material's tolerance for the large volume changes of phosphorus during cycling. The P/G hybrid displayed very high Na storage capability, delivering a reversible capacity of 1700 mAh $g^{-1}$ at a current density of 260 mA $g^{-1}$ after 60 cycles and good rate performance, exhibiting capacity of 1700 to 750 mAh $g^{-1}$ as the current rate changed from 0.2 C to 2 C, as shown in Fig.2.35(b), (d), (f).

A red P − single-walled carbon nanotube composite (red P-SWCNT) was fabricated by Wang's group by a modified vaporization-condensation method.[220] The composite combined P particles into the highly conductive and mechanically strong SWCNT network, which enhances the conductivity of the composite and stabilizes the solid-

electrolyte interphase. P-SWCNT presented promising rate capability, delivering stable desodiation capacities of 700 to 300 mAh/$g_{composite}$, corresponding to the changing current densities from 50 to 2000 mA/$g_{composite}$. The composite also exhibited improved cycling performance, achieving a very stable reversible capacity of 580 mAh/$g_{composite}$ under the current density of 500 mA/$g_{composite}$ over 200 cycles without capacity decay, as shown in Fig. 2.36(a), (c), (e).

Yu's group synthesized a red P/carbon composite (P@N-MPC) with a core/shell structure by confining amorphous red phosphorus in metal-organic framework (MOF)-

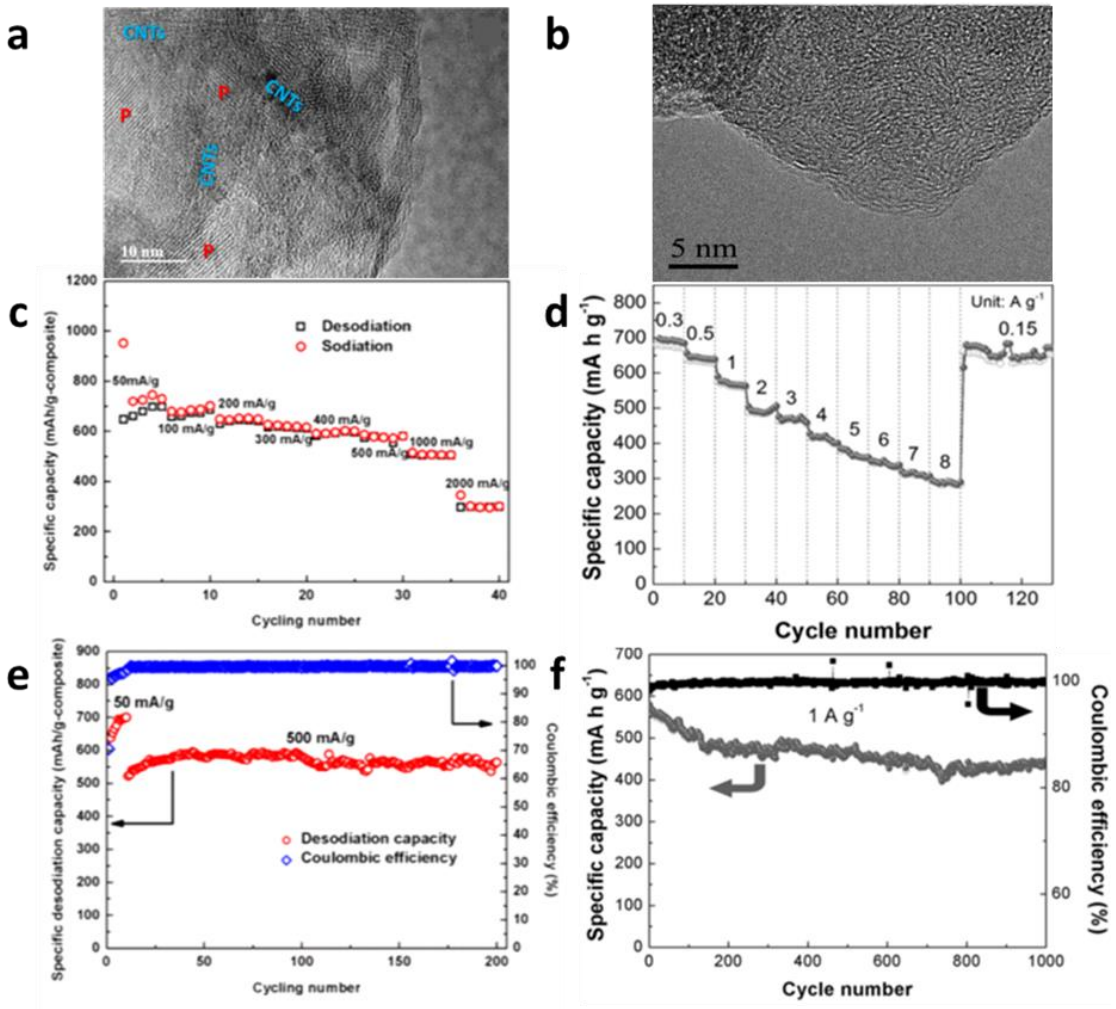


**Figure 2.36** TEM images of PSWCNT (a) and P@N-MPC (b). Rate performance of PSWCNT (c) and P@N-MPC (d). Cycling performance of PSWCNT (e) and P@N-MPC (f). Reproduced with permission [220][224].

structure by confining amorphous red phosphorus in metal-organic framework (MOF)-derived N-doped microporous carbon,[224] as shown in Fig. 2.36(b). In the TEM image of P@N-MPC, no obvious red P residue appears on the surface of the N-doped microporous carbon, which reveals that the micropores in the N-MPC matrix are partially occupied by red P nanoparticles. The P@N-MPC composite displayed improved rate capacity, delivering a reversible capacity ranging from 684 to 291 mAh $g^{-1}$ with the current rate ranging from 0.3 mA $g^{-1}$ to 8 A $g^{-1}$, and exhibited excellent cycling performance with capacity of 450 mAh $g^{-1}$ at 1 A $g^{-1}$ after 1000 cycles, as seen in Fig 2.36(d), (f).

Another strategy to address the drawbacks of P anode is the fabrication of P@RGO composite, where red phosphorus nanodots are densely and uniformly deposited on reduced graphene oxide sheets, as illustrated in Fig. 2.37(a).[225] The resultant P@RGO flexible anode revealed the much better cycling stability than pure red P, achieving a capacity of 914 mAh $g^{-1}$ over 300 cycles at the current density of 1.59 A $g^{-1}$. Excellent rate performance was also observed. The P@RGO flexible anode could deliver average capacities ranging from 1165.4 to 135.3 mAh $g^{-1}$ at various current densities from 159.4 to 47818.3 mA $g^{-1}$, as displayed in Fig. 2.37(d), (g).

Zhang *et al*. also prepared a flexible paper (P@GN) with bread-and-butter-like structure consisting of amorphous P layer@N-doped graphene framework.[226] They selected few-layered N-doped graphene as the substrate and made the P nanoparticles embed on the framework via a phase-transformation route. This disordered and flexible layered structure of P@GN, in which the amorphous P nanoparticles are well dispersed, is clearly confirmed by the SEM and TEM images in Fig. 2.37(b) and (c). P@GN afforded remarkable rate performance, delivering a reversible capacity of 809 mAh $g^{-1}$ at the current density of 1.5 A $g^{-1}$ and long-term cycling stability, achieving the Na storage capacity of 892 mAh $g^{-1}$ at the current rate of 800 mA $g^{-1}$ over 350 cycles, as shown in Fig. 2.37(e).

## 2.4.5. Organic compounds

In recent years, some organic compounds have been chosen as anode materials due to their several advantages, such as their chemical diversity, tunable redox property, in

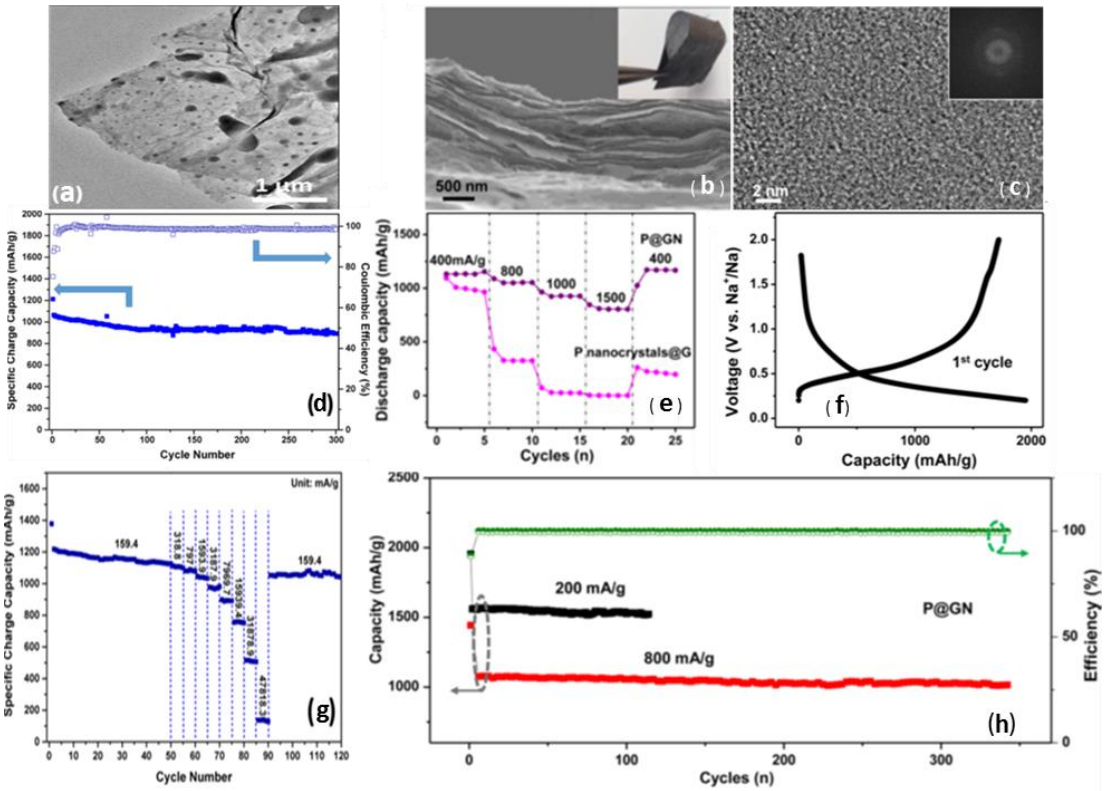


**Figure 2.37** TEM image of P@RGO (a). SEM image of the cross-section of P@GN paper (b), with the inset a photograph of its bending capability. TEM image of P@GN portion (c). Cycling performance of the P@RGO (d). Rate capability of P@GN (e). Discharge/charge profile of a P@GN electrode at 200 mA $g^{-1}$(f). Rate performance of the P@RGO (g). Cycling performance of P@GN at 200 mA $g^{-1}$ and 800 mA $g^{-1}$(h). Reproduced with permission [225][226].

which the redox reaction of organic carbonyl materials is less influenced by the ionic size of alkali ions,[227] light weight, mechanical flexibility, and cost-effective aspects.[228,229] Therefore, the major organic carbonyl compounds, including the conjugated carboxylates,[230,231,232] imides,[233] quinones,[234,235] and Schiff base-groups,[236] are being widely investigated as promising alternative anode materials for SIBs.

Wang *et al.* synthesized conjugated carboxylate, perylene 3,4,9,10-tetracarboxylic dianhydride (PTCDA) and its derivative tetrasodium perylene 3,4,9,10-tetracarboxylic dianhydride (NaPTCDA).[230] As shown in Fig. 2.38, both PTCDA and NaPTCDA revealed good sodium storage performance although there are obvious differences in the

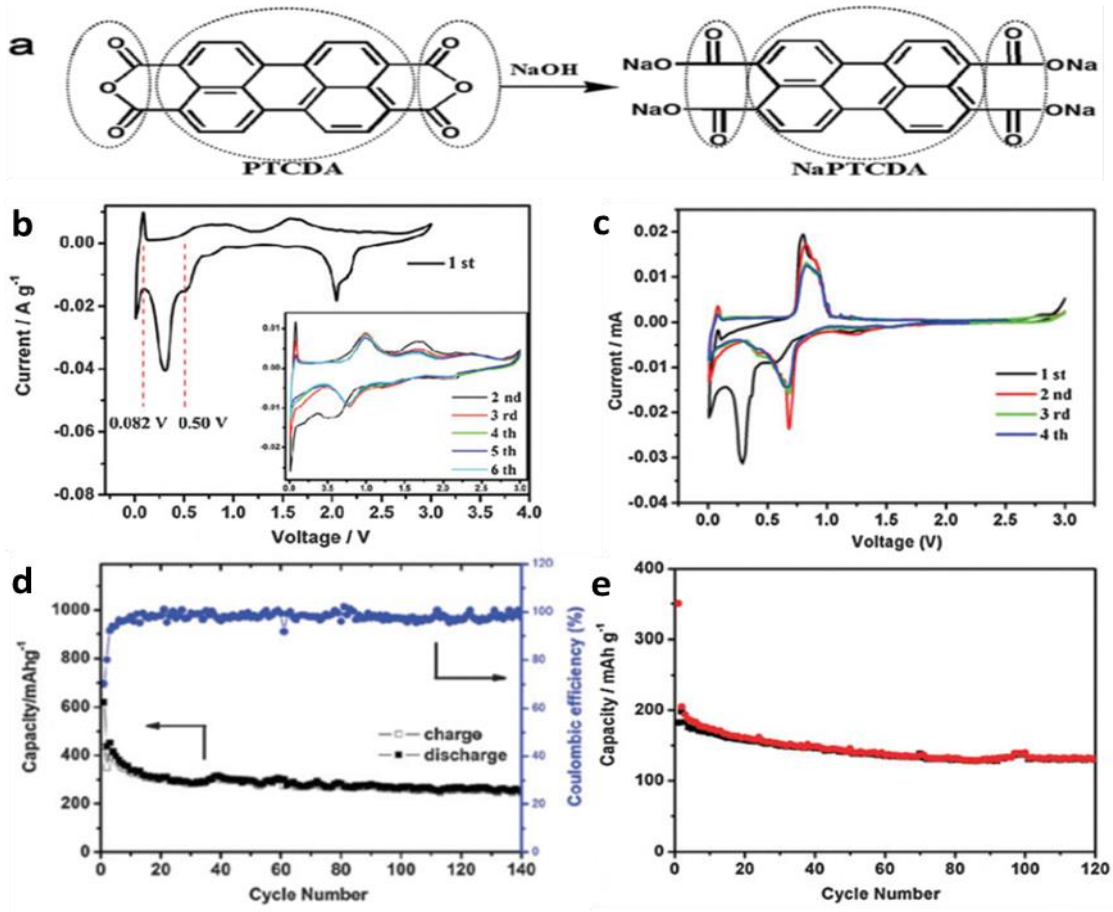


**Figure 2.38** Molecular structures of PTCDA and NaPTCDA (a). CV curves of (b) PTCDA and (c) NaPTCDA electrodes. Cycling performances of (d) PTCDA and (e) NaPTCDA at a current density of 25 mA $g^{-1}$. Reproduced with permission [230].

sodium insertion/extraction process between them, so that they exhibited different Na storage capacity. In comparison, PTCDA displayed much better cycling performance, delivering a reversible capacity of 250.5 mAh $g^{-1}$ at the current rate of 25 mA $g^{-1}$ over 140 cycles, while NaPTCDA could only reach a capacity of 131.1 mAh $g^{-1}$ after 120 cycles under the same current density as PTCDA .

Another polyimide, 1,4,5,8-naphthalenetetracarboxylic dianhydride (NTCDA)-derived polyimide (i.e. PNTCDA) was prepared by Xia's group.[233] PNTCDA displayed excellent cycling stability and a high rate capability, achieving a reversible capacity of 136.6 mAh $g^{-1}$ at 140 mA $g^{-1}$ (1 C) over 500 cycles and a capacity of 84 mAh $g^{-1}$ at 32C, as presented in Fig. 2.39.

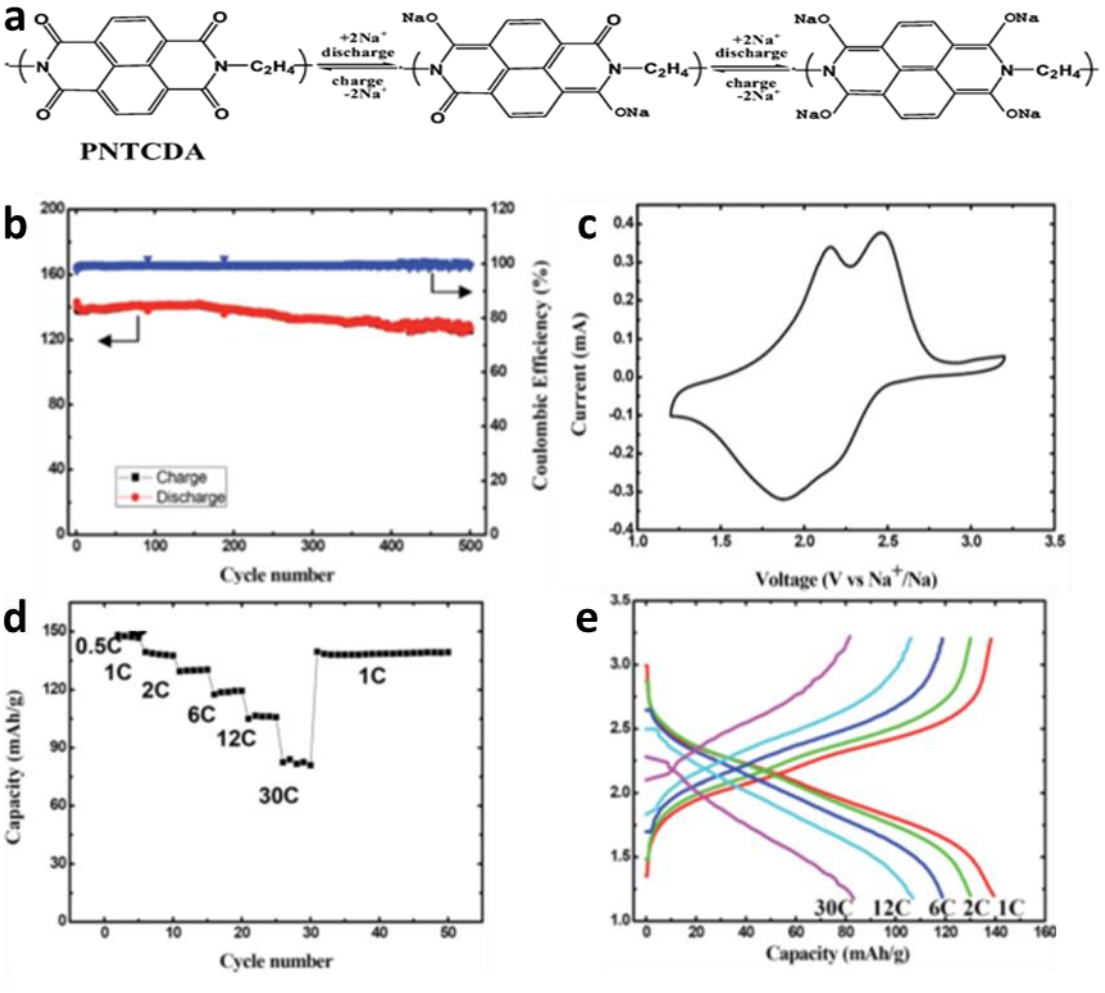


**Figure 2.39** Possible electrochemical redox mechanism of PNTCDA (a). Cycling performance of Na/PNTCDA at 1C (b). CV curve of PNTCDA (c). Discharge capacities of Na/PNTCDA at different current rates (d). Charge–discharge profiles of PNTCDA at varying currents from 1C to 30C (e). Reproduced with permission [233].

## 2.5. Electrolyte

The selection of electrolyte for SIBs has a significant impact on the electrochemical behavior of electrodes. Electrolytes are mainly composed of salts and solvents. In addition, additives which act on formation of surface passivation layers, namely, the solid-electrolyte interphase (SEI), are also added into the electrolytes. In general, the electrolyte used in SIBs should comply with these requirements: (1) chemically stable, (2) electrochemically stable, (3) thermally stable, (4) ionically conductive and

electronically insulating, and (5) having low toxicity with low production cost. These features intrinsically depend on the nature of the salts and the solvents as well as the possible use of additives. Therefore, the salt should meet these requirements: (1) solubility in the solvent, (2) chemical stability without reduction or oxidation, as well as reacting with the cell components. As for the solvent, it should possess these characteristics: (1) be polar with a high dielectric constant, (2) have low viscosity for increasing the ionic mobility, (3) remain inert to the charged surfaces of SIBs during cycling, and (4) have a low melting point and a high boiling point. [237,238] The most commonly employed sodium salts and solvents as well as additives are shown in Fig. 2.40. Their basic properties are also listed in Table 2.3 for Na salts and Table 2.4 for solvents and additives.

## 2.6 Binder

Likewise, the binder plays as important a role as the electrolyte in improving the electrode performance. A desirable binder should have the functions of stabilizing the electrode surface and suppressing electrode distortion during the sodiation-desodiation process. The most commonly used binders such as Polyvinylidenefluoride,

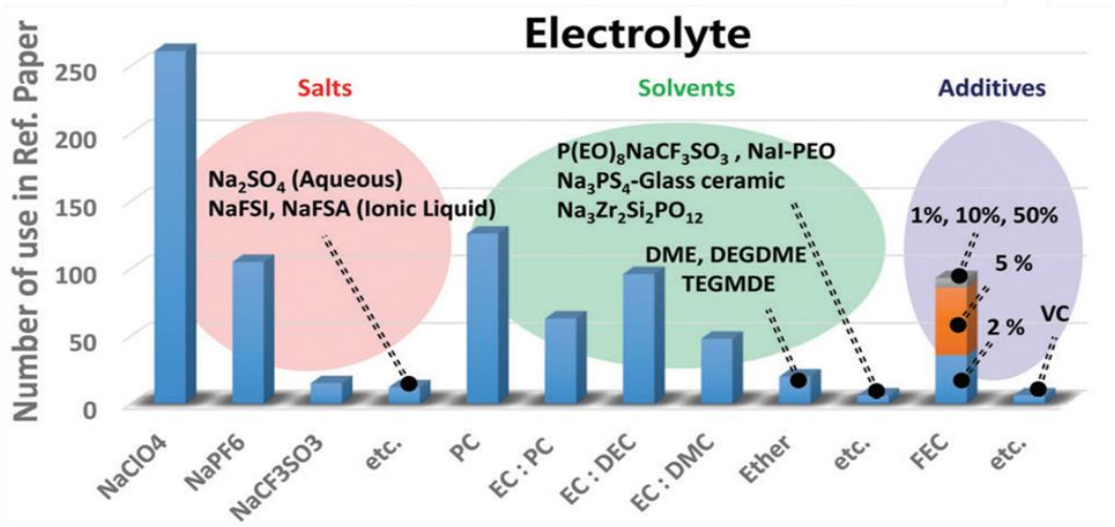


**Figure 2.40** Electrolytes recently used in current SIBs. Reproduced with permission[55].

**Table 2.3** Na-salts used for sodium ion battery electrolytes. Reproduced with permission [237].

| Salt | Anion chemical structure | $M_w$ [g $mol^{-1}$] | $T_m$ [°C] | σ [mS $cm^{-1}$] |
|---|---|---|---|---|
| $NaClO_4$ | 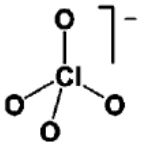 | 122.4 | 468 | 6.4 |
| $NaPF_6$ | 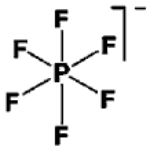 | 167.9 | 300 | 7.98 |
| $NaCF_3SO_3$ | 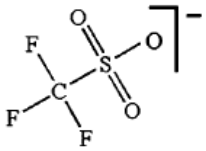 | 172.1 | 248 | 1.7 |
| NaTFSI | 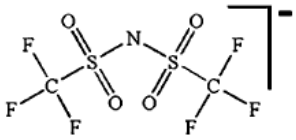 | 303.1 | 257 | 6.2 |
| NaFSI | 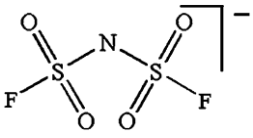 | 203.3 | 118 | |
| $NaBF_4$ | 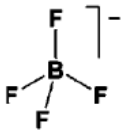 | 109.8 | 384 | |

**Table 2.4** Solvents and additives commonly used for sodium ion battery electrolytes. Reproduced with permission [237].

| Solvent | $T_m$ (°C) | $T_b$ (°C) | $T_f$ (°C) | $\eta$ (cP) 25°C | $\varepsilon$ 25° C | AN (DN) |
|---|---|---|---|---|---|---|
| 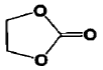 Ethylene carbonate (EC) | 36.4 | 248 | 160 | 1.9 (40 °C) | 89.78 | |
| 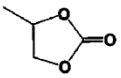 Propylene carbonate (PC) | -48.8 | 242 | 132 | 2.53 | 64.92 | 18.3 |
| 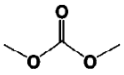 Dimethyl-carbonate (DMC) | 4.6 | 91 | 18 | 0.59 | 3.107 | |
| 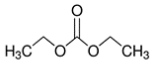 Diethyl carbonate (DEC) | -74.3 | 126 | 31 | 0.75 | 2.805 | |
| 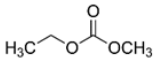 Ethyl methyl carbonate (EMC) | -53 | 110 | | 0.65 | 2.958 | |
| 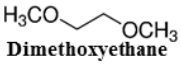 Dimethoxyethane (DME) | -58 | 84 | 0 | 0.46 | 7.18 | 10.9 |
| 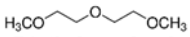 Diethylene glycol dimethyl ether (Diglyme) | -64 | 162 | 57 | 1.06 | 7.4 | 9.9 |
| 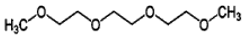 Triethylene glycol dimethyl ether (Triglyme) | -46 | 216 | 111 | 3.39 | 7.53 | 10.5 |
| 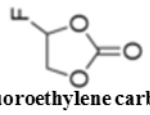 Fluoroethylene carbonate (FEC) | 18 | 212 | 102.2 | | | |

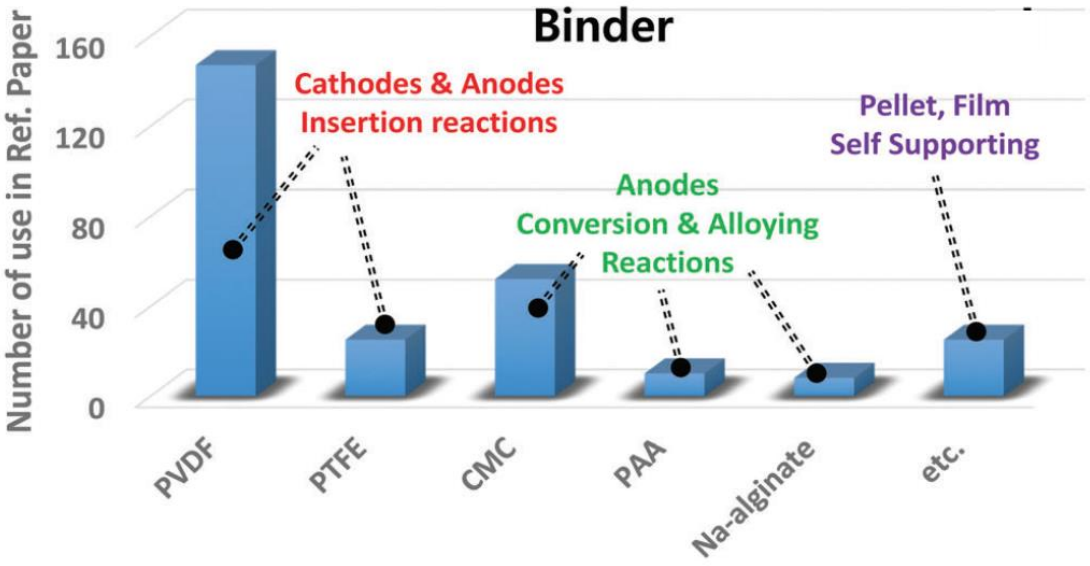


**Figure 2.41** Recent research progress on binders for current SIBs. Reproduced with permission [55].

Polytetrafluoroethylene, Carboxymethyl cellulose, Polyacrylic acid and Sodium alginate are shown in Fig. 2.41.

## 2.7. References

1. Whittingham, M. S., Chemistry of intercalation compounds: Metal guests in chalcogenide hosts. *Prog. Solid State Chem.* **1978,** *12* (1), 41-99.

2. Böhm, H.; Beyermann, G., ZEBRA batteries, enhanced power by doping. *J. Power Sources* **1999,** *84* (2), 270-274.

3. Galloway, R. C.; Haslam, S., The ZEBRA electric vehicle battery: power and energy improvements. *J. Power Sources* **1999,** *80* (1), 164-170.

4. Javadi, T.; Petric, A., Thermodynamic analysis of reaction products observed in ZEBRA cell cathodes. *J. Electrochem. Soc.* **2011,** *158* (6), A700-A704.

5. van Zyl, A., Review of the zebra battery system development. *Solid State Ionics* **1996,** *86*, 883-889.

6. Brett, D.; Aguiar, P.; Brandon, N., System modelling and integration of an intermediate temperature solid oxide fuel cell and ZEBRA battery for automotive applications. *J. Power Sources* **2006,** *163* (1), 514-522.

7. Whittingham, M. S., Electrical energy storage and intercalation chemistry. *Science* **1976,** *192* (4244), 1126-1127.

8.Whittingham, M. S., Chemistry of intercalation compounds: Metal guests in chalcogenide hosts. *Prog. Solid State Chem.* **1978,** *12* (1), 41-99.

9.Whittingham, M., Structure and bonding in the pyridine intercalates of tantalum disulfide. *Mater. Res. Bull.* **1978,** *13* (8), 775-782.

10.Newman, G. H.; Klemann, L. P., Ambient Temperature Cycling of an Na-$TiS_2$ Cell. *J. Electrochem. Soc.* **1980,** *127* (10), 2097-2099.

11. Mizushima, K.; Jones, P.; Wiseman, P.; Goodenough, J. B., $LixCoO_2$ (0< x<-1): A new cathode material for batteries of high energy density. *Mater. Res. Bull.* **1980,** *15* (6), 783-789.

12. Delmas, C.; Braconnier, J.-J.; Fouassier, C.; Hagenmuller, P., Electrochemical intercalation of sodium in $NaxCoO_2$ bronzes. *Solid State Ionics* **1981,** *3*, 165-169.

13. Kanno, R.; Takeda, Y.; Ichikawa, T.; Nakanishi, K.; Yamamoto, O., Carbon as negative electrodes in lithium secondary cells. *J. Power Sources* **1989,** *26* (3-4), 535-543.

14. Mohri, M.; Yanagisawa, N.; Tajima, Y.; Tanaka, H.; Mitate, T.; Nakajima, S.; Yoshida, M.; Yoshimoto, Y.; Suzuki, T.; Wada, H., Rechargeable lithium battery based on pyrolytic carbon as a negative electrode. *J. Power Sources* **1989,** *26* (3-4), 545-551.

15. Yazami, R.; Touzain, P., A reversible graphite-lithium negative electrode for electrochemical generators. *J. Power Sources* **1983,** *9* (3), 365-371.

16. Fong, R.; Von Sacken, U.; Dahn, J. R., Studies of lithium intercalation into carbons using nonaqueous electrochemical cells. *Journal of The Electrochemical Society* **1990,** *137* (7), 2009-2013.

17. Ohzuku, T.; Iwakoshi, Y.; Sawai, K., Formation of Lithium-Graphite Intercalation Compounds in Nonaqueous Electrolytes and Their Application as a Negative Electrode for a Lithium Ion (Shuttlecock) Cell. *J. Electrochem. Soc.***1993,** *140* (9), 2490-2498.

18.Nagaura, T.; Tozawa, K., Lithium ion rechargeable battery. *Prog. Batteries Solar Cells* **1990,** *9*, 209.

19. Endo, M.; Kim, C.; Nishimura, K.; Fujino, T.; Miyashita, K., Recent development of carbon materials for Li ion batteries. *Carbon* **2000,** *38* (2), 183-197.

20.Tarascon, J.-M.; Armand, M., Issues and challenges facing rechargeable lithium batteries. *Nature* **2001,** *414* (6861), 359-367.

21. Armand, M.; Tarascon, J.-M., Building better batteries. *Nature* **2008,** *451* (7179), 652-657.

22. Fergus, J. W., Recent developments in cathode materials for lithium ion batteries. *J. Power Sources* **2010,** *195* (4), 939-954.

23. Scrosati, B.; Garche, J., Lithium batteries: Status, prospects and future. *J. Power Sources* **2010,** *195* (9), 2419-2430.

24.Nitta, N.; Wu, F.; Lee, J. T.; Yushin, G., Li-ion battery materials: present and future. *Mater. Today* **2015,** *18* (5), 252-264.

25. Stevens, D.; Dahn, J., High Capacity Anode Materials for Rechargeable Sodium-Ion Batteries. *J. Electrochem. Soc.* **2000,** *147* (4), 1271-1273.

26. Cao, Y.; Xiao, L.; Sushko, M. L.; Wang, W.; Schwenzer, B.; Xiao, J.; Nie, Z.; Saraf, L. V.; Yang, Z.; Liu, J., Sodium ion insertion in hollow carbon nanowires for battery applications. *Nano Lett.* **2012,** *12* (7), 3783-3787.

27. Li, Y.; Xu, S.; Wu, X.; Yu, J.; Wang, Y.; Hu, Y.-S.; Li, H.; Chen, L.; Huang, X., Amorphous monodispersed hard carbon micro-spherules derived from biomass as a high performance negative electrode material for sodium-ion batteries. *J. Mater. Chem. A* **2015,** *3* (1), 71-77.

28. Guan, Z.; Liu, H.; Xu, B.; Hao, X.; Wang, Z.; Chen, L., Gelatin-pyrolyzed mesoporous carbon as a high-performance sodium-storage material. *J. Mater. Chem. A* **2015,** *3* (15), 7849-7854.

29. Liu, P.; Li, Y.; Hu, Y.-S.; Li, H.; Chen, L.; Huang, X., A waste biomass derived hard carbon as a high-performance anode material for sodium-ion batteries. *J. Mater. Chem. A* **2016,** *4* (34), 13046-13052.

30. Li, Y.; Hu, Y. S.; Titirici, M. M.; Chen, L.; Huang, X., Hard Carbon Microtubes Made from Renewable Cotton as High-Performance Anode Material for Sodium-Ion Batteries. *Adv. Energy Mater.* **2016,** *6* (18).

31. Dahbi, M.; Kiso, M.; Kubota, K.; Horiba, T.; Chafik, T.; Hida, K.; Matsuyama, T.; Komaba, S., Synthesis of hard carbon from argan shells for Na-ion batteries. *J. Mater. Chem. A* **2017**.

32. Okada S.; Takahashi Y.; Kiyabu T.; Doi T.; Yamaki J.; Nishida T.; 210th ECS Meeting Abstracts **602**, 201 (2006).

33. Xiang, X.; Zhang, K.; Chen, J., Recent Advances and Prospects of Cathode aterials for Sodium-Ion Batteries. *Adv. Mater.* **2015,** *27* (36), 5343-5364.

34. Scrosati, B., Recent advances in lithium ion battery materials. *Electrochim. Acta* **2000,** *45* (15), 2461-2466.

35. Nishi, Y., Lithium ion secondary batteries; past 10 years and the future. *J. Power Sources* **2001,** *100* (1), 101-106.

36. Tarascon, J.-M.; Armand, M., Issues and challenges facing rechargeable lithium batteries. *Nature* **2001,** *414* (6861), 359-367.

37. Armand, M.; Tarascon, J.-M., Building better batteries. *Nature* **2008,** *451* (7179), 652-657.

38. Pan, H.; Hu, Y.-S.; Chen, L., Room-temperature stationary sodium-ion batteries for large-scale electric energy storage. *Energy Environ. Sci.* **2013,** *6* (8), 2338-2360.

39. Zu, C.-X.; Li, H., Thermodynamic analysis on energy densities of batteries. *Energy Environ. Sci.* **2011,** *4* (8), 2614-2624.

40. de la Llave, E.; Borgel, V.; Park, K.-J.; Hwang, J.-Y.; Sun, Y.-K.; Hartmann, P.; Chesneau, F.-F.; Aurbach, D., Comparison between Na-Ion and Li-Ion cells: understanding the critical role of the cathodes stability and the anodes pretreatment on the cells behavior. *ACS Appl. Mater. Interfaces* **2016,** *8* (3), 1867-1875.

41. Slater, M. D.; Kim, D.; Lee, E.; Johnson, C. S., Sodium-ion batteries. *Adv. Funct. Mater.* **2013,** *23* (8), 947-958.

42. Adelhelm, P.; Hartmann, P.; Bender, C. L.; Busche, M.; Eufinger, C.; Janek, J., From lithium to sodium: cell chemistry of room temperature sodium–air and sodium–sulfur batteries. *Beilstein journal of nanotechnology* **2015,** *6*, 1016.

43. Kim, Y.; Ha, K. H.; Oh, S. M.; Lee, K. T., High-Capacity Anode Materials for Sodium-Ion Batteries. *Chemistry-A European Journal* **2014,** *20* (38), 11980-11992.

44. Zhuo, H.; Wang, X.; Tang, A.; Liu, Z.; Gamboa, S.; Sebastian, P., The preparation of NaV 1− x Cr x PO 4 F cathode materials for sodium-ion battery. *J. Power Sources* **2006,** *160* (1), 698-703.

45. Whitacre, J.; Tevar, A.; Sharma, S., Na 4 Mn 9 O 18 as a positive electrode material for an aqueous electrolyte sodium-ion energy storage device. *Electrochem. Commun.* **2010,** *12* (3), 463-466.

46. Xiong, H.; Slater, M. D.; Balasubramanian, M.; Johnson, C. S.; Rajh, T., Amorphous TiO2 nanotube anode for rechargeable sodium ion batteries. *J. Phys. Chem. Lett.* **2011,** *2* (20), 2560-2565.

47. Kitajou, A.; Komatsu, H.; Chihara, K.; Gocheva, I. D.; Okada, S.; Yamaki, J.-i., Novel synthesis and electrochemical properties of perovskite-type NaFeF 3 for a sodium-ion battery. *J. Power Sources* **2012,** *198*, 389-392.

48. Jian, Z.; Zhao, L.; Pan, H.; Hu, Y.-S.; Li, H.; Chen, W.; Chen, L., Carbon coated Na 3 V 2 (PO 4) 3 as novel electrode material for sodium ion batteries. *Electrochem. Commun.* **2012,** *14* (1), 86-89.

49. Zhao, L.; Zhao, J.; Hu, Y. S.; Li, H.; Zhou, Z.; Armand, M.; Chen, L., Disodium Terephthalate (Na2C8H4O4) as High Performance Anode Material for Low-Cost Room-Temperature Sodium-Ion Battery. *Adv. Energy Mater.* **2012,** *2* (8), 962-965.

50. Zhu, Y.; Han, X.; Xu, Y.; Liu, Y.; Zheng, S.; Xu, K.; Hu, L.; Wang, C., Electrospun Sb/C fibers for a stable and fast sodium-ion battery anode. *ACS nano* **2013,** *7* (7), 6378-6386.

51. Palomares, V.; Serras, P.; Villaluenga, I.; Hueso, K. B.; Carretero-González, J.; Rojo, T., Na-ion batteries, recent advances and present challenges to become low cost energy storage systems. *Energy Environ. Sci.* **2012,** *5* (3), 5884-5901.

52. Ding, J.; Wang, H.; Li, Z.; Kohandehghan, A.; Cui, K.; Xu, Z.; Zahiri, B.; Tan, X.; Lotfabad, E. M.; Olsen, B. C., Carbon nanosheet frameworks derived from peat moss as high performance sodium ion battery anodes. *ACS nano* **2013,** *7* (12), 11004-11015.

53. Qu, B.; Ma, C.; Ji, G.; Xu, C.; Xu, J.; Meng, Y. S.; Wang, T.; Lee, J. Y., Layered SnS2-Reduced Graphene Oxide Composite–A High-Capacity, High-Rate, and

Long-Cycle Life Sodium-Ion Battery Anode Material. *Adv. Mater.* **2014,** *26* (23), 3854-3859.

54. Luo, C.; Zhu, Y.; Xu, Y.; Liu, Y.; Gao, T.; Wang, J.; Wang, C., Graphene oxide wrapped croconic acid disodium salt for sodium ion battery electrodes. *J. Power Sources* **2014,** *250*, 372-378.

55. Hwang, J.-Y.; Myung, S.-T.; Sun, Y.-K., Sodium-ion batteries: present and future. *Chem. Soc. Rev.* **2017**.

56. Delmas, C.; Fouassier, C.; Hagenmuller, P., Structural classification and properties of the layered oxides. *Physica B+ C* **1980,** *99* (1-4), 81-85.

57. Momma, K.; Izumi, F., VESTA: a three-dimensional visualization system for electronic and structural analysis. *Journal of Applied Crystallography* 2008, *41* (3), 653-658.

58. Shannon, R. D., Revised effective ionic radii and systematic studies of interatomic distances in halides and chalcogenides. *Acta crystallographica section A: crystal physics, diffraction, theoretical and general crystallography* **1976,** *32* (5), 751-767.

59. Mather, G. C.; Dussarrat, C.; Etourneau, J.; West, A. R., A review of cation-ordered rock salt superstructure oxides. *Journal of Materials Chemistry* **2000,** *10* (10), 2219-2230.

60. Billaud, J.; Clément, R. J.; Armstrong, A. R.; Canales-Vázquez, J.; Rozier, P.; Grey, C. P.; Bruce, P. G., β-NaMnO2: a high-performance cathode for sodium-ion batteries. *Journal of the American Chemical Society* **2014,** *136* (49), 17243-17248.

61. Delmas, C.; Braconnier, J.-J.; Fouassier, C.; Hagenmuller, P., Electrochemical intercalation of sodium in NaxCoO2 bronzes. *Solid State Ionics* **1981,** *3*, 165-169.

62. Paulsen, J.; Dahn, J., O 2-Type Li2/3 [Ni1/3Mn2/3] O 2: A New Layered Cathode Material for Rechargeable Lithium Batteries II. Structure, Composition, and Properties. *Journal of the Electrochemical Society* **2000,** *147* (7), 2478-2485.

63. Lu, Z.; Dahn, J., Can All the Lithium be Removed from T 2 Li2/3 [Ni1/3Mn2/3] O 2? *Journal of The Electrochemical Society* **2001,** *148* (7), A710-A715.

64. Lu, Z.; Dahn, J., In Situ X-Ray Diffraction Study of P 2 Na2/3 [Ni1/3Mn2/3] O 2. *Journal of The Electrochemical Society* **2001,** *148* (11), A1225-A1229.

65. Delmas, C.; Braconnier, J.-J.; Hagenmuller, P., A new variety of LiCoO2 with an unusual oxygen packing obtained by exchange reaction. *Mater. Res. Bull.* **1982,** *17* (1), 117-123.

66. Paulsen, J.; Donaberger, R.; Dahn, J., Layered T2-, O6-, O2-, and P2-Type A2/3 [M ‘2+ 1/3M4+ 2/3] O2 Bronzes, A= Li, Na; M ‘= Ni, Mg; M= Mn, Ti. *Chemistry of materials* **2000,** *12* (8), 2257-2267.

67. Lu, Z.; Dahn, J., Effects of Stacking Fault Defects on the X-ray Diffraction Patterns of T2, O2, and O6 Structure Li2/3 [Co x Ni1/3-x Mn2/3] O2. *Chemistry of materials* **2001,** *13* (6), 2078-2083.

68. Carlier, D.; Saadoune, I.; Croguennec, L.; Ménétrier, M.; Suard, E.; Delmas, C., On the metastable O2-type LiCoO 2. *Solid State Ionics* **2001,** *144* (3), 263-276.

69. Eriksson, T. A.; Lee, Y. J.; Hollingsworth, J.; Reimer, J. A.; Cairns, E. J.; Zhang, X.-f.; Doeff, M. M., Influence of substitution on the structure and electrochemistry of layered manganese oxides. *Chemistry of materials* **2003,** *15* (23), 4456-4463.

70. Tournadre, F.; Croguennec, L.; Saadoune, I.; Carlier, D.; Shao-Horn, Y.; Willmann, P.; Delmas, C., On the mechanism of the P2 ‐ Na 0.70 CoO 2→ O2 ‐ LiCoO 2 exchange reaction—Part I: proposition of a model to describe the P2 ‐ O2 transition. *Journal of Solid State Chemistry* **2004,** *177* (8), 2790-2802.

71. Yabuuchi, N.; Kajiyama, M.; Iwatate, J.; Nishikawa, H.; Hitomi, S.; Okuyama, R.; Usui, R.; Yamada, Y.; Komaba, S., P2-type Nax [Fe1/2Mn1/2] O2 made from earth-abundant elements for rechargeable Na batteries. *Nature materials* **2012,** *11* (6), 512-517.

72. Yabuuchi, N.; Kawamoto, Y.; Hara, R.; Ishigaki, T.; Hoshikawa, A.; Yonemura, M.; Kamiyama, T.; Komaba, S., A comparative study of LiCoO2 polymorphs: structural and electrochemical characterization of O2-, O3-, and O4-type phases. *Inorganic chemistry* **2013,** *52* (15), 9131-9142.

73. Mu, L.; Xu, S.; Li, Y.; Hu, Y. S.; Li, H.; Chen, L.; Huang, X., Prototype Sodium-Ion Batteries Using an Air-Stable and Co/Ni-Free O3-Layered Metal Oxide Cathode. *Adv. Mater.* **2015,** *27* (43), 6928-6933.

74. Mendiboure, A.; Delmas, C.; Hagenmuller, P., Electrochemical intercalation and deintercalation of NaxMnO2 bronzes. *Journal of Solid State Chemistry* **1985,** *57* (3), 323-331.

75. Stoyanova, R.; Carlier, D.; Sendova-Vassileva, M.; Yoncheva, M.; Zhecheva, E.; Nihtianova, D.; Delmas, C., Stabilization of over-stoichiometric Mn 4+ in layered Na 2/3 MnO 2. *Journal of Solid State Chemistry* **2010,** *183* (6), 1372-1379.

76. Komaba, S.; Yabuuchi, N.; Nakayama, T.; Ogata, A.; Ishikawa, T.; Nakai, I., Study on the Reversible Electrode Reaction of Na1–x Ni0. 5Mn0. 5O2 for a Rechargeable Sodium-Ion Battery. *Inorganic chemistry* **2012,** *51* (11), 6211-6220.

77. Zhou, Y.-N.; Ding, J.-J.; Nam, K.-W.; Yu, X.; Bak, S.-M.; Hu, E.; Liu, J.; Bai, J.; Li, H.; Fu, Z.-W., Phase transition behavior of NaCrO 2 during sodium extraction studied by synchrotron-based X-ray diffraction and absorption spectroscopy. *J. Mater. Chem. A* **2013,** *1* (37), 11130-11134.

78. Han, M. H.; Gonzalo, E.; Casas-Cabanas, M.; Rojo, T., Structural evolution and electrochemistry of monoclinic NaNiO 2 upon the first cycling process. *J. Power Sources* **2014,** *258*, 266-271.

79. Oh, S.-M.; Myung, S.-T.; Hwang, J.-Y.; Scrosati, B.; Amine, K.; Sun, Y.-K., High Capacity O3-Type Na [Li0. 05 (Ni0. 25Fe0. 25Mn0. 5) 0.95] O2 Cathode for Sodium Ion Batteries. *Chemistry of Materials* **2014,** *26* (21), 6165-6171.

80. Yue, J.-L.; Yin, W.-W.; Cao, M.-H.; Zulipiya, S.; Zhou, Y.-N.; Fu, Z.-W., A quinary layer transition metal oxide of NaNi 1/4 Co 1/4 Fe 1/4 Mn 1/8 Ti 1/8 O 2 as a high-rate-capability and long-cycle-life cathode material for rechargeable sodium ion batteries. *Chem. Commun.* **2015,** *51* (86), 15712-15715.

81. Liu, H.; Xu, J.; Ma, C.; Meng, Y. S., A new O3-type layered oxide cathode with high energy/power density for rechargeable Na batteries. *Chem. Commun.* **2015,** *51* (22), 4693-4696.

82. Kwon, M.-S.; Lim, S. G.; Park, Y.; Lee, S.-M.; Chung, K. Y.; Shin, T. J.; Lee, K. T., P2 Orthorhombic Na0. 7 [Mn1–x Li x] O2+ y as Cathode Materials for Na-Ion Batteries. *ACS Appl. Mater. Interfaces* **2017,** *9* (17), 14758-14768.

83. Yao, H.-R.; Wang, P.-F.; Gong, Y.; Zhang, J.; Yu, X.; Gu, L.; Ouyang, C.; Yin, Y.-X.; Hu, E.; Yang, X.-Q., Designing Air-Stable O3-Type Cathode Materials by

Combined Structure Modulation for Na-Ion Batteries. *Journal of the American Chemical Society* **2017**.

84. de Boisse, B. M.; Carlier, D.; Guignard, M.; Delmas, C., Structural and electrochemical characterizations of P2 and New O3-NaxMn1-yFeyO2 phases prepared by auto-combustion synthesis for Na-ion batteries. *Journal of The Electrochemical Society* **2013,** *160* (4), A569-A574.

85. Singh, G.; del Amo, J. M. L.; Galceran, M.; Pérez-Villar, S.; Rojo, T., Structural evolution during sodium deintercalation/intercalation in Na 2/3 [Fe 1/2 Mn 1/2] O 2. *J. Mater. Chem. A* **2015,** *3* (13), 6954-6961.

86. Liu, Y.; Fang, X.; Zhang, A.; Shen, C.; Liu, Q.; Enaya, H. A.; Zhou, C., Layered P2-Na 2/3 [Ni 1/3 Mn 2/3] O 2 as high-voltage cathode for sodium-ion batteries: The capacity decay mechanism and Al 2 O 3 surface modification. *Nano Energy* **2016,** *27*, 27-34.

87. Bao, S.; Luo, S.; Wang, Z.; Wang, Q.; Hao, A.; Zhang, Y.; Wang, Y., The critical role of sodium content on structure, morphology and electrochemical performance of layered P2-type NaxNi0. 167Co0. 167Mn0. 67O2 for sodium ion batteries. *J. Power Sources* **2017**, *362*, 323-331**.**

88. Lu, J.; Chung, S. C.; Nishimura, S.-i.; Yamada, A., Phase Diagram of Olivine Nax FePO4 (0< x< 1). *Chemistry of Materials* **2013,** *25* (22), 4557-4565.

89. Jian, Z.; Yuan, C.; Han, W.; Lu, X.; Gu, L.; Xi, X.; Hu, Y. S.; Li, H.; Chen, W.; Chen, D., Atomic Structure and Kinetics of NASICON NaxV2 (PO4) 3 Cathode for Sodium-Ion Batteries. *Adv. Funct. Mater.* **2014,** *24* (27), 4265-4272.

90. Koleva, V.; Boyadzhieva, T.; Zhecheva, E.; Nihtianova, D.; Simova, S.; Tyuliev, G.; Stoyanova, R., Precursor-based methods for low-temperature synthesis of defectless NaMnPO 4 with an olivine-and maricite-type structure. *CrystEngComm* **2013,** *15* (44), 9080-9089.

91. Aragon, M.; Lavela, P.; Ortiz, G.; Tirado, J., Effect of iron substitution in the electrochemical performance of Na3V2 (PO4) 3 as cathode for Na-ion batteries. *Journal of The Electrochemical Society* **2015,** *162* (2), A3077-A3083.

92. Barpanda, P.; Avdeev, M.; Ling, C. D.; Lu, J.; Yamada, A., magnetic structure and properties of the Na2CoP2O7 pyrophosphate cathode for sodium-ion batteries: a

supersuperexchange-driven non-collinear antiferromagnet. *Inorganic chemistry* **2012,** *52* (1), 395-401.

93. Kubota, K.; Yokoh, K.; Yabuuchi, N.; Komaba, S., Na2CoPO4F as a High-voltage Electrode Material for Na-ion Batteries. *Electrochemistry* **2014,** *82* (10), 909-911.

94. Ruan, Y.-L.; Wang, K.; Song, S.-D.; Han, X.; Cheng, B.-W., Graphene modified sodium vanadium fluorophosphate as a high voltage cathode material for sodium ion batteries. *Electrochim. Acta* **2015,** *160*, 330-336.

95. Zhao, J.; Mu, L.; Qi, Y.; Hu, Y.-S.; Liu, H.; Dai, S., A phase-transfer assisted solvo-thermal strategy for low-temperature synthesis of Na 3 (VO 1− x PO 4) 2 F 1+ 2x cathodes for sodium-ion batteries. *Chem. Commun.* **2015,** *51* (33), 7160-7163.

96. Li, C.; Miao, X.; Chu, W.; Wu, P.; Tong, D. G., Hollow amorphous NaFePO 4 nanospheres as a high-capacity and high-rate cathode for sodium-ion batteries. *J. Mater. Chem. A* **2015,** *3* (16), 8265-8271.

97. Lim, S. Y.; Kim, H.; Shakoor, R.; Jung, Y.; Choi, J. W., Electrochemical and thermal properties of NASICON structured Na3V2 (PO4) 3 as a sodium rechargeable battery cathode: a combined experimental and theoretical study. *Journal of The Electrochemical Society* **2012,** *159* (9), A1393-A1397.

98. Zhu, C.; Song, K.; van Aken, P. A.; Maier, J.; Yu, Y., Carbon-coated Na3V2 (PO4) 3 embedded in porous carbon matrix: an ultrafast Na-storage cathode with the potential of outperforming Li cathodes. *Nano Lett.* **2014,** *14* (4), 2175-2180.

99. Barpanda, P.; Nishimura, S. i.; Yamada, A., High-Voltage Pyrophosphate Cathodes. *Adv. Energy Mater.* **2012,** *2* (7), 841-859.

100. Longoni, G.; Wang, J. E.; Jung, Y. H.; Kim, D. K.; Mari, C. M.; Ruffo, R., The Na 2 FeP 2 O 7-carbon nanotubes composite as high rate cathode material for sodium ion batteries. *J. Power Sources* **2016,** *302*, 61-69.

101. Chihara, K.; Kitajou, A.; Gocheva, I. D.; Okada, S.; Yamaki, J.-i., Cathode properties of Na 3 M 2 (PO 4) 2 F 3 [M= Ti, Fe, V] for sodium-ion batteries. *J. Power Sources* **2013,** *227*, 80-85.

102. Langrock, A.; Xu, Y.; Liu, Y.; Ehrman, S.; Manivannan, A.; Wang, C., Carbon coated hollow Na 2 FePO 4 F spheres for Na-ion battery cathodes. *J. Power Sources* **2013,** *223*, 62-67.

103. Dai, Z.; Mani, U.; Tan, H. T.; Yan, Q., Advanced Cathode Materials for Sodium-Ion Batteries: What Determines Our Choices? *Small Methods* **2017**.

104. Xu, M.; Wang, L.; Zhao, X.; Song, J.; Xie, H.; Lu, Y.; Goodenough, J. B., Na 3 V 2 O 2 (PO 4) 2 F/graphene sandwich structure for high-performance cathode of a sodium-ion battery. *Physical Chemistry Chemical Physics* **2013,** *15* (31), 13032-13037.

105. Zhang, B.; Dugas, R.; Rousse, G.; Rozier, P.; Abakumov, A. M.; Tarascon, J.-M., Insertion compounds and composites made by ball milling for advanced sodium-ion batteries. *Nature communications* 2016, *7*, 10308.

106.Barpanda, P.; Oyama, G.; Nishimura, S.-i.; Chung, S.-C.; Yamada, A., A 3.8-V earth-abundant sodium battery electrode. *Nature communications* **2014,** *5*.

107. Barpanda, P.; Oyama, G.; Ling, C. D.; Yamada, A., Kröhnkite-Type Na2Fe (SO4) 2· 2H2O as a Novel 3.25 V Insertion Compound for Na-Ion Batteries. *Chemistry of Materials* **2014,** *26* (3), 1297-1299.

108.Singh, P.; Shiva, K.; Celio, H.; Goodenough, J. B., Eldfellite, NaFe (SO 4) 2: an intercalation cathode host for low-cost Na-ion batteries. *Energy Environ. Sci.* **2015,** *8* (10), 3000-3005.

109. Buser, H.; Schwarzenbach, D.; Petter, W.; Ludi, A., The crystal structure of Prussian blue: Fe4 [Fe (CN) 6] 3. xH2O. *Inorganic Chemistry* **1977,** *16* (11), 2704-2710.

110. Lu, Y.; Wang, L.; Cheng, J.; Goodenough, J. B., Prussian blue: a new framework of electrode materials for sodium batteries. *Chem. Commun.* **2012,** *48* (52), 6544-6546.

111. You, Y.; Wu, X.-L.; Yin, Y.-X.; Guo, Y.-G., High-quality Prussian blue crystals as superior cathode materials for room-temperature sodium-ion batteries. *Energy Environ. Sci.* **2014,** *7* (5), 1643-1647.

112. Wessells, C. D.; McDowell, M. T.; Peddada, S. V.; Pasta, M.; Huggins, R. A.; Cui, Y., Tunable reaction potentials in open framework nanoparticle battery electrodes for grid-scale energy storage. *ACS nano* **2012,** *6* (2), 1688-1694.

113. Wessells, C. D.; Peddada, S. V.; McDowell, M. T.; Huggins, R. A.; Cui, Y., The effect of insertion species on nanostructured open framework hexacyanoferrate battery electrodes. *Journal of the Electrochemical Society* **2011,** *159* (2), A98-A103.

114. Wessells, C. D.; Huggins, R. A.; Cui, Y., Copper hexacyanoferrate battery electrodes with long cycle life and high power. *Nature communications* **2011,** *2*, 550.

115.Wu, X.; Deng, W.; Qian, J.; Cao, Y.; Ai, X.; Yang, H., Single-crystal FeFe (CN) 6 nanoparticles: a high capacity and high rate cathode for Na-ion batteries. *J. Mater. Chem. A* ***2013,*** *1 (35), 10130-10134.*

116. Song, Z.; Zhou, H., Towards sustainable and versatile energy storage devices: an overview of organic electrode materials. *Energy Environ. Sci.* **2013,** *6* (8), 2280-2301.

117. Liang, Y.; Tao, Z.; Chen, J., Organic electrode materials for rechargeable lithium batteries. *Adv. Energy Mater.* **2012,** *2* (7), 742-769.

118. Nishide, H.; Oyaizu, K., Toward flexible batteries. *Science* **2008,** *319* (5864), 737-738.

119. Chen, H.; Armand, M.; Demailly, G.; Dolhem, F.; Poizot, P.; Tarascon, J. M., From Biomass to a Renewable LiXC6O6 Organic Electrode for Sustainable Li-Ion Batteries. *ChemSusChem* **2008,** *1* (4), 348-355.

120. Wang, S.; Wang, L.; Zhu, Z.; Hu, Z.; Zhao, Q.; Chen, J., All Organic Sodium-Ion Batteries with Na4C8H2O6. *Angewandte Chemie* **2014,** *126* (23), 6002-6006.

121. Chihara, K.; Chujo, N.; Kitajou, A.; Okada, S., Cathode properties of Na 2 C 6 O 6 for sodium-ion batteries. *Electrochim. Acta* **2013,** *110*, 240-246.

122. Zhao, R.; Zhu, L.; Cao, Y.; Ai, X.; Yang, H. X., An aniline-nitroaniline copolymer as a high capacity cathode for Na-ion batteries. *Electrochem. Commun.* **2012,** *21*, 36-38.

123. Zhang, S.; Huang, W.; Hu, P.; Huang, C.; Shang, C.; Zhang, C.; Yang, R.; Cui, G., Conjugated microporous polymers with excellent electrochemical performance for lithium and sodium storage. *J. Mater. Chem. A* **2015,** *3* (5), 1896-1901.

124. Wang, Y.; Ding, Y.; Pan, L.; Shi, Y.; Yue, Z.; Shi, Y.; Yu, G., Understanding the Size-Dependent Sodium Storage Properties of Na2C6O6-Based Organic Electrodes for Sodium-Ion Batteries. *Nano Lett.* 2016, *16* (5), 3329-3334.

125. Balogun, M.-S.; Luo, Y.; Qiu, W.; Liu, P.; Tong, Y., A review of carbon materials and their composites with alloy metals for sodium ion battery anodes. *Carbon* **2016,** *98*, 162-178.

126. Mei, Y.; Huang, Y.; Hu, X., Nanostructured Ti-based anode materials for Na-ion batteries. *J. Mater. Chem. A* **2016,** *4* (31), 12001-12013.

127. Klein, F.; Jache, B.; Bhide, A.; Adelhelm, P., Conversion reactions for sodium-ion batteries. *Physical Chemistry Chemical Physics* **2013,** *15* (38), 15876-15887.

128. Chevrier, V.; Ceder, G., Challenges for Na-ion negative electrodes. *Journal of The Electrochemical Society* **2011,** *158* (9), A1011-A1014.

129. Mortazavi, M.; Ye, Q.; Birbilis, N.; Medhekar, N. V., High capacity group-15 alloy anodes for Na-ion batteries: Electrochemical and mechanical insights. *J. Power Sources* **2015,** *285*, 29-36.

130.Alcántara, R.; Jiménez-Mateos, J. M.; Lavela, P.; Tirado, J. L., Carbon black: a promising electrode material for sodium-ion batteries. *Electrochem. Commun.* **2001,** *3* (11), 639-642.

131. Luo, W.; Schardt, J.; Bommier, C.; Wang, B.; Razink, J.; Simonsen, J.; Ji, X., Carbon nanofibers derived from cellulose nanofibers as a long-life anode material for rechargeable sodium-ion batteries. *J. Mater. Chem. A* **2013,** *1* (36), 10662-10666.

132.Wang, Y.-X.; Chou, S.-L.; Liu, H.-K.; Dou, S.-X., Reduced graphene oxide with superior cycling stability and rate capability for sodium storage. *Carbon* **2013,** *57*, 202-208.

133. Hong, K.-l.; Qie, L.; Zeng, R.; Yi, Z.-q.; Zhang, W.; Wang, D.; Yin, W.; Wu, C.; Fan, Q.-j.; Zhang, W.-x., Biomass derived hard carbon used as a high performance anode material for sodium ion batteries. *J. Mater. Chem. A* **2014,** *2* (32), 12733-12738.

134. Yan, Y.; Yin, Y. X.; Guo, Y. G.; Wan, L. J., A Sandwich-Like Hierarchically Porous Carbon/Graphene Composite as a High-Performance Anode Material for Sodium-Ion Batteries. *Adv. Energy Mater.* **2014,** *4* (8).

135. Xu, J.; Wang, M.; Wickramaratne, N. P.; Jaroniec, M.; Dou, S.; Dai, L., High-performance sodium ion batteries based on a 3D anode from nitrogen-doped graphene foams. *Adv. Mater.* **2015,** *27* (12), 2042-2048.

136. Stevens, D.; Dahn, J., High Capacity Anode Materials for Rechargeable Sodium-Ion Batteries. *Journal of the Electrochemical Society* **2000,** *147* (4), 1271-1273.

137. Cao, Y.; Xiao, L.; Sushko, M. L.; Wang, W.; Schwenzer, B.; Xiao, J.; Nie, Z.; Saraf, L. V.; Yang, Z.; Liu, J., Sodium ion insertion in hollow carbon nanowires for battery applications. *Nano Lett.* **2012,** *12* (7), 3783-3787.

138. Li, Y.; Xu, S.; Wu, X.; Yu, J.; Wang, Y.; Hu, Y.-S.; Li, H.; Chen, L.; Huang, X., Amorphous monodispersed hard carbon micro-spherules derived from biomass as a high performance negative electrode material for sodium-ion batteries. *J. Mater. Chem. A* **2015,** *3* (1), 71-77.

139. Guan, Z.; Liu, H.; Xu, B.; Hao, X.; Wang, Z.; Chen, L., Gelatin-pyrolyzed mesoporous carbon as a high-performance sodium-storage material. *J. Mater. Chem. A* **2015,** *3* (15), 7849-7854.

140. Liu, P.; Li, Y.; Hu, Y.-S.; Li, H.; Chen, L.; Huang, X., A waste biomass derived hard carbon as a high-performance anode material for sodium-ion batteries. *J. Mater. Chem. A* **2016,** *4* (34), 13046-13052.

141. Dahbi, M.; Kiso, M.; Kubota, K.; Horiba, T.; Chafik, T.; Hida, K.; Matsuyama, T.; Komaba, S., Synthesis of hard carbon from argan shells for Na-ion batteries. *J. Mater. Chem. A* **2017**.

142.Li, Y.; Hu, Y. S.; Titirici, M. M.; Chen, L.; Huang, X., Hard Carbon Microtubes Made from Renewable Cotton as High-Performance Anode Material for Sodium-Ion Batteries. *Adv. Energy Mater.* **2016,** *6* (18).

143. Wang, Y.-X.; Chou, S.-L.; Liu, H.-K.; Dou, S.-X., Reduced graphene oxide with superior cycling stability and rate capability for sodium storage. *Carbon* **2013,** *57*, 202-208.

144. Wang, H. g.; Wu, Z.; Meng, F. l.; Ma, D. l.; Huang, X. l.; Wang, L. m.; Zhang, X. b., Nitrogen-Doped Porous Carbon Nanosheets as Low-Cost, High-Performance Anode Material for Sodium-Ion Batteries. *ChemSusChem* **2013,** *6* (1), 56-60.

145.Yan, Y.; Yin, Y. X.; Guo, Y. G.; Wan, L. J., A Sandwich-Like Hierarchically Porous Carbon/Graphene Composite as a High-Performance Anode Material for Sodium-Ion Batteries. *Adv. Energy Mater.* **2014,** *4* (8).

146. Fu, L.; Tang, K.; Song, K.; van Aken, P. A.; Yu, Y.; Maier, J., Nitrogen doped porous carbon fibres as anode materials for sodium ion batteries with excellent rate performance. *Nanoscale* **2014,** *6* (3), 1384-1389.

147. Fan, J. M.; Chen, J. J.; Zhang, Q.; Chen, B. B.; Zang, J.; Zheng, M. S.; Dong, Q. F., An Amorphous Carbon Nitride Composite Derived from ZIF-8 as Anode Material for Sodium-Ion Batteries. *ChemSusChem* **2015,** *8* (11), 1856-1861.

148. Alcántara, R.; Jaraba, M.; Lavela, P.; Tirado, J., NiCo2O4 spinel: First report on a transition metal oxide for the negative electrode of sodium-ion batteries. *Chemistry of Materials* **2002,** *14* (7), 2847-2848.

149. Komaba, S.; Mikumo, T.; Yabuuchi, N.; Ogata, A.; Yoshida, H.; Yamada, Y., Electrochemical insertion of Li and Na ions into nanocrystalline Fe3O4 and α-Fe2O3 for rechargeable batteries. *Journal of The Electrochemical Society* **2010,** *157* (1), A60-A65.

150. Hariharan, S.; Saravanan, K.; Ramar, V.; Balaya, P., A rationally designed dual role anode material for lithium-ion and sodium-ion batteries: case study of eco-friendly Fe 3 O 4. *Physical Chemistry Chemical Physics* **2013,** *15* (8), 2945-2953.

151. Park, D.-Y.; Myung, S.-T., Carbon-coated magnetite embedded on carbon nanotubes for rechargeable lithium and sodium batteries. *ACS Appl. Mater. Interfaces* **2014,** *6* (14), 11749-11757.

152. Liu, S.; Wang, Y.; Dong, Y.; Zhao, Z.; Wang, Z.; Qiu, J., Ultrafine Fe3O4 Quantum Dots on Hybrid Carbon Nanosheets for Long-Life, High-Rate Alkali-Metal Storage. *ChemElectroChem* **2016,** *3* (1), 38-44.

153. Valvo, M.; Lindgren, F.; Lafont, U.; Björefors, F.; Edström, K., Towards more sustainable negative electrodes in Na-ion batteries via nanostructured iron oxide. *J. Power Sources* **2014,** *245*, 967-978.

154. Koo, B.; Chattopadhyay, S.; Shibata, T.; Prakapenka, V. B.; Johnson, C. S.; Rajh, T.; Shevchenko, E. V., Intercalation of sodium ions into hollow iron oxide nanoparticles. *Chemistry of Materials* **2013,** *25* (2), 245-252.

155. Rahman, M. M.; Glushenkov, A. M.; Ramireddy, T.; Chen, Y., Electrochemical investigation of sodium reactivity with nanostructured Co 3 O 4 for sodium-ion batteries. *Chem. Commun.* **2014,** *50* (39), 5057-5060.

156. Rahman, M. M.; Sultana, I.; Chen, Z.; Srikanth, M.; Li, L. H.; Dai, X. J.; Chen, Y., Ex situ electrochemical sodiation/desodiation observation of Co 3 O 4 anchored carbon nanotubes: a high performance sodium-ion battery anode produced by pulsed plasma in a liquid. *Nanoscale* **2015,** *7* (30), 13088-13095.

157. Deng, Q.; Wang, L.; Li, J., Electrochemical characterization of Co3O4/MCNTs composite anode materials for sodium-ion batteries. *Journal of Materials Science* **2015,** *50* (11), 4142-4148.

158. Jian, Z.; Liu, P.; Li, F.; Chen, M.; Zhou, H., Monodispersed hierarchical Co 3 O 4 spheres intertwined with carbon nanotubes for use as anode materials in sodium-ion batteries. *J. Mater. Chem. A* **2014,** *2* (34), 13805-13809.

159 . Klavetter, K. C.; Garcia, S.; Dahal, N.; Snider, J. L.; de Souza, J. P.; Cell, T. H.; Cassara, M. A.; Heller, A.; Humphrey, S. M.; Mullins, C. B., Li-and Na-reduction products of meso-Co 3 O 4 form high-rate, stably cycling battery anode materials. *J. Mater. Chem. A* **2014,** *2* (34), 14209-14221.

160. Dou, Y.; Wang, Y.; Tian, D.; Xu, J.; Zhang, Z.; Liu, Q.; Ruan, B.; Ma, J.; Sun, Z.; Dou, S. X., Atomically thin Co3O4 nanosheet-coated stainless steel mesh with enhanced capacitive Na+ storage for high-performance sodium-ion batteries. *2D Materials* **2016,** *4* (1), 015022.

161.Wang, Y.; Wang, C.; Wang, Y.; Liu, H.; Huang, Z., Superior sodium-ion storage performance of Co 3 O 4@ nitrogen-doped carbon: derived from a metal–organic framework. *J. Mater. Chem. A* **2016,** *4* (15), 5428-5435.

162. Gu, M.; Kushima, A.; Shao, Y.; Zhang, J.-G.; Liu, J.; Browning, N. D.; Li, J.; Wang, C., Probing the failure mechanism of SnO2 nanowires for sodium-ion batteries. *Nano Lett.* **2013,** *13* (11), 5203-5211.

163. Dirican, M.; Lu, Y.; Ge, Y.; Yildiz, O.; Zhang, X., Carbon-confined SnO2-electrodeposited porous carbon nanofiber composite as high-capacity sodium-ion battery anode material. *ACS Appl. Mater. Interfaces* **2015,** *7* (33), 18387-18396.

164. Lu, Y. C.; Ma, C.; Alvarado, J.; Kidera, T.; Dimov, N.; Meng, Y. S.; Okada, S., Electrochemical properties of tin oxide anodes for sodium-ion batteries. *J. Power Sources* **2015,** *284*, 287-295.

165. Su, D.; Xie, X.; Wang, G., Hierarchical Mesoporous SnO Microspheres as High Capacity Anode Materials for Sodium-Ion Batteries. *Chemistry-A European Journal* **2014,** *20* (11), 3192-3197.

166. Xie, X.; Chen, S.; Sun, B.; Wang, C.; Wang, G., 3D Networked Tin Oxide/Graphene Aerogel with a Hierarchically Porous Architecture for High-Rate

Performance Sodium-Ion Batteries. *ChemSusChem* **2015,** *8* (17), 2948-2955.

167. Kalubarme, R. S.; Lee, J.-Y.; Park, C.-J., Carbon encapsulated tin oxide nanocomposites: an efficient anode for high performance sodium-ion batteries. *ACS Appl. Mater. Interfaces* **2015,** *7* (31), 17226-17237.

168. Xie, X.; Su, D.; Zhang, J.; Chen, S.; Mondal, A. K.; Wang, G., A comparative investigation on the effects of nitrogen-doping into graphene on enhancing the electrochemical performance of SnO 2/graphene for sodium-ion batteries. *Nanoscale* **2015,** *7* (7), 3164-3172.

169. Su, D.; Wang, C.; Ahn, H.; Wang, G., Octahedral tin dioxide nanocrystals as high capacity anode materials for Na-ion batteries. *Physical Chemistry Chemical Physics* **2013,** *15* (30), 12543-12550.

170. Pei, L.; Jin, Q.; Zhu, Z.; Zhao, Q.; Liang, J.; Chen, J., Ice-templated preparation and sodium storage of ultrasmall SnO2 nanoparticles embedded in three-dimensional graphene. *Nano Research* **2015,** *8* (1), 184-192.

171. Yuan, S.; Huang, X. l.; Ma, D. l.; Wang, H. g.; Meng, F. z.; Zhang, X. b., Engraving Copper Foil to Give Large-Scale Binder-Free Porous CuO Arrays for a High-Performance Sodium-Ion Battery Anode. *Adv. Mater.* **2014,** *26* (14), 2273-2279.

172. Wang, L.; Zhang, K.; Hu, Z.; Duan, W.; Cheng, F.; Chen, J., Porous CuO nanowires as the anode of rechargeable Na-ion batteries. *Nano Research* **2014,** *7* (2), 199-208.

173. Zhang, X.; Qin, W.; Li, D.; Yan, D.; Hu, B.; Sun, Z.; Pan, L., Metal–organic framework derived porous CuO/Cu 2 O composite hollow octahedrons as high performance anode materials for sodium ion batteries. *Chem. Commun.* **2015,** *51* (91), 16413-16416.

174. Liu, H.; Cao, F.; Zheng, H.; Sheng, H.; Li, L.; Wu, S.; Liu, C.; Wang, J., In situ observation of the sodiation process in CuO nanowires. *Chem. Commun.* 2015, *51* (52), 10443-10446.

175. Lu, Y.; Zhang, N.; Zhao, Q.; Liang, J.; Chen, J., Micro-nanostructured CuO/C spheres as high-performance anode materials for Na-ion batteries. *Nanoscale* 2015, *7* (6), 2770-2776.

176. Zhang, Z.; Feng, J.; Ci, L.; Tian, Y.; Xiong, S., Mental-organic framework derived CuO hollow spheres as high performance anodes for sodium ion battery. *Materials Technology* 2016, *31* (9), 497-500.

177. Jiang, Y.; Hu, M.; Zhang, D.; Yuan, T.; Sun, W.; Xu, B.; Yan, M., Transition metal oxides for high performance sodium ion battery anodes. *Nano Energy* 2014, *5*, 60-66.

178. Zou, F.; Chen, Y.-M.; Liu, K.; Yu, Z.; Liang, W.; Bhaway, S. M.; Gao, M.; Zhu, Y., Metal organic frameworks derived hierarchical hollow NiO/Ni/graphene composites for lithium and sodium storage. *ACS nano* 2015, *10* (1), 377-386.

179. López, M. C.; Lavela, P.; Ortiz, G. F.; Tirado, J. L., Transition metal oxide thin films with improved reversibility as negative electrodes for sodium-ion batteries. *Electrochem. Commun.* 2013, *27*, 152-155.

180. Zhang, Z.; Zhao, X.; Li, J., Facile Synthesis of Nanostructured MnO2 as Anode Materials for Sodium-Ion Batteries. *ChemNanoMat* 2016, *2* (3), 196-200.

181. He, Y.; Xu, P.; Zhang, B.; Du, Y.; Bo, S.; Han, X.; Peng, H., Ultrasmall MnO Nanoparticles Supported on Nitrogen-Doped Carbon Nanotubes as Efficient Anode Materials for Sodium Ion Batteries. *ACS Appl. Mater. Interfaces* **2017**.

182. Zhou, Q.; Liu, L.; Huang, Z.; Yi, L.; Wang, X.; Cao, G., Co 3 S 4@ polyaniline nanotubes as high-performance anode materials for sodium ion batteries. *J. Mater. Chem. A* **2016,** *4* (15), 5505-5516.

183. Douglas, A.; Carter, R.; Oakes, L.; Share, K.; Cohn, A. P.; Pint, C. L., Ultrafine iron pyrite (FeS2) nanocrystals improve sodium–sulfur and lithium–sulfur conversion reactions for efficient batteries. *ACS nano* **2015,** *9* (11), 11156-11165.

184. Wang, Y.-X.; Yang, J.; Chou, S.-L.; Liu, H. K.; Zhang, W.-x.; Zhao, D.; Dou, S. X., Uniform yolk-shell iron sulfide-carbon nanospheres for superior sodium-iron sulfide batteries. *Nature communications* **2015,** *6*.

185. Feng, L.-L.; Li, G.-D.; Liu, Y.; Wu, Y.; Chen, H.; Wang, Y.; Zou, Y.-C.; Wang, D.; Zou, X., Carbon-armored Co9S8 nanoparticles as all-pH efficient and durable H2-evolving electrocatalysts. *ACS Appl. Mater. Interfaces* 2015, *7* (1), 980-988.

186. Zhou, Q.; Liu, L.; Huang, Z.; Yi, L.; Wang, X.; Cao, G., Co 3 S 4@ polyaniline nanotubes as high-performance anode materials for sodium ion batteries. *J. Mater. Chem. A* **2016,** *4* (15), 5505-5516.

187. Su, D.; Dou, S.; Wang, G., Ultrathin MoS2 Nanosheets as Anode Materials for Sodium-Ion Batteries with Superior Performance. *Adv. Energy Mater.* **2015,** *5* (6).

188. Xiong, X.; Luo, W.; Hu, X.; Chen, C.; Qie, L.; Hou, D.; Huang, Y., Flexible membranes of MoS2/C nanofibers by electrospinning as bin-free anodes for high-performance sodium-ion batteries. *Scientific reports* **2015,** *5*.

189. Qin, W.; Li, D.; Zhang, X.; Yan, D.; Hu, B.; Pan, L., ZnS nanoparticles embedded in reduced graphene oxide as high performance anode material of sodium-ion batteries. *Electrochim. Acta* **2016,** *191*, 435-443.

190. Zhou, T.; Pang, W. K.; Zhang, C.; Yang, J.; Chen, Z.; Liu, H. K.; Guo, Z., Enhanced sodium-ion battery performance by structural phase transition from two-dimensional hexagonal-SnS2 to orthorhombic-SnS. *Acs Nano* **2014,** *8* (8), 8323-8333.

191. Qu, B.; Ma, C.; Ji, G.; Xu, C.; Xu, J.; Meng, Y. S.; Wang, T.; Lee, J. Y., Layered SnS2-Reduced Graphene Oxide Composite–A High-Capacity, High-Rate, and Long-Cycle Life Sodium-Ion Battery Anode Material. *Adv. Mater.* **2014,** *26* (23), 3854-3859.

192. Wu, L.; Lu, H.; Xiao, L.; Qian, J.; Ai, X.; Yang, H.; Cao, Y., A tin (ii) sulfide–carbon anode material based on combined conversion and alloying reactions for sodium-ion batteries. *J. Mater. Chem. A* **2014,** *2* (39), 16424-16428.

193. Hu, Z.; Wang, L.; Zhang, K.; Wang, J.; Cheng, F.; Tao, Z.; Chen, J., MoS2 nanoflowers with expanded interlayers as high-performance anodes for sodium-ion batteries. *Angewandte Chemie* **2014,** *126* (47), 13008-13012.

194. Morito, H.; Yamada, T.; Ikeda, T.; Yamane, H., Na–Si binary phase diagram and solution growth of silicon crystals. *Journal of Alloys and Compounds* **2009,** *480* (2), 723-726.

195. Xu, Y.; Swaans, E.; Basak, S.; Zandbergen, H. W.; Borsa, D. M.; Mulder, F. M., Reversible Na-Ion Uptake in Si Nanoparticles. *Adv. Energy Mater.* **2016,** *6* (2).

196. Abel, P. R.; Lin, Y.-M.; de Souza, T.; Chou, C.-Y.; Gupta, A.; Goodenough, J. B.; Hwang, G. S.; Heller, A.; Mullins, C. B., Nanocolumnar germanium thin films as a high-rate sodium-ion battery anode material. *J. Phys. Chem. C* **2013,** *117* (37), 18885-18890.

197. Baggetto, L.; Keum, J. K.; Browning, J. F.; Veith, G. M., Germanium as negative electrode material for sodium-ion batteries. *Electrochem. Commun.* **2013,** *34*, 41-44.

198. Xu, Y.; Zhu, Y.; Liu, Y.; Wang, C., Electrochemical performance of porous carbon/tin composite anodes for sodium-ion and lithium-ion batteries. *Adv. Energy Mater.* **2013,** *3* (1), 128-133.

199. Liu, Y.; Zhang, N.; Jiao, L.; Chen, J., Tin Nanodots Encapsulated in Porous Nitrogen-Doped Carbon Nanofibers as a Free-Standing Anode for Advanced Sodium-Ion Batteries. *Adv. Mater.* **2015,** *27* (42), 6702-6707.

200. Kim, Y.; Park, Y.; Choi, A.; Choi, N. S.; Kim, J.; Lee, J.; Ryu, J. H.; Oh, S. M.; Lee, K. T., An amorphous red phosphorus/carbon composite as a promising anode material for sodium ion batteries. *Adv. Mater.* **2013,** *25* (22), 3045-3049.

201. Li, W.-J.; Chou, S.-L.; Wang, J.-Z.; Liu, H.-K.; Dou, S.-X., Simply mixed commercial red phosphorus and carbon nanotube composite with exceptionally reversible sodium-ion storage. *Nano Lett.* **2013,** *13* (11), 5480-5484.

202. Qian, J.; Chen, Y.; Wu, L.; Cao, Y.; Ai, X.; Yang, H., High capacity Na-storage and superior cyclability of nanocomposite Sb/C anode for Na-ion batteries. *Chem. Commun.* **2012,** *48* (56), 7070-7072.

203. Darwiche, A.; Marino, C.; Sougrati, M. T.; Fraisse, B.; Stievano, L.; Monconduit, L., Better cycling performances of bulk Sb in Na-ion batteries compared to Li-ion systems: an unexpected electrochemical mechanism. *Journal of the American Chemical Society* **2012,** *134* (51), 20805-20811.

204. Su, D.; Dou, S.; Wang, G., Bismuth: A new anode for the Na-ion battery. *Nano Energy* **2015,** *12*, 88-95.

205. Sottmann, J.; Herrmann, M.; Vajeeston, P.; Hu, Y.; Ruud, A.; Drathen, C.; Emerich, H.; Fjellvåg, H.; Wragg, D. S., How crystallite size controls the reaction path in nonaqueous metal ion batteries: the example of sodium bismuth alloying. *Chemistry of Materials* **2016,** *28* (8), 2750-2756.

206. Komaba, S.; Matsuura, Y.; Ishikawa, T.; Yabuuchi, N.; Murata, W.; Kuze, S., Redox reaction of Sn-polyacrylate electrodes in aprotic Na cell. *Electrochem. Commun.* **2012,** *21*, 65-68.

207. Kim, C.; Lee, K.-Y.; Kim, I.; Park, J.; Cho, G.; Kim, K.-W.; Ahn, J.-H.; Ahn, H.-J., Long-term cycling stability of porous Sn anode for sodium-ion batteries. *J. Power Sources* **2016,** *317*, 153-158.

208. Yabuuchi, N.; Kubota, K.; Dahbi, M.; Komaba, S., Research development on sodium-ion batteries. *Chem. Rev.* **2014,** *114* (23), 11636-11682.

209. Wang, J. W.; Liu, X. H.; Mao, S. X.; Huang, J. Y., Microstructural evolution of tin nanoparticles during in situ sodium insertion and extraction. *Nano Lett.* **2012,** *12* (11), 5897-5902.

210. Wang, J.; Eng, C.; Chen-Wiegart, Y.-c. K.; Wang, J., Probing three-dimensional sodiation-desodiation equilibrium in sodium-ion batteries by in situ hard X-ray nanotomography. *Nature communications* **2015,** *6*.

211. Ying, H.; Zhang, S.; Meng, Z.; Sun, Z.; Han, W.-Q., Ultrasmall Sn nanodots embedded inside N-doped carbon microcages as high-performance lithium and sodium ion battery anodes. *J. Mater. Chem. A* **2017,** *5* (18), 8334-8342.

212. Ellis, L. D.; Hatchard, T. D.; Obrovac, M. N., Reversible insertion of sodium in tin. *Journal of the Electrochemical Society* **2012,** *159* (11), A1801-A1805.

213. Kume, T.; Iwai, Y.; Sugiyama, T.; Ohashi, F.; Ban, T.; Sasaki, S.; Nonomura, S., NaSi and Si clathrate prepared on Si substrate. *physica status solidi (c)* **2013,** *10* (12), 1739-1741

214. V. V. Kulish, O. I. Malyi, M. F. Ng, Z. Chen, S. Manzhos and P. Wu, Phys. Chem. Chem. Phys., 2014, 16, 4260–4267.

215.Zhang, L.; Hu, X.; Chen, C.; Guo, H.; Liu, X.; Xu, G.; Zhong, H.; Cheng, S.; Wu, P.; Meng, J., In operando mechanism analysis on nanocrystalline silicon anode material for reversible and ultrafast sodium storage. *Adv. Mater.* 2017, *29* (5)

216. Park, C. M.; Sohn, H. J., Black phosphorus and its composite for lithium rechargeable batteries. *Adv. Mater.* **2007,** *19* (18), 2465-2468.

217. Qian, J.; Wu, X.; Cao, Y.; Ai, X.; Yang, H., High capacity and rate capability of amorphous phosphorus for sodium ion batteries. *Angewandte Chemie* **2013,** *125* (17), 4731-4734.

218.Yabuuchi, N.; Matsuura, Y.; Ishikawa, T.; Kuze, S.; Son, J. Y.; Cui, Y. T.; Oji, H.; Komaba, S., Phosphorus Electrodes in Sodium Cells: Small Volume Expansion by Sodiation and the Surface-Stabilization Mechanism in Aprotic Solvent. *ChemElectroChem* **2014,** *1* (3), 580-589.

219. Song, J.; Yu, Z.; Gordin, M. L.; Hu, S.; Yi, R.; Tang, D.; Walter, T.; Regula, M.; Choi, D.; Li, X., Chemically bonded phosphorus/graphene hybrid as a high performance anode for sodium-ion batteries. *Nano Lett.* **2014,** *14* (11), 6329-6335.

220. Zhu, Y.; Wen, Y.; Fan, X.; Gao, T.; Han, F.; Luo, C.; Liou, S.-C.; Wang, C., Red phosphorus–single-walled carbon nanotube composite as a superior anode for sodium ion batteries. *ACS nano* **2015,** *9* (3), 3254-3264.

221. Sun, J.; Lee, H.-W.; Pasta, M.; Yuan, H.; Zheng, G.; Sun, Y.; Li, Y.; Cui, Y., A phosphorene–graphene hybrid material as a high-capacity anode for sodium-ion batteries. *Nat. Nanotechnol.* **2015,** *10* (11), 980-985.

222. Gao, H.; Zhou, T.; Zheng, Y.; Liu, Y.; Chen, J.; Liu, H.; Guo, Z., Integrated Carbon/Red Phosphorus/Graphene Aerogel 3D Architecture via Advanced Vapor-Redistribution for High-Energy Sodium-Ion Batteries. *Adv. Energy Mater.* **2016,** *6* (21).

223. Dahbi, M.; Yabuuchi, N.; Fukunishi, M.; Kubota, K.; Chihara, K.; Tokiwa, K.; Yu, X.-f.; Ushiyama, H.; Yamashita, K.; Son, J.-Y., Black phosphorus as a high-capacity, high-capability negative electrode for sodium-ion batteries: investigation of the electrode/electrolyte interface. *Chemistry of materials* **2016,** *28* (6), 1625-1635.

224. Li, W.; Hu, S.; Luo, X.; Li, Z.; Sun, X.; Li, M.; Liu, F.; Yu, Y., Confined Amorphous Red Phosphorus in MOF-Derived N-Doped Microporous Carbon as a Superior Anode for Sodium-Ion Battery. *Adv. Mater.* **2017,** *29* (16).

225. Liu, Y.; Zhang, A.; Shen, C.; Liu, Q.; Cao, X.; Ma, Y.; Chen, L.; Lau, C.; Chen, T.-C.; Wei, F., Red Phosphorus Nano-Dots on Reduced Graphene Oxide as a Flexible and Ultra-Fast Anode for Sodium-Ion Batteries. *ACS nano* **2017**.

226. Zhang, C.; Wang, X.; Liang, Q.; Liu, X.; Weng, Q.; Liu, J.; Yang, Y.; Dai, Z.; Ding, K.; Bando, Y., Amorphous phosphorus/nitrogen-doped graphene paper for ultrastable sodium-ion batteries. *Nano Lett.* **2016,** *16* (3), 2054-2060.

227.Häupler, B.; Wild, A.; Schubert, U. S., Carbonyls: powerful organic materials for secondary batteries. *Adv. Energy Mater.* **2015,** *5* (11).

228.Zhao, L.; Zhao, J.; Hu, Y. S.; Li, H.; Zhou, Z.; Armand, M.; Chen, L., Disodium Terephthalate (Na2C8H4O4) as High Performance Anode Material for Low-Cost Room-Temperature Sodium-Ion Battery. *Adv. Energy Mater.* **2012,** *2* (8), 962-965.

229. Park, Y.; Shin, D. S.; Woo, S. H.; Choi, N. S.; Shin, K. H.; Oh, S. M.; Lee, K. T.; Hong, S. Y., Sodium terephthalate as an organic anode material for sodium ion batteries. *Adv. Mater.* **2012,** *24* (26), 3562-3567.

230. Wang, H.-g.; Yuan, S.; Si, Z.; Zhang, X.-b., Multi-ring aromatic carbonyl compounds enabling high capacity and stable performance of sodium-organic batteries. *Energy Environ. Sci.* **2015,** *8* (11), 3160-3165.

231. Wu, X.; Jin, S.; Zhang, Z.; Jiang, L.; Mu, L.; Hu, Y.-S.; Li, H.; Chen, X.; Armand, M.; Chen, L., Unraveling the storage mechanism in organic carbonyl electrodes for sodium-ion batteries. *Science advances* **2015,** *1* (8), e1500330.

232. Wang, Y.; Kretschmer, K.; Zhang, J.; Mondal, A. K.; Guo, X.; Wang, G., Organic sodium terephthalate@ graphene hybrid anode materials for sodium-ion batteries. *RSC Advances* **2016,** *6* (62), 57098-57102.

233. Chen, L.; Li, W.; Wang, Y.; Wang, C.; Xia, Y., Polyimide as anode electrode material for rechargeable sodium batteries. *RSC Advances* **2014,** *4* (48), 25369-25373.

234. Luo, C.; Zhu, Y.; Xu, Y.; Liu, Y.; Gao, T.; Wang, J.; Wang, C., Graphene oxide wrapped croconic acid disodium salt for sodium ion battery electrodes. *J. Power Sources* **2014,** *250*, 372-378.

235. Zhu, Z.; Li, H.; Liang, J.; Tao, Z.; Chen, J., The disodium salt of 2, 5-dihydroxy-1, 4-benzoquinone as anode material for rechargeable sodium ion batteries. *Chem. Commun.* **2015,** *51* (8), 1446-1448.

236. López-Herraiz, M.; Castillo-Martínez, E.; Carretero-González, J.; Carrasco, J.; Rojo, T.; Armand, M., Oligomeric-Schiff bases as negative electrodes for sodium ion

batteries: unveiling the nature of their active redox centers. *Energy Environ. Sci.* **2015,** *8* (11), 3233-3241.

237. Ponrouch, A.; Monti, D.; Boschin, A.; Steen, B.; Johansson, P.; Palacin, M., Non-aqueous electrolytes for sodium-ion batteries. *J. Mater. Chem. A* **2015,** *3* (1), 22-42.

238. Kim, H.; Hong, J.; Park, K.-Y.; Kim, H.; Kim, S.-W.; Kang, K., Aqueous rechargeable Li and Na ion batteries. *Chem. Rev.* **2014,** *114* (23), 11788-11827.

# Chapter 3

# Experimental Procedure

## 3.1. Overview

The general procedure in this thesis work is illustrated in Scheme 3.1. Three different anode materials, a phosphorus/N-doped carbon nanofiber (P/NCF), $SnO_2$–polypyrrole nanotubes and carbon-encapsulated Sn@N-doped carbon tubes (C@Sn@N-Doped Carbon) were first fabricated via facile chemical vapor deposition (CVD) and hydrothermal methods, respectively. Thereafter, these materials were characterized by a series of techniques, such as X-ray diffraction (XRD), Raman spectroscopy, Fourier transform infrared spectroscopy (FTIR), X-ray photoelectron spectroscopy (XPS), thermogravimetric analysis (TGA), Brunauer-Emmett-Teller (BET) measurements, scanning electron microscopy (SEM), transmission electron microscopy (TEM), etc. Their electrochemical performances were finally measured for SIBs.

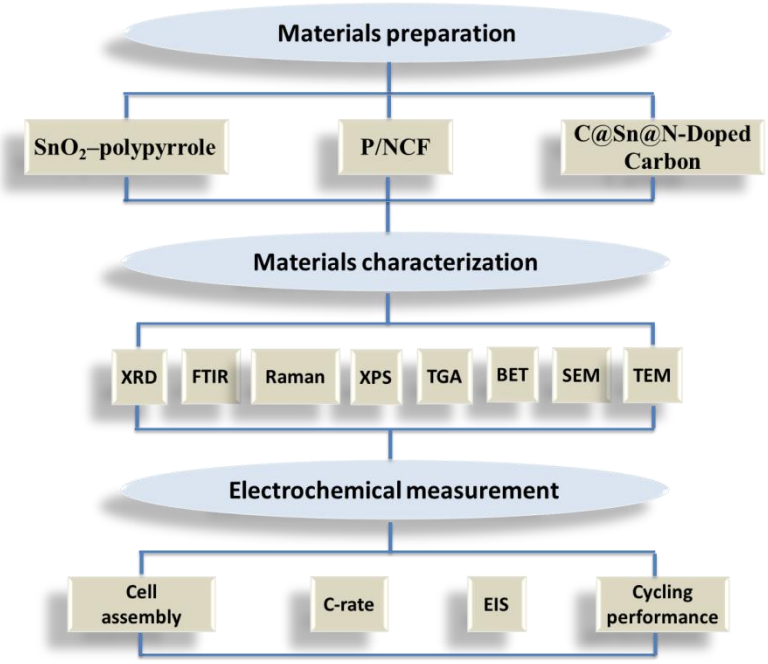


**Scheme 3.1** The general procedure of this thesis work.

## 3.2. Chemicals and Materials

The chemicals and materials used in this work are listed in Table 3.1.

**Table 3.1** Chemicals and materials used in this work.

| Materials/Chemicals | Formula | Purity (%) | Supplier |
|---|---|---|---|
| Cetyltrimethylammonium bromide (CTAB) | $CH_3(CH_2)_{15}N(Br)(CH_3)_3$ | $98^+$ | Sigma |
| Pyrrole | $C_4H_5N$ | $98^+$ | Sigma |
| Ammonium persulfate (APS) | $(NH_4)_2S_2O_8$ | $98^+$ | Sigma |
| Red phosphorus | P | $97^+$ | Sigma |
| Iron (III) chloride | $FeCl_3$ | $97^+$ | Sigma |
| Methyl orange | $C_{14}H_{14}N_3NaO_3S$ | N/A | Sigma |
| Hexamethylenetetramine | $C_6H_{12}N_4$ | N/A | Sigma |
| Urea | $NH_2CONH_2$ | $98^+$ | Sigma |
| Tin (II) chloride dehydrate | $SnCl_2{\cdot}2H_2O$ | $96^+$ | Sigma |
| Ammonia solution | $NH_3{\cdot}H_2O$ | 28 | Sigma |
| Formaldehyde solution | HCHO | 37 | Sigma |
| Resorcinol | $C_6H_4$-1,3-$(OH)_2$ | $98^+$ | Sigma |
| Carboxymethyl cellulose (CMC) | $C_8H_{16}NaO_8$ | N/A | Sigma |
| Carbon | C | $99^+$ | Sigma |
| Copper foil | Cu | N/A | China |
| Sodium metal | Na | 99.9 | Sigma |
| Sodium perchlorate | $NaClO_4$ | $98^+$ | Sigma |
| Ethylene carbonate (EC) | $C_3H_4O_3$ | $99^+$ | Sigma |
| Diethyl carbonate (DEC) | $(C_2H_5O)_2CO$ | $99^+$ | Sigma |
| Fluoroethylene carbonate (FEC) | $C_3H_3FO_3$ | $99^+$ | Sigma |

## 3.3. Materials Preparation

### 3.3.1. Polymerization

Polymerization is a chemical process in which the monomer molecules react together to form polymeric compounds (i.e. polymer chains) with different structures. It is mainly categorized into four kinds: (1) Step-growth. The polymers are defined as polymers formed by the stepwise reaction between functional groups of monomers, usually containing heteroatoms such as nitrogen or oxygen. (2) Chain-growth polymerization. It involves the linking together of molecules incorporating double or triple carbon-carbon bonds. (3) Photopolymerization. Most photopolymerization reactions are chain-growth polymerizations that are initiated by the absorption of visible or ultraviolet light. (4) Physical polymer reaction engineering. This involves producing a high-molecular-weight, uniform product by controlling the initiation, propagation, and termination rates during chain polymerization and also removing excess concentrated heat during these exothermic reactions. In this work, I use the polymerization of pyrrole to form polypyrrole (PPy) matrix.

### 3.3.2. Chemical Vapour Deposition (CVD) Method

Chemical vapor deposition (CVD) is a chemical process applied for producing high quality, high-performance, solid materials. Generally, CVD runs in a closed device with some controlling valves. In typical CVD, the substrate is exposed to one or more volatile precursors, which react and/or decompose on the substrate surface to produce the desired deposit. For nanomaterial-preparation processes the CVD method is widely used to deposit materials in various forms, such as monocrystalline, amorphous, and epitaxial. In this doctoral work, I utilize N-doped carbon nanofiber as matrix to host the red phosphorus nanoparticles to form the phosphorus/N-doped carbon nanofiber (P/NCN).

### 3.3.3. Hydrothermal Method

Hydrothermal synthesis is a low-cost and environmentally friendly technique, which can be used as a method to synthesize the desired materials with the desired morphology and crystal structure. The preparation process is carried out in an apparatus

consisting of a stainless-steel pressure vessel called an autoclave. The parameters of the hydrothermal synthesis need to be controlled in a sophisticated way, including the temperature, pH value, pressure, surfactant, solution/suspension concentration, etc. In this experimental work, I used 4748 Acid Digestion Bombs with 45 ml capacity to fabricate $SnO_2$@PPy and $SnO_2$@N-doped carbon nanotubes.

# 3.4. Characterization Techniques

## 3.4.1. X-ray Powder Diffraction (XRD)

X-ray diffraction (XRD) is a basic technique to determine the structural characterization of materials. X-rays can be regarded the waves of electromagnetic radiation while crystals are regular arrays of atoms. When X-rays strike the crystals, the periodic lattice found in the crystalline structures serves as a diffraction grating for electromagnetic radiation with wavelengths of a similar order of magnitude. X-rays scattered by each set of lattice planes at a unique angle will be scattered coherently "in-phase'' in certain directions to meet the standard of constructive interference that is determined by Bragg's law:

$$2d\sin\theta = n\lambda \qquad (3.1)$$

Where $d$ represents the distance between lattice planes, $\lambda$ is the X-ray wavelength of the incident beam, and $n$ is an integer, while $\theta$ denotes the angle of incidence with the lattice plane. In an X-ray diffractometer, the Cu anode is irradiated by a beam of high-energy electrons under vacuum conditions, while a hatch in the X-ray tube permits X-rays to go through with little damping. In this work, a GBC MMA diffractometer was used with Cu Kα radiation, $\lambda$ = 1.54056 A˚. The powder samples were loaded onto a small disc-shaped sample holder, which was put on one axis of the diffractometer and tilted by an angle $\theta$, while a detector rotated around it on an arm with a $2\theta$ angle.

## 3.4.2. Fourier transform infrared (FTIR)

Infrared spectroscopy (IR spectroscopy or vibrational spectroscopy) is a common method based on absorption spectroscopy, due to its interaction with a sample. It

exploits the fact that molecules absorb frequencies that are characteristic of their structure. The infrared spectrum of a sample is recorded by passing a beam of infrared light through the sample. When the frequency of the IR is the same as the vibrational frequency of a bond or collection of bonds, absorption occurs. Measurement of the transmitted light displays how much energy was absorbed at each frequency (or wavelength). The entire wavelength range is covered using a Fourier transform instrument. In this doctoral work, a Nicolet Avatar 360 FTIR Fourier transform infrared spectrometer was used to collect FTIR spectra. The samples were mixed with KBr powder, which acts as the background file, followed by placing the samples in a sample cup.

### 3.4.3. Raman Spectroscopy

Raman spectroscopy is commonly used in chemistry to provide a fingerprint by which molecules can be identified. It can observe vibrational, rotational, and other low-frequency modes in a system. In a Raman spectrometer, a laser beam interacts with molecular vibrations, phonons, or other excitations of the sample, leading to characteristic shifts in laser phonons. In this work, Raman spectra were collected using a JOBIN Yvon Horiba Raman Spectrometer model HR800 with a 10 mW helium/neon laser at 632.8 nm excitation in the range of 200 to 2000 $cm^{-1}$.

### 3.4.4. X-ray Photoelectron Spectroscopy (XPS)

X-ray photoelectron spectroscopy (XPS) is a surface-sensitive technique to investigate the elemental composition and the quantity of those elements existing within the sample surface, the chemical and electronic states of the identified elements, the binding energy of the electronic states, etc. In this doctoral work, X-ray photoelectron spectroscopy (XPS) was conducted using a SPECS PHOIBOS 100 Analyser installed in a high-vacuum chamber with base pressure below 10-8 mbar. X-ray excitation was provided by Al Kα radiation with photon energy $h\nu$ = 1486.6 eV at the high voltage of 12 kV and power of 120 W. The XPS binding energy spectra were collected at the pass energy of 20 eV in the fixed analyzer transmission mode. Analysis of the XPS data was carried out using the commercial CasaXPS 2.3.15 software package. All the spectra were calibrated by C 1s = 284.6 eV.

### 3.4.5. Thermogravimetric Analysis (TGA)

Thermogravimetric analysis (TGA) is a thermal analysis method to investigate the chemical changes or physical weight variations of materials with increasing temperature. In this doctoral work, a Mettler Toledo TGA/DSC1 was employed in measuring the PPy, N-doped carbon, SnO2, and Sn contents in the samples.

### 3.4.6. Brunauer-Emmett-Teller (BET)

The Brunauer-Emmett-Teller (BET) method is a very important analysis technique to identify the physical adsorption of gas molecules on a solid surface and measure the specific surface area of a material. It is conductedat liquid nitrogen temperature (77 K) over different relative pressures. In order to get accurate results, pre-drying and degassing are necessary. The surface area of samples can be calculated using experimental points at a relative pressure of $P/P_0$ = 0.05-0.25. Pore size distributions can also be obtained via the Barrett-Joyner-Halenda (BJH) method, depending on the amount of nitrogen absorbed at a relative pressure of $P/P_0$ = 0.99. In this work, nitrogen sorption was measured by a Quantachrome Autosorb-IQ MP.

### 3.4.7. Scanning Electron Microscopy (SEM)

A scanning electron microscope (SEM) is a type of electron microscope which scans the sample with a high-energy beam of electrons to form images of it. The electrons interact with atoms of the sample, generating various signals that can be detected and contain information on the sample's surface topography or composition, and other properties including electrical conductivity, etc. Usually, SEM is equipped with some other detectors which have other analytical capabilities such as energy-dispersive X-ray spectroscopy (EDS, EDX, or XEDS). EDS is an analytical technique that is used to detect the elemental analysis or chemical characteristics of a sample. Its characterization capabilities rely on an interaction between some source of X-ray excitation and the sample, because each element has a unique atomic structure, allowing a unique set of peaks on its X-ray spectrum. In my doctoral work, field emission scanning electron microscopy (FESEM; JEOL JSM-7500FA) was employed to detect the morphology and elemental mapping of the samples.

### 3.4.8. Transmission Electron Microscopy (TEM)

Transmission electron microscopy (TEM) is a microscopy technique where an electron beam is transmitted through an ultra-thin specimen, interacting with the sample when it passes through. TEM can be used to observe the morphology, lattice spacing, crystal orientation, and electronic structure. Its selected area electron diffraction (SAED) capability can be used to identify crystal structures and examine crystal defects. Scanning transmission electron microscopy (STEM) is a form of TEM modified by adding a system which rasters the beam across the sample to form the image. In this doctoral work, TEM of the samples was carried out using transmission electron microscopy (TEM, JEOL 2011, 200 keV) and scanning transmission electron microscope (STEM, JEOL ARM200F).

## 3.5. Electrochemical Measurements

### 3.5.1. Electrode Preparation for SIBs and Half-Cell Assembly

Electrodes were prepared by mixing active materials, conductive carbon black, and binder (carboxymethyl cellulose (CMC)) in a predetermined weight ratio. After thoroughly grinding the electrode constituents with a mortar and pestle, an appropriate solvent (deionized water) was added into the mixture. An electrode slurry could be formed by mixing in a rotary mixer. This was followed by coating it on copper foil, then drying in a vacuum oven overnight at 80 °C, followed by pressing it with a pressure of 20 MPa. The average mass loading for an electrode was 1.2 mg $cm^{-2}$. Then, the electrodes were assembled in 2032-type coin cells in an Ar-filled glove box. Sodium foil was cut by the doctor blade technique from a sodium cube stored in mineral oil, and it then was used as both reference and counter electrode. A schematic diagram of the Na half-cell assembly is displayed in Figure 3.2. The working electrode was first placed at the positive cap, and then 2 drops of electrolyte were dropped in. Then, the separator was placed on top of the working electrode followed by dropping an extra 2 drops of the electrolyte. The Na electrode, steel spacer, spring and negative cap were placed subsequently. Finally, the coin cell was sealed.

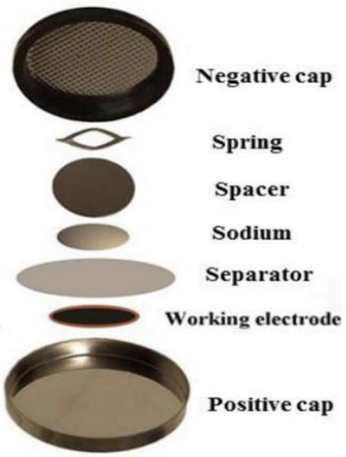


**Scheme 3.2** Schematic illustration of half-cell assembly.

### 3.5.2. Cyclic Voltammetry (CV)

Cyclic voltammetry (CV) is an important electroanalytical technique used to detect the electrochemical activity of electrode materials including the electron transfer kinetics, the presence of intermediates, and the reversibility of a redox reaction. In a typical CV experiment, the potential of a working electrode is scanned with a specified scan rate, and then the response current is collected. In this doctoral work, the CV data were obtained from a Biologic VPM-3 electrochemical workstation. All the CV testing is based on the two-electrode model, in which sodium foil acts as the reference electrode and counter electrode.

### 3.5.3. Galvanostatic Charge-Discharge

Galvanostatic charge-discharge testing was conducted in constant current density mode to test the capacity and cycling performance of the materials in a certain voltage range. This testing technique can also be used to estimate the rate capability of the electrode materials by using a variety of current densities. The charge or discharge capacity can be calculated from the applied current and the total time. In this doctoral work, galvanostatic charge-discharge measurement data were collected on a Land Battery Tester.

### 3.5.4. Electrochemical Impedance Spectroscopy (EIS)

Electrochemical impedance spectroscopy (EIS) is an important experimental measurement technique to investigate the inner resistance of a sodium-ion cell. EIS can measure the charge transfer resistance, double layer capacitance, and ohmic resistance of a cell. Usually, the impedance spectrum of a cell includes a high-frequency semicircle and a low-frequency linear tail, respectively. The semicircle is attributed to the kinetic processes reflecting the charge transfer resistance and the double layer capacitance. The linear tail relates to the diffusion of alkali ions into the bulk of the electrode materials from the electrolyte. In this doctoral thesis, EIS data were obtained on a Biologic VPM3 electrochemical workstation.

# Chapter 4

# A phosphorus/N-doped carbon nanofiber composite as an anode material for sodium-ion batteries

## 4.1. Introduction

Currently, SIBs are believed the promising alternatives to lithium ion batteries (LIBs) in large-scale applications. But the critical problem of lower energy density limits the further development of SIBs. It is an especially great challenge to obtain a promising anode material for SIBs, because the commercial graphite used in LIBs is not suitable for SIBs due to the larger size of the sodium ion compared to the lithium ion.

Recently, elemental phosphorus (P) was found to be an attractive anode material,[1–3] as it can give a high theoretical specific capacity of 2596 mA h $g^{-1}$ to form the $Na_3P$ phase.[4] In addition to the high capacity, utilization of phosphorus as an anode material has the advantages of natural abundance and low cost. Phosphorus shows great potential as an anode material for the next generation of sodium batteries, which should be capable of offering high energy density as power sources at low cost. It has been reported, however, that sodium batteries with P as the anode have some problems related to the low utilization efficiency of the active materials and poor cycle life.[5] This is because red phosphorus has very low electrical conductivity ($1 \times 10^{14}$ S $cm^{-1}$),[6] which leads to poor electrochemical accessibility and low utilization of the phosphorus in the electrode. Studies of the Na–P binary system have indicated that each phosphorus atom can accommodate up to 3 sodium atoms, leading to the formation of the $Na_3P$ phase, accompanied by a volume expansion of 300%.[7–10] This huge volume change would give rise to the disintegration of the electrode and loss of electronic contact between the P

particles, resulting in the formation of cracks, followed by pulverization of the active mass particles and permanent capacity loss.

To solve the problems of the low conductivity and large volume changes in P anodes, several research efforts have been focused on the development of composites consisting of phosphorus and carbonaceous materials, which have yielded better capacity retention and cycle life than pure P anodes.[7–9,11] Its relatively low mass, good electronic conductivity, reasonable Na-insertion capability, and small volume expansion, coupled with softness and compliance, make carbon the best active matrix.[12,13]

The pioneering research on P anodes was conducted by Yang's[7] and Lee's[8] groups, who developed phosphorus anodes through the high-energy ball-milling of red phosphorus and carbon black. Yang and co-workers reported that amorphous red phosphorus/carbon composites could deliver a high capacity of 1764 mA h $g^{-1}$ at a current density of 250 mA $g^{-1}$.[7] The study by Lee's group presented a slightly higher capacity of 1890 mA h $g^{-1}$ at a lower current density of 143 mA $g^{-1}$ with 30 cycles of battery performance.[8] Our group recently prepared high-performance composites by simply hand-grinding commercial microscale red phosphorus and carbon nanotubes, and the as-prepared composites could deliver a reversible capacity of 1675 mA h $g^{-1}$.[9]

Inspired by these examples of success, I have prepared phosphorus/N-doped carbon nanotuber composites (P/NCFs) in this work by using N-doped carbon and red phosphorus via an evaporation/deposition strategy. Compared with the ball-milling method for preparing a phosphorus/carbon composite, the vaporization–condensation method has more advantages, such as uniform adsorption of the phosphorus, keeping the original morphology of N-doped carbon tubers, etc. There have been many reports on using N-doped carbon as an efficient strategy to improve the electrochemical performance of carbon-based both Li-storage and Na-storage anodes.[14–18] In the N-doped carbon which is derived from the precursor of polypyrrole (PPy), the presence of nitrogen species on the carbon surface can lead to a pseudo-capacitive interaction between the electrolyte ions and the nitrogen-containing functional groups because of its heteroatomic defects. On the other hand, the structure of the porous tuber in our N-doped carbon is another attractive characteristic for composite formulations, in such

aspects as enhancing capacity, surface wettability, and electronic conductivity.[20] Based on the above advantages, we used the PPy precursor as the source of carbon, then sintered it in an argon atmosphere to obtain N-doped carbon nanotubers, and further obtained the phosphorus/N-doped carbon nanotuber composite (P/NCF) by loading with phosphorus. The P/NCF exhibited capacity as high as 731 mA h $g^{-1}$ at 100 mA $g^{-1}$ after 55 cycles. In this paper, we refer to the specific capacity of the P/NCF composite based on red phosphorus.

## 4.2. Experimental Section

### 4.2.1. Synthesis of N-doped carbon nanofibers

The starting materials, cetyltrimethylammonium bromide (CTAB), pyrrole, ammonium persulfate (APS), and red phosphorus, were purchased from Australia Sigma-Aldrich Pty. Ltd. All the chemicals were of analytical grade and used as purchased without further treatment. The precursor polypyrrole (PPy) was synthesized by the solution chemistry method.[21] The synthetic process was as follows: 0.72 g CTAB was dissolved in 200 ml deionized water, and 0.33 g pyrrole was added into the CTAB

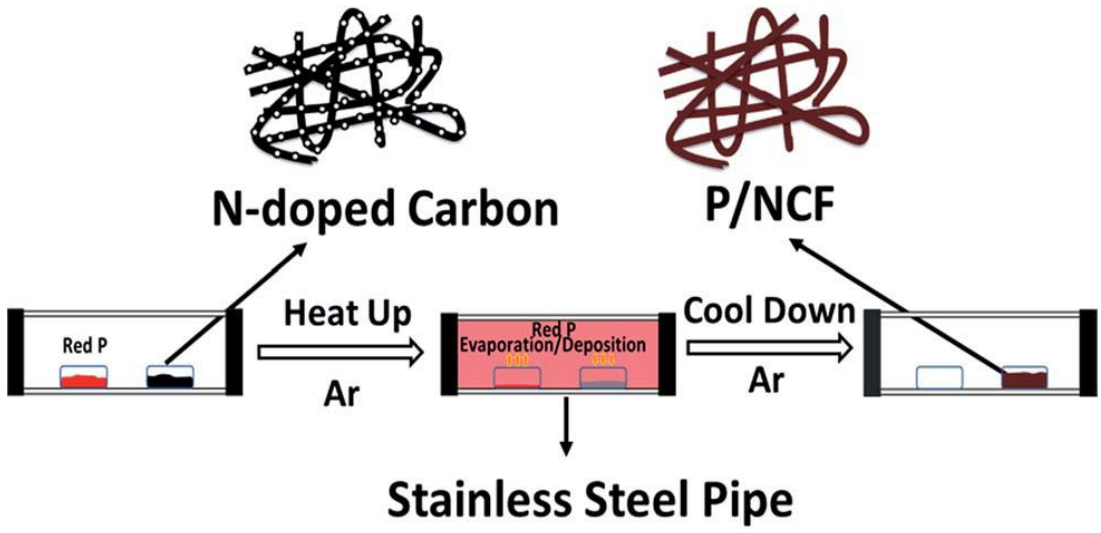


**Scheme 4. 1.** Schematic illustration of the preparation of P/NCF.

solution and ultrasonically vibrated for 5 minutes. Then, a solution of 1.13 g APS dissolved in 20 ml deionized water was added into the previous solution and stirred for 24 h at room temperature. A black precipitate (PPy nanofibers) was obtained by centrifugation. The PPy nanofibers were dried overnight at 80 °C in an oven under vacuum. The as-synthesized PPy was heated to 600 °C at a heating rate of 5 °C $min^{-1}$ and kept for 4 h under an argon atmosphere in a tube furnace to form nitrogendoped carbon nanofiber webs.

### 4.2.2. Preparation of P/NCF

Red phosphorus was washed with distilled water to remove any oxides before processing. Red phosphorus (0.2 g) and N-doped carbon (0.2 g) were placed in a sealed stainless-steel pipe, which was filled with pure argon. The stainless-steel pipe was first heated to 450 °C with a heating rate of 5 °C $min^{-1}$ in a tube furnace, and kept at that temperature for 3 h. During this time, the stainless pipe was filled with phosphorus vapour (see Scheme 1). Subsequently, the stainless-steel pipe was cooled to 260 °C at a cooling rate of 1°C $min^{-1}$ and then held at that temperature for 18 h. The aim of this step was to reduce the speed at which vaporized phosphorus atoms condense into the solid state and avoid forming white phosphorus. Phosphorus exists in the gas–liquid–solid triple point state at 260 °C. Maintaining this step for a long time will also help to impregnate the phosphorus into the pores of the N-doped carbon fibers so as to complete the evaporation/deposition process. Finally, P/NCF was obtained by cooling the stainless steel pipe to room temperature. Scheme 4.1 clearly displays the above preparation process.

### 4.2.3. Characterization

The structures of the obtained P/NCF and precursors were characterized by powder X-ray diffraction (XRD; GBC MMA diffractometer) with Cu Ka radiation at a scan rate of 4 ° $min^{-1}$. Raman spectra were collected using a JOBIN Yvon Horiba Raman spectrometer model HR800, with a 10 mW helium/neon laser at 632.8 nm excitation in the range of 200 to 2000 $cm^{-1}$. Thermogravimetric analysis (TGA) measurements were carried out in flowing argon at a heating rate of 5 °C $min^{-1}$ using a Mettler Toledo

TGA/DSC1. X-ray photoelectron spectroscopy (XPS) was conducted using a SPECS PHOIBOS 100 Analyser installed in a high-vacuum chamber with the base pressure below $10^{-8}$ mbar, X-ray excitation was provided by Al Ka radiation with photon energy $hv$ = 1486.6 eV at a high voltage of 12 kV and a power of 120 W. The XPS binding energy spectra were recorded with a pass energy of 20 eV in the fixed analyser transmission mode. Analysis of the XPS data was carried out using the commercial Casa XPS 2.3.15 software package. All the spectra were calibrated with $C_{1s}$ = 284.6 eV. The Brunauer–Emmett–Teller (BET) surface area and pore size distribution (PSD) were measured by nitrogen adsorption–desorption using a Quantachrome Autosorb-IQ MP instrument. The morphology of the samples was investigated by field-emission scanning electron microscopy (FESEM; JEOL JSM-7500FA).

### 4.2.4. Electrochemical measurements

The electrochemical measurements were conducted using 2032-type coin cells. The working electrode was prepared by coating a slurry containing 80 wt% active materials, 10 wt% Super-P (carbon black), and 10 wt% carboxymethyl cellulose (CMC) binder on a copper foil substrate. Then, the electrode film was dried in a vacuum oven at 80 °C overnight. The electrolyte used in this work was 1.0 mol $L^{-1}$ $NaClO_4$ in an ethylene carbonate (EC)–diethyl carbonate (DEC) solution (1:1 v/v), with 5 wt% addition of fluoroethylene carbonate (FEC). All the cells were assembled in a glovebox filled with argon and tested at room temperature. Galvanostatic charge–discharge testing was conducted on a Land Test System with a cut-off voltage range of 0–2.5 V (vs. $Na/Na^+$) at a constant current of 100 mA $g^{-1}$. Cyclic voltammetry measurements were conducted at a scan rate of 0.1 mV $s^{-1}$ on an SP-300 Potentiostat Galvanostat electrochemical workstation.

## 4.3. Results and Discussion

Fig.4.1a shows the X-ray diffraction (XRD) patterns of the commercial red P, N-doped carbon, and P/NCF. For the red P, the peaks centred at 15 ° and 34 ° are attributed to the $d_{013}$ and $d_{318}$ planes.[15,16] For the N-doped carbon, the diffraction peak at 24.5 °, corresponds to a d-spacing of 0.36 nm, which is very close to 0.34 nm, i.e., the

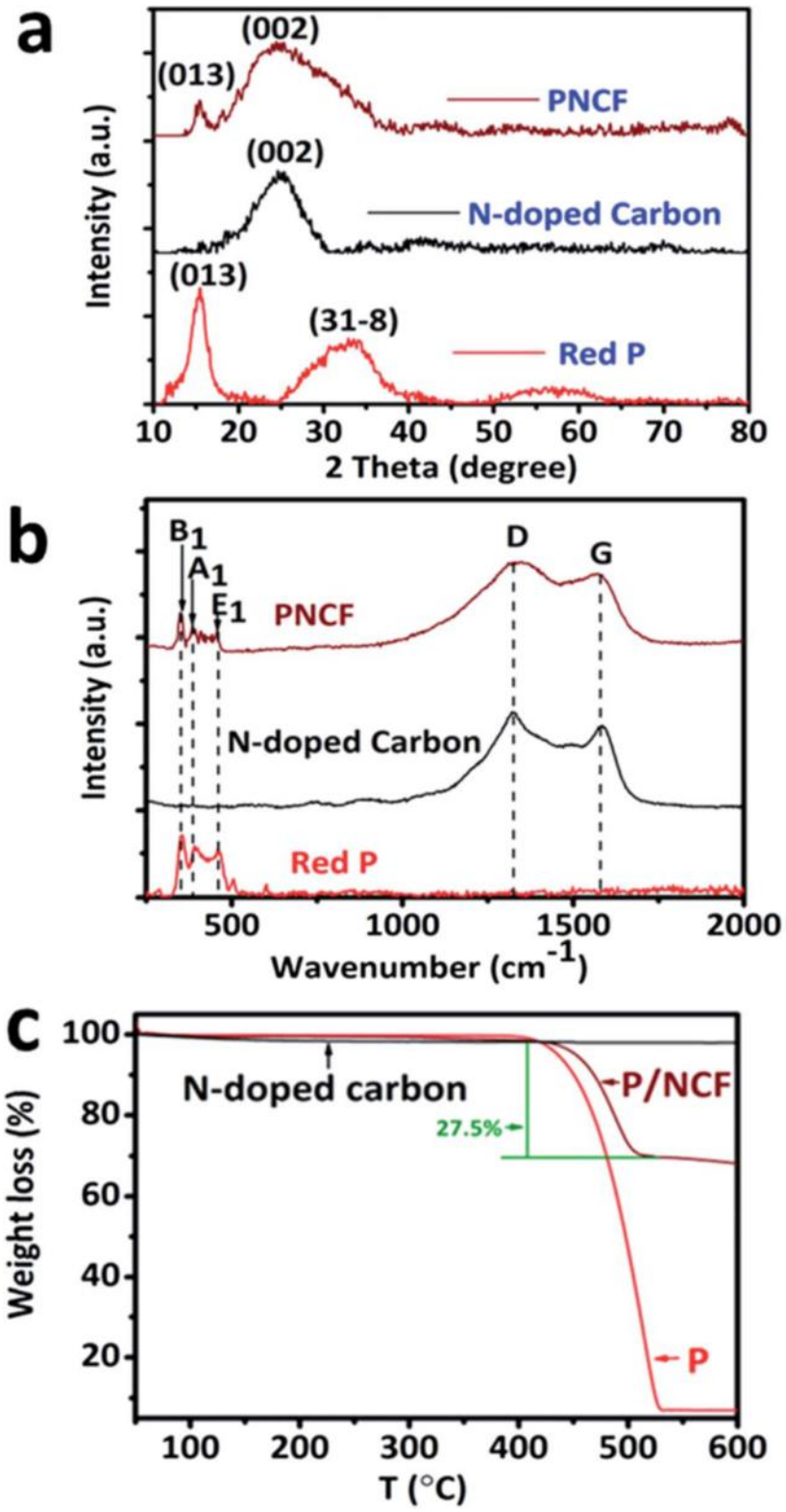


**Figure 4.1** XRD patterns (a), Raman spectra (b) and TGA curves (c) of red phosphorus, N-doped carbon, and P/NCF.

$d_{002}$ plane in graphite.[18] In the P/NCF pattern, there is a broad peak at 24.5 ° , which is considered to be a merger of N-doped carbon and red P peaks, and a characteristic peak of red P is also clearly observed at 15 °, although the intensity is weak. These peaks confirm the presence of red P in the composite. Fig.4.1b shows the Raman spectra of red P, N-doped carbon and P/NCF. In the spectrum of amorphous red phosphorus, there are three bands from 300 to 500 $cm^{-1}$, which are characteristic peaks of red P.[15] The red P largely consists of $P_7$ and $P_9$ cages arranged to form pentagonal tubes in paired layers; $P_9$ cages are considered to be responsible for the sharp peak at approximately 350 $cm^{-1}$. The G mode of N-doped carbon (~1580 $cm^{-1}$) involves an $E_{2g}$ symmetrical bond stretching motion of pairs of C $sp^2$ atoms, while the D band (~1350 $cm^{-1}$) is attributed to the breathing mode of six-membered rings.[19] The Raman pattern of P/NCF exhibits two characteristic peaks at 1350 $cm^{-1}$ and 1580 $cm^{-1}$, which are attributed to N-doped carbon. The Raman intensity and wavenumber of both the D- and G-bands are unchanged in the spectrum of P/NCF, indicating that the carbon matrix and the adsorbed phosphorus have no interaction in P/NCF. Also, we can see that the three bands from 300 to 500 $cm^{-1}$, the characteristic peaks of red phosphorus, weakly appear in the composite. These traces, evident in the range of 350–480 $cm^{-1}$, verify the presence of elemental phosphorus in the composite. This result is in accordance with the conclusion drawn from the XRD and XPS.

The thermogravimetric analysis (TGA) curve of P/NCF is shown in Fig.4.1c. There is an obvious weight loss at about 450 °C under an argon atmosphere, a much higher temperature than for the pure red phosphorus, which shows a clear weight loss at about 410 °C, the temperature at which red phosphorus sublimes. This high temperature indicates that phosphorus in the composite is relatively more stable than elemental phosphorus, which is due to the adsorption of phosphorus on the surface of the carbon. The content of P in the P/NCF was determined to be about 27.5 wt% from the TGA curves.

X-ray photoelectron spectroscopy (XPS) was used to further investigate the interaction between the PPy, N-doped carbon and red phosphorus. In Fig.4.2, the deconvolution of the N1s spectrum identifies the surface functionalities of PPy (Fig.4.

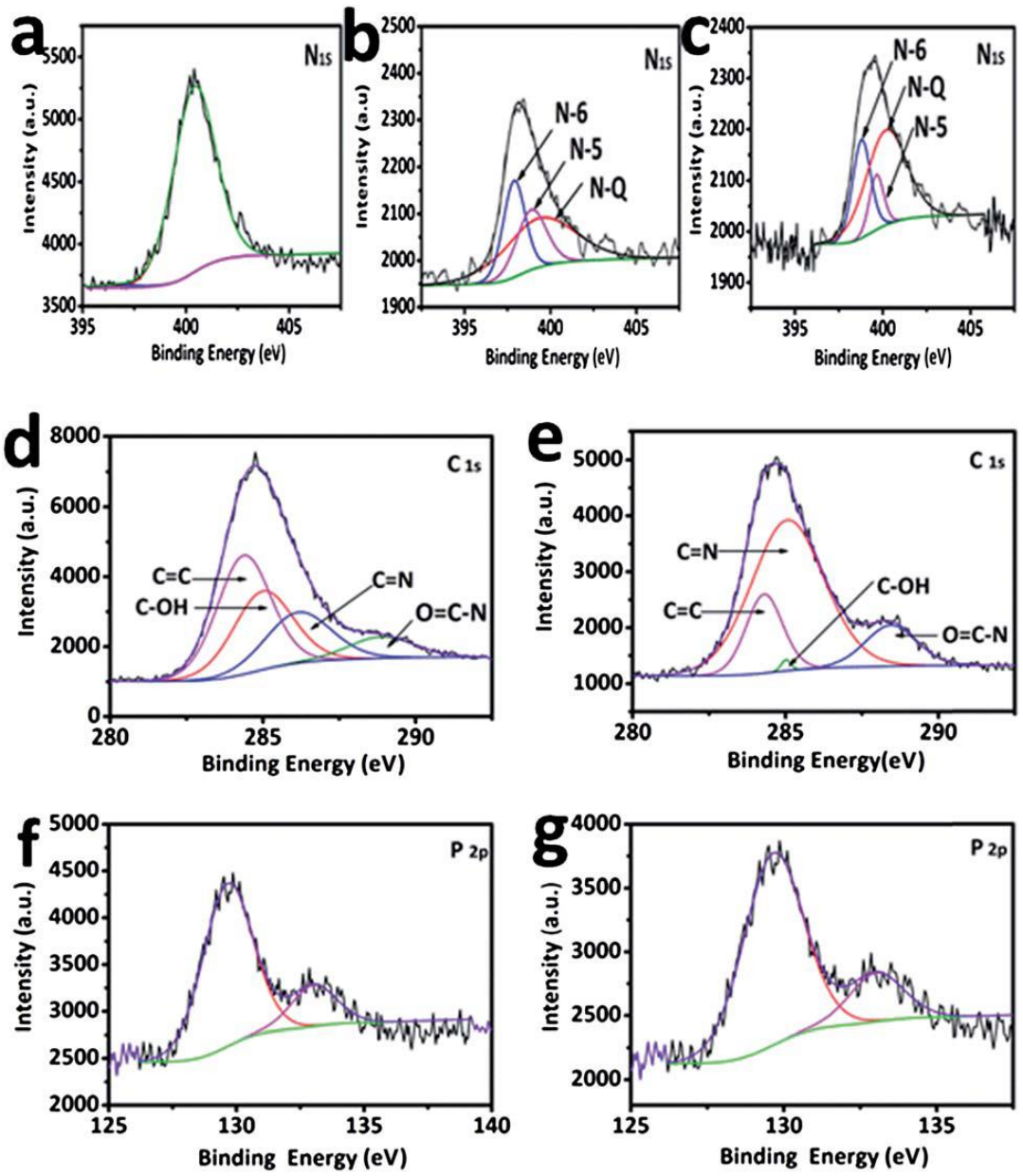


**Figure 4.2** High resolution $N_{1s}$ XPS spectra of PPy (a), N-doped carbon (b), and P/NCF (c). $C_{1s}$ XPS spectra of N-doped carbon (d), and P/NCF (e). $P_{2p}$ XPS spectra of red P (f), and P/NCF (g).

2a), N-doped carbon (Fig.4.2b) and P/NCF (Fig.4.2c). There is only one fitted component peak at 400.4 eV for PPy, which is attributed to pyrrolic nitrogen. Regarding the N-doped carbon, there are three fitted component peaks at 397.9, 398.9, and 399.8 eV, which are assigned to pyridinic (N-6), pyrrolic/pyridone (N-5), and quaternary (N-Q) nitrogen, respectively. This sequence is consistent with the literature.[21] For P/NCF, the

sequence of N-6, N-5 and N-Q peaks is the same as that of N-doped carbon. There are only some changes of intensities. In N-doped carbon, the $C_{1s}$ spectrum can be fitted into the following bands: C=C (284.5 eV), C–OH (285.4 eV), C $_{sp2}$ linked to N (285.9 eV), and C doubly bound to O and singly to C (287.6 eV) (Fig. 4.2c).[21,22] In the case of the $C_{1s}$ spectrum in the P/NCF composite, the intensity of some peaks apparently changed due to the effects on bonding of the encapsulation of the P (Fig.4.2d). Two peaks centered at 129.8 and 134.0 eV were observed in the $P_{2p}$ XPS spectrum of the phosphorus (Fig. 4.2e). The peak at 129.8 eV is attributed to $P_{2p3/2}$, and the other one, which has a relatively low intensity at 134.0 eV, may come from phosphates.[23] In the case of P/NCF, there was no significant change in the positions of the P peaks, but the intensity clearly decreased (Fig.4.2f). Here, we also measured the C, N and O contents in PPy fibers and N-doped carbon fibers by XPS. The mass concentration of PPy was $C_{1s}$ 68.58%, $N_{1s}$ 19.23%, and $O_{1s}$ 12.18%. As for N-doped carbon, it was the following, $C_{1s}$ 78.69%, $N_{1s}$ 9.64%, and $O_{1s}$ 11.67%. From these data, we can see that the N content decreased significantly due to the pyrolysis of PPy.

In this paper, we used the Quantachrome Autosorb-iQ MP to measure the BET surface area and pore size distribution of N-doped carbon and composite P/NCF with the BJH model. As shown in Fig.4.3a, $N_2$ adsorption–desorption isotherms of N-doped carbon can be identified as type IV isotherms in the International Union of Pure and Applied Chemistry (IUPAC) classification with a typical mesoporous hysteresis loop. The adsorption–desorption hysteresis of N-doped carbon is very clear, suggesting that it possesses a large volume of mesopores. This conclusion is fully supported by the pore size distribution curves obtained from the $N_2$ isotherms based on density functional theory calculations (Fig.4.3c). The porosity data, including the BET surface area, pore volume, and average pore diameter for all samples, are summarized in Table 4.1.

N-doped carbon presents a high surface area of 158 $m^2 g^{-1}$ and a large pore volume of 0.34 $cm^3 g^{-1}$, with the predominant pore size around 17.7 nm, which helps to efficiently absorb and hold the phosphorus active material. It should be noted that after loading phosphorus into the micropores or mesopores of N-doped carbon, the specific surface area and pore volume of N-doped carbon decrease rapidly, with 75.62 $m^2 g^{-1}$ and 0.28

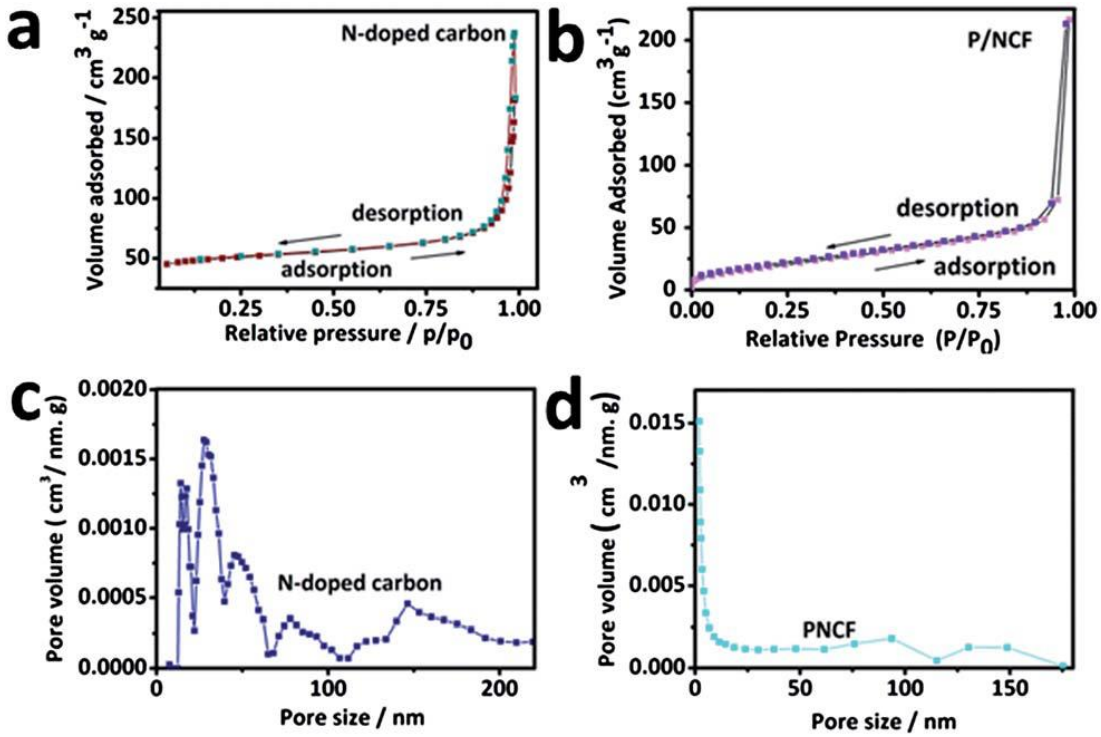


**Figure 4.3** Porosity characterization of N-doped carbon (a) and P/NCF (b) by N2 adsorption–desorption isotherms. Pore size distribution of N-doped carbon (c), and P/NCF (d).

**Table 4.1** Key pore characteristics of N-doped carbon and P/NCF

| Material | Surface area ($m^2$ $g^{-1}$) | Pore volume ($cm^3$ $g^{-1}$) | Average pore size (nm) |
|---|---|---|---|
| N-doped carbon | 158.0 | 0.34 | 17.7 |
| Phosphorus | 2.5 | 0.009 | |
| P/NCF | 75.6 | 0.28 | 7.2 |

$cm^3$ $g^{-1}$ retained, respectively. This indicates that most of the nanopores in the N-doped carbon are occupied by the phosphorus element.

The morphologies of the as-synthesized PPy, N-doped carbon and P/NCF were characterized by scanning electron microscopy (SEM), as displayed in Fig.4.4. The image of PPy shows a homogeneous morphology of cross-linked nanofibers less than 100 nm in diameter (Fig.4.4a). After being carbonized at 600 °C for 4 h, the interconnected nanofiber structure of the PPy is still maintained (Fig.4.4b). As for P/NCF, it can be seen that the diameter of the P/NCF nanofibers is larger than that of N-doped carbon (Fig.4.4c). This indicates that the fibres of N-doped carbon are covered by phosphorus in P/NCF.

Transmission electron microscopy (TEM) was further used to investigate the structure of P/NCF. As shown in Fig.4.5a and b, P/NCF maintains the fibrous structure of N-doped carbon, while the phosphorus impregnation has increased the average fiber diameter from less than 100 to 125 nm. These images are entirely consistent with the SEM image in Fig.4.4c. The TEM selected area electron diffraction (SAED) pattern in the inset of (Fig.4.5b) also shows a diffuse ring for the red P, which confirms its amorphous nature.[24]

The energy dispersive spectroscopy (EDS) mapping images reveal the distributions of the elements C (Fig.4.5d), N (Fig.4.5e), and P (Fig.4.5f) in P/NCF. In the elemental mapping of P, the points clearly demonstrate that most of the phosphorus was homogeneously distributed in the N-doped carbon fibers.

Fig. 4.6 shows the cycling performances of P/NCF (a), N-doped carbon (c), and red P (e) between 2.5 V and 0 V at a current density of 100 mA $g^{-1}$. It can be seen that the P/NCF composite electrode exhibits a high reversible capacity of over 850 mA h $g^{-1}$ in the first 10 cycles and maintains a reversible capacity of 731 mA h $g^{-1}$ after 55 cycles. It also presents an excellent coulombic efficiency of over 99.6%. The retained capacity for N-doped carbon is approximately 130 mA h $g^{-1}$ after 55 cycles (c). The cycling performance of red P is very low, with no more than 25 mA h $g^{-1}$ capacity (e), even from the beginning. Fig.4.6 shows the discharge–charge voltage profiles of the initial three cycles for P/NCF (b), N-doped carbon (d), and red P (f). During the first cycle, the 1st cycle discharge and 2nd cycle charge capacities of the P/NCF composite electrode are 2752 and 1275 mA h $g^{-1}$, respectively, giving an initial coulombic efficiency of 46.3%. The large capacity loss of the first cycle was mainly attributed to the irreversibl

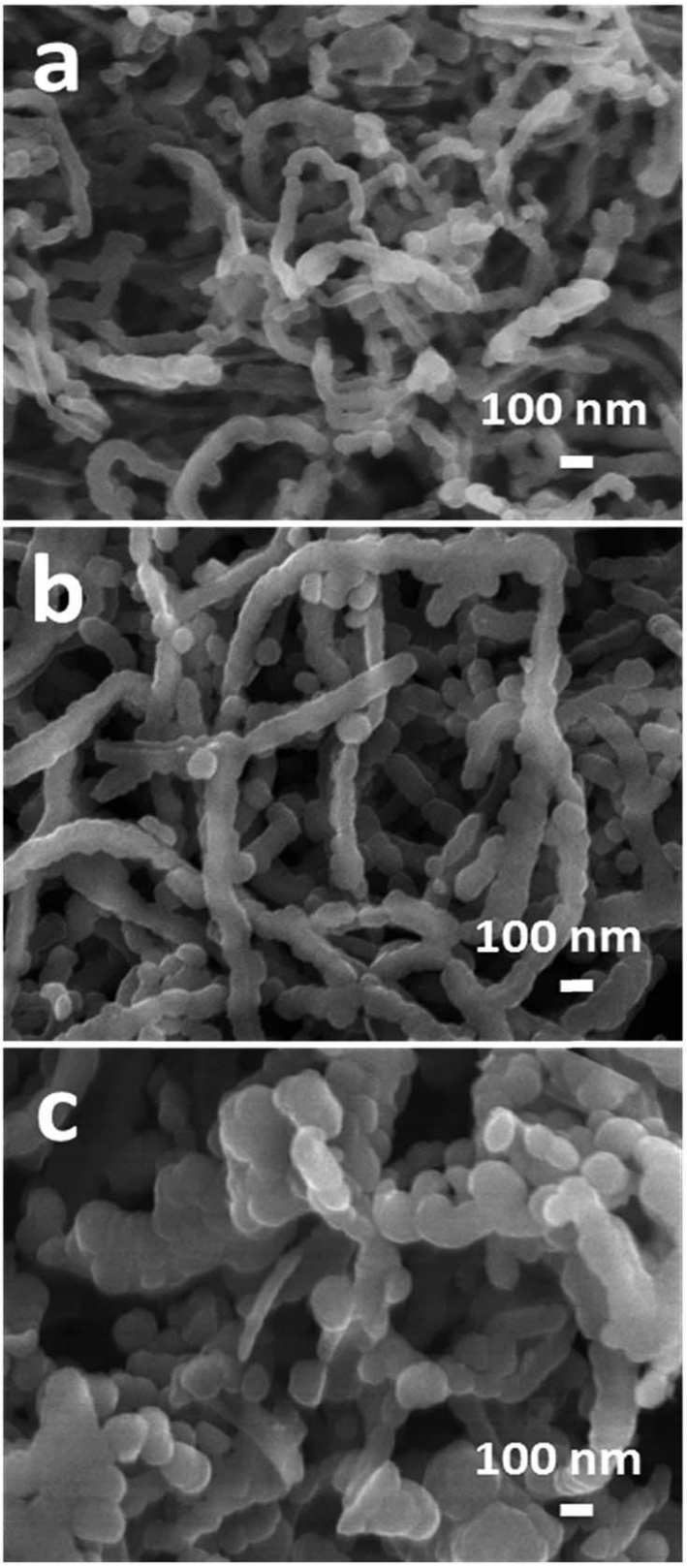


**Figure 4.4** SEM images of the samples: PPy (a), N-doped carbon (b), and P/NCF (c).

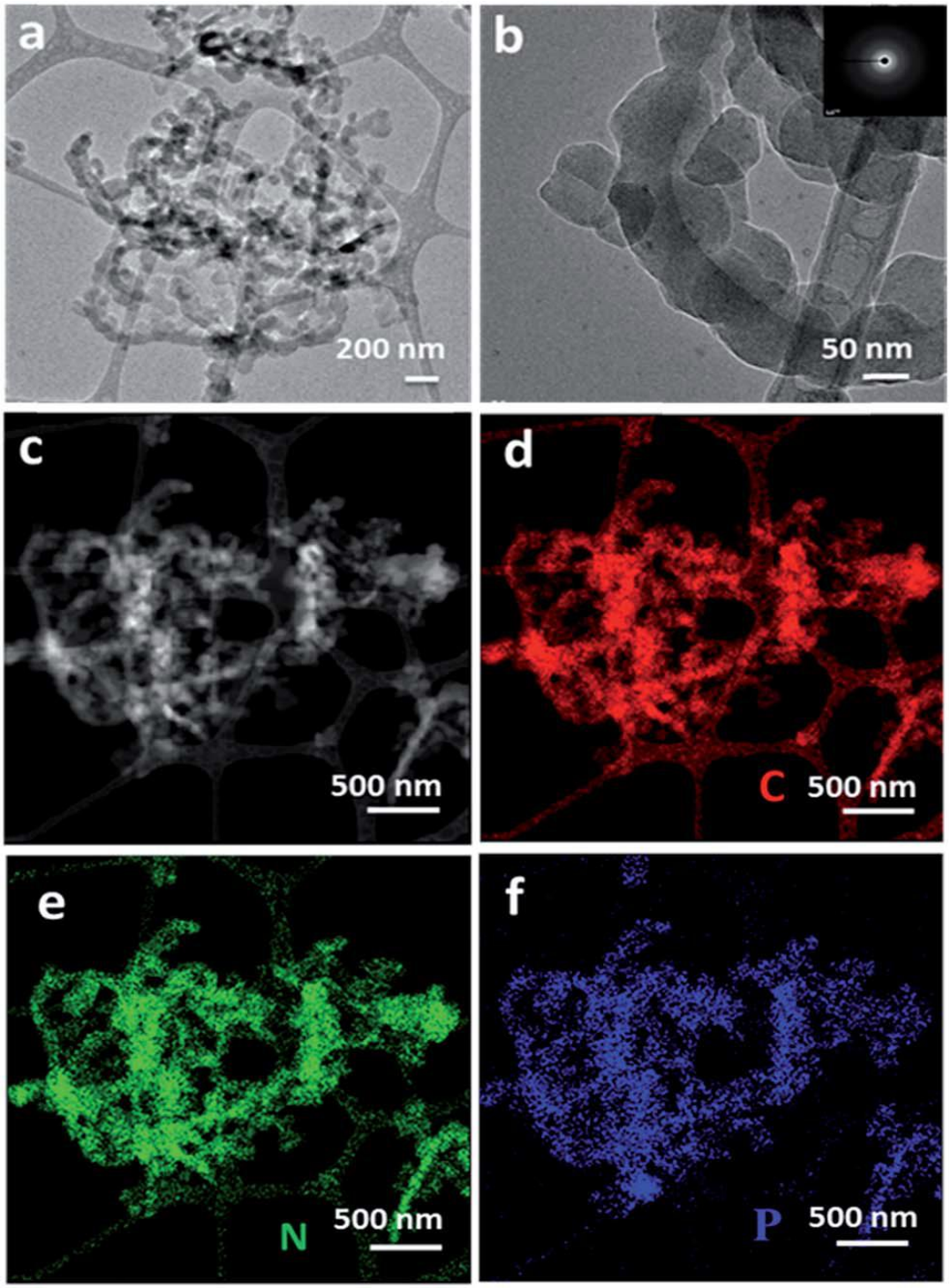


**Figure 4.5** TEM images obtained from P/NCF: low magnification image (a), and high magnification image (b), with the corresponding electron diffraction pattern shown in the inset of (b). Dark background image (c) with corresponding EDS elemental mapping of C (d), N (e), and P (f).

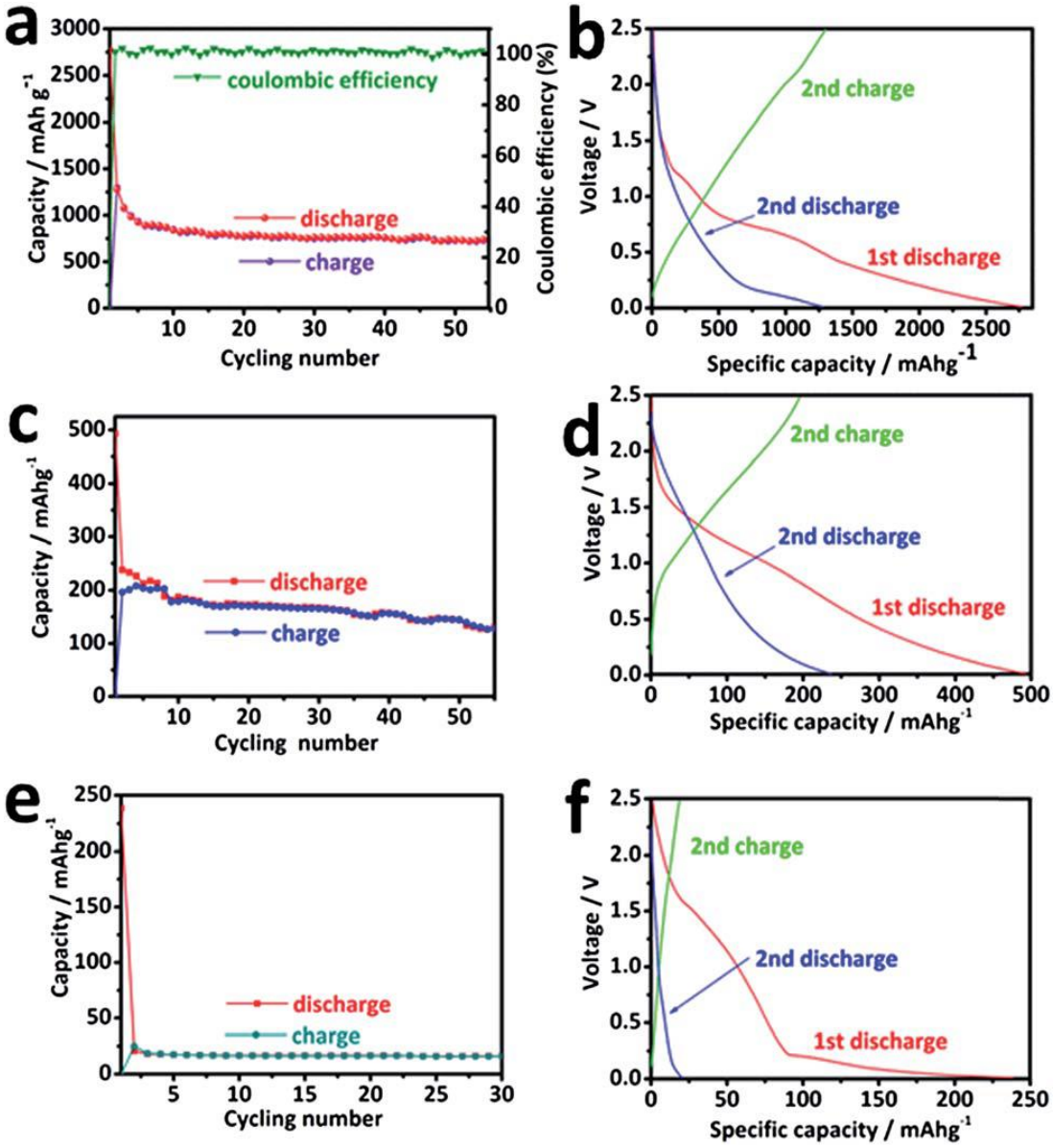


**Figure 4.6** Cycling performance of P/NCF (a), N-doped carbon (c) and red P (e) at a current density of 100 mA $g^{-1}$. Charge–discharge profiles of P/NCF (b), N-doped carbon (d) and red P (e) with a current density of 100 mA $g^{-1}$.

formation of the solid electrolyte interphase (SEI) layer on the electrode surface and irreversible Na insertion into the P/NCF matrix. Nevertheless, the capacity loss only occurs in the first few cycles, and after that, the coulombic efficiency approaches 100%, indicating the excellent capacity retention of P/NCF. The initial discharge–charge voltage profiles for N-doped carbon display a 1st cycle discharge capacity of 493 mA h

$g^{-1}$, and a much lower initial coulombic efficiency of 39.8%. From the discharge–charge voltage profiles of red P, it can be seen that even in the 1st discharge state, the specific capacity is only 238 mA h $g^{-1}$. The initial coulombic efficiency is merely 10.4%, so this result further demonstrates that pure red P cannot accommodate much $Na^+$ insertion.

Fig. 4.7a shows the cyclic voltammetry (CV) curves for P/NCF at a scan rate of 0.1 mV $s^{-1}$ between 0 and 2.5 V (vs. $Na/Na^+$). A broad peak around 1.0 V (vs. $Na/Na^+$) is observed during the first cathodic scan, which is attributed to the reduction of the electrolyte to form the SEI layer. In the subsequent cathodic scans, a small weak peak around 0.4 V (vs. $Na/Na^+$), which overlaps with the SEI peak in the first cathodic scan, is observed and could be ascribed to the initial sodiation of red P. When the potential was further scanned around 0.1 V, another small sharp cathodic peak with a noticeable shoulder appeared between 0.25 and 0 V, corresponding to further sodium ion insertion. During the anodic scans, a strong peak at around 0.63 V with a shoulder at around 0.71 V and another weak peak around 1.5 V (all vs. $Na/Na^+$) are observed, which should be attributed to the desodiation of different $Na_xP$ compounds. These peaks possibly correspond to a stepwise sodium ion deinsertion from the fully charged $Na_3P$ phase to form the $Na_2P$, NaP, and $NaP_7$ intermediates, respectively.[7,8]

To better understand the reason for the improved cyclability of the P/NCF electrode compared with the red P electrode, electrochemical impedance spectroscopy (EIS) of the P/NCF electrodes and red P electrodes was conducted using a sine wave of 10 m V amplitude over a frequency range of 100 kHz to 0.01 Hz. The Nyquist plots and the fitting model using an equivalent circuit are compared in Fig.4.7b, with the equivalent circuit as the inset. The plots for the P/NCF electrodes display one compressed semicircle in the high frequency region and a sloping line in the low frequency region. The intercept on the Zreal axis in the high frequency region represents the total resistance of the electrolyte, separator, and electrical contacts ($R_i$). The semicircle in the high frequency range reflects the charge transfer resistance ($R_{ct}$), which represents the impedance associated with sodium ion transport through surface films and charge transfer at the electrode/electrolyte interface. The inclined line in the low frequency region represents the Warburg impedance ($W$), related to the charge transfer, by sodium ion diffusion through the material or electrolyte. CPE in the equivalent circuit is a

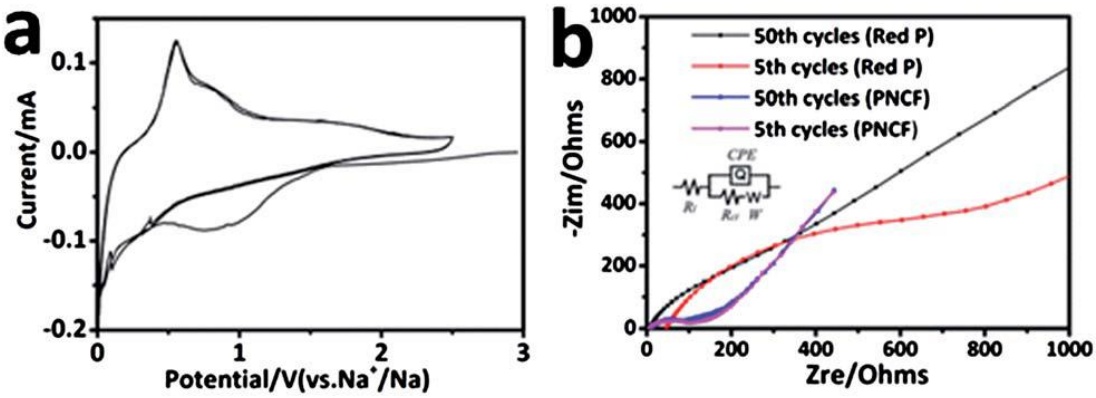


**Figure 4.7** (a) CV curves of P/NCF scanned at a rate of 0.1 mV $s^{-1}$. (b) Nyquist plot and equivalent circuit model of red P and P/NCF in the charged state.

constant phase element, reflecting double layer capacitance. It can be seen that the diameters of the semicircles for P/NCF for both the 5th cycle and 50th cycle are the same, demonstrating a charge transfer resistance of 101.5 Ω, which indicates well-maintained electrical contact and a relatively stable SEI layer. This is because of the large surface area and good conductive network from the N-doped carbon, which could relieve the volume changes in the P particles during charge and discharge processes. In contrast, the charge transfer resistance ($R_{ct}$) of the cell with the P electrode in the 5th cycle has a very big value of 800 Ω, which further confirms that P has very low electrical conductivity.

## 4.4. Conclusion

In summary, I have used a simple method to prepare a nanostructured phosphorus composite material (P/NCF) from N-doped carbon and red phosphorus, in which the porous carbon serves as the electronically conductive support matrix. In view of its high capacity for sodium storage, the phosphorus composite shows promise for applications in electrochemical energy storage devices. The results also give clear evidence of the utility of N-doped carbon fiber for enhancing the electrochemical performance of red phosphorus as an anode material for sodium-ion batteries. This preparation strategy is simple, yet very effective, and because of its versatility, could potentially be extended to other electrically conductive support matrices for the preparation of other phosphorus

composites for sodium ion batteries.

## 4.5. References

1. Qian, J.; Wu, X.; Cao, Y.; Ai, X.; Yang, H., High capacity and rate capability of amorphous phosphorus for sodium ion batteries. *Angewandte Chemie* **2013,** *125* (17), 4731-4734.

2. Li, W.; Chou, S. L.; Wang, J. Z.; Kim, J. H.; Liu, H. K.; Dou, S. X., $Sn_{4+x}P_3$@ Amorphous Sn‐P Composites as Anodes for Sodium‐Ion Batteries with Low Cost, High Capacity, Long Life, and Superior Rate Capability. *Adv. Mater.* **2014,** *26* (24), 4037-4042.

3. Yabuuchi, N.; Matsuura, Y.; Ishikawa, T.; Kuze, S.; Son, J. Y.; Cui, Y. T.; Oji, H.; Komaba, S., Phosphorus Electrodes in Sodium Cells: Small Volume Expansion by Sodiation and the Surface‐Stabilization Mechanism in Aprotic Solvent. *ChemElectroChem* **2014,** *1* (3), 580-589.

4. Sangster, J. M., Na-P (Sodium-Phosphorus) System. *Journal of phase equilibria and diffusion* **2010,** *31* (1), 62-67.

5. Marino, C.; Debenedetti, A.; Fraisse, B.; Favier, F.; Monconduit, L., Activated-phosphorus as new electrode material for Li-ion batteries. *Electrochem. Commun.* **2011,** *13* (4), 346-349.

6. Extance, P.; Elliott, S., Pressure dependence of the electrical conductivity of amorphous red phosphorus. *Philosophical Magazine B* **1981,** *43* (3), 469-483.

7. Capacity, H., Rate Capability of Amorphous Phosphorus for Sodium Ion Batteries Qian, Jiangfeng; Wu, Xianyong; Cao, Yuliang; Ai, Xinping; Yang, Hanxi. *Angewandte Chemie, International Edition* **2013,** *52* (17), 4633-4636.

8. Kim, Y.; Park, Y.; Choi, A.; Choi, N. S.; Kim, J.; Lee, J.; Ryu, J. H.; Oh, S. M.; Lee, K. T., An amorphous red phosphorus/carbon composite as a promising anode material for sodium ion batteries. *Adv. Mater.* **2013,** *25* (22), 3045-3049.

9. Li, W.-J.; Chou, S.-L.; Wang, J.-Z.; Liu, H.-K.; Dou, S.-X., Simply mixed commercial red phosphorus and carbon nanotube composite with exceptionally reversible sodium-ion storage. *Nano Lett.* **2013,** *13* (11), 5480-5484.

10. Wang, L.; He, X.; Li, J.; Sun, W.; Gao, J.; Guo, J.; Jiang, C., Nano‐Structured

Phosphorus Composite as High‐Capacity Anode Materials for Lithium Batteries. *Angewandte Chemie International Edition* **2012,** *51* (36), 9034-9037.

11. Song, J.; Yu, Z.; Gordin, M. L.; Hu, S.; Yi, R.; Tang, D.; Walter, T.; Regula, M.; Choi, D.; Li, X., Chemically bonded phosphorus/graphene hybrid as a high performance anode for sodium-ion batteries. *Nano Lett.* **2014,** *14* (11), 6329-6335.

12. Ng, S. H.; Wang, J.; Wexler, D.; Konstantinov, K.; Guo, Z. P.; Liu, H. K., Highly Reversible Lithium Storage in Spheroidal Carbon‐Coated Silicon Nanocomposites as Anodes for Lithium‐Ion Batteries. *Angewandte Chemie International Edition* **2006,** *45* (41), 6896-6899.

13. Kurita, N.; Endo, M., Molecular orbital calculations on electronic and Li-adsorption properties of sulfur-, phosphorus-and silicon-substituted disordered carbons. *Carbon* **2002,** *40* (3), 253-260.

14. Shin, W. H.; Jeong, H. M.; Kim, B. G.; Kang, J. K.; Choi, J. W., Nitrogen-doped multiwall carbon nanotubes for lithium storage with extremely high capacity. *Nano Lett.* **2012,** *12* (5), 2283-2288.

15. Lota, G.; Fic, K.; Frackowiak, E., Carbon nanotubes and their composites in electrochemical applications. *Energy Environ. Sci.* **2011,** *4* (5), 1592-1605.

16. Wang, H. g.; Wu, Z.; Meng, F. l.; Ma, D. l.; Huang, X. l.; Wang, L. m.; Zhang, X. b., Nitrogen‐Doped Porous Carbon Nanosheets as Low‐Cost, High‐Performance Anode Material for Sodium‐Ion Batteries. *ChemSusChem* **2013,** *6* (1), 56-60.

17. Fu, L.; Tang, K.; Song, K.; van Aken, P. A.; Yu, Y.; Maier, J., Nitrogen doped porous carbon fibres as anode materials for sodium ion batteries with excellent rate performance. *Nanoscale* **2014,** *6* (3), 1384-1389.

18. Wang, Z.; Qie, L.; Yuan, L.; Zhang, W.; Hu, X.; Huang, Y., Functionalized N-doped interconnected carbon nanofibers as an anode material for sodium-ion storage with excellent performance. *Carbon* **2013,** *55*, 328-334.

19. Wu, Z.; Ren, W.; Xu, L.; Li, F.; Cheng, H., ACS Nano 2011, 5, 5463. *Shao, S. Zhang, MH Engelhard, G. Li, G. Shao, Y. Wang, J. Liu, IA Aksay, Y. Lin, J. Mater. Chem* **2010,** *20*, 7491.

20. Fuge, G.; May, P.; Rosser, K.; Pearce, S.; Ashfold, M., Laser Raman and X-ray

photoelectron spectroscopy of phosphorus containing diamond-like carbon films grown by pulsed laser ablation methods. *Diamond and related materials* **2004,** *13* (4), 1442-1448.

21. Burg, P.; Fydrych, P.; Cagniant, D.; Nanse, G.; Bimer, J.; Jankowska, A., The characterization of nitrogen-enriched activated carbons by IR, XPS and LSER methods. *Carbon* **2002,** *40* (9), 1521-1531.

22. Mao, Y.; Duan, H.; Xu, B.; Zhang, L.; Hu, Y.; Zhao, C.; Wang, Z.; Chen, L.; Yang, Y., Lithium storage in nitrogen-rich mesoporous carbon materials. *Energy Environ. Sci.* **2012,** *5* (7), 7950-7955.

23. Sun, J.; Zheng, G.; Lee, H.-W.; Liu, N.; Wang, H.; Yao, H.; Yang, W.; Cui, Y., Formation of stable phosphorus–carbon bond for enhanced performance in black phosphorus nanoparticle–graphite composite battery anodes. *Nano Lett.* **2014,** *14* (8), 4573-4580.

24. Park, C. M.; Sohn, H. J., Black phosphorus and its composite for lithium rechargeable batteries. *Adv. Mater.* **2007,** *19* (18), 2465-2468.

# Chapter 5

# 3-D structured $SnO_2$–polypyrrole nanotubes applied in Na-ion batteries

## 5.1. Introduction

As is well known, it is still a big challenge to develop suitable anode materials for Na-ion batteries because of the larger ionic radius of $Na^+$ compared to that of $Li^+$, which causes greater volume changes during cycling and lower gravimetric and volumetric energy densities. These innate characteristics are directly limiting the feasibility of insertion materials for SIBs, including some cathode and anode materials. To bypass these deficiencies, many carbon-based materials have been extensively investigated, such as hard carbons, which can achieve reversible capacities from 200 to 290 mA h $g^{-1}$ for more than 180 and 100 cycles, respectively.[1,2] Reduced graphene oxide, could achieve a reversible capacity of 174.3 mA h $g^{-1}$ over 250 cycles.[3] N-Doped carbon composite, which showed a reversible capacity of 155.2 mA h $g^{-1}$ after 260 cycles,[4] retained a reversible capacity of 243 mA h $g^{-1}$ after 100 cycles,[5] and achieved a specific capacity of 175 mA h $g^{-1}$ after 2000 cycles etc.[6] Some non-carbonaceous materials such as metal oxide materials also have been studied for SIBs.[7–11] Among these materials, $SnO_2$-based materials have attracted more interest because $SnO_2$ can deliver high specific capacities by acting as an alloying material to store Na. It has been demonstrated that $SnO_2$ can be an attractive anode for SIBs, with a capacity of 667 mA h $g^{-1}$, based on the following reactions:

$$4\,SnO_2 + 16Na^+ + 16e^- \longrightarrow 4Sn + 8Na_2O \quad (1)$$

$$4\,Sn + 15Na^+ + 16e^- \longrightarrow 4Na_{15}Sn_4 \text{ (ref. 20)} \quad (2)$$

Similarly, the main disadvantages of $SnO_2$ are the expansion and shrinkage of the active material particles during Na insertion/extraction, leading to particle pulverization/exfoliation and rapidly decreasing capacity in these materials.[11,12] On the

other hand, studies have shown that the diffusion speed of $Na^+$ is 30 times slower than that of $Li^+$ in $SnO_2$ particles.[13] Much research has been carried out to solve this problem, such as by decreasing the particle size of the active material to the nanoscale [14] and loading some materials as buffer layers.[11,15–21] In recent years, with the persistent efforts focused on exploring new anode materials for sodium storage, some three-dimensional (3-D) structured composites have been recognised to have sodium storage capability. There are many reports of $SnO_2$ nanoparticles loaded onto graphene,[17] anchored on reduced graphene oxide frameworks [22] and confined in mesoporous carbon.[23]

Polypyrrole (PPy), in particular consisting of tubes with a 3-D structure, as a kind of conducting polymer, not only acts as an electrically conducting agent, which is beneficial for reducing resistance and enhancing the rate capability of the cell, but also as a matrix or binder, which can provide efficient transport pathways for electrons and mitigate the pulverization of the electrode brought about by the huge volume expansion during the charging/discharging process. This unique hierarchical structure not only provides good structural robustness and short ion/electron diffusion pathways, but also promotes the diffusion of the electrolyte into the inner spaces of the material, as well as providing sufficient open channels for fast $Na^+$ migration. There are many reports on using PPy as a matrix to synthesize $SnO_2$ based composites [24–28] for anode materials. Recently, Du and Wang reported the synthesis of $SnO_2$@-polypyrrole nanotubes with microwave-assisted method.[29] The pyrolyzed composite displayed very excellent capability for Li-storage as the PPy NTs can accommodate large volume change of the electrode material during $Li^+$ insertion/extraction, which prevented $SnO_2$ nanoparticles from pulverizing and electrical isolating during cycling. Combining PPy tubes with $SnO_2$ nanoparticles to fabricate $SnO_2$-based anode material in SIBs has not been explored, however. In term of the above advantages, I also adopted PPy as the substrate material and anchored the active $SnO_2$ nanoparticles on its' surface. Herein, I report the in situ hydrothermal synthesis of $SnO_2$–PPy nanotubes with a 3-D structure. In the composites, $SnO_2$ nanoparticles are homogeneously distributed on the surfaces of the PPy nanotubes. This unique hierarchical structure not only provides good structural robustness and short ion/electron diffusion pathways, but also has benefits for electrolyte penetration and Na transport. The obtained 3-D structured $SnO_2$–PPy

nanotube network showed a good reversible capacity of nearly 288 mA h $g^{-1}$ when discharging at 100 mA $g^{-1}$, with more than 69.1% capacity retention and stable coulombic efficiency of 99.6% over 150 cycles. Good rate capability is observed, based on current rate variation during cycling from 50 mA $g^{-1}$ to 1 A $g^{-1}$.

## 5.2. Experimental Section

### 5.2.1. Synthesis of PPy tubes

The PPy tubes were synthesized according to a previous report [30] with some modifications. The process of synthesis was as follows: 1.95 g of $FeCl_3$ was added to 150 mL a solution containing 98 mg methyl orange (MO) in deionized water under constant stirring. A flocculent precipitate appeared immediately. Then, 0.484 g (0.5 mL) of pyrrole monomer was added into the mixture and the mixture was continuously stirred for 24 hours at room temperature. After that, the thus-formed PPy precipitate was washed several times with deionized water/ethanol, until the filtrate was colourless and neutral. Finally, the precipitate was dried under vacuum at 60 °C for 24 h.

### 5.2.2 Preparation of the $SnO_2$@PPy nanocomposites

In a typical procedure, 0.035 g hexamethylenetetramine (HMTA) and 0.02 g urea were dissolved in 30 mL ethanol, and then 0.1 g PPy was dispersed into the foregoing solution by ultrasonic treatment for 0.5 h. 0.1 g of $SnCl_2{\cdot}2H_2O$ was added to the preceding mixture and stirred in for 30 minutes. Subsequently, the resulting blend was transferred into a Teflon-lined autoclave and heated up to 120 °C for 10 h. When the precipitates were cooled down to room temperature naturally, then washed it with distilled water and ethanol for several times. Drying the precipitates in a vacuum oven overnight at 60 °C, the final product (denoted as $SnO_2$–PPy-1) was obtained. $SnO_2$–PPy-2 was obtained by adjusting the weight of $SnCl_2{\cdot}2H_2O$ to 0.15 g. For comparison, pure $SnO_2$ nanoparticles were prepared with the same conditions without the addition of PPy.

## 5.2.3. Characterizations

The powder X-ray diffraction (XRD; GBC MMA diffractometer) equipped with Cu Ka radiation at a scan rate of 2 °C $min^{-1}$ was used to identify the structures of the as-prepared $SnO_2$–PPy composites and the precursors. The weight ratio between $SnO_2$ and PPy was determined by thermogravimetric analysis (TGA) using a Mettler Toledo TGA/DSC1 between 40 °C and 800°C at a heating rate of 5 °C $min^{-1}$ in air. The valence state of Sn was evaluated by X-ray photoelectron spectroscopy (XPS) using a SPECS PHOIBOS 100 Analyzer equipped with a high-vacuum chamber with base pressure below $10^{-8}$ mbar, with the X-ray excitation generated by Al Ka radiation at the high voltage of 12 kV and power of 120 W. The data were analyzed with the Casa XPS 2.3.15 software package. All the spectra were calibrated by C1s = 284.6 eV. Field emission scanning electron microscopy (FESEM; JEOL JSM-7500FA) and high-resolution transmission electron microscopy (HRTEM; JEOL JSM-2010) were used to investigate the morphology of the samples.

## 5.2.4. Electrochemical Measurements

The electrochemical performance testing was carried out via 2032-type coin cells. The working electrode was prepared by preparing a slurry in the mass ratio of 80 wt% active material, 10 wt% Super-P (carbon black) and 10 wt% carboxymethyl cellulose (CMC) binder, and coating it on copper foil substrate. Then the electrode film was dried in a vacuum oven at 80 °C overnight. An electrolyte with 1.0 mol $L^{-1}$ $NaClO_4$ in an ethylene carbonate (EC)–diethyl carbonate (DEC) solution (1: 1 v/v), with 5 wt% addition of fluoroethylene carbonate (FEC), was used in this work. All the cells were assembled in a glove box filled with argon gas and measured at room temperature. Galvanostatic charge–discharge testing was carried out on a Land Test System with a cut-off voltage range from 0.01 to 1.5 V (vs. $Na/Na^+$) at different current densities. The capacities are calculated based on the weight of the composites. Cyclic voltammetry and electrochemical impedance measurements were conducted using a Biologic VMP-3 electrochemical workstation from to 2.5 V (vs. $Na/Na^+$) at a scan rate of 0.1 mV $s^{-1}$.

## 5.3. Results and Discussion

The XRD patterns of the PPy, $SnO_2$ particles, and the $SnO_2$–PPy-1 and $SnO_2$–PPy-2 composites are displayed in Fig.5.1a. The PPy spectrum reveals a clear broad peak at about 23.8° corresponding to its' amorphous nature, which is due to the scattering from PPy chains at the interplanar spacing.[31–33] The XRD pattern of the $SnO_2$ nanoparticles was characterized by several peaks which could be ascribed to the tetragonal $SnO_2$ structure (cassiterite, PDF no. 01-0625) without any impurity. These large peaks clearly demonstrated the formation of small $SnO_2$ particles with a nanocrystalline nature. From the XRD patterns of the obtained $SnO_2$–PPy-1 and $SnO_2$–PPy-2 composites, we find very similar broad peaks that could also be indexed to the tetragonal $SnO_2$ structure (cassiterite, PDF no. 01-0625). No other characteristic peaks can be seen, suggesting that the $SnO_2$ nanoparticles have covered the surfaces of the PPy.

For quantifying the amount of PPy in the $SnO_2$–PPy composites, thermogravimetric analysis (TGA) measurements were carried out in air. The TGA curves of pure PPy and its composites are shown in Fig.5.1b. It can also be seen that both pure PPy and its composites show weight loss in the temperature range of 250–650 °C, which is in accordance with the oxidation of PPy, although the temperatures at which weight loss ends in the three samples have some differences. For pure PPy and $SnO_2$–PPy-1, there was no difference. $SnO_2$–PPy-2 required a higher temperature to oxidize PPy compared to pure PPy. This phenomenon could be the result of the greater amount of $SnO_2$ loaded onto the PPy, which delayed the PPy oxidation process. After the initial oxidation of PPy, no further weight change was observed in the composites. Therefore, the weight change due to the oxidation of PPy can be directly converted into the amount of PPy in the $SnO_2$–PPy composites. Using this approach, we calculated that the amounts of PPy in the $SnO_2$–PPy-1 and $SnO_2$–PPy-2 composites were 61.4 wt% and, 38.4 wt%, respectively.

The Fourier transform infrared (FTIR) spectra of bare $SnO_2$, PPy, $SnO_2$–PPy-1, and $SnO_2$–PPy-2 are shown in Fig.5.1c. In the spectrum for $SnO_2$, a strong vibration around 609 $cm^{-1}$ is observed in the low wave number range, which is indexed to the antisymmetric Sn–O–Sn mode of tin oxide. In the spectrum for PPy, the band centered

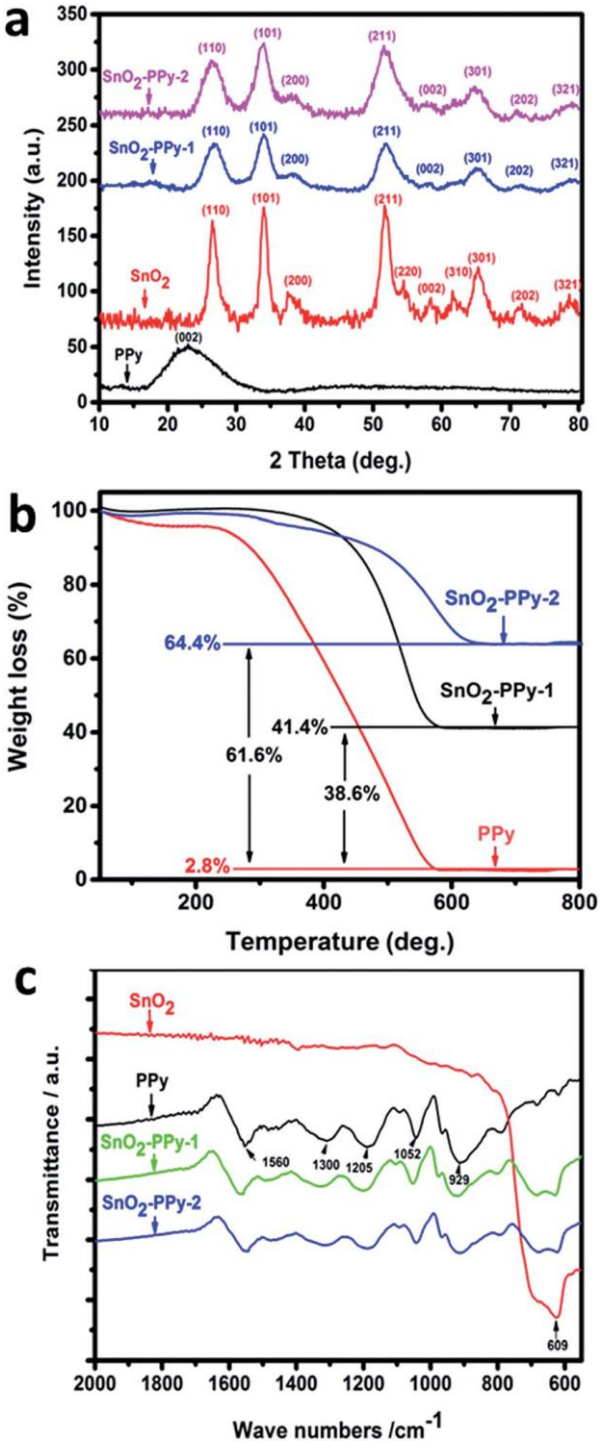


**Figure 5.1** XRD patterns (a), TGA curves (b) and FTIR spectra (c) of PPy, bare $SnO_2$ and $SnO_2$–PPy composite.

at 1560 $cm^{-1}$ corresponds to typical C=C in plane vibration, while the characteristic bands at 1300 and 1205 $cm^{-1}$ are connected with C–C and C–H ring stretching, respectively. The sharp peak at 1052 $cm^{-1}$ is ascribed to C–H in-plane vibrations. The

band at 929 $cm^{-1}$ can be attributed to N–H in-plane vibrations.[34] In the spectra of $SnO_2$–PPy-1 and $SnO_2$–PPy-2, all the characteristic bonds for both $SnO_2$ and PPy can be clearly observed. Therefore, the FTIR results confirm the presence of both PPy and $SnO_2$ in the $SnO_2$–PPy nanocomposites.

To investigate the interaction between the PPy, $SnO_2$ and $SnO_2$–PPy-2, X-ray photoelectron spectroscopy (XPS) was used to detect the chemical states of elements. Peaks for C, Sn, and O in $SnO_2$–PPy-2 were founded in the XPS survey spectrum, as shown in Fig.5. 2a. The $Sn_{3d}$ XPS spectra of $SnO_2$ and $SnO_2$–PPy-2 were collected to investigate the changes in the chemical state of tin before and after the hydrothermal reaction. In Fig.5.2b, for both materials, there are two peaks, and the binding energy interval between them is 8 eV, which is consistent with the energy splitting of Sn or $SnO_2$.[35] For bare $SnO_2$, the peaks found at 497.7 eV and 505.7 eV correspond to the $3d_{5/2}$ and $3d_{3/2}$ curves of Sn (IV) in $SnO_x$.[36,37] When $SnO_2$ is coated with PPy, $Sn_{3d}$ peaks are shifted towards lower binding energies, i.e., 486.9 eV and 494.9 eV. These differences in the peak locations are obviously induced by the presence of PPy, which is conductive, while the bare $SnO_2$ nanoparticles behave as an insulator in term of the XPS results.[23] In the $C_{1s}$ spectra for bare $SnO_2$ and $SnO_2$–PPy-2, there is no obvious peak change, which means the absence of C–Sn bonds. This result indicates that no chemical reaction occurred during the preparation and that the composite structure is held together by van der Waals forces.

The morphologies of PPy, bare $SnO_2$, $SnO_2$–PPy-1 and $SnO_2$–PPy-2 were characterized by scanning electron microscopy (SEM), as shown in Fig.5.3. The image of PPy shows a homogeneous morphology of strip-like 3-D structured tubes about 300–450 nm in diameter (Fig.5.3a and e). For $SnO_2$–PPy-1 and $SnO_2$–PPy-2, in Fig. 3b, c, f and g, the coarse surface can be clearly observed, with the diameters of the tubes apparently increased compared to PPy. There is not obvious difference in the shape of $SnO_2$–PPy-1 and $SnO_2$–PPy-2. Fig.5.3d and h show the bare $SnO_2$ nanoparticles at different magnifications. The size of the $SnO_2$ particles is similar to that in the composites. The uniformity of the material composition was also confirmed by energy dispersive X-ray spectroscopy (EDS) mapping, as illustrated in Fig.5.4. For the

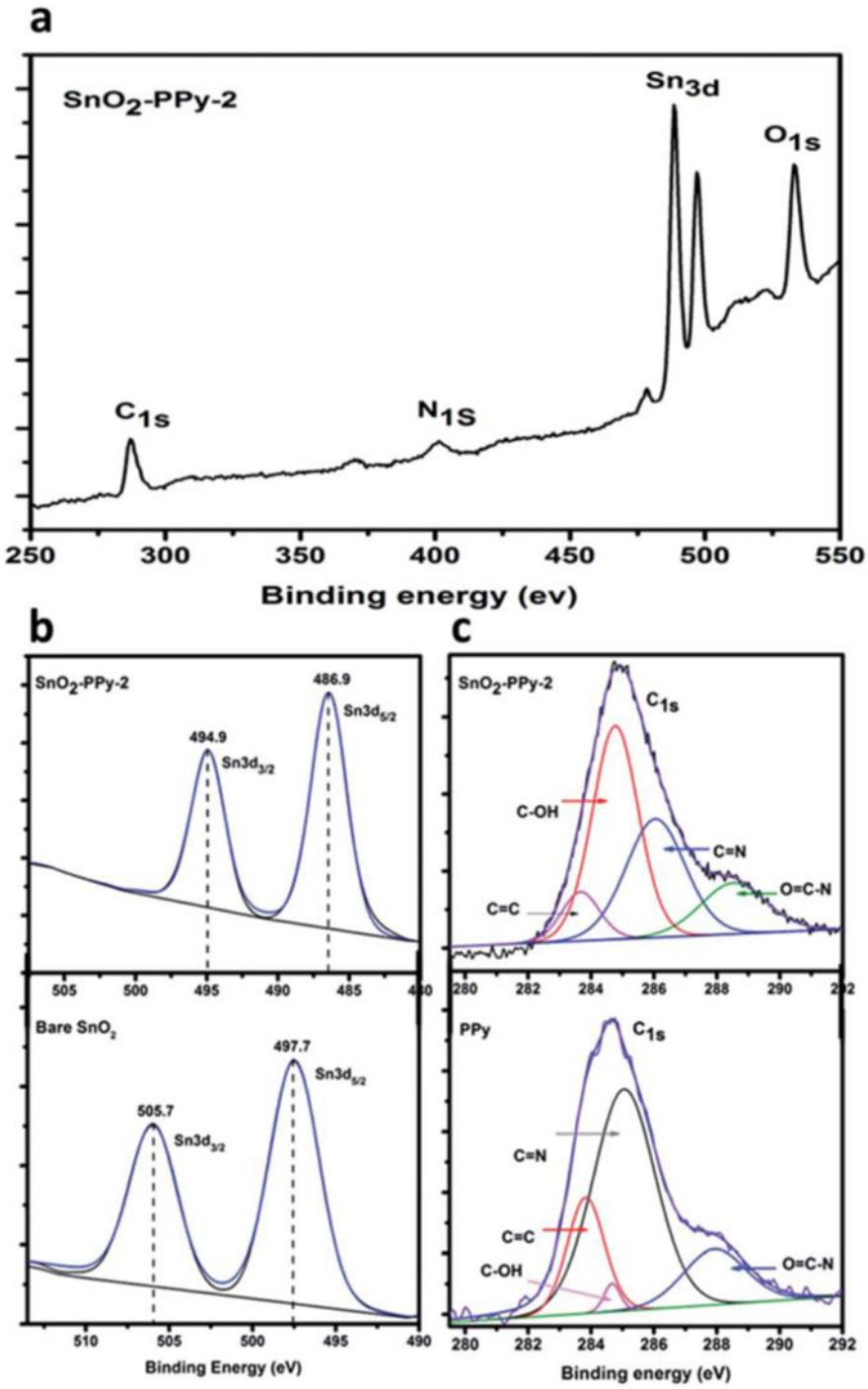


**Figure 5.2** XPS spectra: survey spectrum (a) for $SnO_2$–PPy-2 (PPy 38.4%) composite, and high-resolution spectra of $Sn_{3d}$ (b) for bare $SnO_2$ and $SnO_2$–PPy-2 composite, and $C_{1s}$ (c) for PPy and $SnO_2$–PPy-2 (PPy 38.4%) composite.

elemental mapping of Sn and O, the points clearly indicate that the $SnO_2$ was homogeneously distributed on the PPy tubes.

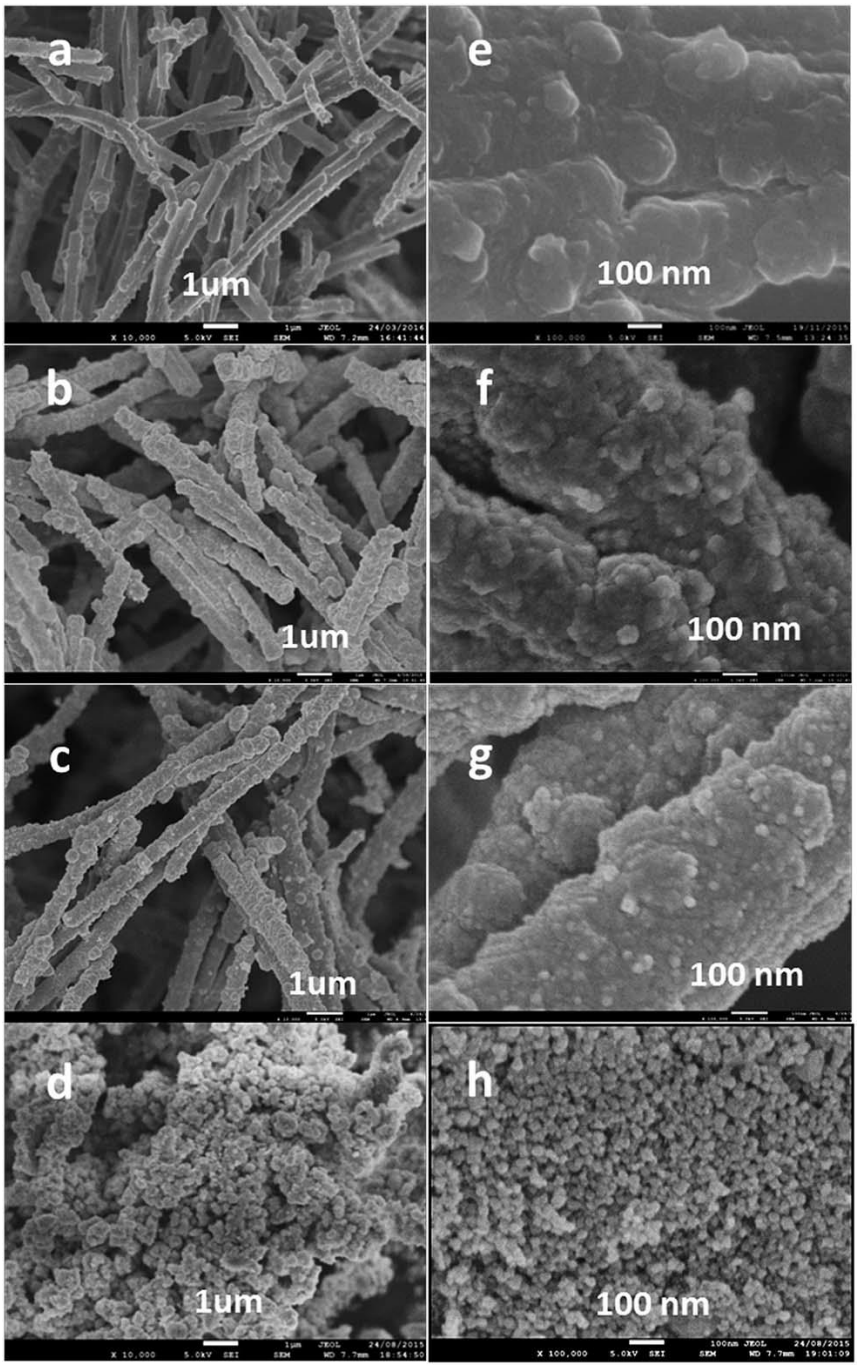


**Figure 5.3** SEM images at low magnification of PPy (a), $SnO_2$–PPy-1 (PPy 61.4%) (b), $SnO_2$–PPy-2 (PPy 38.4%) (c), and bare $SnO_2$ (d); and SEM images at high magnification of PPy (e), $SnO_2$–PPy-1 (PPy 61.4%) (f), $SnO_2$–PPy-2 (PPy 38.4%) (g), and bare $SnO_2$ (h).

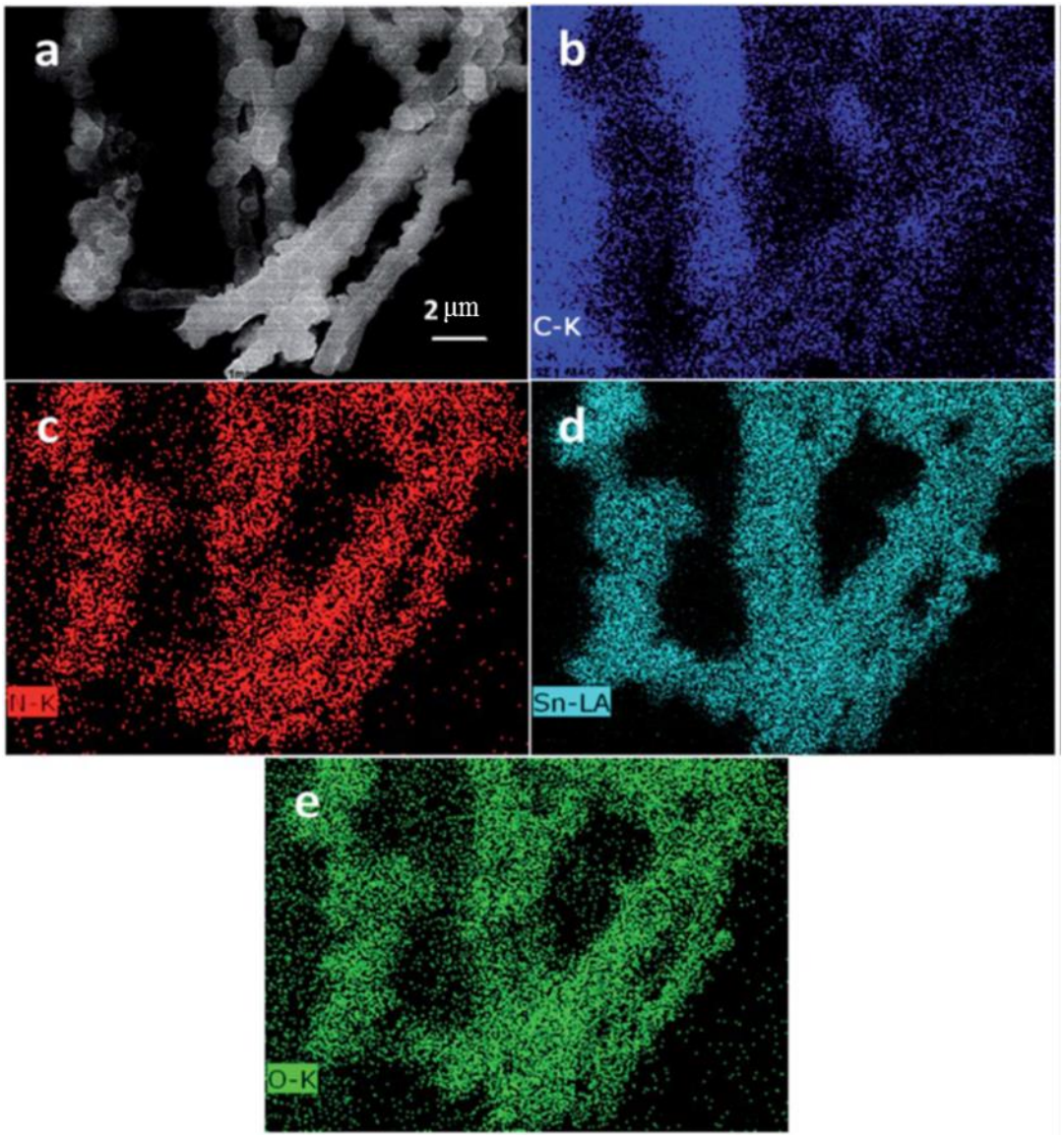


**Figure 5.4** Dark field image of $SnO_2$–PPy-2 (PPy 38.4%) (a), with corresponding EDS elemental mappings of C (b), N (c), Sn (d), and O (e).

Transmission electron microscopy (TEM) was further used to investigate the changes in structure between PPy and $SnO_2$–PPy-1, $SnO_2$–PPy-2 composites. As displayed in Fig.5.5a–c before coating with $SnO_2$, the diameter of PPy is less than 450 nm. The diameters of the tubes were significantly increased for the both composites, and the diameters are larger than 550 nm, Fig.5.5e and 5f all exhibit the (110) and (101) lattice fringes, which are found to reflect d-spacings of 0.343 and 0.263 nm, respectively. Meanwhile, the selected area electron diffraction (SAED) pattern (Fig.5.5d) is well

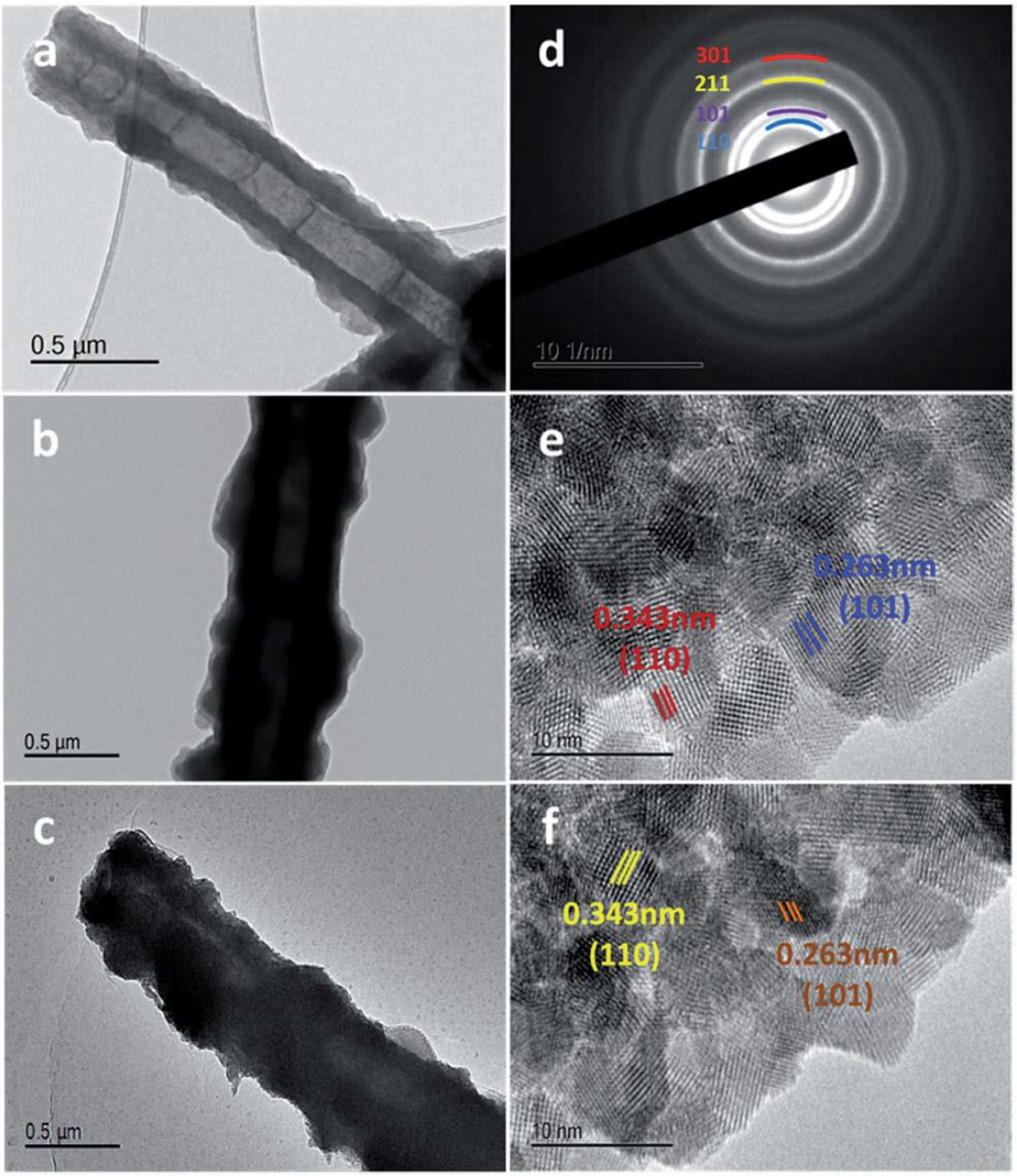


**Figure 5.5** TEM image of PPy (a), low magnification images of $SnO_2$–PPy-1 (PPy 61.4%) (b) and $SnO_2$–PPy-2 (PPy 38.4%) (c), SAED pattern of $SnO_2$–PPy-2 (PPy 38.4%) (d), high magnification images of $SnO_2$–PPy-1 (PPy 61.4%) (e) and $SnO_2$–PPy-2 (PPy 38.4%) (f).

ascribed to the pure phase of $SnO_2$, corresponding to the diffraction peaks of the (110), (101), (211), and (301) planes in the XRD pattern.

In addition, we used V-Sorb 2800P specific surface area analyser to measure the BET surface areas of PPy and composites. As shown on Table 5.1, the specific surface area of PPy tubes is only 12.65 $m^2\ g^{-1}$. After loading $SnO_2$ on it, the specific surface areas of $SnO_2$–PPy-1 and $SnO_2$–PPy-2 composites increased to 44.04 $m^2\ g^{-1}$ and 48.32 $m^2\ g^{-1}$ respectively, due to the $SnO_2$ nanoparticles were loaded on the tubes. For composites, the average pore size which represents the size of pores formed by $SnO_2$ nanoparticles. These pores provide the path to accommodate to the insertion/extraction of sodium ions. As for $SnO_2$–PPy-2, its surface area is bigger than $SnO_2$–PPy-1. This can be inferred to the more content of $SnO_2$ in $SnO_2$–PPy-2.

The capacity and coulombic efficiency of the $SnO_2$–PPy-1 and, $SnO_2$–PPy-2 composites as a function of cycle number, at a constant current density of 100 mA $g^{-1}$ with a cut-off voltage range from 0.01 to 1.5 V (vs. $Na/Na^+$), are presented in Fig.5.6a over 150 cycles. To clarify the contribution of the PPy matrix and the bare $SnO_2$ to the electrochemical performance of the $SnO_2$–PPy composites, they were also tested under the same current and voltage conditions. The reversible charge capacity of the $SnO_2$–PPy-2 composite is about 288 mA h $g^{-1}$ after 150 cycles, corresponding to 69.1% of the initial charge capacity. Even though the reversible charge capacity (246.2 mA h $g^{-1}$) of the $SnO_2$–PPy-1 composite is relatively lower than that of the $SnO_2$– PPy-2 due to the lower content of $SnO_2$, the capacity retention of 74.2% is higher than for $SnO_2$–PPy-2. This indicates that a smaller amount of $SnO_2$ nanoparticles can decrease the agglomeration of bare $SnO_2$. The reversible charge capacity is much lower than that of $SnO_2$–PPy-2, however, and the capacity fading is apparent. The contribution of PPy to the capacity of the $SnO_2$–PPy composites can be neglected.

**Table 5.1** Key pore characteristics of PPy, $SnO_2$–PPy-1 and $SnO_2$–PPy-2

| Material | Surface area ($m^2\ g^{-1}$) | Pore volume ($cm^3\ g^{-1}$) | Average pore size (nm) |
|---|---|---|---|
| PPy | 12.65 | 0.899 | 116.68 |
| $SnO_2$–PPy-1 | 44.04 | 0.332 | 97.01 |
| $SnO_2$–PPy-2 | 48.32 | 0.302 | 95.27 |

The coulombic efficiency for both $SnO_2$–PPy-1 and $SnO_2$–PPy-2 is near 100%, beginning from the second cycle, indicating that electrons/Na ions are no longer trapped in secondary parasitic reactions that can be introduced by further electrolyte degradation. The stable electrochemical performance of the $SnO_2$–PPy composite and the enhanced capacity benefit from the synergetic effects generated by $SnO_2$ particles on the PPy framework.[23] This promotes greater conductivity of the $SnO_2$ particles in the case of $SnO_2$–PPy than in the case of nano-$SnO_2$, as suggested by the XPS results (Fig.5. 2b).

In addition, the charge/discharge rate capability of the $SnO_2$, $SnO_2$–PPy-1 and $SnO_2$–PPy-2 composites were investigated at increasing current rates by progressively increasing the current rate from 50 mA $g^{-1}$ up to 1 A $g^{-1}$ and finally returning it to 100 mA $g^{-1}$, in order to test the robustness of the samples. Fig.5.6b shows the cycling performances of the samples under these different current rate conditions. In the case of $SnO_2$–PPy-2, the reversible charge capacity of the composite decreases from 428.7 (50 mA $g^{-1}$), to 400.2 (0.1 A $g^{-1}$), 354.2 (0.2 A $g^{-1}$), 290.1 (0.4 A $g^{-1}$), 260.2 (0.8 A $g^{-1}$), and 160.3 mA h $g^{-1}$ (1 A $g^{-1}$), respectively, and the composite was found to successfully return to 398.9 mA h $g^{-1}$ (recovering 99.7% of its initial capacity) after 60 cycles when the current density was returned to 0.1 A $g^{-1}$. The rate capability of $SnO_2$–PPy-1 shows lower reversible charge capacity compared to $SnO_2$–PPy-2. This result is due to the few cycling in rate capability test for two samples, the good capacity retention of $SnO_2$ – PPy-1 can not display. As for the bare $SnO_2$, we can find this trend that with the increasing of current density, the capacity degraded more severely compared to both composites. Fig.5.6c and d show the discharge–charge voltage profiles of the initial three cycles for $SnO_2$–PPy-2 and bare $SnO_2$. The 1st cycle discharge and 2nd cycle charge capacities of $SnO_2$–PPy-2 composite electrode are 1040.6 and 416.6 mA h $g^{-1}$, respectively, giving an initial coulombic efficiency of 40%. This is due to the formation of an irreversible solid electrolyte interphase (SEI) layer on the electrode surface and irreversible Na insertion into the active materials. The initial discharge–charge voltage profiles for bare $SnO_2$ display the 1st cycle discharge capacity of 1217.3 mA h $g^{-1}$ and the 2nd cycle charge capacity of 300.2 mA h $g^{-1}$, giving a much lower initial coulombic efficiency of 24.7%. The electrochemical reactions of the $SnO_2$–PPy-2 nanocomposites

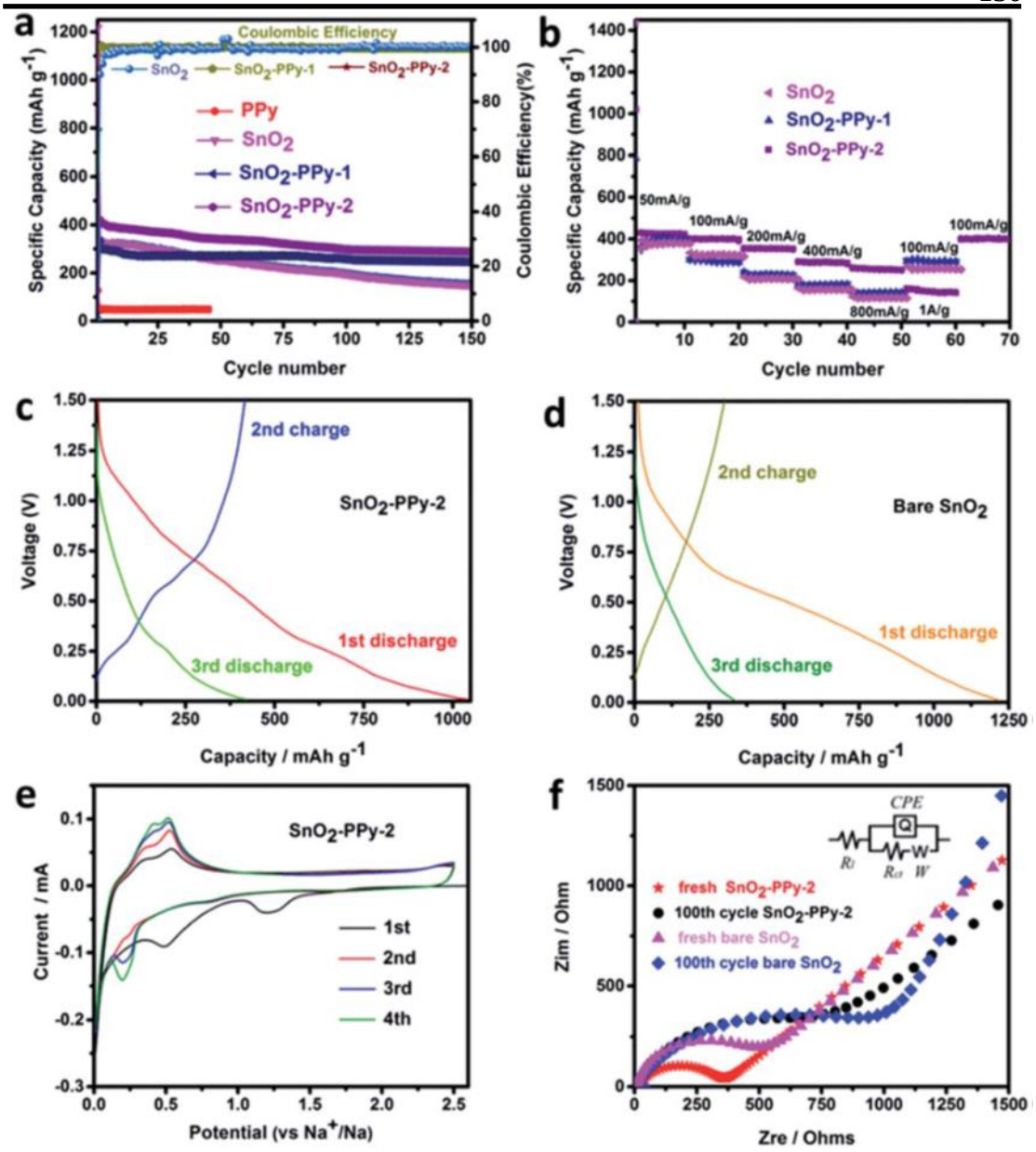


**Figure 5.6** Cycling performances (a) of $SnO_2$–PPy-1 (PPy 61.4%), $SnO_2$–PPy-2 (PPy 38.4%), bare PPy, and $SnO_2$. Rate capability (b) of $SnO_2$–PPy-1 (PPy 61.4%), $SnO_2$–PPy-2 (PPy 38.4%) and bare $SnO_2$. Charge–discharge profiles for the first 3 cycles of $SnO_2$–PPy-2 (PPy 38.4%) (c) and bare $SnO_2$ (d). Cyclic voltammetry curves for the first 4 cycles of $SnO_2$–PPy-2 (PPy 38.4%) (e). Nyquist plots and equivalent circuit model inset) of $SnO_2$–PPy-2 (PPy 38.4%) and bare $SnO_2$ (f) for the fresh electrodes and after 100 cycles.

were studied by cyclic voltammetry (CV). As shown in Fig.5.6e, there is an irreversible transformation of $SnO_2$ into Sn in the initial discharge process. Weak and irreversible shoulder peaks are seen at 1.4 and 0.6 V in the first negative scan. These peaks are attributed to some irreversible decomposition of the electrolyte, which forms a (SEI) film on the surface of the $SnO_2$–PPy-2 composite, and to irreversible reactions between $Na^+$ and the active materials. Two reductive peaks are observed at 0.28 and 0.02 V in the following cycles with different intensities, which are in accordance with the transformation of Sn into $Na_xSn$ alloys. In conformity with the Na–Sn binary alloy phase diagrams and previous reports,[11,38] a-NaSn, $Na_9Sn_4$, $Na_3Sn$, and $Na_{15}Sn_4$ are the main stable phases. It can be inferred that the reductive peak located at 0.28 V is related to the formation of a two-phase alloy of a-NaSn and $Na_9Sn_4$. Another reductive peak positioned at around 0.02 V is considered to be due to the formation of single phase $Na_3Sn$ and $Na_{15}Sn_4$. In the reverse positive scan, two oxidative peaks are obviously observed at approximately 0.28 V and 0.5 V, which indicates that the phase transitions during the de-alloying process had become clear. A hump that appeared at 0.28 V can be mainly assigned to the dealloying reactions of $Na_3Sn$, and $Na_{15}Sn_4$. The peak at 0.5 V is due to the $Na_9Sn_4$ de-alloying reactions.[39]

To verify the effects of PPy towards improving the cyclability of $SnO_2$–PPy-2 electrode, which had better electronic conductivity compared to the bare $SnO_2$ electrode. Electrochemical impedance spectroscopy (EIS) measurement was carried out. The Nyquist plots and the fitting model using an equivalent circuit are depicted in Fig.5.6f, with the equivalent circuit as the inset. Where $R_i$ represents the total resistance of the electrolyte, separator, and electrical contacts. The charge transfer resistance ($R_{ct}$) can be calculated from the semicircle within the high frequency region, which reflects the impedance related to the sodium ion transport through the film surface and charge transfer between the electrode/electrolyte interfaces. The Warburg impedance ($W$) is observed from the inclined line in the low frequency region and represents the charge transfer by sodium ion diffusion through the material or electrolyte. The constant phase element (CPE) in the equivalent circuit is used to simulate an ideal capacitance. It can be observed that the sizes of the depressed semicircles for bare $SnO_2$ in the fresh

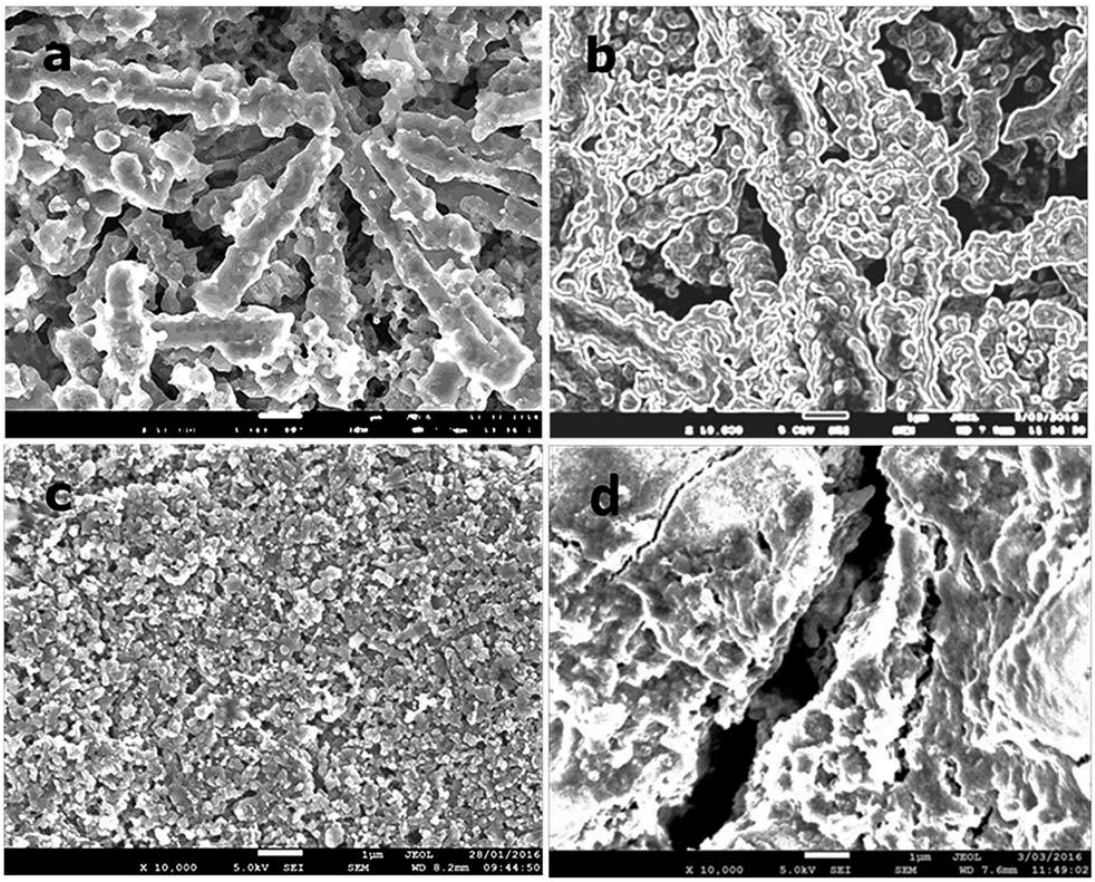


**Figure 5.7** SEM images of the $SnO_2$–PPy-2 (PPy 38.4%) composite electrodes before the Na-storage test (a) and after 100 cycles (b), and of bare $SnO_2$ before the Na-storage test (c) and after 100 cycles (d). Scale bar = 1 mm.

electrode and after 100 cycles have changed significantly, which indicates that the charge transfer resistance ($R_{ct}$) has increased from 494.8 to 898.57 Ω. For $SnO_2$–PPy-2, from the fresh cell to after 100 cycles, $R_{ct}$ of the electrode changed from 358.05 to 715.98 Ω, respectively. This implies that the electronic conductivity of the $SnO_2$–PPy-2 sample was enhanced and benefited from the good electrical conductivity of the PPy in the composite, where it serves as both an active material and a conductor. The morphology of bare $SnO_2$ electrode after cycling shows very obvious cracks (Fig.5.7d). No cracks were observed for the $SnO_2$–PPy-2 composite electrode after cycling (Fig.5.7b), which is attributed to the $SnO_2$–PPy-2 3-D structure with void space between the tubes, which could accommodate large volume changes during cycling. Furthermore, the homogeneous distribution of $SnO_2$ nanoparticles on the PPy tube network is the key

factor that provides the balancing force over the whole composite electrode and enhances the long-term electrochemical properties. These results are in good agreement with the EIS conclusions.

## 5.4. Conclusion

$SnO_2$ nanoparticles were successfully coated on the surfaces of a PPy nanotube network via a simple, convenient, and environmentally friendly method. The obtained 3-D structured $SnO_2$–PPy nanotube network demonstrates good performance as an anode for application in SIBs, especially with regards to the cyclability (over 150 cycles), with a high coulombic efficiency of 99.6% and good rate capability, recovering up to 99.7% of the initial charge capacity after several current variation cycles from 50 mA $g^{-1}$ to 1 A $g^{-1}$. These outcomes are attributed to the uniform coating of nanoscale tin dioxide particles on the PPy matrix with unique 3-D structure, which can significantly improve electronic conductivity of composites and acts as a buffer to alleviate the strain resulting from the volume changes in the electrodes during the cycling. At the same time, the diffusion speed of sodium ions is accelerated. On the other hand, a positive synergetic effect between the PPy interfaces and the $SnO_2$ particles is responsible for maximization of the $SnO_2$ conductivity. This is confirmed by the highly uniform distribution of particles. It is further demonstrated by the inferior performance of bare $SnO_2$ particles with similar particle size. Accordingly, the results clearly demonstrate that the coated $SnO_2$ particles on the PPy tubes generate synergetic effects during the cycling, enabling PPy to act as a conductor, which maximizes its utilization during nsertion/extraction.

## 5.5. References

1. Ponrouch, A.; Marchante, E.; Courty, M.; Tarascon, J.-M.; Palacin, M. R., In search of an optimized electrolyte for Na-ion batteries. *Energy Environ. Sci.* **2012,** *5* (9), 8572-8583.

2. Li, Y.; Xu, S.; Wu, X.; Yu, J.; Wang, Y.; Hu, Y.-S.; Li, H.; Chen, L.; Huang, X., Amorphous monodispersed hard carbon micro-spherules derived from biomass as a

high performance negative electrode material for sodium-ion batteries. *J. Mater. Chem. A* **2015,** *3* (1), 71-77.

3. Wang, Y.-X.; Chou, S.-L.; Liu, H.-K.; Dou, S.-X., Reduced graphene oxide with superior cycling stability and rate capability for sodium storage. *Carbon* **2013,** *57*, 202-208.

4. Wang, H. g.; Wu, Z.; Meng, F. l.; Ma, D. l.; Huang, X. l.; Wang, L. m.; Zhang, X. b., Nitrogen-Doped Porous Carbon Nanosheets as Low-Cost, High-Performance Anode Material for Sodium-Ion Batteries. *ChemSusChem* **2013,** *6* (1), 56-60.

5. Fu, L.; Tang, K.; Song, K.; van Aken, P. A.; Yu, Y.; Maier, J., Nitrogen doped porous carbon fibres as anode materials for sodium ion batteries with excellent rate performance. *Nanoscale* **2014,** *6* (3), 1384-1389.

6. Fan, J. M.; Chen, J. J.; Zhang, Q.; Chen, B. B.; Zang, J.; Zheng, M. S.; Dong, Q. F., An Amorphous Carbon Nitride Composite Derived from ZIF-8 as Anode Material for Sodium-Ion Batteries. *ChemSusChem* **2015,** *8* (11), 1856-1861.

7. Senguttuvan, P.; Rousse, G.; Seznec, V.; Tarascon, J.-M.; Palacin, M. R., Na2Ti3O7: lowest voltage ever reported oxide insertion electrode for sodium ion batteries. *Chemistry of Materials* **2011,** *23* (18), 4109-4111.

8. Alcántara, R.; Jaraba, M.; Lavela, P.; Tirado, J., $NiCo_2O_4$ spinel: First report on a transition metal oxide for the negative electrode of sodium-ion batteries. *Chemistry of Materials* **2002,** *14* (7), 2847-2848.

9. Sun, Q.; Ren, Q.-Q.; Li, H.; Fu, Z.-W., High capacity Sb 2 O 4 thin film electrodes for rechargeable sodium battery. *Electrochem. Commun.* **2011,** *13* (12), 1462-1464.

10. Xiong, H.; Slater, M. D.; Balasubramanian, M.; Johnson, C. S.; Rajh, T., Amorphous TiO2 nanotube anode for rechargeable sodium ion batteries. *J. Phys. Chem. Lett.* **2011,** *2* (20), 2560-2565.

11. Xiao, L.; Cao, Y.; Xiao, J.; Wang, W.; Kovarik, L.; Nie, Z.; Liu, J., High capacity, reversible alloying reactions in SnSb/C nanocomposites for Na-ion battery applications. *Chem. Commun.* **2012,** *48* (27), 3321-3323.

12. Yabuuchi, N.; Kubota, K.; Dahbi, M.; Komaba, S., Research development on sodium-ion batteries. *Chem. Rev.* **2014,** *114* (23), 11636-11682.

13. Gu, M.; Kushima, A.; Shao, Y.; Zhang, J.-G.; Liu, J.; Browning, N. D.; Li, J.; Wang, C., Probing the failure mechanism of SnO2 nanowires for sodium-ion batteries. *Nano Lett.* **2013,** *13* (11), 5203-5211.

14. Su, D.; Wang, C.; Ahn, H.; Wang, G., Octahedral tin dioxide nanocrystals as high capacity anode materials for Na-ion batteries. *Physical Chemistry Chemical Physics* **2013,** *15* (30), 12543-12550.

15. Meng, X.; Zhong, Y.; Sun, Y.; Banis, M. N.; Li, R.; Sun, X., Nitrogen-doped carbon nanotubes coated by atomic layer deposited SnO 2 with controlled morphology and phase. *Carbon* **2011,** *49* (4), 1133-1144.

16. Wang, Y.; Su, D.; Wang, C.; Wang, G., $SnO_2$@ MWCNT nanocomposite as a high capacity anode material for sodium-ion batteries. *Electrochem. Commun.* **2013,** *29*, 8-11.

17. Su, D.; Ahn, H.-J.; Wang, G., $SnO_2$@ graphene nanocomposites as anode materials for Na-ion batteries with superior electrochemical performance. *Chem. Commun.* **2013,** *49* (30), 3131-3133.

18. Zhang, Y.; Xie, J.; Zhang, S.; Zhu, P.; Cao, G.; Zhao, X., Ultrafine tin oxide on reduced graphene oxide as high-performance anode for sodium-ion batteries. *Electrochim. Acta* **2015,** *151*, 8-15.

19. Kalubarme, R. S.; Lee, J.-Y.; Park, C.-J., Carbon encapsulated tin oxide nanocomposites: an efficient anode for high performance sodium-ion batteries. *ACS Appl. Mater. Interfaces* **2015,** *7* (31), 17226-17237.

20. Dirican, M.; Lu, Y.; Ge, Y.; Yildiz, O.; Zhang, X., Carbon-confined SnO2-electrodeposited porous carbon nanofiber composite as high-capacity sodium-ion battery anode material. *ACS Appl. Mater. Interfaces* **2015,** *7* (33), 18387-18396.

21. Pei, L.; Jin, Q.; Zhu, Z.; Zhao, Q.; Liang, J.; Chen, J., Ice-templated preparation and sodium storage of ultrasmall SnO2 nanoparticles embedded in three-dimensional graphene. *Nano Research* **2015,** *8* (1), 184-192.

22. Wang, Y.-X.; Lim, Y.-G.; Park, M.-S.; Chou, S.-L.; Kim, J. H.; Liu, H.-K.; Dou, S.-X.; Kim, Y.-J., Ultrafine SnO 2 nanoparticle loading onto reduced graphene oxide as anodes for sodium-ion batteries with superior rate and cycling performances. *J. Mater. Chem. A* **2014,** *2* (2), 529-534.

23. Jahel, A.; Ghimbeu, C. M.; Darwiche, A.; Vidal, L.; Hajjar-Garreau, S.; Vix-Guterl, C.; Monconduit, L., Exceptionally highly performing Na-ion battery anode using crystalline SnO 2 nanoparticles confined in mesoporous carbon. *J. Mater. Chem. A* **2015,** *3* (22), 11960-11969.

24. Yuan, L.; Wang, J.; Chew, S. Y.; Chen, J.; Guo, Z.; Zhao, L.; Konstantinov, K.; Liu, H.-K., Synthesis and characterization of SnO 2–polypyrrole composite for lithium-ion battery. *J. Power Sources* **2007,** *174* (2), 1183-1187.

25. Cui, L.; Shen, J.; Cheng, F.; Tao, Z.; Chen, J., SnO 2 nanoparticles@ polypyrrole nanowires composite as anode materials for rechargeable lithium-ion batteries. *J. Power Sources* **2011,** *196* (4), 2195-2201.

26. Chou, S.-L.; Gao, X.-W.; Wang, J.-Z.; Wexler, D.; Wang, Z.-X.; Chen, L.-Q.; Liu, H.-K., Tin/polypyrrole composite anode using sodium carboxymethyl cellulose binder for lithium-ion batteries. *Dalton Transactions* **2011,** *40* (48), 12801-12807.

27. Gao, X.; Luo, W.; Zhong, C.; Wexler, D.; Chou, S.-L.; Liu, H.-K.; Shi, Z.; Chen, G.; Ozawa, K.; Wang, J.-Z., Novel germanium/polypyrrole composite for high power lithium-ion batteries. *Scientific reports* **2014,** *4*, 6095.

28. Zhao, Y.; Li, J.; Wang, N.; Wu, C.; Dong, G.; Guan, L., Fully reversible conversion between SnO2 and Sn in SWNTs@ SnO2@ PPy coaxial nanocable as high performance anode material for lithium ion batteries. *J. Phys. Chem. C* **2012,** *116* (35), 18612-18617.

29. Du, X.; Yang, T.; Lin, J.; Feng, T.; Zhu, J.; Lu, L.; Xu, Y.; Wang, J., Microwave-assisted synthesis of SnO2@ polypyrrole nanotubes and their pyrolyzed composite as anode for lithium-ion batteries. *ACS Appl. Mater. Interfaces* **2016,** *8* (24), 15598-15606.

30. Yang, X.; Zhu, Z.; Dai, T.; Lu, Y., Facile Fabrication of Functional Polypyrrole Nanotubes via a Reactive Self-Degraded Template. *Macromol. Rapid Commun.* **2005,** *26* (21), 1736-1740.

31. Chougule, M. A.; Pawar, S. G.; Godse, P. R.; Mulik, R. N.; Sen, S.; Patil, V. B., Synthesis and characterization of polypyrrole (PPy) thin films. *Soft Nanoscience Letters* **2011,** *1* (01), 6.

32. Sakthivel, S.; Boopathi, A., Synthesis and study of polypyrrole thin films by SILAR method. *JOURNAL OF CHEMISTRY* **2014,** *4* (3), 144-149.

33. Ouyang, J.; Li, Y., Great improvement of polypyrrole films prepared electrochemically from aqueous solutions by adding nonaphenol polyethyleneoxy (10) ether. *Polymer* **1997,** *38* (15), 3997-3999.

34. Cho, G.; Fung, B. M.; Glatzhofer, D. T.; Lee, J.-S.; Shul, Y.-G., Preparation and characterization of polypyrrole-coated nanosized novel ceramics. *Langmuir* **2001,** *17* (2), 456-461.

35. Park, M.-S.; Kang, Y.-M.; Kim, J.-H.; Wang, G.-X.; Dou, S.-X.; Liu, H.-K., Effects of low-temperature carbon encapsulation on the electrochemical performance of SnO 2 nanopowders. *Carbon* **2008,** *46* (1), 35-40.

36. Briggs, D., Auger and X-ray photoelectron spectroscopy. *Practical Surface Analysis.* **1983,** *1*, Chapter 9.

37. Wagner, C.; Riggs, W.; Davis, L.; Moulder, J.; Muilenberg, G., Handbook of X-ray Photoelectron Spectroscopy (Perkin-Elmer, 1979). *and 78*, 48.

38. Liu, Y.; Xu, Y.; Zhu, Y.; Culver, J. N.; Lundgren, C. A.; Xu, K.; Wang, C., Tin-coated viral nanoforests as sodium-ion battery anodes. *Acs Nano* **2013,** *7* (4), 3627-3634.

39. Qian, J.; Chen, Y.; Wu, L.; Cao, Y.; Ai, X.; Yang, H., High capacity Na-storage and superior cyclability of nanocomposite Sb/C anode for Na-ion batteries. *Chem. Commun.* **2012,** *48* (56), 7070-7072.

# Chapter 6

# Carbon Encapsulated Sn@N-doped Carbon Nanotubes as Anode Materials for Application in SIBs

## 6.1. Introduction

For exploring rational anode materials for SIBs, Many alloying materials have been attracting wide attentions, because they can store a large number of sodium ions in the host structure with a relatively low operating potential leading a high specific capacity during the electrochemical insertion/extraction reaction .[1,2,3] In particular, metallic Sn, with the theoretical capacity of 847 mA h $g^{-1}$ based on the alloying/dealloying mechanism ($Na_{15}Sn_4$)[4-7] has been considered to be a prospective anode material for SIBs. Pure Sn can only achieve very poor cycling performance, however, with dramatic capacity decline over only a few cycles owing to the issue of pulverization.[4] It would thus be a good idea to encapsulate Sn in a confined volume with enough space for volume expansion during Na insertion to avoid pulverization. Generally, it is more convenient to prepare $SnO_2$ nanoparticles than to obtain metallic Sn nanoparticles directly. Additionally, $SnO_2$ can be reduced to metallic Sn by hydrogen reduction at high temperature under an inert atmosphere, and it has unique structures. Many strategies have been employed to alleviate the volume expansion,[8,9] such as depositing Sn film on hierarchical wood fibers, which displayed stable cycling performance for 400 cycles with an initial capacity of 339 mAh $g^{-1}$,[10] using carbonized filter paper decorated with Sn@C nanospheres, which showed a high and stable capacity of 550 μAh $cm^{-2}$ over 100 cycles at 50 mA $cm^{-2}$,[11] and using ultra-small Sn nanoparticles

embedded in carbon, which achieved a high-rate capacity of 349 mAh $g^{-1}$, even at 4000 mA $g^{-1}$, and a stable capacity of ≅ 415 mAh $g^{-1}$ after 500 cycles at 1000 mA $g^{-1}$.[12]

N-doped submicron diameter carbon tubes derived from polypyrrole (PPy) precursor represent a very promising functional material. They have many advantages, especially due to the effects of heteroatom defects. The nitrogen species which they contain can promote pseudo-capacitive mutual effects between the nitrogen-containing functional groups and the electrolyte ions, in these respects as boosting surface wettability, electronic conductivity, capacity, etc. From another aspect, N-doped carbon tubes with three-dimensional (3-D) structure as a matrix not only provide effective transport pathways for charge carriers to shorten ion/electron diffusion distances and good structural robustness to relieve electrode collapse due to the huge volume changes during cycling, but also enhance the diffusion of electrolyte into interior space in the composite to facilitate the interfacial reactions, as well as providing adequate access for fast $Na^+$ transport.

There are some reports that make use of N-doped carbon as a conducting polymer and mechanical buffer to enhance the electrochemical properties of carbon-based Na-storage anodes.[13-16] Coating Sn nanoparticles onto N-doped carbon tubes to fabricate Sn-based anode material for SIBs has not yet been reported. Here, I report a user-friendly hydrothermal method taking N-doped carbon tubes as the matrix to anchor the Sn nanoparticles onto its surfaces and obtain C@Sn@N-doped carbon nanotube composites. In the first step, the precursor $SnO_2$@N-doped carbon was obtained via a hydrothermal approach. In the as-prepared product, $SnO_2$ nanoparticles were loaded homogeneously on the N-doped carbon framework. Next, resorcinol-formaldehyde resin as carbon source was deposited on the surface of the $SnO_2$@N-doped carbon and, then pyrolyzed to finish the carbon coating process. Here, the coated carbon can play two roles. Firstly, it can play the role of a dispersing agent to prevent the agglomeration of Sn nanoparticles, when $SnO_2$ is reduced by $H_2$. On the other hand, it provides a good tensile force to alleviate the volume expansion of Sn nanoparticles during continuous sodiation/desodiation processes, thereby helping to improve the cycling stability. In the composites, the surfaces of N-doped carbon nanotubes are covered with evenly distributed carbon-coated Sn nanoparticles. The obtained 3-D C@Sn@N-doped carbon

tube network displayed the good reversible capacity of 398.4 mAh $g^{-1}$ on discharging at 100 mA $g^{-1}$ with capacity retention of 67.3 % and very high Coulombic efficiency of 99.7% after 150 cycles. Meanwhile, good rate capability was also obtained, based on varying the current density from 50 mA $g^{-1}$ to 2 A $g^{-1}$ during cycling.

## 6.2. Experimental Section

### 6.2.1. Synthesis of N-doped carbon tubes

The N-doped carbon tubes were prepared by pyrolyzing the precursor polypyrrole (PPy). The synthesis of PPy was carried out by the method in a previous report [17] with some modifications. Firstly, 65 mg methyl orange (MO) was dissolved in 100 ml deionized water, and then 1.25 g of $FeCl_3$ was added into the solution under constant stirring. Subsequently, an obvious flocculent precipitate appeared. Then, 0.3 g of pyrrole monomer was added into the mixture, which was stirred overnight in ambient air. After that, the PPy precipitate was centrifuged with distilled water and ethanol, up to the filter liquor was colorless and neutral. Soon afterwards, the precipitate was placed in a ceramic boat and moved into a tube furnace. The tube was heated to 100 °C at a heating rate of 2°C/min under argon atmosphere and kept at that temperature for 8 h. Then, the tube was heated to 600 °C with a heating rate of 5 °C/min and maintained at that temperature for 4 h. Finally, the N-doped carbon tubes were obtained.

### 6.2.2. Making of $SnO_2$@N-doped carbon composites

In a typical procedure, 0.1 g N-doped carbon was dispersed into 30 ml of ethanol undergoing ultrasonic processing for 0.5 h. Then, 0.025 g urea and 0.03 g hexamethylenetetramine (HMTA) were added into this solution under continued ultrasonic treatment for 15 min. Subsequently, 0.1g $SnCl_2{\bullet}2H_2O$ was put into the before-mentioned mixture and stirred for 0.5h. Then, the miscible liquid was transferred into a Teflon-lined autoclave. Where it was quickly heated to 120 °C and kept at that temperature for 10 h. The autoclave was naturally cooled down to the ambient temperature, and deionized water and ethanol were employed to wash the precipitate several times. The precipitate was dried in a vacuum oven at 60 °C overnight, and the final product (denoted as $SnO_2$@N-doped carbon-I) was obtained. $SnO_2$@N-doped

carbon-II and $SnO_2$@N-doped carbon-III were prepared by adjusting the weight of $SnCl_2$•$2H_2O$ to 0.15 g or 0.2 g, respectively.

### 6.2.3. Fabrication of C@Sn@N-doped carbon nanocomposites

0.1 g of $SnO_2$@N-doped carbon-I was dispersed in 50 ml deionized water under stirring. 5 mg of cetyl-trimethylammonium bromide (CTAB) along with 0.5 ml of $NH_3$•$H_2O$, 28% solution, were added to the first solution and vigorously stirred for 20 mins. Next, 80 μL formaldehyde solution (37% wt% in $H_2O$) and 60 mg resorcinol were put into the solution and stirred overnight. After that, the precipitate was centrifuged and washed with ethanol three times. The precipitate was then moved into a tube furnace for carbonization. The sample was heated to 350 °C with a heating rate of 1 °/min under $N_2$ atmosphere and kept at that temperature for 2 h, then heated to 600 °C for 4 h with the same heating rate. When the temperature was cooled down to 550 °C at the end of the 4h, the protection gas was changed to 5% Ar/$H_2$, and the sample was kept under those conditions for 2 h. Then, the final composite (denoted as C@Sn@N-doped carbon-I) was collected when the temperature of the tube furnace was reduced to room temperature. C@Sn@N-doped carbon-II and C@Sn@N-doped carbon-III were also prepared from the $SnO_2$@N-doped carbon-II or $SnO_2$@N-doped carbon-III by the same procedure, respectively. The above preparation processes are clearly displayed in Scheme 6.1.

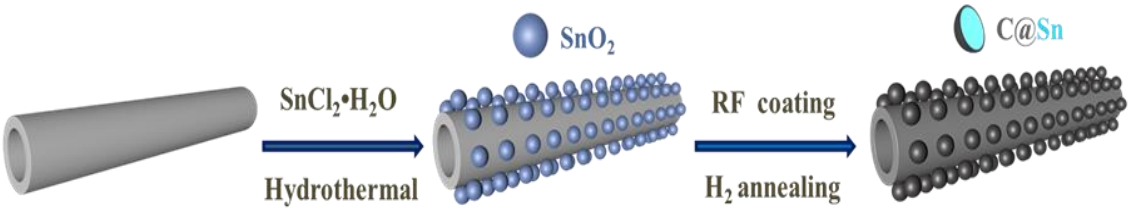


**Scheme 6.1** Schematic illustration of the synthesis processes for the fabrication of C@Sn@N-doped carbon.

### 6.2.4. Materials Characterization

X-ray powder diffraction (XRD; GBC MMA), with the diffractometer configured with Cu Kα radiation at a scanning speed of 2° $min^{-1}$, was used to evaluate the structural changes between the precursors and the as-prepared C@Sn@N-doped carbon composites. The content of Sn in the composites was measured through thermogravimetric analysis (TGA; Mettler Toledo TGA/DSC) carried out from 50 °C to 800 °C at a heating rate of 5 °C $min^{-1}$ in air. X-ray photoelectron spectroscopy (XPS; SPECS PHOIBOS 100 Analyzer), using the spectrometer installed in a high-vacuum chamber with the base pressure below $10^{-8}$ mbar, and the X-ray excitation generated by Al Kα radiation at the high voltage of 12 kV and power of 120 W was employed to identify the valence state of the Sn in the composites. The Casa XPS 2.3.15 software package was used to analyze the data obtained. All spectra were calibrated by $C_{1s}$ = 284.6 eV. The morphology of the samples was surveyed by field emission scanning electron microscopy (FESEM; JEOL JSM-7500FA) and high-resolution transmission electron microscopy (HRTEM; JEOL JSM-2010).

## 6.2.5. Electrochemical Measurements

C@Sn@N-doped carbon composite (80 wt%) was mixed with acetylene black (10 wt%) and carboxymethyl cellulose binder (10 wt%) to prepare the working electrode slurry. The slurry was casted onto copper foil substrates, followed by drying in a vacuum oven overnight at 80 °C. The mass loading of the active material in the electrode film was about 1.2 mg $cm^{-2}$. 1 M $NaClO_4$ dissolved in a solution of ethylene carbonate (EC) and dimethyl carbonate (DEC) (1:1 v/v) containing 5% (by weight) addition of fluoroethylene carbonate (FEC) served as electrolyte. The electrochemical performance testing was carried out via 2032-type coin cells. All the cells were assembled in an argon-filled glove box and measured under ambient conditions. Galvanostatic charge–discharge measurements were carried out via a Land Test System in the cut-off voltage range of 0.01-1.5 V (vs. $Na/Na^+$) at current density of 100 mA $g^{-1}$. The capacity was calculated based on the weight of the whole composite. Cyclic voltammetry and electrochemical impedance testing were carried out via a Biologic VMP-3 electrochemical workstation in the voltage range of 0.005 V-2.5 V (vs. $Na/Na^+$) with a scanning rate of 0.1 mV $s^{-1}$**.** Electrochemical impedance spectroscopy (EIS) was conducted using a CHI 660B electrochemical workstation.

## 6.3. Results and Discussion

The successful preparation of the C@Sn@N-doped carbon nanocomposites is evidenced by XRD (Fig.6.1a). The XRD pattern of N-doped carbon shows a diffraction peak at 24.5°, reflecting to *d*-spacing of 0.36 nm, which comes close to 0.34 nm, i.e., the $d_{002}$ plane spacing in graphite.[18] The XRD pattern of pure Sn is characterized by several peaks that can be assigned to β-metallic Sn with a tetragonal structure (JCPDS card no. 04-0673). In the three composites, C@Sn@N-doped carbon-I, C@Sn@N-doped carbon-II, and C@Sn@N-doped carbon-III, we find that the sharp diffraction peaks appear in the same positions as for pure Sn. Meanwhile, the characteristic peak of N-doped carbon is no longer visible, which could be attributed to the Sn nanoparticles that cover the surfaces of N-doped carbon.

To quantify the amount of Sn in the C@Sn@N-doped carbon composites, thermogravimetric analysis (TGA) was conducted in air. From the TGA curves shown in Fig.1b and 1c, it can be found that pure Sn shows a weight increase of 126.95%, which is very consistent with the following reaction: $Sn + O_2 \longrightarrow SnO_2$. The N-doped carbon was easily burned out, and only 1.8% residue was left. This amount could be neglected in determining the Sn content of the composites. From the curves of the three composites shown in Fig.6.1c, we find that all the samples display weight loss in the temperature range from 300 to 550 °C, which is in conformity with the oxidation of N-doped carbon. There were some differences between the composites and the N-doped carbon in the starting temperature of the weight loss. This phenomenon could be due to the large amount of Sn loaded onto the N-doped carbon, which postponed the N-doped carbon oxidation process. From 550°C onwards, the weight increase began, which meant that the oxidation of Sn occurred simultaneously. Based on the results of Fig.6.1b, we calculated that the amounts of Sn in C@Sn@N-doped carbon-I, C@Sn@N-doped carbon-II, and C@Sn@N-doped carbon-III % were 50.3%, 62.6%, and 70.7%, respectively.

To measure the interactions among the N-doped carbon, the Sn, and the C@Sn@N-doped carbon, the chemical status of elements was analysed via X-ray photoelectron spectroscopy (XPS). By comparing Fig.6.2a and 6.2e, we can find an obvious change in the Sn peak from N-doped carbon to the composites. All the peaks for C, N, and Sn in

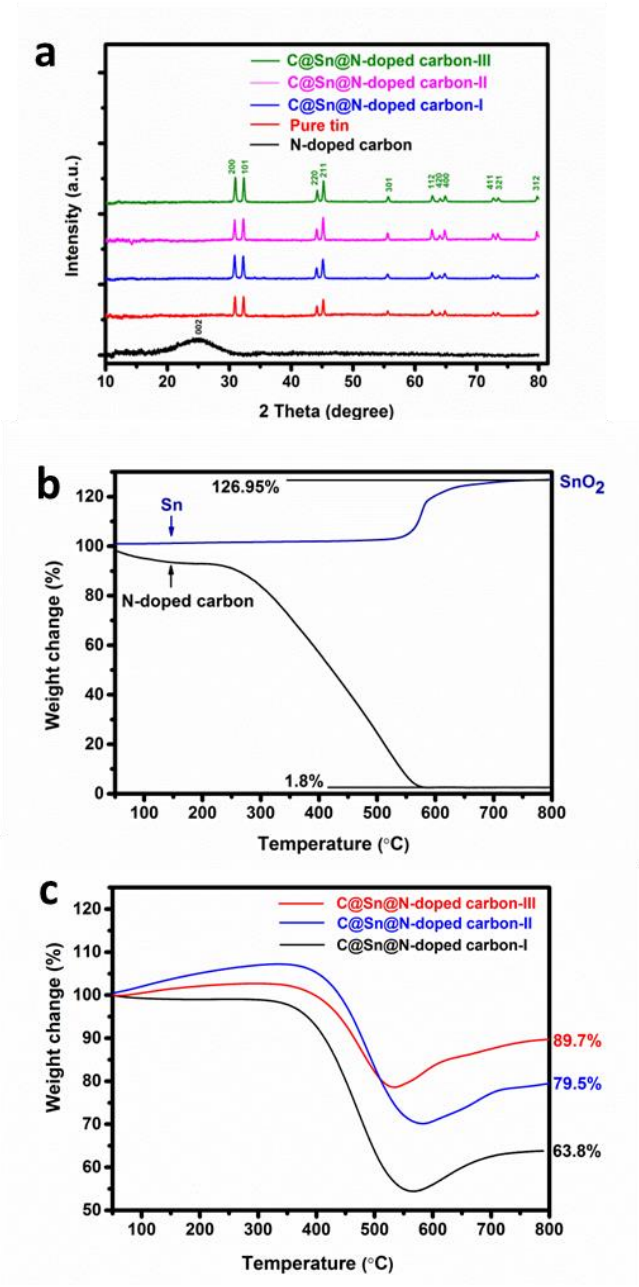


**Figure 6.1** XRD patterns of all three samples along with pure tin and N-doped carbon (a). TGA curves of pure Sn particles and N-doped carbon in air (b), and of C@Sn@N-doped carbon composites in air (c).

C@Sn@N-doped carbon-II appear in the XPS survey spectrum. The $Sn_{3d}$ XPS spectrum of Sn and C@Sn@N-doped carbon-II were obtained to analyse the change in the chemical state of Sn before and after reduction.

In Fig. 6.2c and 6.2g, by comparing the positions of the two peaks for $Sn_{3d}$ for pure Sn and the composite, it is clear that they all display the same binding energy interval of

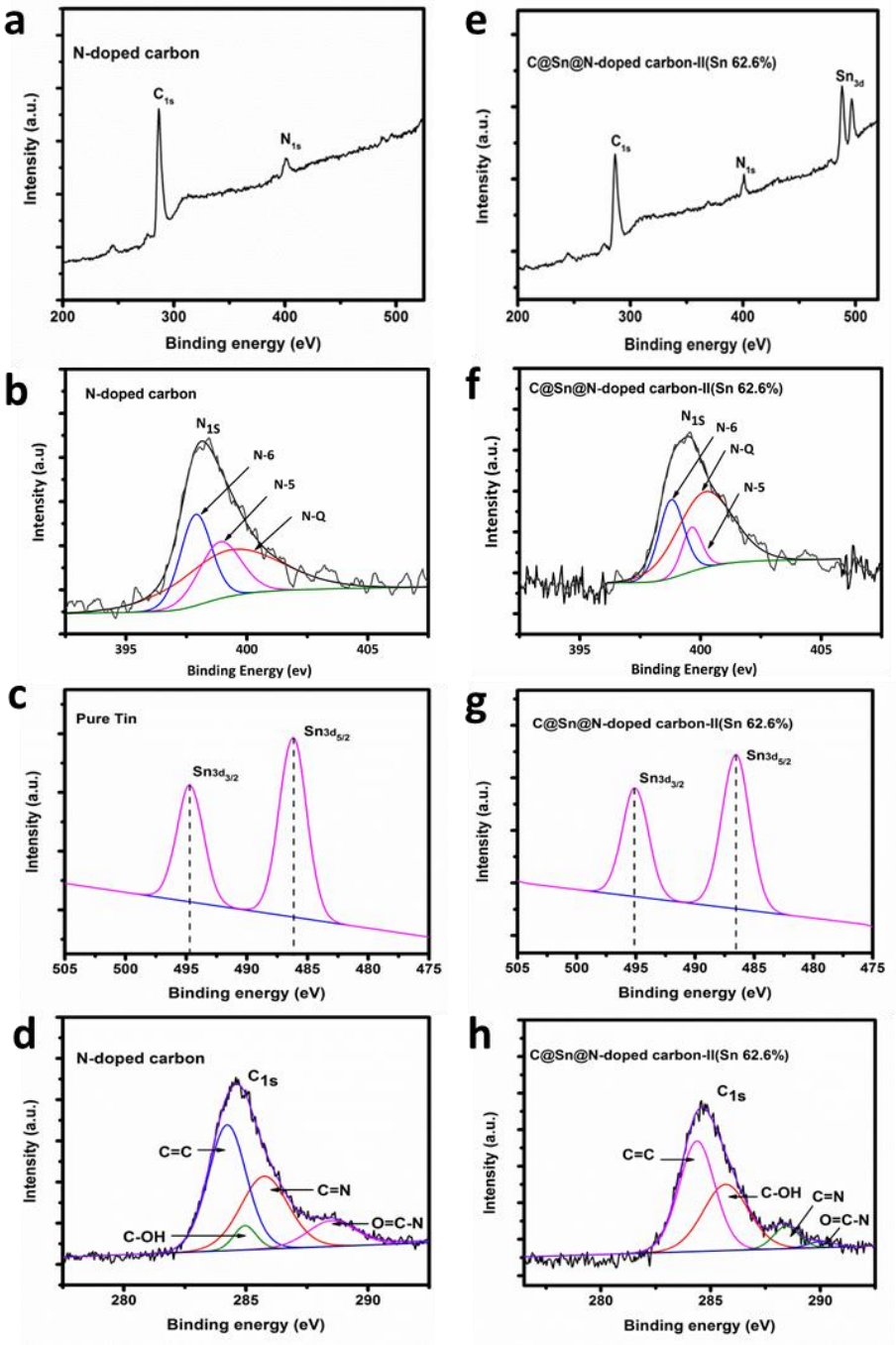


**Figure 6.2** XPS survey spectra: (a) N-doped carbon, (e) C@Sn@N-doped carbon-II (Sn 62.6%); XPS high resolution spectra: (b) $N_{1s}$ for N-doped carbon, (f) $N_{1s}$ for C@Sn@N-doped carbon-II (Sn 62.6%), (c) $Sn_{3d}$ for pure Sn, (g) $Sn_{3d}$ for C@Sn@N-doped carbon-II (Sn 62.6%). (d) $C_{1s}$ for N-doped carbon, (h) $C_{1s}$ for C@Sn@N-doped carbon-II (Sn62.6%).

8 eV, which is in accordance with the energy splitting of Sn.[19] For bare Sn, the peaks found at 485.9 eV and 494.9 eV correspond to the $3d_{5/2}$ and $3d_{3/2}$ peaks of Sn.[20] When

Sn was coated with N-doped carbon, the $Sn_{3d}$ peaks were shifted to higher binding energies, i.e., 486.3 eV and 495.3 eV. These changes in the peak positions were obviously affected by the presence of N-doped carbon, and in terms of conductivity, the bare Sn is better than the N-doped carbon.[21,22] In the $C_{1s}$ spectra for N-doped carbon (Fig.6.2d) and C@Sn@N-doped carbon-II (Fig.6.2h), no new peaks appeared, which means that C–Sn bonds do not exist. These spectra also showed that the peaks corresponding to C=N, C-OH, O=C-N in $C_{1s}$ from N-doped carbon to C@Sn@N-doped carbon-II shifting to higher binder energy. There also showed the peaks corresponding to C=N, C-OH, and O=C-N in $C_{1s}$ were shifted to higher binding energy from N-doped carbon to C@Sn@N-doped carbon-II. This was mainly because when C@Sn particles were coated with N-doped carbon, the electronic conductivity of the C@Sn@N-doped carbon-II was lower than that of the N-doped carbon shown on Fig.6.6f. Similar phenomena can be found in a previous report.[21] From the $N_{1s}$ spectrum for N-doped carbon (Fig.6.2b) and C@Sn@N-doped carbon-II (Fig.6.2f), we can see that pyridinic (N-6), pyrrolic/pyridone (N-5), and quaternary (N-Q) nitrogen are all present. Table 6.1 displays the content ratio changes for pyridinic N, pyrrolic N, and quaternary N from N-doped carbon to C@Sn@N-doped carbon respectively. These results reveal that no chemical reaction took place in the synthesis process and that all components are bound together by van der Waals forces.

**Table 6.1** Nitrogen configurations derived from peak analysis of N 1s in N-doped carbon and C@Sn@N-doped carbon (Sn 62.6%)

| Sample | Quaternary % | Pyrrolic % | Pyridinic % |
|---|---|---|---|
| N-doped carbon | 52.32 | 28.31 | 19.37 |
| C@Sn@N-doped carbon-II (Sn 62.6%) | 56.26 | 20.13 | 23.61 |

The morphology changes from N-doped carbon to the precursor $SnO_2$@N-doped carbon composites were investigated by scanning electron microscopy (SEM). The image of N-doped carbon shows strip-like 3-D structured tubes with relatively smooth surfaces in Fig.6.3a and 6.3b. For $SnO_2$@N-doped carbon-I, $SnO_2$@N-doped carbon-II, and $SnO_2$@N-doped carbon-III, in Fig.6.3c, 6.3e, and 6.3g, rough surfaces can be easily found, and the diameter of the composite tubes has obviously increased compared with N-doped carbon. These images clearly demonstrate that the $SnO_2$ nanoparticles are uniformly distributed on the N-doped carbon tubes.

Fig.6.3 also displays the differences in morphology between $SnO_2$@N-doped carbon and C@Sn@N-doped carbon composites. By comparing the images shown in Fig.6.3d, 6.3f, and 6.3h, we can find that after the resorcinol-formaldehyde (RF) coating and the carbonization in the following reduction, the surface of the C@Sn@ N-doped carbon composite has become much smoother than for the precursor $SnO_2$@N-doped carbon. This phenomenon is due to the very small carbon nanoparticles covering the surfaces of the Sn particles. The size of the carbon particles is much smaller than that of the $SnO_2$ particles.

The homogeneity of the element composition was also measured by energy dispersive X-ray spectroscopy (EDS) mapping. From the elemental mapping images of C, N, and Sn as displayed in Fig.6.4, it can be clearly observed that there is a uniform distribution of Sn on the N-doped carbon tubes.

The changes in the structure between the N-doped carbon and the C@Sn@N–doped carbon composites were further investigated by using transmission electron microscopy (TEM). As displayed in Fig.6.5a, the N-doped carbon tube is open on one end and sealed on the other end. This property is beneficial for stable anchoring of the Sn particles on the tube. Before the coating with Sn, the diameter of the N-doped carbon tubes was no greater than 300 nm. From the images of the three composites (Fig.6.5b, 6.5c, and 6.5d), obvious changes in the diameter of the tubes can be observed. The diameters for the three samples were significantly increased to about 350 nm, 470 nm, and 640 nm, respectively. Fig. 5e shows the (200) and (301) lattice fringes, which were measured to have spacing of 0.29 and 0.165 nm, respectively. Furthermore, pure phase Sn can be identified on the selected area electron diffraction (SAED) pattern (Fig.6.5f),

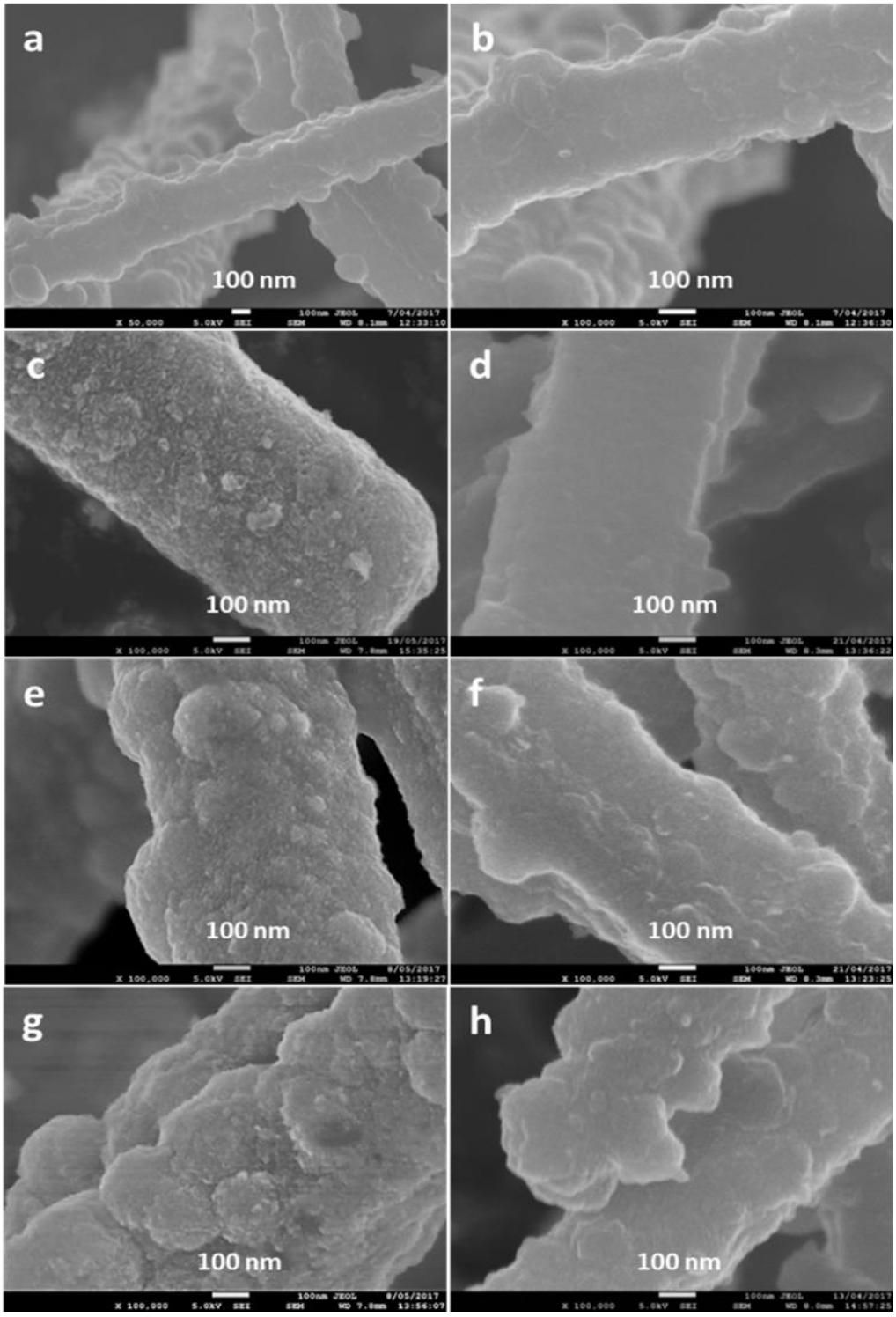


**Figure 6.3** SEM images of (a,b) N-doped carbon at different magnifications, (c) $SnO_2$@N-doped carbon-I, (d) C@Sn@N-doped carbon-I (Sn 50.3%), (e) $SnO_2$@N-doped carbon-II, (f) C@Sn@N-doped carbon-II (Sn 62.6%), (g) $SnO_2$@N-doped carbon-III, (h) C@Sn@N-doped carbon-III (Sn70.7%).

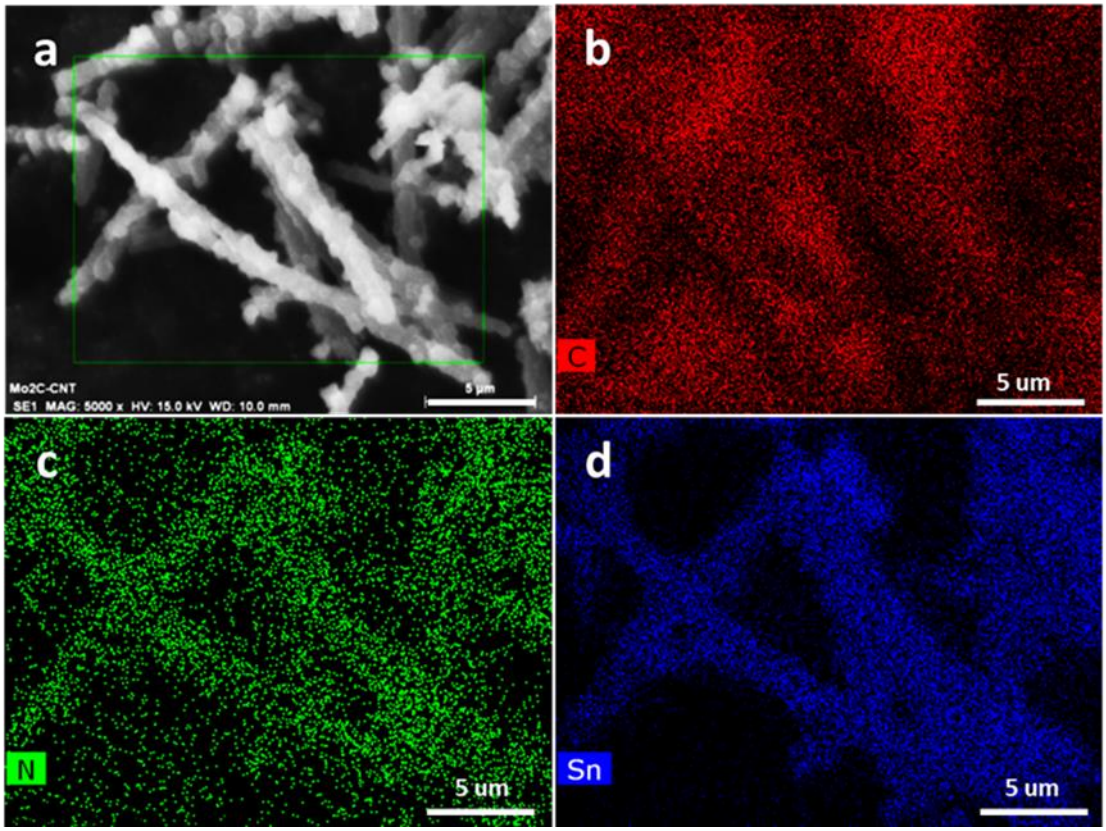


**Figure 6.4** Dark field image of C@Sn@N-doped carbon-II (Sn 62.6%) (a), corresponding EDS mappings of C (b), N (c), and Sn (d) in C@Sn@N-doped carbon-II (Sn 62.6%).

which is indexed to the diffraction peaks of the (200), and (301) planes as shown on the XRD patterns.

The cycling performances of the C@Sn@N-doped carbon-I, C@Sn@N-doped carbon-II, and C@Sn@N-doped carbon-III composites at a current density of 100 mA $g^{-1}$, within a cut-off voltage range of 0.01-1.5 V (vs. $Na/Na^{+}$) over 150 cycles, are displayed in Fig.6.6a. The reversible charge capacities of the C@Sn@N-doped carbon-I, C@Sn@N-doped carbon-II, and C@Sn@N-doped carbon-III composites are 303.5, 398.4, and 340 mAh $g^{-1}$, respectively, after 150 cycles, corresponding to 55.8%, 67.3%, and 50.3% of their initial charge capacities. From this trend, we can find that C@Sn@N-doped carbon-II has the best reversible charge capacity and capacity retention. In the case of C@Sn@N-doped carbon-I, due to the lesser amount of Sn, the charge capacity is the smallest, but its capacity retention is higher than that of C@Sn@N-doped carbon-III. As for C@Sn@N-doped carbon-III, even though it has the

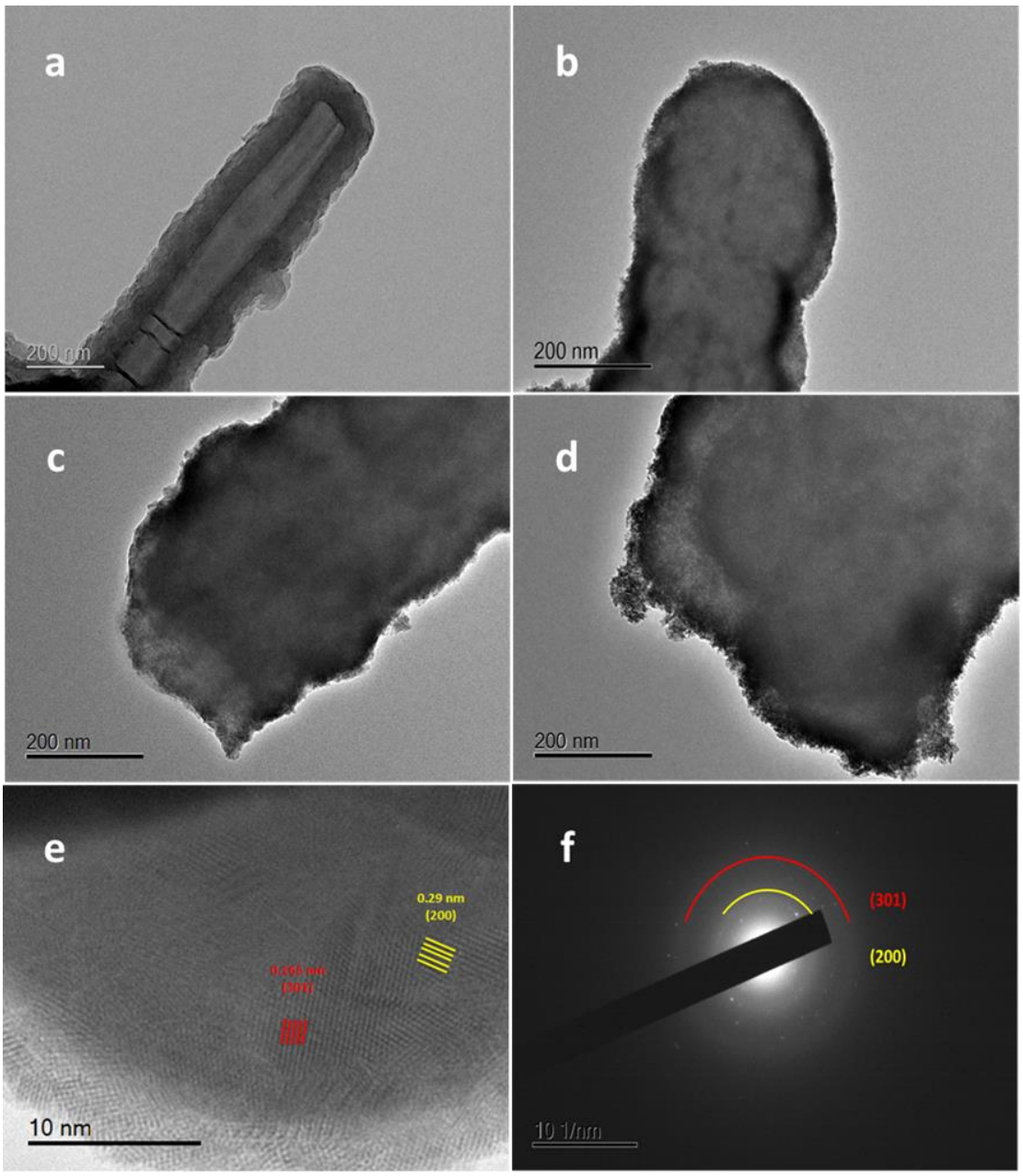


**Figure 6.5** TEM image of N-doped carbon tube (a), low magnification TEM images of C@Sn@N-doped carbon-I (Sn 50.3%) (b), C@Sn@N-doped carbon-II (Sn 62.6%) (c), C@Sn@N-doped carbon-III (Sn 70.7%) (d), high magnification image (e) and SAED pattern (f) of C@Sn@N-doped carbon-II (Sn 62.6%).

biggest amount of Sn and the highest initial charge capacity, the capacity fading is apparent. This phenomenon can be attributed to the agglomeration caused by the presence of more Sn particles. In this regard, the coating carbon and the N-doped carbon

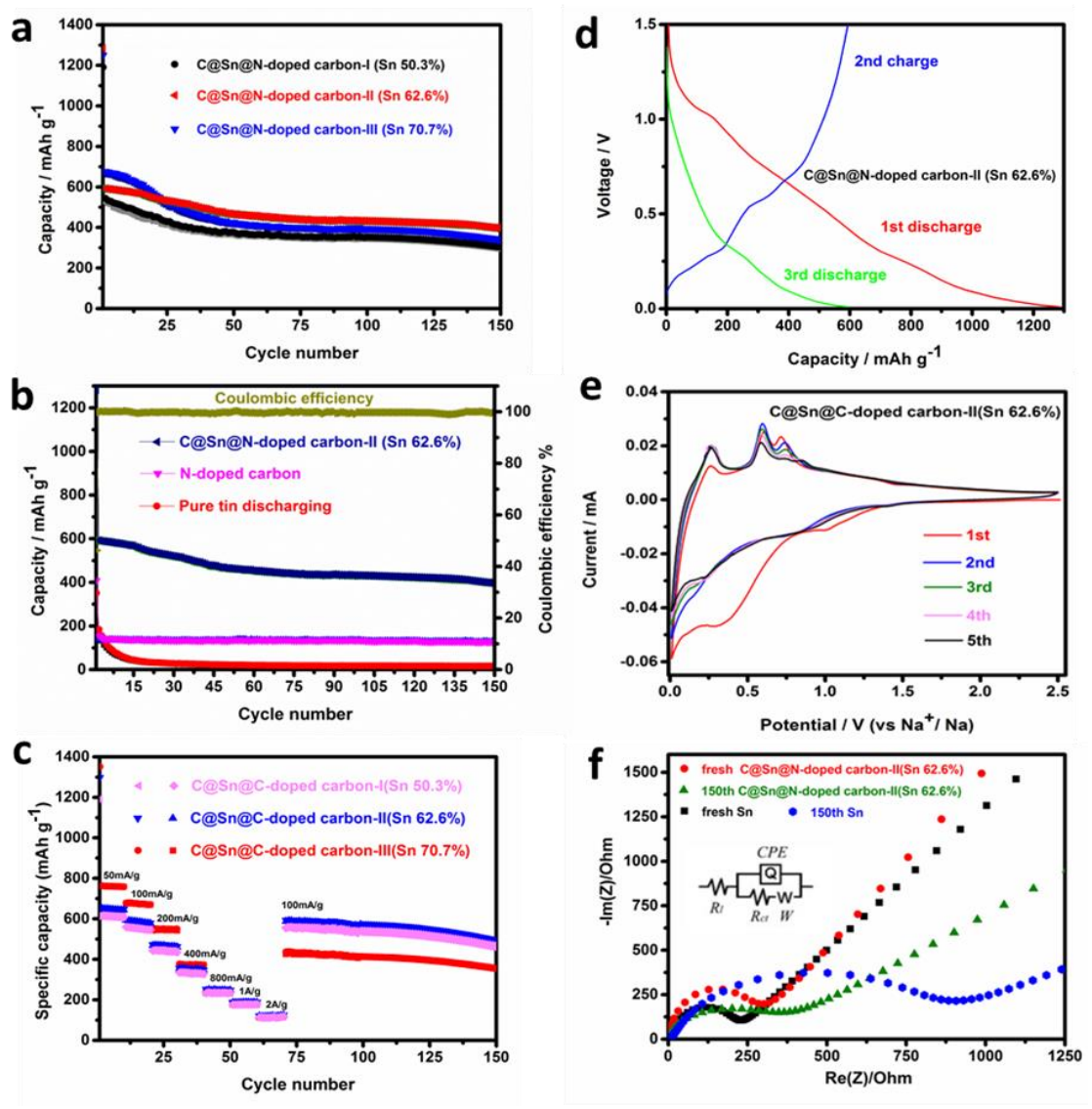


**Figure 6.6** Cycling performances of the C@Sn@N-doped carbon composites (a); Cycling performance comparison of C@Sn@N-doped carbon-II (Sn 62.6%), N-doped carbon, and pure Sn particles (b); Rate capability of C@Sn@N-doped carbon composites (c); Charge-discharge curves for the first 3 half cycles of C@Sn@N-doped carbon-II (Sn 62.6%)(d); Cyclic voltammograms for the first 5 cycles of C@Sn@N-doped carbon-II (Sn 62.6%) (e); Impedance plots of fresh N-doped carbon, C@Sn@N-doped carbon-II (Sn 62.6%), and bare Sn particle electrodes, and plots after 150 cycles. Inset is the equivalent circuit model for the analysis (f).

also take on indispensable roles. First, the coating carbon layer can hold back the agglomeration of Sn nanoparticles and provide a good tensile force to alleviate the

volume expansion of Sn nanoparticles during the continuous sodiation/desodiation processes. On the other hand, the N-doped carbon matrix, due to its porous structure with large surface area ensures the uniform dispersion of Sn nanoparticles. At the same time, N-doped carbon with its 3-D structure also provides short ion/electron pathways to promote the diffusion of the $Na^+$ ion into the internal spaces of the composites. Furthermore, the good structural robustness of N-doped carbon is very useful for accommodating the huge volume changes in the charging/discharging process and mitigating the pulverization of the electrode. Therefore, the best reversible charge capacity and capacity retention come from the optimum ratio of Sn with respect to the carbon layer and N-doped carbon.

To distinguish the contributions of the N-doped carbon substrate and the bare Sn to the electrochemical properties of the C@Sn@N-doped carbon composites, the three samples were also tested with the same current density and cut-off voltage, as shown in Fig.6.6b. The preserved capacity of the N-doped carbon was about 125.6 mA h $g^{-1}$ after 150 cycles. The contribution of pure Sn particles to the capacity of the C@Sn@N-doped carbon composites can be neglected due to their strong agglomeration during cycling. In Fig.6.6b, we also find that the coulombic efficiency for C@Sn@N-doped carbon-II is close to 100%, starting from the second cycle, demonstrating that electrons/Na ions were no longer being captured in parasitic reactions, which could be maintained by further electrolyte degeneration.

Furthermore, the rate capabilities of the C@Sn@N-doped carbon-I, C@Sn@N-doped carbon-II, and C@Sn@N-doped carbon-III composites were investigated by augmenting the current density step by step from 50 mA $g^{-1}$ up to 2 A $g^{-1}$ and finally returning to 100 mA $g^{-1}$. The cycling performances of all the composites with different current densities are shown in Fig.6.6c. In the case of C@Sn@N-doped carbon-I, the reversible charge capacity decreased from 610.6 (50 mA $g^{-1}$), to 546.2 (0.1A $g^{-1}$), 437.2 (0.2 A $g^{-1}$), 327.3 (0.4 A $g^{-1}$), 233.6 (0.8 A $g^{-1}$), 177.4 (1 A $g^{-1}$), and 117.1 mAh $g^{-1}$ (2 A $g^{-1}$), respectively, and then it increased to 559.1 mAh $g^{-1}$ (recovering 99.9 % of its initial capacity) after 70 cycles when the current density was returned to 0.1 A $g^{-1}$. The rate capability of C@Sn@N-doped carbon-II displayed the highest reversible charge capacity among the composites. The values changed according to the following trend,

647.2 (50 mA $g^{-1}$), to 579 (0.1 A $g^{-1}$), 463.4 (0.2 A $g^{-1}$), 347 (0.4 A $g^{-1}$), 247.6 (0.8 A $g^{-1}$), 188.1 (1 A $g^{-1}$), and 124.1 mAh $g^{-1}$ (2 A $g^{-1}$). When the current density was returned to 0.1 A $g^{-1}$, the capacity recovered to 592.8 mAh $g^{-1}$ (regaining 99.9 % of its initial capacity) after 70 cycles. As for C@Sn@N-doped carbon-III, it displayed much higher capacity at low current density. With increasing current rate, the capacity declined more quickly, and it showed very poor recovery capability compared to the other composites. The results are as follows: 758.1 (50 mA $g^{-1}$), to 670.1 (100 mA $g^{-1}$), 549.5 (200 mA $g^{-1}$), 371.4 (400 mA $g^{-1}$), 235.2 (800 mA $g^{-1}$), 178.6 (1 A $g^{-1}$), and 117.9 mAh $g^{-1}$ (2 A $g^{-1}$). After the current rate was restored to 0.1 A $g^{-1}$, the capacity could only reach 436.5 mAh $g^{-1}$ (very low capacity retention, recovering only 64.3% of its initial capacity) after 70 cycles.

A comparison of the performance of C@Sn@N-doped carbon with some C/Sn-based anode materials is presented in Table 6.2. From there, it can be seen that the overall performance of the C@Sn@N-doped carbon is very good in terms of reversible capacity (398.4 mA h $g^{-1}$ at 100 mA $g^{-1}$), although it is not the very best performance.

Fig.6.6d displays the discharge–charge voltage profiles of the initial three half cycles for C@Sn@N-doped carbon-II. The 1$^{st}$ half cycle discharge and 2$^{nd}$ half cycle charge capacities of the C@Sn@N-doped carbon-II composite electrode are 1283.1 and 593.3 mAh $g^{-1}$, respectively, delivering an initial coulombic efficiency of 46%. This is believed to be due to the creation of a solid electrolyte interphase (SEI) film between the Sn nanoparticles and the electrolyte.

To analyze the electrochemical reactions occurring in the C@Sn@N-doped carbon-II electrode, cyclic voltammetry (CV) was conducted. It can be observed in Fig.6.6e, there is a cathodic slope from 1.38 to 1.05 V in the first negative scan, which is attributed to the interaction between $Na^+$ and the surface functional groups of carbon.[13] In the following cathodic scan, a broad integrated peak starting at 0.75 V and ending at 0.3V can be detected, which is assigned to the formation of the SEI layer, with the alloying between Sn and Na forming $NaSn_5$ and, NaSn, and promoting $Na^+$ insertion into carbon. The two weakly reductive peaks appearing at 0.2 and 0.01 V indicate the formation of $Na_9Sn_4$ and $Na_{15}Sn_4$.[23,24] In the following anodic scan, three well-defined oxidative peaks can be observed at 0.2, 0.55, and 0.7 V, which are assigned to de-sodiation from

**Table 6.2** Performance comparison of our current work with previously published reports related to C/Sn-based anode materials for SIBs.

| Materials | Rate performance | Reversible capacity | Cycles | Ref. |
|---|---|---|---|---|
| Sn/Cu Nanocomposite | 126 mA h $g^{-1}$ at 1.69A $g^{-1}$ | 420 mA h $g^{-1}$ at 169 mA $g^{-1}$ | 100 | [8] |
| C/Sn/Ni/TMV | ------ | 405 mA h $g^{-1}$ at 50 mA $g^{-1}$ | 150 | [9] |
| Sn@Wood fiber | ------ | 145 mA h $g^{-1}$ at 84 mA $g^{-1}$ | 400 | [10] |
| Sn@CNT-CP | 299 uA h $cm^{-2}$ at 1 mA $cm^{-2}$ | 377 uA h $cm^{-2}$ at 0.5 mA $cm^{-2}$ | 100 | [11] |
| 8-Sn@C | 349 mA h $g^{-1}$ at 4A $g^{-1}$ | 415 mA h $g^{-1}$ at 1A $g^{-1}$ | 500 | [12] |
| Porous C/Sn | ------ at 20 mA $g^{-1}$ | 200 mA h $g^{-1}$ | 15 | [23] |
| C@Sn@N-doped carbon | 124.1 mAh $g^{-1}$ at 2 A $g^{-1}$ | 398.4 mA h $g^{-1}$ at 100 mA $g^{-1}$ | 150 | this study |

$Na_9Sn_4$, NaSn, and $NaSn_5$, respectively. From the second cathodic scan, three dominant reduction peaks appearing at 0.75 V, 0.2 V, and 0.01 V are considered to be due to the formation of $Na_xSn$, $Na_9Sn_4$, and $Na_{15}Sn_4$.[25] The above analysis results are very similar to the results from the charge–discharge curves of the C@Sn@N-doped carbon-II electrode shown in Fig.6.6d.

By conducting electrochemical impedance spectroscopy (EIS), we further analysed the effects of N-doped carbon towards improving the cyclability of C@Sn@N-doped carbon electrode, which had better retention of electronic conductivity than the bare Sn

electrode. Fig.6.6f. displays the Nyquist plots, with the insert showing the equivalent electrical circuit, wherein, the total resistance of the electrolyte and cell components is represented by $R_t$. The charge transfer resistance ($R_{ct}$), appearing as the depressed semicircle in the high frequency range, reflects the impedance connected to the passage of the $Na^+$ ions through the film surface and the charge transfer between the active material and the electrolyte. The Warburg impedance ($W$) can be found from the sloping line located in the low frequency region. It is attributed to the charge transfer due to sodium ion diffusion inside the active material or electrolyte. The constant phase element (CPE) is used to replace the pure capacitance. It can be observed that the charge transfer resistance ($R_{ct}$) of bare Sn has changed significantly between the fresh electrode and after 150 cycles. The value increased from 230.3 to 906.9 Ω. This result is consistent with the changes in the morphology of the Sn electrode after cycling, as shown in Fig.7.7b and 7.7d, where the morphology of the bare Sn electrode after cycling features very obvious cracks. For C@Sn@N-doped carbon-II, the charge transfer resistance ($R_{ct}$) changed slightly from 284.1 to 328.9 Ω after experiencing cycling from the fresh cell to over 150 cycles. This small change demonstrates that the C@Sn@N-doped carbon-II electrode can maintain its electrical conductivity very well. As shown in Fig.6.7a and 6.7c, there are no obvious cracks in the C@Sn@N-doped carbon composite electrode after cycling, which is attributed to the 3-D structural features of C@Sn@N-doped carbon-II, which provides void space between the tubes that could withstand the large volume expansion during charging/discharging. Furthermore, the homogeneous distribution of Sn nanoparticles on the surface of the N-doped carbon matrix is also an important factor in providing homogeneity to the whole composite, so as to keep the electrochemical properties stable. The improved electrochemical performance of the C@Sn@N-doped carbon composites compared with pure Sn is due to the synergistic effects generated among the Sn nanoparticles, the carbon coating layer on the surfaces of the Sn nanoparticles and the N-doped carbon conductive matrix. Firstly, the Sn nanoparticles as the main active component are responsible for the main contribution to the high specific capacity. Secondly, the carbon coating layer on the Sn nanoparticles serves multiple functions: (i) The carbon coating layer acts as an adhesive interface to bind the Sn nanoparticles and the N-doped carbon network together to form

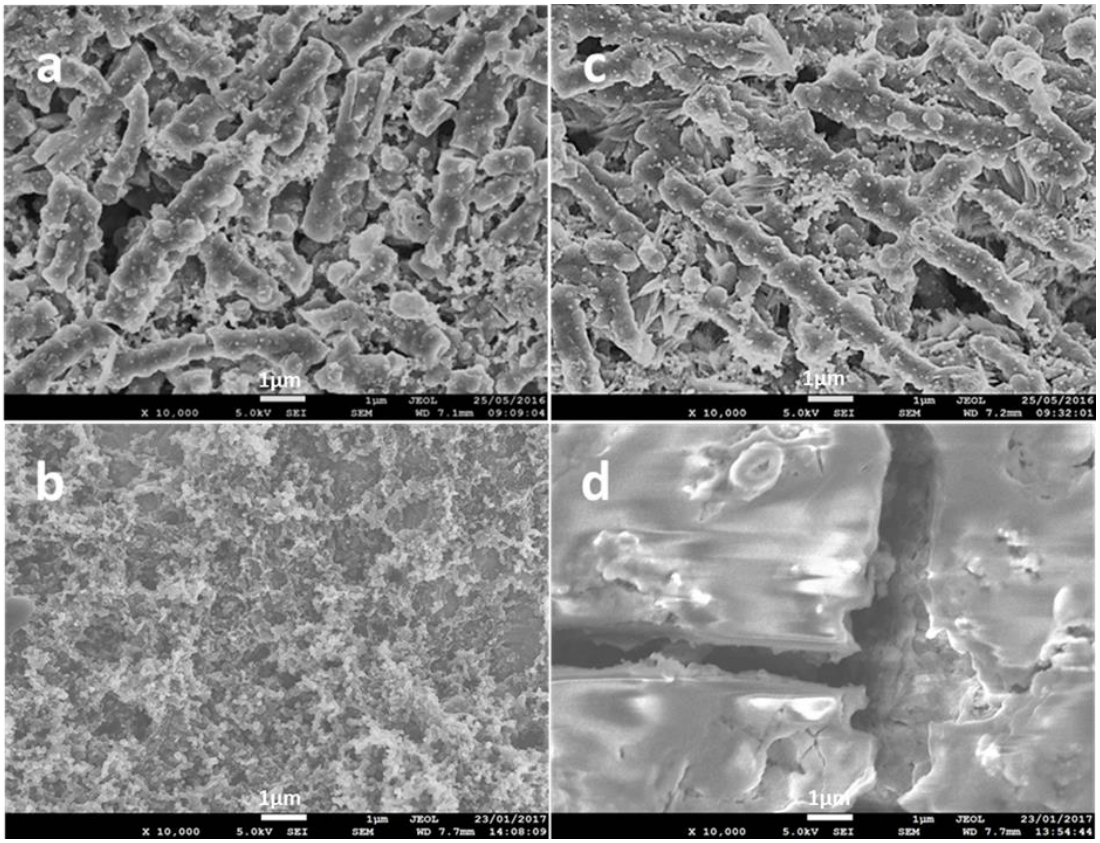


**Figure 6.7** SEM images of C@Sn@N-doped carbon-II (Sn 62.6%) composite electrodes before the charge/discharge testing (a), after 150 charge/discharge cycles (c); Fresh Sn particle electrode (b), and Sn particle electrode after 150 cycles (d).

a conducting matrix to improve the conductivity of the composite; (ii) The carbon coating layer can withstand the large volume expansion of the electrode in the process of cycling to maintain the integrity of the electrode; (iii) The carbon coating layer prevents agglomeration of Sn nanoparticles during cycling to improve cycling stability. Lastly, the N-doped carbon network with 3-D structure not only enables sufficient infiltration of electrolyte, but also provides more reactive sites arising from the nitrogen doping.[26] Furthermore, the N-doped carbon can contribute capacity to the Na-ion batteries, as shown in Fig. 6b. Therefore, the C@Sn@N-doped carbon composites exhibit improved electrochemical performance, resulting from both the structure of the carbon coated Sn nanoparticles and the continuous 3-D reaction network formed by the N-doped carbon.

## 6.4. Conclusions

In summary, C@Sn@N-doped carbon composites were obtained with Sn particles confined in the framework of N-doped carbon via an easy, convenient, and environmentally friendly approach. The 3-D structured C@Sn@N-doped carbon tube network exhibited good electrochemical properties as a candidate anode that could be applied in SIBs, in terms of its cycling performance (up to 150 cycles), with 99.7% coulombic efficiency and good rate capability. The initial charge capacity was restored to 99.7% after continuous current alteration from 50 mA $g^{-1}$ to 2 A $g^{-1}$. The good experimental results are mainly attributed to the homogeneous distribution of carbon-encapsulated Sn nanoparticles on the N-doped carbon matrix with its distinct 3-D structure, which plays the role of alleviating the stress caused by the volume expansion of the electrode during the charge/discharge process. From another aspect, the carbon coating on the surfaces of the Sn nanoparticles can maintain the stability of the electrode structure by inhibiting the growth and agglomeration of Sn grains and reducing the polarization effect. Therefore, the results clearly demonstrate that the improved electrochemical performance of the C@Sn@N-doped carbon composites benefits from the synergistic effect generated among the carbon coated Sn nanoparticles and the N-doped carbon conductive matrix, which makes it possible to obtain the best utilization of $Na^+$ during insertion/extraction.

## 6.5. References

1. Chevrier, V.; Ceder, G., Challenges for Na-ion negative electrodes. *Journal of The Electrochemical Society* **2011,** *158* (9), A1011-A1014.

2. Mortazavi, M.; Ye, Q.; Birbilis, N.; Medhekar, N. V., High capacity group-15 alloy anodes for Na-ion batteries: Electrochemical and mechanical insights. *J. Power Sources* **2015,** *285*, 29-36.

3. Galloway, R. C.; Haslam, S., The ZEBRA electric vehicle battery: power and energy improvements. *J. Power Sources* **1999,** *80* (1), 164-170.

4. Li, Z.; Ding, J.; Mitlin, D., Tin and Tin Compounds for Sodium Ion Battery Anodes: Phase Transformations and Performance. *Acc. Chem. Res.* 2015**,** *48* (6), 1657-1665.

5. Wang, J. W.; Liu, X. H.; Mao, S. X.; Huang, J. Y., Microstructural Evolution of Tin Nanoparticles During in Situ Sodium Insertion and Extraction. *Nano Lett.* 2012**,** *12* (11), 5897-5902.

6. Komaba, S.; Matsuura, Y.; Ishikawa, T.; Yabuuchi, N.; Murata, W.; Kuze, S., Redox Reaction of Sn-Polyacrylate Electrodes in Aprotic Na Cell. *Electrochem. Commun.* 2012**,** *21*, 65-68.

7. Farbod, B.; Cui, K.; Kalisvaart, W. P.; Kupsta, M.; Zahiri, B.; Kohandehghan, A.; Lotfabad, E. M.; Li, Z.; Luber, E. J.; Mitlin, D., Anodes for Sodium Ion Batteries Based on Tin–Germanium–Antimony Alloys. *ACS nano* 2014**,** *8* (5), 4415-4429.

8. Lin, Y.-M.; Abel, P. R.; Gupta, A.; Goodenough, J. B.; Heller, A.; Mullins, C. B., Sn–Cu Nanocomposite Anodes for Rechargeable Sodium-Ion Batteries. *ACS Appl. Mater. Interfaces* 2013**,** *5* (17), 8273-8277.

9. Liu, Y.; Xu, Y.; Zhu, Y.; Culver, J. N.; Lundgren, C. A.; Xu, K.; Wang, C., Tin-Coated Viral Nanoforests as Sodium-Ion Battery Anodes. *Acs Nano* 2013**,** *7* (4), 3627-3634.

10. Zhu, H.; Jia, Z.; Chen, Y.; Weadock, N.; Wan, J.; Vaaland, O.; Han, X.; Li, T.; Hu, L., Tin Anode for Sodium-Ion Batteries Using Natural Wood Fiber as a Mechanical Buffer and Electrolyte Reservoir. *Nano Lett.* 2013**,** *13* (7), 3093-3100.

11. Xie, X.; Kretschmer, K.; Zhang, J.; Sun, B.; Su, D.; Wang, G., Sn@ Cnt Nanopillars Grown Perpendicularly on Carbon Paper: A Novel Free-Standing Anode for Sodium Ion Batteries. *Nano Energy* 2015**,** *13*, 208-217.

12. Liu, Y.; Zhang, N.; Jiao, L.; Tao, Z.; Chen, J., Ultrasmall Sn Nanoparticles Embedded in Carbon as High-Performance Anode for Sodium-Ion Batteries. *Adv. Funct. Mater.* 2015**,** *25* (2), 214-220.

13. Wang, H. g.; Wu, Z.; Meng, F. l.; Ma, D. l.; Huang, X. l.; Wang, L. m.; Zhang, X. b., Nitrogen-Doped Porous Carbon Nanosheets as Low-Cost, High-Performance Anode Material for Sodium-Ion Batteries. *ChemSusChem* 2013**,** *6* (1), 56-60.

14. Fu, L.; Tang, K.; Song, K.; van Aken, P. A.; Yu, Y.; Maier, J., Nitrogen Doped Porous Carbon Fibres as Anode Materials for Sodium Ion Batteries with Excellent Rate Performance. *Nanoscale* 2014**,** *6* (3), 1384-1389.

15. Wang, Z.; Qie, L.; Yuan, L.; Zhang, W.; Hu, X.; Huang, Y., Functionalized N-Doped Interconnected Carbon Nanofibers as an Anode Material for Sodium-Ion Storage with Excellent Performance. *Carbon* 2013**,** *55*, 328-334.

16. Ruan, B.; Wang, J.; Shi, D.; Xu, Y.; Chou, S.; Liu, H.; Wang, J., A Phosphorus/N-Doped Carbon Nanofiber Composite as an Anode Material for Sodium-Ion Batteries. *J. Mater. Chem. A* 2015**,** *3* (37), 19011-19017.

17. Yang, X.; Zhu, Z.; Dai, T.; Lu, Y. Facile Fabrication of Functional Polypyrrole Nanotubes Via a Reactive Self-Degraded Template. *Macromol. Rapid Commun.* 2005, 26, 1736−1740.

18. Yang, X.; Zhu, Z.; Dai, T.; Lu, Y., Facile Fabrication of Functional Polypyrrole Nanotubes Via a Reactive Self-Degraded Template. *Macromol. Rapid Commun.* 2005**,** *26* (21), 1736-1740.

19. Park, M.-S.; Kang, Y.-M.; Kim, J.-H.; Wang, G.-X.; Dou, S.-X.; Liu, H.-K., Effects of Low-Temperature Carbon Encapsulation on the Electrochemical Performance of Sno 2 Nanopowders. *Carbon* 2008**,** *46* (1), 35-40.

20. Zhu, Z.; Wang, S.; Du, J.; Jin, Q.; Zhang, T.; Cheng, F.; Chen, J., Ultrasmall Sn Nanoparticles Embedded in Nitrogen-Doped Porous Carbon as High-Performance Anode for Lithium-Ion Batteries. *Nano Lett.* 2013**,** *14* (1), 153-157.

21. Jahel, A.; Ghimbeu, C. M.; Darwiche, A.; Vidal, L.; Hajjar-Garreau, S.; Vix-Guterl, C.; Monconduit, L., Exceptionally Highly Performing Na-Ion Battery Anode Using Crystalline $SnO_2$ Nanoparticles Confined in Mesoporous Carbon. *J. Mater. Chem. A* 2015**,** *3* (22), 11960-11969.

22.http://chemistry.about.com/od/moleculescompounds/a/Table-Of-Electrical-Resistivity -And-Conductivity.htm

23. Xu, Y.; Zhu, Y.; Liu, Y.; Wang, C., Electrochemical Performance of Porous Carbon/Tin Composite Anodes for Sodium-Ion and Lithium-Ion Batteries. *Adv. Energy Mater.* 2013**,** *3* (1), 128-133.

24. Chen, W.; Deng, D., Sodium-Cutting: A New Top-Down Approach to Cut Open Nanostructures on Nonplanar Surfaces on a Large Scale. *Chem. Commun.* 2014**,** *50* (87), 13327-13330.

25. Liu, Y.; Xu, Y.; Zhu, Y.; Culver, J. N.; Lundgren, C. A.; Xu, K.; Wang, C., Tin-Coated Viral Nanoforests as Sodium-Ion Battery Anodes. *ACS Nano* 2013**,** *7* (4), 3627-3634.

26. Su, F.; Poh, C. K.; Chen, J. S.; Xu, G.; Wang, D.; Li, Q.; Lin, J.; Lou, X. W., Nitrogen-Containing Microporous Carbon Nanospheres with Improved Capacitive Properties. *Energy Environ. Sci.* 2011**,** *4* (3), 717-724.

# Chapter 7

# General Conclusions and Outlook

## 7.1. General Conclusions

This doctoral work investigates some promising anode materials for SIBs, phosphorus-based and tin–based electrodes, chosen for their potential high capacity for sodium storage and ability to sustain long-term cycling. By adopting a facile CVD method, phosphorus/N-doped carbon nanofiber composite was prepared. Through a simple hydrothermal approach, 3-D structured $SnO_2$–polypyrrole nanotubes and carbon-encapsulated Sn@N-doped carbon nanotubes were fabricated. Both phosphorus-based and tin–based composites were combined with conductive N-doped carbon nanofibers or PPy nanotubes and showed improved electrochemical performance owing to their stable 3-D structured matrix, which played the role of alleviating the stress caused by the volume expansion of the electrode during the charge−discharge process.

### 7.1.1. A phosphorus/N-doped carbon nanofiber (P/NCF)

P/NCF was fabricated via a simple CVD approach adopting N-doped carbon nanofibers as the matrix to host the red phosphorus nanoparticles. The P/NCF composite electrode exhibited a high reversible capacity of over 850 mA h $g^{-1}$ in the first 10 cycles and maintained a reversible capacity of 731 mA h $g^{-1}$ after 55 cycles. The N-doped carbon nanofibers play a crucial role in the P/NCF composite. The N-doped carbon fibers with porous structure can effectively alleviate the enormous stresses from the volume expansion of the P particles and reduces the pulverization of particles. On the other hand, the presence of nitrogen species on the carbon surface can lead to a pseudo-capacitive interaction between the electrolyte ions and the nitrogen-containing

functional groups, enhancing capacity, surface wettability, and electronic conductivity. My work gives clear evidence of the utility of N-doped carbon fiber for enhancing the electrochemical performance of red phosphorus as an anode material for sodium-ion batteries.

### 7.1.2. $SnO_2$–polypyrrole nanotubes ($SnO_2$–PPy nanotube)

$SnO_2$–PPy nanotube was prepared by a facile hydrothermal method. The PPy tubes were adopted as the substrate material, and the active $SnO_2$ nanoparticles were anchored on their surfaces. The obtained 3-D structured $SnO_2$–PPy nanotube network demonstrated good performance as an anode for application in SIBs, especially with regards to the cyclability (over 150 cycles), with a high coulombic efficiency of 99.6% and good rate capability, recovering up to 99.7% of the initial charge capacity after several current variation cycles from 50 mA $g^{-1}$ to 1 A $g^{-1}$. These outcomes are attributed to the uniform coating of nanoscale tin dioxide particles on the PPy matrix with its unique 3-D structure, which can significantly improve the electronic conductivity of composites and acts as a buffer to alleviate the strain resulting from the volume changes in the electrode during cycling.

### 7.1.3. Carbon-encapsulated Sn@N-doped carbon tubes (C@Sn@N-Doped Carbon)

C@Sn@N-Doped Carbon nanotube composite with 3-D structure was obtained via a user-friendly hydrothermal method taking N-doped carbon nanotubes as the substrate and confining the Sn nanoparticles on their surfaces. The C@Sn@N-doped carbon nanotube network displayed the good reversible capacity of 398.4 mAh $g^{-1}$ on discharging at 100 mA $g^{-1}$, with capacity retention of 67.3 % and very high Coulombic efficiency of 99.7% after 150 cycles. Meanwhile, good rate capability was also obtained, based on varying the current density from 50 mA $g^{-1}$ to 2 A $g^{-1}$ during cycling. The good experimental results are mainly attributed to the homogeneous distribution of carbon-encapsulated Sn nanoparticles on the N-doped carbon matrix with its distinct 3-

D structure, which plays the role of alleviating the stress caused by the volume expansion of the electrode during the charge/discharge process. From another aspect, the carbon coating on the surfaces of the Sn nanoparticles can maintain the stability of the electrode structure by inhibiting the growth and agglomeration of Sn grains and reducing the polarization effect. The results clearly demonstrated that the improved electrochemical performance of the C@Sn@N-doped carbon composites benefits from the synergistic effect generated between the carbon coated Sn nanoparticles and the N-doped carbon conductive matrix, which makes it possible to obtain the best utilization of $Na^+$ during insertion/extraction.

## 7.2. Outlook

This doctoral work mainly focused on facile preparation strategies for phosphorus or tin-based anode materials and on characterizing their electrochemical performance in SIBs. The investigated materials all possess the outstanding advantages of non-toxicity, high specific capacity, and low cost, making them promising electrode candidates for SIBs. The synthesis methods utilized in this doctoral work were just simple CVD and hydrothermal methods. The morphologies of all these materials are 3-D structures. This not only provides good structural robustness and short ion/electron diffusion pathways, but also promotes the diffusion of the electrolyte into the inner spaces of the material, as well as providing sufficient open channels for fast $Na^+$ migration. To improve the cycling performance of the electrode materials in SIBs, the main strategies used in this doctoral work involved forming alloy compounds or composites with carbon. The shortcoming of this strategy is that inactive carbon and metal materials are introduced, reducing the total specific capacity of the electrodes. Therefore, in future work, I will focus on optimizing the structure of N-doped carbon with other transition metal elements.

# Appendix: Publications

**1, Boyang Ruan,** Jun Wang, Dongqi Shi, Yanfei Xu, Shulei Chou, Huakun Liu and Jiazhao Wang* A phosphorus/N-doped carbon nanofiber composite as an anode material for sodium-ion batteries, *Journal of Materials Chemistry A*, 2015, 3, 19011-19017. IF = 8.262 (Results presented in Chapter 4)

**2, Boyang Ruan,** Haipeng Guo, Qiannan Liu, Dongqi Shi, Shulei Chou, Huakun Liu, Guohua Chen and Jiazhao Wang*, 3-D structured $SnO_2$–polypyrrole nanotubes applied in Na-ion batteries, *RSC Adv.*, 2016, 6, 103124-103131. IF =3.108 (Results presented in Chapter 5)

**3**, **Boyang Ruan**, Hai-peng Guo, Yuyang Hou, Qiannan Liu, Yuanfu Deng, Guohua Chen, Shu-lei Chou, Hua-kun Liu, Jia-zhao Wang*, Carbon Encapsulated Sn@N-doped Carbon Nanotubes as Anode Materials for Application in SIBs, ***ACS Applied Materials & Interfaces***, 2017, 9, 37682−37693. IF = 7.504 (Results presented in Chapter 6)

**4**, Yuhai Dou, Yunxiao Wang, Dongliang Tian, Jiantie Xu, Zhijia Zhang, Qiannan Liu1, **Boyang Ruan,** JianminMa*, Ziqi Sun* and Shi Xue Dou* Atomically thin Co3O4 nanosheet-coated stainless steel mesh with enhanced capacitive $Na^+$ storage for high-performance sodium-ion batteries, ***2D Materials***, 2017,4,015022. IF =6.937

**5**, Haipeng Guo, **Boyang Ruan,** Lili Liu, Lei Zhang, Zhanliang Tao, Shulei Chou, Jiazhao Wang,* and Huakun Liu*, Capillary-Induced Ge Uniformly Distributed in N-Doped Carbon Nanotubes with Enhanced Li-Storage Performance, ***Small*** 2017, 13, 1700920. IF = 8.643

**6**, Yuhai Dou, Jiantie Xu, **Boyang Ruan**, Qiannan Liu, Yuede Pan, Ziqi Sun,* and Shi Xue Dou*, Atomic Layer-by-Layer $Co_3O_4$/Graphene Composite for High Performance Lithium-Ion Batteries, ***Adv. Energy Mater.*** 2016, 6, 1501835. IF = 16.721

**7,** Qiannan Liu, Yuhai Dou, **Boyang Ruan**, Ziqi Sun,* Shu-Lei Chou,* and Shi Xue Dou, Carbon-Coated Hierarchical $SnO_2$ Hollow Spheres for Lithium Ion Batteries, ***Chem. Eur. J.*** 2016, 22, 5853 – 5857. IF =5.317

**8,** Lei Wang, **Boyang Ruan**, Jiantie Xu, Hua Kun Liu* and Jianmin Ma*, Amorphous carbon layer contributing Li storage capacity to $Nb_2O_5$@C nanosheets, ***RSC Adv.,*** 2015, 5, 36104-36107. IF = 3.108